



**NIST Internal Report
NIST IR 8455**

Low-GWP Non-Flammable Alternative Refrigerant Blends for HFC-134a: Final Report

*Strategic Environmental Research and Development
Program Project: WP 19-1385*

Principal Investigators:
Piotr A. Domanski
Mark O. McLinden

Co-Authors:
Valeri I. Babushok
Ian H. Bell
Tara J. Fortin
Michael J. Hegetschweiler
Marcia L. Huber
Mark A. Kedzierski
Dennis K. Kim
Lingnan Lin
Gregory T. Linteris
Stephanie L. Outcalt
W. Vance Payne
Richard A. Perkins
Aaron Rowane
Harrison Skye

This publication is available free of charge from:
<https://doi.org/10.6028/NIST.IR.8455>

NIST Internal Report
NIST IR 8455

Low-GWP Non-Flammable Alternative Refrigerant Blends for HFC-134a: Final Report

*Strategic Environmental Research and Development
Program Project: WP 19-1385*

Piotr A. Domanski
Valeri I. Babushok
Michael J. Hegetschweiler
Lingnan Lin
Mark A. Kedzierski
Dennis K. Kim
Gregory T. Linteris
W. Vance Payne
Harrison Skye

*Building Energy and Environment Division
Engineering Laboratory*

Mark O. McLinden
Ian H. Bell
Tara J. Fortin
Stephanie Outcalt
Richard A. Perkins
Aaron Rowane

*Applied Chemicals and Materials Division
Material Measurement Laboratory*

This publication is available free of charge from:
<https://doi.org/10.6028/NIST.IR.8455>

January 2023



U.S. Department of Commerce
Gina M. Raimondo, Secretary

National Institute of Standards and Technology
Laurie E. Locascio, NIST Director and Under Secretary of Commerce for Standards and Technology

Certain commercial entities, equipment, or materials may be identified in this document in order to describe an experimental procedure or concept adequately. Such identification is not intended to imply recommendation or endorsement by the National Institute of Standards and Technology, nor is it intended to imply that the entities, materials, or equipment are necessarily the best available for the purpose.

NIST Technical Series Policies

[Copyright, Fair Use, and Licensing Statements](#)

[NIST Technical Series Publication Identifier Syntax](#)

Publication History

Approved by the NIST Editorial Review Board on 2023-01-03

How to Cite this NIST Technical Series Publication

Domanski, P., McLinden, M., Babushok, V., Bell, I., Fortin, T., Hegetschweiler, M., Kedzierski, M., Kim, D., Lin, L., Linteris, G., Outcalt, S., Payne, W., Perkins, R., Rowane, A., and Skye, H. (2023), Low-GWP Non-Flammable Alternative Refrigerant Blends for HFC-134a: Final Report. National Institute of Standards and Technology, Gaithersburg, MD, NIST Interagency/Internal Report (NISTIR) 8455. <https://doi.org/10.6028/NIST.IR.8455>

NIST Author ORCID iDs

Domanski, P.	0000-0003-1915-2170
McLinden, M.	0000-0002-1082-309X
Babushok, V.	0000-0001-9257-6872
Bell, I.	0000-0003-1091-9080
Fortin, T.	0000-0001-6150-8930
Hegetschweiler, M.	0000-0003-4164-7436
Kedzierski, M.	0000-0001-5051-1819
Kim, D.	0000-0003-0188-9895
Lin, L.	0000-0002-0813-7613
Linteris, G.	0000-0001-7232-5742
Outcalt, S.	0000-0001-8143-7316
Payne, W.	0000-0003-2852-1302
Perkins, R.	0000-0002-8526-6742
Rowane, A.	0000-0001-7605-0774
Skye, H.	0000-0001-6118-0699

Contact Information

piotr.domanski@nist.gov

mark.mclinden@nist.gov

Abstract

This project addresses the objectives of the Statement of Need number WPSON-17-02 for “No/Low Global Warming Potential Alternatives to Ozone Depleting Refrigerants” issued by the Strategic Environmental Research and Development Program (SERDP), the U.S. Department of Defense (DoD) environmental science and technology program, planned and executed in full partnership with the U.S. Department of Energy and the U.S. Environmental Protection Agency. The goal of this Statement of Need was to identify low global-warming-potential (GWP), non-flammable refrigerants to replace HFC-134a (GWP = 1300) in military equipment.

This work is a follow-on to the SERDP limited-scope project WP-2740, carried out at NIST, which used thermodynamic cycle simulation models alone to screen over 100 000 refrigerant blends and identified over 20 candidate HFC-134a replacements. In the present study we narrowed the pool of blend candidates down to three “best” blends, demonstrated their performance through “drop-in” tests in a military environmental control unit (ECU) in environmental chambers over a wide range of operating conditions. Through simulation the laboratory-measured performance was extrapolated to that of ECUs equipped with a compressor modified for each blend to provide the same system capacity while maintaining the isentropic efficiency of the original HFC-134a compressor.

The project involved preliminary experimental and analytical tasks in support of the final project task. These included measurements of thermodynamic and transport properties of the novel fluids considered and an update of simulation methods for these properties, fundamental tests exploring the flammability characteristics including calculation methods, fundamental measurements and modeling of forced-convection heat transfer performance, and measurements of cycle performance of candidate blends in a laboratory mini-breadboard heat pump apparatus as the final qualification step of the “best” blends for full-scale testing in the ECU.

The project’s conclusion is that R-513A (GWP = 573) and a blend we call Tern-1 [R-134a/1234yf/1234ze(E) (49.2/33.9/16.9^{*}), GWP = 640] are good replacement blends for HFC-134a offering a similar capacity and coefficient of performance at GWP reduction of 66 % and 51 %, respectively. These fluids do not present any significant application difficulties. If greater reduction in GWP is desirable, R-515B (GWP = 344) can be considered but it requires further challenging research and developmental work.

The GWP reduction also depends on the stringency of the military requirements for “non-flammability”. At the time of execution of the project, military requirements for non-flammability had not been established. For this reason, we used the ASTM E681 test method as stipulated by ASHRAE Standard 34 for qualifying non-flammability. If military requirements for ‘non-flammability’ are more stringent than the E681 standard, a smaller reduction of GWP will be possible with qualifying blends.

^{*} Composition stated as mass fraction (%)

Executive Summary

Introduction

Concerns about the stratospheric ozone layer and climate change resulted in regional [1] and global [2, 3] regulations that limit the production and consumption of fluorinated refrigerants, which are the dominant fluids currently used in refrigeration and air-conditioning systems, including military equipment. In the United States, the use of high-GWP hydrofluorocarbon (HFC) refrigerants is regulated by the American Innovation and Manufacturing (AIM) Act [4], which directed the U.S. Environmental Protection Agency to establish a phasedown program and sector-based HFC restrictions to facilitate the transition to next-generation technologies.

The above concerns and regulations have spurred intensive global research for next generation hydrofluoroolefin (HFO) low-GWP fluids. These research efforts showed that the availability of low-GWP refrigerants varies between applications and is rather limited for medium- and high-pressure systems. Notable applications where HFC-134a was already successfully replaced by low-GWP refrigerants are mobile air conditioners (HFO-1234yf, mildly flammable) and domestic refrigerators (isobutane, highly flammable); however, these fluids are not acceptable for military systems due to their flammability. Prior screening studies [5] found that all single-component refrigerants that could serve with good performance as a replacement for HFC-134a are at least mildly flammable. For this reason, the search for non-flammable replacements for HFC-134a in military systems is focused on refrigerant blends.

Objectives

This work addresses the objectives of the Statement of Need number WPSON-17-02 “No/Low Global Warming Potential Alternatives to Ozone Depleting Refrigerants”, issued by the Strategic Environmental Research and Development Program (SERDP), the U.S. Department of Defense (DoD) environmental science and technology program, planned and executed in full partnership with the U.S. Department of Energy and the U.S. Environmental Protection Agency. The goal of this Statement of Need was to identify low global-warming-potential (GWP), non-flammable refrigerants to replace HFC-134a (GWP = 1300) in military equipment. The selection criteria also include coefficient of performance (COP), volumetric capacity (Q_{vol}), and toxicity.

This work is a follow-on of the SERDP limited-scope project WP-2740, which screened over 100 000 refrigerant blends and identified over 20 promising HFC-134a replacements [6]. The objective of this core project was to narrow the pool of blend candidates down to three “best” fluids, experimentally verify their non-flammability, and demonstrate their performance through tests in an HFC-134a military ECU in environmental chambers over a wide range of operating conditions. In a post-experimental phase, this work also evaluated the performance potential of the candidate blends through ECU simulations with the compressor and heat exchangers optimized for each of the blends.

Technical Approach

The starting point of this core project was the outcome of the limited-scope project [6], which identified over 20 candidate low-GWP blends following an exhaustive, simulation-based search and evaluation of over 100 000 two- and three-component blends among a slate of 13 single-component refrigerants, which were subsequently expanded to 14 refrigerants [7]. At the outset

of this project, we selected four blends as preliminary candidates, from which the final three blends to be evaluated by test in the ECU were selected. The criteria for blend selection consisted of the following parameters:

- Non-flammability
- Minimum GWP
- Maximum COP
- Volumetric capacity (Q_{vol}) matching that of the baseline HFC-134a
- Market availability

The following four blends were selected:

- **R-513A:** [R-134a/1234yf (44/56^{*})], GWP = 573. R-513A was identified in our limited-scope study (blend # 2). A1 ASHRAE safety classification.
- **R-450A:** [R-134a/1234ze(E) (42/58^{*})], GWP = 547. R-450A was not specifically identified in the limited-scope study; however, its make-up and performance are similar to those for blend # 9 [(R-134a/1234ze(E) (60/40^{*})]. A1 ASHRAE safety classification.
- **Tern-1:** [R-134a/1234yf/1234ze(E) (49.2/33.9/16.9^{*})], GWP = 640. This blend was identified in our limited-scope study (blend #4); it has not been classified by ASHRAE, but is expected to be “A1” based on its toxicity and flammability.
- **R-515B:** [R-1234ze(E)/227ea (91.1/8.9^{*})], GWP = 344. R-515B was not identified in the limited-scope study; however, we subsequently applied our screening analyses to it and found it to be promising. A1 ASHRAE safety classification. It has a significantly lower GWP than those of other fluids.

The project involved preliminary experimental and analytical tasks prior to ECU testing in the environmental chambers. These tasks included measurements of thermodynamic and transport properties of the considered novel fluids and an update of simulation methods for their properties, fundamental tests exploring the flammability characteristics including calculation methods, fundamental measurements and modeling of forced-convection heat transfer performance, and measurements of cycle performance of candidate blends in a laboratory mini-breadboard heat pump apparatus as the final qualification step of the “best” blends for full-scale testing in the ECU (Figure 1).

* Composition stated as mass fraction (%)

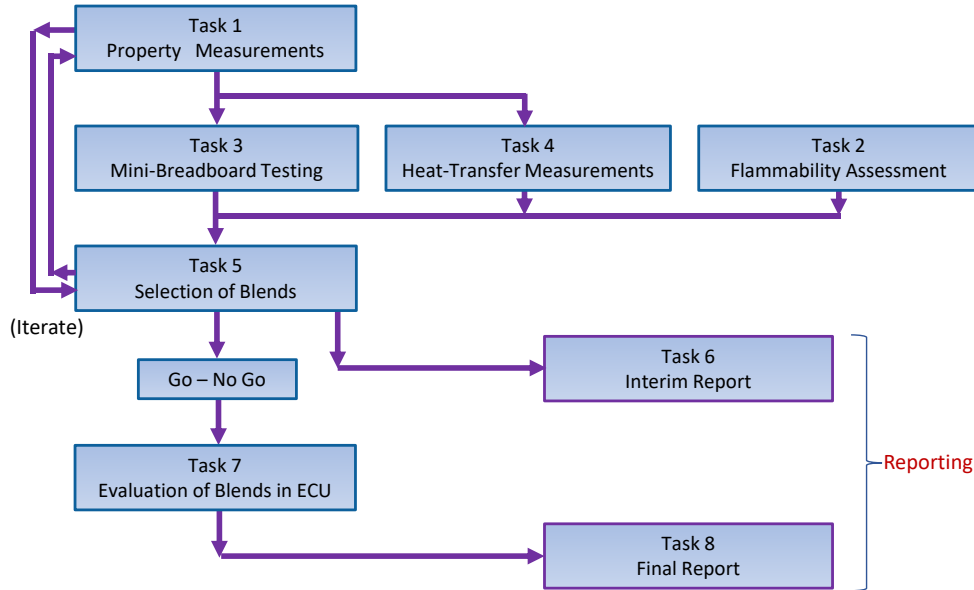


Figure 1 (Exec. Summary). Project tasks

Results and Discussion

Task 1. Experimental Measurements of Blend Properties and Development of Mixture Equation of State

We have carried out measurements on the thermophysical properties of refrigerant blends comprising next generation hydrofluoroolefins, HFO-1234yf, HFO-1234ze(E), mixed with traditional hydrofluorocarbons, HFC-134a, HFC-125, and HFC-227ea. These HFOs have very low GWP values (order of 1) but are slightly flammable; they were mixed with the nonflammable, but high-GWP, HFCs to obtain nonflammable blends with moderate values of GWP. Accurate property data are the backbone of any project to identify and verify new refrigerants; they are essential for cycle analysis, heat transfer analysis, and the analysis of system tests. These data have allowed us to improve the refrigerant mixture models needed for conducting tests in the MBHP, (Task 3), refrigerant two-phase heat-transfer tests (Task 4), and ECU tests and detailed simulations (Task 7).

While the improved property models were important for these tasks, no major deficiencies were identified in the models used in the limited-scope project; therefore, the selection of “best” blends made in the limited-scope project remained valid. These data, along with literature data, were used to develop a mixture model optimized for these HFO-containing blends; this optimized model was then used in the detailed simulations of Task 7.

For three blends (at two compositions each) we have completed comprehensive measurements comprising vapor-liquid equilibria (VLE), density (p , ρ , T , x), speed of sound, thermal conductivity, and viscosity; these measurements covered a combined temperature range of 230 K to 400 K, with pressures up to 50 MPa. For three additional blends (also at two compositions each) we carried out VLE measurements. The measurements were selected to provide an optimal data set for the purposes of fitting mixture property models. These models will be incorporated into future versions of REFPROP [8] and, thus, be made available to the entire HVAC industry.

Task 2. Flammability Assessment

It is essential in military applications that any low-GWP replacement for HFC-134a be non-flammable. This is challenging, however, since for molecules containing only hydrogen, fluorine, and carbon, there is a trade-off between GWP and flammability. The common changes to the molecules (adding hydrogen atoms or double bonds) to make them more reactive in the troposphere and hence lower their atmospheric lifetime (which lowers GWP), also makes them more flammable. Thus, one desires to make the molecules, or mixtures of compounds, have the lowest GWP possible while still maintaining non-flammable behavior. A further challenge arises, however, in that flammable behavior is not a distinct boundary, but depends upon the environment to which the refrigerant is exposed.

The primary goal of the present refrigerant flammability work was to experimentally assess the flammability of the promising blends considered for performance testing in the ECU in the environmental chambers. In the preliminary work, an empirical model of flammability based on the adiabatic flame temperature and the fluorine to hydrogen ratio of the reactants was used to create a flammability index [9] and rank a list of candidate blends with regard to their flammability. Only blends predicted to be non-flammable were considered for further study. Nonetheless, it was essential these predictions be verified by a test.

All four selected candidate blends are non-flame propagating in the modified E681 test specified in ASHRAE Standard 34. We also used a more stringent test, the Japanese high-pressure gas law test (JHPGL), in which the explosion pressure in a 2 L combustion chamber with a fused platinum wire ignition source is used, as a metric for flammability. Three of four candidate blends, Tern-1, R-513A, R-450A, had similar pressure rise (0.451 , 0.474 , and $0.262 \cdot 10^{-2}$ kPa*), while one (R-515B) had a higher pressure rise ($1.56 \cdot 10^{-2}$ kPa). Tests with binary blends of HFC-134a and HFO-1234yf with increasing fractions of HFC-134a showed that an HFC-134a mole fraction of 0.30 was required to pass the E681 tests, and at this composition, the explosion pressure in the JHPGL test was $1.27 \cdot 10^{-2}$ kPa. Hence, it appears that R-515B is close to the edge of passing the E681 test, while the other blends pass the test more easily.

A new parameter has been developed for characterizing the flammability. The overall reaction rate is a fundamentally based parameter that can be used to correlate experimental flammability results between test methods, or with full-scale test results. It is easily calculated for any arbitrary mixtures of interest and can be used to predict their flammability. In the present work, a detailed kinetic model has been developed and validated, and used to estimate the overall chemical reaction rate of the candidate blends. Both the E681 flame propagating/non-propagating boundary, as well as the JHPGL test explosion pressure were well correlated with the calculated overall reaction rate for each blend. Moreover, the calculated overall reaction rate predicts that for the candidate blends the effect of humidity in the air will be small for an increase from 0% to 50% relative humidity (r.h.), but large for an increase from 50% r.h. to 100% r.h. (all r.h. evaluated at $23\text{ }^{\circ}\text{C}$). Thus, levels of humidity above 0.014 moles $\text{H}_2\text{O}/\text{mole}$ air (50% r.h. at $23\text{ }^{\circ}\text{C}$) may have large effects on the flammability of the blends, and should be considered in any full-scale tests to be used to specify the degree of non-flammability required in military applications.

* The units 'bar' and 'atm' are commonly used units of pressure in combustion research and have a valuable physical interpretation; however, they are not SI units and hence cannot be used in NIST publications. In the present paper, we substitute ' $\cdot 10^{-2}$ kPa' for bar to retain the physical nature but make it conform to SI.

Task 3. Testing of Selected Blends in a Mini-Breadboard Heat Pump

The Mini-Breadboard Heat Pump (MBHP) was used to experimentally evaluate HFC-134a and four candidate low-GWP blends: R-513A, R-450A, R-515B, and Tern-1. The purpose of these tests was to: (1) validate the CYCLE_D-HX simulation model [10, 11] used in the limited-scope project [6], and (2) qualify the three “best” blends for testing in a military ECU (Task 7). Performance of each fluid was measured over a range of capacity including (1.3, 1.5, and 1.7) kW, where 1.5 kW was the rating point. The varying capacity provided measurements to verify the model’s prediction ability over a range of mass and heat flux. The test-to-test variation, largely driven by compressor efficiency, yielded representative average COP and Q_{vol} values with (0.5 to 1.0) % confidence intervals. In total, 121 tests were conducted.

All experimental tests were then simulated using CYCLE_D-HX. For R-513A, R-450A, and R-515B in the basic cycle (tests without the liquid-line/suction-line heat exchanger, LLSL-HX), the model-predicted values were within the confidence intervals of the experimental results. For Tern-1, the model overpredicted the experimental data by about 3 %. Importantly, the model provided the same relative COP and Q_{vol} ranking as the experimental data.

Task 4. Refrigerant Forced-Convection Heat-Transfer Testing

An experimental apparatus was used to establish and measure 432 convective-boiling heat-transfer coefficients for R-515B, R-450A, R-513A, and HFC-134a in a micro-fin tube. The measured heat-transfer coefficients were local.

The measured data were used to develop an improved correlation for the local Nusselt number for the micro-fin tube. The new correlation predicted 82.8 % of the measured convective boiling Nusselt numbers for R-515B, R-450A, R-513A, and HFC-134a to within ± 20 %. The data taken and the new correlation were tailored for use in Task 7 for simulations of the ECU system.

Task 5. Selection of Three Blends for Testing in Military ECU

We selected R-513A [R-134a/1234yf (44/56)[†]], Tern-1 [R-134a/1234yf/1234ze(E) (49.2/33.9/16.9)^{*}], and R-515B [R-1234ze(E)/227ea (91.1/8.9)^{*}] for ECU testing in the NIST environmental chambers. Each of these blends has the potential of being a fluid of choice depending on the weights applied to the selection criteria (GWP, COP, Q_{vol} , flammability characteristics). The main merits of R-513A (GWP = 573) and Tern-1 (GWP = 640) were their performance. We selected R-515B (GWP = 344) to provide an assessment of performance of this lower-GWP and lower-pressure blend should lower-GWP values be mandated in the future.

Task 6. Interim Report

The Interim Report summarized project’s results leading to tests of three blends in the ECU.

Task 7. Evaluation of Blend Performance in ECU

Military ECU Specifications and Test Facility

The tested system was a military HFC-134a air conditioner with a 19.9 kW (68000 Btu/h) rated cooling capacity (Figure 2). It was comprised of a 3-phase powered scroll compressor, finned-tube evaporator and blower, microchannel condenser and fan, and controls. The unit was designed to run continuously at part load by modulating its capacity using a hot-gas bypass with

[†] Compositions stated as mass fraction (%)

a tempering expansion valve and an evaporator pressure regulating (EPR) valve. This arrangement of components and controls would have made it impossible to execute a test program with different refrigerants. Therefore, for the purpose of this study, we disabled the hot-gas bypass and fully opened the EPR valve to produce a basic vapor-compression cycle.

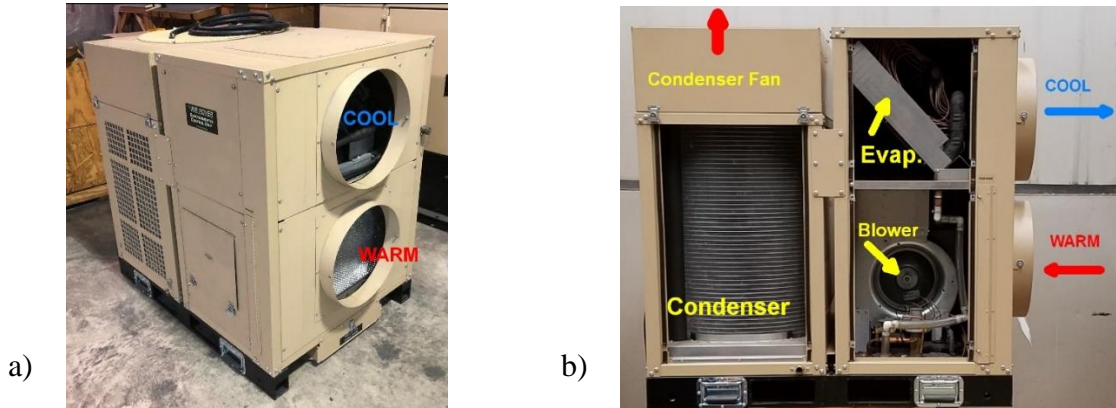


Figure 2 (Exec. Summary). ECU before installation (a). The condenser protective grid and covers for evaporator and blower were removed on the unit’s left-side in picture (b).

The test facility consisted of two adjacent environmental chambers. The ECU was installed in the outdoor chamber and supplied the conditioned air to the indoor chamber through the attached ductwork. Figure 3 shows the nozzle chamber setup used to measure the volumetric flow rate of air.

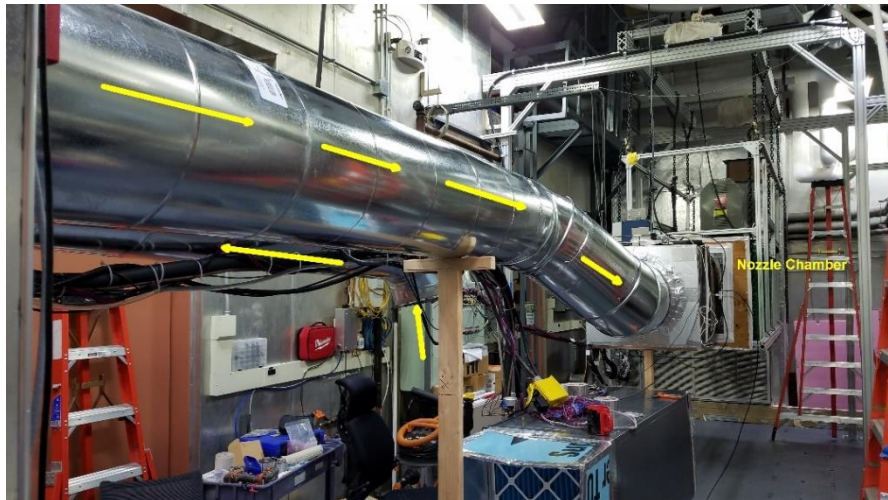


Figure 3 (Exec. Summary). Connecting ducts and nozzle chamber located in the indoor environmental chamber

The primary measurement of ECU capacity was the air enthalpy method, and the refrigerant enthalpy method served as the secondary measurement. All ductwork was thoroughly insulated and leak-tested before testing began. For standard rating points, the air-side and refrigerant-side measurements closed the energy balance within 6%.

The test metrics included four test points prescribed by the indoor condition of 26.7 °C (80.0 °F) drybulb and 15.8 °C (60.5 °F) dewpoint and four outdoor conditions: 27.8 °C (82 °F), 35.0 °C (95.0 °F), 46.1 °C (115.0 °F), and 51.7 °C (125.0 °F). For each refrigerant, the ECU was charged with refrigerant according to the procedure recommended by the manufacturer while operating at 26.7 °C (80.0 °F) indoor drybulb, 15.8 °C (60.5 °F) indoor dewpoint, and 35.0 °C (95.0 °F) outdoor drybulb. In this process, the thermostatic expansion valve (TXV) and refrigerant charge were adjusted to produce an evaporator exit superheat and condenser subcooling per manufacturer’s instruction. We refer to these tests as “drop-in” tests.

Performance of Candidate Replacement Refrigerants

Figures 4 and 5 show absolute values of air-side capacity and COP, respectively, for HFC-134a, R515B, Tern-1 and R-513A measured in environmental chambers during “drop-in” tests. The error bars reflect measurement uncertainty at the 95 % confidence level. The figure shows that there is no statistically significant difference in capacity of HFC-134a, Tern-1 and R-513A, and no statistically significant difference in COP for all fluids. R-515B has a 17 % to 23 % lower capacity than the other three fluids because it is a lower pressure fluid.

Figures 6 and 7 show differences in “drop in” capacity and COP for the tested blends with respect to the values for HFC-134a. R-513A provides a somewhat higher capacity at all test conditions. Its COP is below that of HFC-134a at 27.8 °C and 35.0 °C outdoor temperature; however, its COP is better at the higher outdoor temperature even as it delivers a higher capacity.

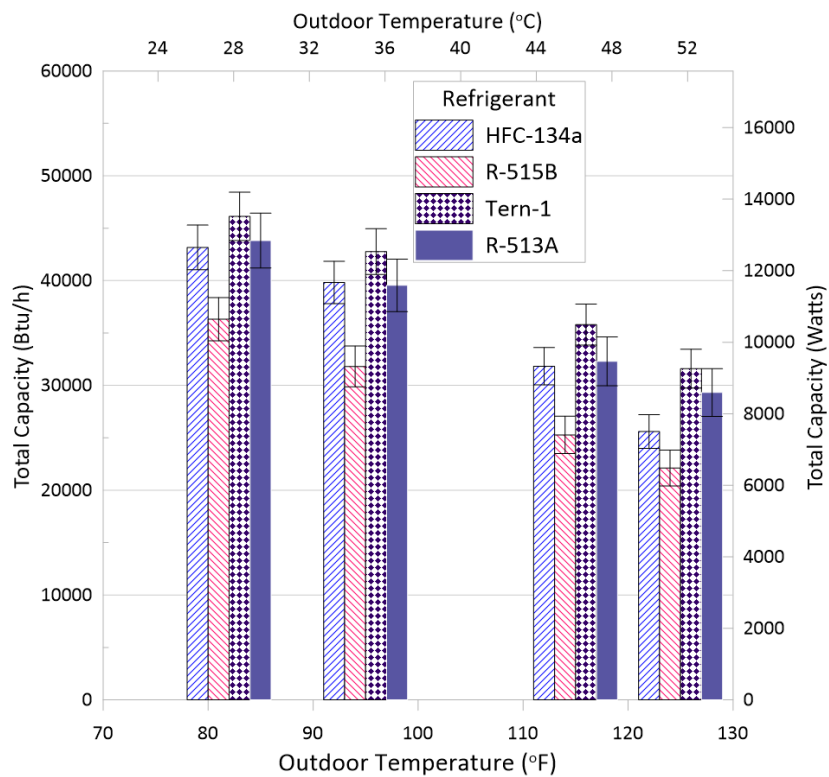


Figure 4 (Exec. Summary). ECU total capacity (air side) at outdoor temperatures 27.8 °C (82 °F), 35.0 °C (95 °F), 46.1 °C (115 °F), and 51.7 °C (125 °F) (center of bars)

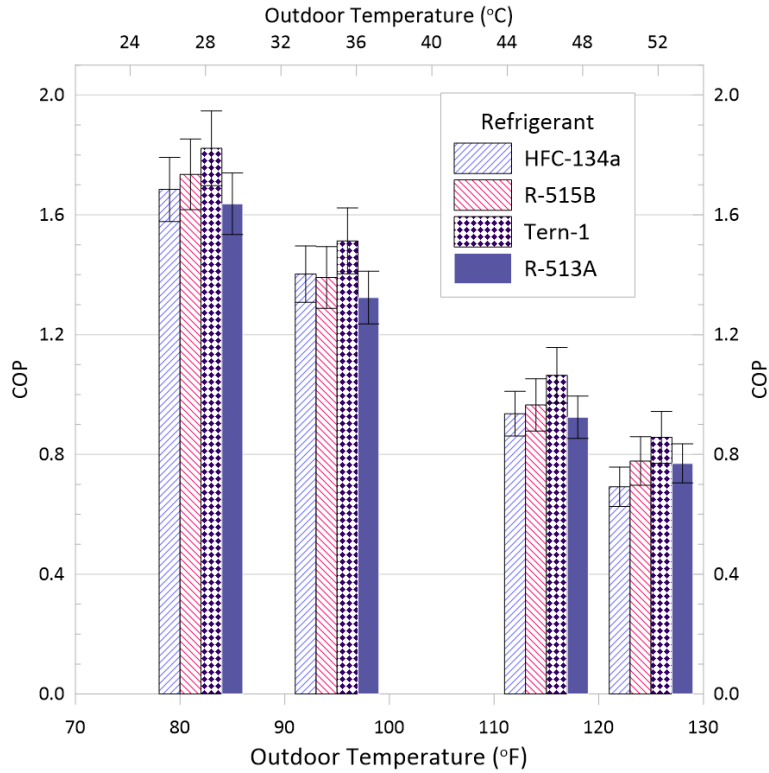


Figure 5 (Exec. Summary). ECU COP at outdoor temperatures 27.8 °C (82 °F), 35.0 °C (95 °F), 46.1 °C (115 °F), and 51.7 °C (125 °F) (center of bars)

Tern-1 performance appears to be similar to that of HFC-134a, both in terms of capacity and COP. On the other hand, R-515B achieves lower capacity by as much as 23 %. In this “drop-in” application with a much lower capacity, the COP of R-515B is comparable to that of HFC-134a.

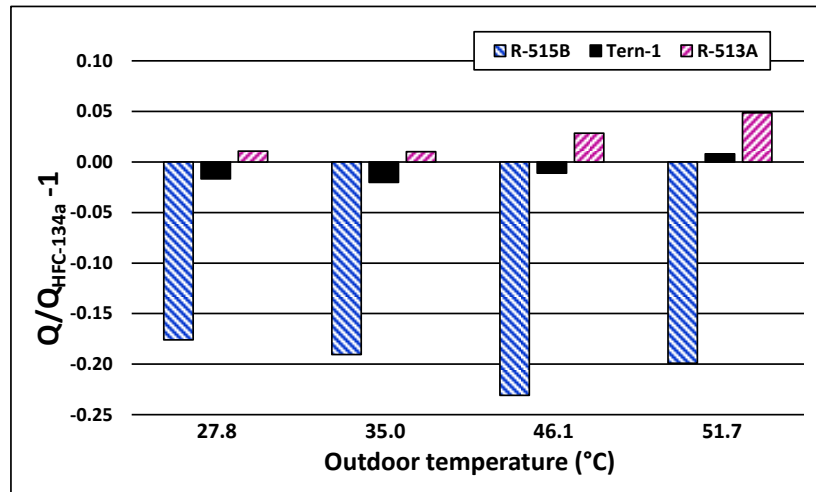


Figure 6 (Exec. Summary). Capacity difference for R-515B, Tern-1, and R-513A versus HFC-134a, referenced to HFC-134a capacity, based on ECU tests at outdoor temperatures 27.8 °C, 35.0 °C, 46.1 °C, and 51.7 °C

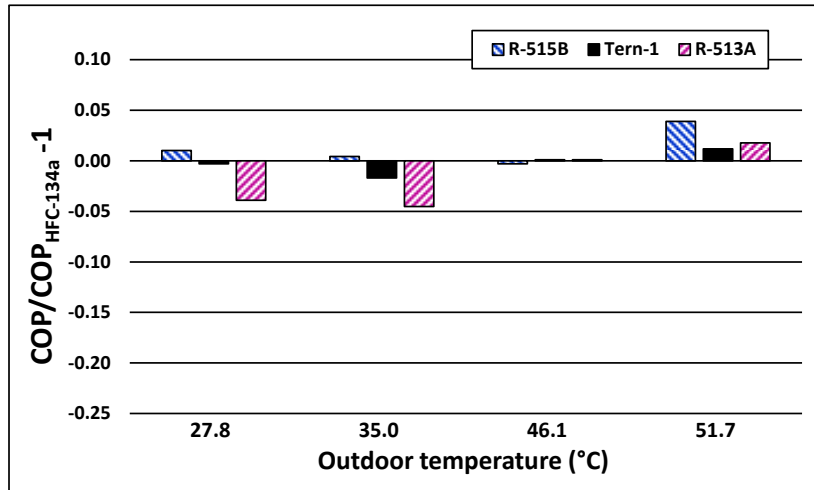


Figure 7 (Exec. Summary). COP difference for R-515B, Tern-1, and R-513A versus HFC-134a, referenced to HFC-134a COP, based on ECU “drop in” tests at outdoor temperatures 27.8 °C, 35.0 °C, 46.1 °C, and 51.7 °C

In addition to laboratory “drop-in” tests, the study used simulation models to extrapolate test results to an evaluation scenario under which each fluid operated in an ECU with a compressor that would provide the same capacity at the 35.0 °C temperature test with the isentropic efficiency matching that of HFC-134a (Figure 8 and 9). The R-513A and Tern-1 blends still provide the best performance compared to HFC-134a.

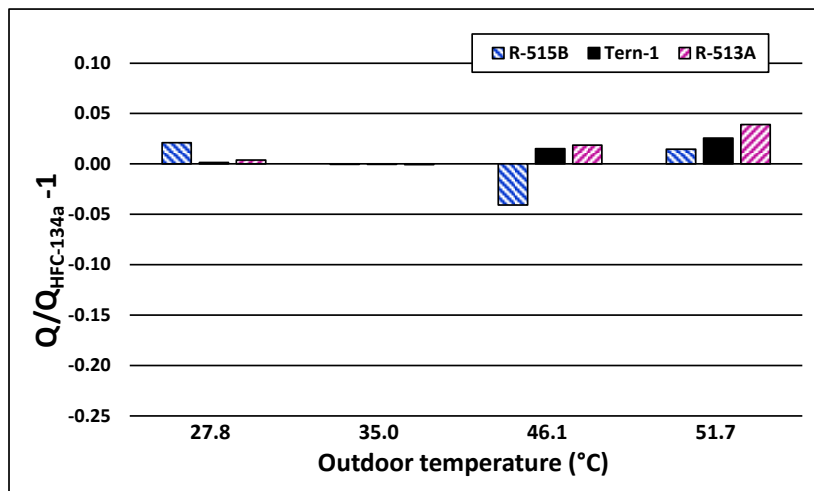


Figure 8 (Exec. Summary). Capacity difference for R-515B, Tern-1, and R-513A versus HFC-134a, referenced to HFC-134a capacity, for ECUs with capacity matching that of HFC-134a at the 35.0 °C test condition; based on ACSIM simulations at outdoor temperatures 27.8 °C, 35.0 °C, 46.1 °C, and 51.7 °C

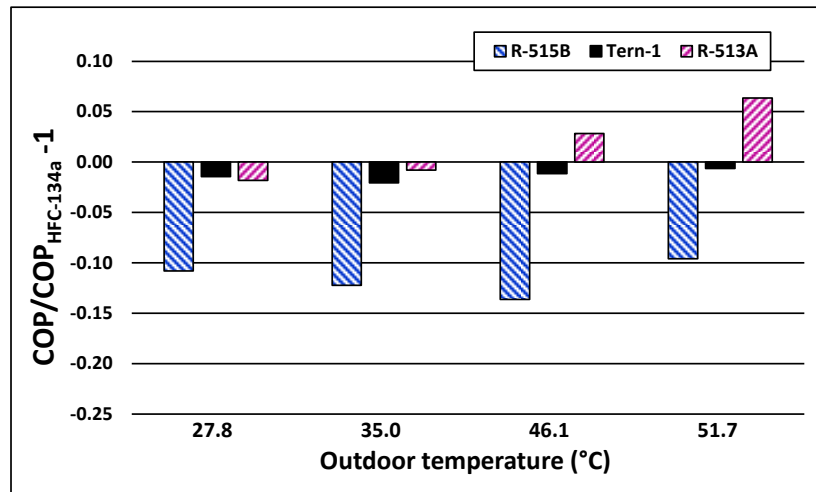


Figure 9 (Exec. Summary). COP difference for R-515B, Tern-1, and R-513A versus HFC-134a, referenced to HFC-134a COP, for ECUs with capacity matching that of HFC-134a at the 35.0 °C test condition; based on ACSIM simulations at outdoor temperatures 27.8 °C, 35.0 °C, 46.1 °C, and 51.7 °C

Implications for Future Research and Benefits

This study developed new measurements and data on non-flammable, low-GWP candidate replacements for HFC-134a, which included thermophysical properties, flammability characteristics, two-phase heat transfer performance, and cycle performance. This information will assist the HVAC industry in its transition to low-GWP systems.

For the studied ECU system, the R-513A and Tern-1 blends provide comparable capacity and COP to that of HFC-134a and offer GWP reductions of 66 % and 51 %, respectively. They can be implemented without major redesign of currently used components or other difficulties. If greater reduction in GWP is desirable, R-515B (74 % GWP reduction) can be considered, but its use requires further research and developmental work.

While the tested blends pass the ASTM E681 test as stipulated by ASHRAE Standard 34 for qualifying ‘non-flammability’ of refrigerants, some pass more easily than others, as determined from the other tests and modeling. There is a trade-off between ‘non-flammability’ and GWP. If military requirements for ‘non-flammability’ are more stringent than the E681 standard, the less flammable of the three (Tern-1 and R-513A) might still pass a more stringent criterion while R-515B would likely fail. If better flammability behavior than Tern-1 and R-513A is required, the less flammable blends identified in the earlier phase of the project would need to be selected, and then evaluated experimentally to verify their predicted performance and flammability. These less flammable fluids would have a reduction of GWP of about 50 % as compared to R-134a.

A live-fire test program in conjunction with modeling should be carried out to establish a representative test for assessing ‘non-flammability’ for the military environment. We recommend HFC-134a to be tested at high ambient temperature and high humidity as a benchmark. We suggest live-fire tests of HFC-134a with increasing amounts of added HFO-1234yf to enable correlation to the small-scale experimental and numerical results.

Key Words

Air conditioning; Coefficient of performance; Cycle simulation; Flammability; Low GWP; HFC-134a replacement; Refrigerants; Vapor compression; Volumetric capacity.

Table of Contents

Abstract.....	i
Executive Summary	ii
Key Words	xii
List of Tables	xv
List of Figures.....	xviii
List of Acronyms	xxii
Nomenclature	xxiii
Acknowledgements	xxv
1. Objective.....	1
2. Background	1
3. Materials and Methods	2
3.1. Results of the limited-scope project	2
3.2. Project structure.....	3
4. Results and Discussion	4
4.1. Task 1: Experimental Measurements of Blend Properties and Development of Mixture Equation of State	4
4.1.1. Purpose and Approach.....	4
4.1.2. Vapor-Liquid Equilibrium (VLE) Measurements.....	6
4.1.3. Pressure-Density-Temperature (P, ρ, T, x) Measurements.....	6
4.1.4. Speed of Sound Measurements.....	7
4.1.5. Viscosity Measurements.....	8
4.1.6. Thermal Conductivity Measurements.....	9
4.1.7. Model Development (Subtask 1c).....	9
4.2. Task 2: Flammability Testing	16
4.2.1. Introduction	16
4.2.2. E681 tests and Japanese High-Pressure Gas Law tests	17
4.2.3. Improvements in Predictive Model	24
4.2.4. Interpretation of E681 and JHPGL Experimental Results	27
4.2.5. Coordination with Full-Scale Testing	30
4.2.6. Summary of Flammability.....	31
4.3. Task 3: Testing of Selected Blends in a Mini-Breadboard Heat Pump.....	32
4.3.1. Test Apparatus.....	32
4.3.2. Test Protocol.....	34

4.3.3.	Model simulation of tests	36
4.3.4.	Test Results and CYCLE_D-HX Model Validation	37
4.4.	Task 4: Refrigerant Forced-Convection Heat-Transfer Testing	44
4.4.1.	Test Apparatus.....	44
4.4.2.	Data Analysis and Correlation Development.....	46
4.5.	Task 5: Selection of Final Blends for Testing in Military ECU	50
4.5.1.	Preliminary Selection of Four Blends	50
4.5.2.	Evaluation of “New” Fluids	50
4.5.3.	Selection of Three Blends for Testing in ECU.....	52
4.6.	Experimental Evaluation of Blend Performance in ECU.....	55
4.6.1.	Military ECU Specifications and Operation	55
4.6.2.	Test Facility.....	56
4.6.3.	Test Protocol and Metrics.....	58
4.6.4.	ECU Test Results	59
4.7.	Modeling of Blend Performance in an Optimized ECU	67
4.7.1.	Modeling Methods	67
4.7.2.	Modeling Procedure	75
4.7.3.	Optimization of Heat Exchangers	76
4.8.	Comparison of Performance of Alternative Fluids	80
4.8.1.	Performance of Three Blends in Original ECU (“drop-in” tests in environmental chambers).....	80
4.8.2.	Performance of Three Blends in Modified ECUs Matching HFC-134a Capacity at 35 °C Test	81
4.8.3.	Performance Carbon Dioxide in ECU Having HFC-134a Capacity at 35 °C Test Condition	82
5.	Conclusions and Implications for Future Research/Implementation.....	84
	Literature Cited	87
	Appendix A: Details of Experiments and Modeling.....	95
A.1.	Task 1 - Details of Thermophysical Properties Measurements and Modeling....	95
A.1.2.	Density (p, ρ, T, x) Measurements	104
A.1.3.	Liquid-Phase Speed of Sound.....	127
A.1.4.	Liquid-phase Viscosity Measurements.....	149
A.1.5.	Liquid-phase Thermal Conductivity Measurements	166
A.1.6.	Mixture Preparation.....	175
A.1.7.	Mixture Modeling.....	176
A.1.8.	Mixture Parameter File for Use With REFPROP (HMX.bnc).....	190

A.2. Task 2 - Flammability Experiments and Test Data	194
A.2.1. ASHRAE Standard 34 E681 Test Data	194
A.2.2. Japanese High-Pressure Gas Law Test	197
A.2.3. Constant Volume (2 L) Laminar Burning Velocity Measurements	205
A.3 Task 4 - Tabulated Flow-Boiling Heat-Transfer Measurements	215
A.4 Task 7 - Evaluation of blend performance in a military ECU	231
Appendix B: List of Scientific/Technical Publications	234

List of Tables

Table 3.1-1. Selected “best” blends from the limited-scope project [7] (sorted by GWP [12])	2
Table 4.1-1. Refrigerant blend properties measured in the current work.	5
Table 4.1-2. Mixture parameters (Eqs. 4.1-6 – 4.1.9) obtained from fitting experimental data. Components in each binary pair are sorted by normal boiling point temperatures, and the order is significant.....	11
Table 4.2-1. Modeling and test results for candidate blends (reactants at 296 K, 101 kPa, and 50 % r.h.).....	19
Table 4.3-1. MBHP: HFC-134a baseline test operating targets and control parameters.....	35
Table 4.3-2. MBHP: Test targets and parameters.....	36
Table 4.3-3. MBHP: Executed test matrix.....	36
Table 4.5-1. Selected properties of blends tested in ECU	53
Table 4.6-1. Measurement uncertainties	58
Table 4.6-2. Representative ECU test data for HFC-134a at four outdoor temperatures	60
Table 4.6-3. Representative ECU test data for R-515B at four outdoor temperatures	61
Table 4.6-4. Representative ECU test data for Tern-1 at four outdoor temperatures	62
Table 4.6-5. Representative ECU test data for R-513A at four outdoor temperatures	63
Table A.1-1. Measured vapor-liquid equilibria (VLE) data for the system R-1234yf/134a at a molar composition of (0.320/0.680).	97
Table A.1-2. Measured vapor-liquid equilibria (VLE) data for the system R-1234yf/134a at a molar composition of (0.647/0.353).	98
Table A.1-3. Measured vapor-liquid equilibria (VLE) data for the system R-134a/1234ze(E) at a molar composition of (0.334/0.666).	98
Table A.1-4. Measured vapor-liquid equilibria (VLE) data for the system R-134a/1234ze(E) at a molar composition of (0.663/0.337).	99
Table A.1-5. Measured vapor-liquid equilibria (VLE) data for the system R-1234yf/1234ze(E) at a molar composition of (0.324/0.676).....	99
Table A.1-6. Measured vapor-liquid equilibria (VLE) data for the system R-1234yf/1234ze(E) at a molar composition of (0.638/0.362).....	100
Table A.1-7. Measured vapor-liquid equilibria (VLE) data for the system R-125/1234yf at a molar composition of (0.349/0.651).	101
Table A.1-8. Measured vapor-liquid equilibria (VLE) data for the system R-125/1234yf at a molar composition of (0.664/0.336).	101

Table A.1-9. Measured vapor-liquid equilibria (VLE) data for the system R-1234ze(E)/227ea at a molar composition of (0.3347/0.6653).....	102
Table A.1-10. Measured vapor-liquid equilibria (VLE) data for the system R-1234ze(E)/227ea at a molar composition of (0.680/0.320).....	102
Table A.1-11. Measured vapor-liquid equilibria (VLE) data for the system R-1234yf/152a at a molar composition of (0.3653/0.6347)	103
Table A.1-12. Measured vapor-liquid equilibria (VLE) data for the system R-1234yf/152a at a molar composition of (0.6851/0.3149).	103
Table A.1-13. Measured (p, ρ, T, x) data for the system R-1234yf/134a at a molar composition of (0.33634/0.66366).....	108
Table A.1-14. Measured (p, ρ, T, x) data for the system R-1234yf/134a at a molar composition of (0.66759/0.33241).....	111
Table A.1-15. Measured (p, ρ, T, x) data for the system R-134a/1234ze(E) at a molar composition of (0.33250/0.66750).....	114
Table A.1-16. Measured (p, ρ, T, x) data for the system R-134a/1234ze(E) at a molar composition of (0.66356/0.33644).....	117
Table A.1-17. Measured (p, ρ, T, x) data for the system R-1234yf/1234ze(E) at a molar composition of (0.33584/0.66416).....	119
Table A.1-18. Measured (p, ρ, T, x) data for the system R-1234yf/1234ze(E) at a molar composition of (0.66660/0.33340).....	122
Table A.1-19. Dew points derived from vapor-phase measurements.....	126
Table A.1-20. Measured speed of sound data for the system R-1234yf/134a at a molar composition of (0.33634/0.66366).....	131
Table A.1-21. Measured speed of sound data for the system R-1234yf/134a at a molar composition of (0.66759/0.33241).....	134
Table A.1-22. Measured speed of sound data for the system R-134a/1234ze(E) at a molar composition of (0.32916/0.67084).....	136
Table A.1-23. Measured speed of sound data for the system R-134a/1234ze(E) at a molar composition of (0.67102/0.32898).....	140
Table A.1-24. Measured speed of sound data for the system R-1234yf/1234ze(E) at a molar composition of (0.33584/0.66416).....	145
Table A.1-25. Measured speed of sound data for the system R-1234yf/1234ze(E) at a molar composition of (0.66660/0.33340).....	147
Table A.1-26. Measured viscosity data for the system R-1234yf/134a at a molar composition of (0.3194/0.6806).....	154
Table A.1-27. Measured viscosity data for the system R-1234yf/134a at a molar composition of (0.6469/0.3531).....	156
Table A.1-28. Measured viscosity data for the system R-134a/1234ze(E) at a molar composition of (0.3330/0.6670).	158
Table A.1-29. Measured viscosity data for the system R-134a/1234ze(E) at a molar composition of (0.6622/0.3378).	160
Table A.1-30. Measured viscosity data for the system R-1234yf/1234ze(E) at a molar composition of (0.3224/0.6776).....	162
Table A.1-31. Measured viscosity data for the system R-1234yf/1234ze(E) at a molar composition of (0.6418/0.3582).....	164

Table A.1-32. Representative thermal conductivity data measured for the system R-1234yf/134a at a molar composition of (0.320/0.680).....	169
Table A.1-33. Representative thermal conductivity data measured for the system R-1234yf/134a at a molar composition of (0.647/0.353).....	170
Table A.1-34. Representative thermal conductivity data measured for the system R-134a/1234ze(E) at a molar composition of (0.334/0.666).....	171
Table A.1-35. Representative thermal conductivity data measured for the system R-134a/1234ze(E) at a molar composition of (0.663/0.337).....	172
Table A.1-36. Representative thermal conductivity data measured for the system R-1234yf/1234ze(E) at a molar composition of (0.323/0.677).	173
Table A.1-37. Representative thermal conductivity data measured for the system R-1234yf/1234ze(E) at a molar composition of (0.642/0.358).	174
Table A.1-38. Binary interaction parameters for the ECS models for viscosity and thermal conductivity for use with REFPROP v10.0	182
Table A.1-39. Coefficients for entropy scaling of thermal conductivity data (Eq. A.1-56).	190
Table A.2-1. E681 test results for R-513A, NIST-ternary blend, R-450A, R-515B, and blends of R-1234yf/134a at a molar composition of (0.26/0.74), (0.28/0.72), and (0.30/0.70).	194
Table A.2-2. Japanese High-Pressure Gas Law test results obtained at NIST for: R-513A, NIST-ternary blend, R-450A, R-515B, and blends of R-1234yf/134a, all with dry or 50 % r.h. air as listed.....	199
Table A.2-3. Fitting parameters for the variation of SL with ϕ , T_u and P for experimental burning velocity data obtained in 2-L experiment from pressure rise data for R-152a/134a and R-152a/1234yf mixtures. Data presented for 298 K, 101 kPa initial conditions, and dry air (<2% r.h.) of wet air (50 % r.h.) as noted.	210
Table A.2-4. Experimental burning velocity data obtained in 2-L experiment from pressure rise data for R-152a/134a and R-152a/1234yf mixtures. Data presented for 298K, 101 kPa initial conditions, dry air (<2% r.h.) and wet air (50 % r.h.) as noted. Blend compositions given in mole fraction.	211
Table A.3-1. Measured flow-boiling heat-transfer data for R-515B, R-450A, R-513A, and HFC-134a.....	215
Table A.4-1. Comparison of test and simulation results for ECU using HFC-134a	231
Table A.4-2. Comparison of test and simulation results for ECU using R-515B.....	231
Table A.4-3. Comparison of test and simulation results for ECU using Tern-1	232
Table A.4-4. Comparison of test and simulation results for ECU using R-513A	232
Table A.4-5. Relative refrigerant-side capacity and COP of R-515B, Tern-1, R-513A versus HFC-134a from ECU laboratory tests	233
Table A.4-6. Relative refrigerant-side capacity and COP of R-515B, Tern-1, R-513A versus HFC-134a from modified ECU simulations with matching capacity at 35.0 °C test.....	233
Table A.4-7. Relative refrigerant-side capacity and COP of CO ₂ versus HFC-134a from modified ECU simulations with matching capacity at 35.0 °C test.....	233

List of Figures

Figure 3.2-1. Project tasks	3
Figure 4.1-1. Measured (P, ρ, T, x) points for the R-1234yf/1234ze(E) blend at a composition of (0.6666/0.3334) molar; left: pressure versus temperature; right: density versus temperature; \diamond , measured points; line, phase boundary; *, critical point.....	7
Figure 4.1-2. Measured speed of sound points for the R-1234yf/1234ze(E) blend at a composition of (0.6666/0.3334) mole fraction; left: pressure versus temperature; right: sound speed versus temperature; symbols are measured points and lines connect points along an isochore; red line is phase boundary.	8
Figure 4.1-3. Relative deviations in measured densities compared to the values predicted by the mixture model. The average combined expanded uncertainty in the experimental data is shown by dashed lines and listed in the figure title.....	12
Figure 4.1-4. Relative deviations in measured speed of sound compared to the values predicted by the mixture model. The average combined expanded uncertainty in the measured data is shown by dashed lines and listed in the figure title.	13
Figure 4.2-1. Left image: schematic of ASTM 681 test vessel; Right two images: visual images from HFC-32/HFC-134a blend (0.35 /0.65 mass fraction) below and above the lean flammability limit[40, 41].	18
Figure 4.2-2. Equilibrium explosion pressure of candidate blends (Tern-1, R-513A, R-450A, and R-515B) together with experimental results in the JHPGL test as a function of blend volume fraction in air (50 % r.h.)	21
Figure 4.2-3. Explosion pressure of candidate blends in JHPGL test as a function of blend volume fraction in air (left frame: dry air; right, moist)	22
Figure 4.2-4. Explosion pressure of candidate blends (Tern-1, R-513A, R-450A, and R-515B) in JHPGL test as a function of blend volume fraction in air (solid lines: dry air; dashed lines: moist air; note different scales).....	23
Figure 4.2-5. Explosion pressure in the JHPGL test for binary blends of HFC-134a with HFO-1234yf as function of volume fraction the blend in air. Different curves show results for varying volume fractions of HFC-134a/HFO-1234yf in the blend (left frame: dry air; right: moist).	24
Figure 4.2-6. Peak explosion pressure in the JHPGL test for binary blends of HFC-134a with HFO-1234yf as function the volume fraction of HFC-134a in the blend, for moist (50 % r.h.) and dry (< 2 % r.h.) air	24
Figure 4.2-7. Laminar burning velocity of R-152a/134a (left frame) and R-152a/1234yf (right frame) mixtures with air as a function of the equivalence ratio	26
Figure 4.2-8. Calculated vs. measured laminar burning velocity (peak over all ϕ) of twenty-one refrigerant/N ₂ /O ₂ flames for which experimental data are available in the literature [66-68].....	26
Figure 4.2-9. Overall chemical reaction ω_{psr} as a function of volume fraction in air determined via perfectly stirred reactor simulations for the blend R-1234yf/134a. Each curve refers to one blend ratio: top curve, 100% HFO-1234yf, bottom curve 100 % HFC-134a; Frames: 0 % r.h. (dry), 50 % r.h., and 100 % r.h.	27
Figure 4.2-10. Peak (over all ϕ for each blend) chemical reaction ω_{psr} as a function of volume fraction of HFC-134a in the blend of R-1234yf/134a. Individual curves are shown for varying water vapor in the air (0 %, 50 %, 75 % and 100 % r.h.)	28
Figure 4.2-11. Explosion pressure in the JHPGL test vs. overall chemical reaction ω_{psr} (both peak over all ϕ) for R-513A, R-450A, R-515B and the Tern-1 blend and the R-1234yf/134a	

blends at increasing HFC-134a volume fraction. Dotted line is a polynomial fit to all the data to aid in visualization. (Initial conditions: 296 K, 101 kPa, 50 % r.h.).....	29
Figure 4.2-12. Peak (over all ϕ for each blend) chemical reaction ω_{psr} for R-513A, R-450A, R-515B and the NIST blend. Data are shown for the Nominal, WCF, and WCFE compositions in air ($T = 296$ K) and 0 %, 50 %, and 100 % r.h.	30
Figure 4.3-1. Photos of the MBHP test apparatus	32
Figure 4.3-2. Schematic of the MBHP test apparatus.....	33
Figure 4.3-3. MBHP: Schematics of annular heat exchanger including (a) refrigerant tube lengths, (b) cross section of annular heat exchanger, (c) detailed cross-section of microfin tube, and (d) helix angle of microfins.....	34
Figure 4.3-4. Cooling COP for HFC-134a and the replacement candidates (a) without LLSL-HX and (b) with LLSL-HX.	39
Figure 4.3-5. Cooling volumetric capacity for HFC-134a and the replacement candidates (a) without LLSL-HX and (b) with LLSL-HX	39
Figure 4.3-6. Compressor isentropic efficiency (a) without LLSL-HX and (b) with LLSL-HX.	40
Figure 4.3-7. Compressor volumetric efficiency (a) without LLSL-HX and (b) with LLSL-HX	40
Figure 4.3-8. Compressor speed (a) without LLSL-HX and (b) with LLSL-HX.....	41
Figure 4.3-9. R-450A measurement and model prediction of: (a) evaporator and.....	43
Figure 4.4-1. Schematic of flow boiling test apparatus	44
Figure 4.4-2. Cross section of flow-boiling test section	45
Figure 4.4-3. Detailed schematic of test section (counterflow)	46
Figure 4.4-4. Comparison between measured Nusselt numbers and those predicted by the Hamilton et al. correlation [77].....	48
Figure 4.4-5. Comparison between measured Nusselt numbers and those predicted by the new correlation given by Eq. (4.4-5).....	49
Figure 4.6-1. ECU before installation (a). The condenser protective grid and the covers for evaporator coil and blower were removed on the unit's left-side in picture (b).....	55
Figure 4.6-2. ECU schematic with installed instrumentation. Symbol X designates the disabled valve on the hot-gas bypass. P and T designate pressure and temperature sensors.....	56
Figure 4.6-3. Schematic of ECU installation in environmental chambers	56
Figure 4.6-4. Connecting ducts and nozzle chamber located in indoor environmental chamber.	57
Figure 4.6-5. Data acquisition screen for data monitoring	58
Figure 4.6-6. Heat transfer to the ECU and ductwork at different outdoor air temperatures	64
Figure 4.6-7. ECU total air-side capacity at outdoor temperatures 27.8 °C (82 °F), 35.0 °C (95 °F), 46.1 °C (115 °F), and 51.7 °C (125 °F) (center of bars)	65
Figure 4.6-8. ECU latent capacity at outdoor temperatures 27.8 °C (82 °F), 35.0 °C (95 °F), 46.1 °C (115 °F), and 51.7 °C (125 °F) (center of bars)	65
Figure 4.6-9. ECU total power at outdoor temperatures 27.8 °C (82 °F), 35.0 °C (95 °F), 46.1 °C (115 °F), and 51.7 °C (125 °F) (center of bars)	66
Figure 4.6-10. ECU COP at outdoor temperatures 27.8 °C (82 °F), 35.0 °C (95 °F), 46.1 °C (115 °F), and 51.7 °C (125 °F) (center of bars)	66
Figure 4.7-1. Right side of the evaporator in the ECU package (a) with infrared image (b)	69
Figure 4.7-2. Evaporator fin spacing (cm scale).....	69
Figure 4.7-3. Evaporator refrigerant circuitry.....	69

Figure 4.7-4. Infrared image of evaporator air side exit (view from the top, looking down). The left side of the image (a) corresponds to the near-side edge of the coil shown in Figure 4.7-1, (b) shows further right in the same picture.....	70
Figure 4.7-5. Evaporator air velocity profile measured at air inlet to coil. Refrigerant feeding tubes are on the right side. The grid origin is at the top of the coil.	71
Figure 4.7-6. Conceptual representation of a heat exchanger in EVAP-COND	71
Figure 4.7-7. EVAP-COND side-view representation of the ECU evaporator with one-dimensional inlet air velocity profile.	72
Figure 4.7-8. Configuration of the condenser (view from the top).....	72
Figure 4.7-9. Infrared image of condenser air side inlet.....	73
Figure 4.7-10. Condenser right-side air velocity measured at the protective grid.....	74
Figure 4.7-11. EVAP-COND side-view representation of the equivalent finned-tube condenser used in ECU simulations.....	75
Figure 4.7-12. Design data of the of the equivalent finned-tube condenser used in ECU simulations	75
Figure 4.7-13. Optimized refrigerant circuitry designs for R-515B, Tern-1, R-513A and HFC-134a evaporator.....	78
Figure 4.7-14. Optimized refrigerant circuitry design for CO ₂ evaporator	78
Figure 4.8-1. Capacity difference for R-515B, Tern-1, and R-513A versus HFC-134a, referenced to HFC-134a capacity, based on ECU tests at outdoor temperatures 27.8 °C, 35.0 °C, 46.1 °C, and 51.7 °C.....	80
Figure 4.8-2. COP difference for R-515B, Tern-1, and R-513A versus HFC-134a, referenced to HFC-134a COP, based on ECU tests at outdoor temperatures 27.8 °C, 35.0 °C, 46.1 °C, and 51.7 °C.....	81
Figure 4.8-3. Capacity difference for R-515B, Tern-1, and R-513A versus HFC-134a, referenced to HFC-134a capacity, for ECUs with capacity matching that of HFC-134a at the 35.0 °C test condition; based on ACSIM simulations at outdoor temperatures 27.8 °C, 35.0 °C, 46.1 °C, and 51.7 °C.....	81
Figure 4.8-4. COP difference for R-515B, Tern-1, and R-513A versus HFC-134a, referenced to HFC-134a COP, for ECUs with capacity matching that of HFC-134a at the 35.0 °C test condition; based on ACSIM simulations at outdoor temperatures 27.8 °C, 35.0 °C, 46.1 °C, and 51.7 °C.....	82
Figure 4.8-5. Capacity difference of CO ₂ in basic ECU and ECU with LLSL-HX versus capacity of HFC-134a, referenced to HFC-134a capacity, for ECUs with capacity matching that of HFC-134a at the 35.0 °C test condition; based on ACSIM.CO ₂ simulations at outdoor temperatures 27.8 °C, 35.0 °C, 46.1 °C, and 51.7 °C (center of bars).....	83
Figure 4.8-6. COP difference of CO ₂ in basic ECU and ECU with LLSL-HX versus COP of HFC-134a, referenced to HFC-134a COP, for ECUs with capacity matching that of HFC-134a at the 35.0 °C test condition; based on ACSIM.CO ₂ simulations at outdoor temperatures 27.8 °C, 35.0 °C, 46.1 °C, and 51.7 °C (center of bars).....	83
Figure A.1-1. Schematic of instrument for vapor liquid equilibria measurements. Main components include a stainless steel equilibrium cell housed in a thermostated aluminum block, standard platinum resistance thermometer (SPRT), and two oscillating quartz crystal pressure transducers (PT1 and PT2) with maximum pressure ranges of 0.7 MPa and 7 MPa.	95
Figure A.1-2. Two-sinker densimeter	104
Figure A.1-3. Sinkers in the two-sinker densimeter (shown removed from measuring cell).....	105

Figure A.1-4. Dual-path, pulse-echo, speed of sound instrument.	127
Figure A.1-5. Instrument rack for the pulse-echo speed of sound instrument.....	128
Figure A.1-6. Schematic diagram of the measuring cell inside the pressure vessel.....	129
Figure A.1-7. Schematic of the main body of the OPV instrument.....	149
Figure A.1-8. Experimental setup for viscosity measurements. It includes: (1) a vacuum system, (2) a circulator, (3) a syringe pump, (4) the OPV, (5) a sample cylinder mount, (6) various instrument readouts and controls, and (7) a computer.	150
Figure A.1-9. Circuit diagram of the Wheatstone bridge and long and short hot wire arrangement.....	167
Figure A.1-10. Effect of density on the thermal conductivity for binary mixtures of R-1234yf, R- 134a, and R-1234ze(E) at temperatures ranging from 200 K to 340 K.....	168
Figure A.1-11. Deviation plot for viscosity of R-134a/1234yf mixtures as a function of temperature	183
Figure A.1-12. Deviation plot for thermal conductivity of R-134a/1234yf mixtures as a function of temperature	183
Figure A.1-13. Deviation plot for viscosity of R-134a/R-1234ze(E) mixtures as a function of temperature	184
Figure A.1-14. Deviation plot for thermal conductivity of R-134a/1234ze(E) mixtures as a function of temperature.....	185
Figure A.1-15. Deviation plot for viscosity of R-1234yf/1234ze(E) mixtures as a function of temperature.	186
Figure A.1-16. Deviation plot for thermal conductivity of R-1234yf/R-1234ze(E) mixtures as a function of temperature.....	186
Figure A.1-17. Deviation plot for viscosity of R-125/R-1234ze(E) mixtures as a function of temperature	187
Figure A.1-18. Deviation plot for thermal conductivity of R-125/R-1234ze(E) mixtures as a function of temperature.....	188
Figure A.2-1. Spherical 2-L chamber for JHPGL tests and constant volume method laminar burning velocity measurements	197
Figure A.2-2. Plumbing schematic diagram for 2-L chamber	198
Figure A.2-3. Experimental pressure trace P, flame radius r_f , flame stretch rate κ , and gas temperature (unburned T_u and burned T_b) as a function of time.....	207
Figure A.2-4. Three-dimensional plot of burning velocity as a function of pressure P and unburned gas temperature T_u	208

List of Acronyms

AAD	average absolute deviation (statistical measure)
AC	air conditioning
AHRI	Air-Conditioning, Heating and Refrigeration Institute
ANSI	American National Standards Institute
ARL	Army Research Laboratory
ASHRAE	American Society of Heating Refrigerating and Air-Conditioning Engineers
ASTM	American Society for Testing and Materials
CFC	chlorofluorocarbon
COP	coefficient of performance
ECS	extended corresponding states (model for properties)
ECU	environmental control unit
EEV	electronic expansion valve
EOS	equation of state
GWP	global warming potential
HFC	hydrofluorocarbon
HFO	hydrofluoroolefin
HTF	heat-transfer fluid
HVAC	heating, ventilating, and air-conditioning
ISO	International Organization for Standardization
JHPGL	Japanese High-Pressure Gas Law Test
LBV	laminar burning velocity
MBHP	mini breadboard heat pump
NBP	normal boiling point
NSD	no statistical difference
OPV	oscillating piston viscometer
TXV	thermostatic expansion valve
VLE	vapor-liquid equilibrium

Nomenclature

Symbols

A_c	cross-sectional area (m^2)
B_{nd}	local Bond number = $(\rho_l - \rho_v)geD_h/(\sigma N)$, (-)
Bo	local boiling number = $\frac{q''}{G_r i_{fg}}$, (-)
c_p	specific heat ($J\ kg^{-1}\ K^{-1}$)
C	coefficients given in Eq. (3.4.5)
Co	convection number, $\left(\frac{1-x_q}{x_q}\right)^{0.8} \left(\frac{\rho_v}{\rho_l}\right)^{0.5}$
D_e	equivalent inner diameter of smooth tube (m)
D_h	hydraulic diameter of micro-fin tube (m)
e	fin height (mm)
g	acceleration due to gravity (m/s^2)
G	total mass velocity ($kg\ m^{-2}\ s^{-1}$)
$h_{2\phi}$	local two-phase heat-transfer coefficient ($W\ m^{-2}\ K^{-1}$)
i_{fg}	latent heat of vaporization ($J\ kg^{-1}$)
k	refrigerant thermal conductivity ($W\ m^{-1}\ K^{-1}$)
N	total number of microfins in cross section (-)
Nu	local Nusselt number based on D_h
\dot{m}	mass flow rate ($kg\ s^{-1}$)
M_w	molar mass ($g\ mole^{-1}$)
p	wetted perimeter (m)
P	local fluid pressure (Pa)
P_c	critical fluid pressure (Pa)
(p, ρ, T, x)	pressure, density, temperature, composition
Pr	liquid refrigerant Prandtl number = $\frac{c_p \mu}{k} \Big _{r,l}$, (-)
Q_{air}	air-side capacity (W)
Q_{ref}	refrigerant-side capacity (W)
Q_{vol}	volumetric capacity ($kJ\ m^{-3}$)
q''	local heat flux based on tube inner surface area ($W\ m^{-2}$)
Re	all liquid, refrigerant Reynolds number based on D_h , $Re = \frac{G_r D_h}{\mu_{r,l}}$
s	distance between fins (mm)
T	temperature (K)
t_b	bottom thickness of fin (mm)
t_w	tube wall thickness (mm)
U	expanded relative uncertainty (%)
x_q	thermodynamic mass quality (-)
z	axial distance (m)

Greek Symbols

α	helix angle ($^{\circ}$), learning rate
β	fin angle ($^{\circ}$)
ϕ	fuel-air equivalence ratio
ΔL	incremental length (m)
ΔT_s	$T_s - T_w$ (K)
η	dynamic viscosity (mPa s)
λ	thermal conductivity ($\text{W m}^{-1} \text{K}^{-1}$)
μ	viscosity (Pa·s)
ν	specific volume, $x_q \nu_v + (1-x_q) \nu_l$ ($\text{m}^3 \text{kg}^{-1}$)
ρ	density (kg m^{-3})
σ	surface tension (kg s^{-2})
ω	overall chemical rate (s^{-1})

Subscripts

b	bubble point
c	critical condition
d	dew point
f	water
i	inside, inlet
l	liquid
o	outlet, exit
p	prediction, single component
psr	perfectly stirred reactor
r	refrigerant
s	saturated state
v	vapor
w	heat transfer surface

Acknowledgements

This work was supported by the Strategic Environmental Research and Development Program; Project WP19-1385: WP-2740 Follow-On: Low-GWP Alternative Refrigerant Blends for HFC-134a.

1. Objective

This work addresses the objectives of the Statement of Need number WPSO-17-02 “No/Low Global Warming Potential Alternatives to Ozone Depleting Refrigerants” issued by the Strategic Environmental Research and Development Program (SERDP), the U.S. Department of Defense (DoD) environmental science and technology program, planned and executed in full partnership with the U.S. Department of Energy and the U.S. Environmental Protection Agency. The goal of this Statement of Need was to identify low global-warming-potential (GWP), non-flammable refrigerants to replace HFC-134a (GWP = 1300) in military equipment. The selected fluids should have zero ozone depletion potential (ODP) and a low global warming potential (GWP). The selection criteria also include COP, volumetric capacity (Q_{vol}), and toxicity.

This work is a follow-on of the SERDP limited-scope project WP-2740, which screened over 100 000 refrigerant blends created from a pool of 13 fluids using thermodynamic cycle simulation models and identified over 20 promising HFC-134a replacement blends [6]. The objective of this core project was to narrow the pool of blend candidates down to three “best” fluids, experimentally verify their non-flammability, and demonstrate their performance through tests in an HFC-134a military ECU in environmental chambers over a wide range of operating conditions. In a post-experimental phase, this work also evaluated the performance potential of the candidate blends through ECU simulations with compressor and heat exchangers optimized for each blend.

2. Background

Stratospheric ozone depletion and climate change have resulted in regional [1] and global [2, 3] regulations that limit the production and consumption of fluorinated refrigerants, which are the dominant fluids currently used in refrigeration and air-conditioning systems, including military equipment. In the United States, the use of high-GWP hydrofluorocarbon (HFC) refrigerants is regulated by the American Innovation and Manufacturing (AIM) Act [4], which directed the U.S. Environmental Protection Agency to establish a phasedown program and sector-based HFC restrictions to facilitate the transition to next-generation technologies.

The above concerns and regulations spurred intensive global research for new generation, low-GWP fluids. These research efforts showed that the availability of low-GWP refrigerants varies between applications and is rather limited for medium- and high-pressure systems. Notable applications where HFC-134a was already successfully replaced by low-GWP refrigerants are mobile air conditioners (HFO-1234yf, mildly flammable) and domestic refrigerators (isobutane, highly flammable); these fluids are not acceptable for military systems due to their flammability. Prior research [5] demonstrated that all single-component refrigerants that could serve with good performance as a replacement for HFC-134a are at least mildly flammable. For this reason, both the limited-scope project and this follow-on core project evaluated refrigerant binary and ternary blends to explore the possibility of formulating a non-flammable blend that would satisfy the requirements of military ECU systems.

3. Materials and Methods

3.1. Results of the limited-scope project

The limited-scope project [6] identified over 20 candidate low-GWP blends following an exhaustive, simulation-based search and evaluation of over 100 000 two- and three-component blends among a slate of 13 single-component refrigerants, subsequently expanded to four-component blends [7] (Table 3.1-1). In addition to HFC-134a, the single-component refrigerants included in the search were HFC-227ea, HFC-125, HFC-143a, HFC-134, HFC-32, HFC-152a, HFC-41, HFO-1234yf, HFO-1234ze(E), HFO-1234ze(Z), HFC-1243zf, and R-744 (CO₂) (listed in order of decreasing GWP).

Table 3.1-1. Selected “best” blends from the limited-scope project [7] (sorted by GWP [12])

Blend #	Components	Composition (molar)	GWP	$\bar{\Pi}^*$	COP/ COP _{R-134a}	$Q_{vol}/$ $Q_{vol, R-134a}$
<i>Class 1 nonflammable (predicted)</i>						
1	R-134a/1234yf	0.44/0.56	537	-0.1	0.987	1.025
2	R-134a/1234yf**	0.468/0.532	573	-0.4	0.988	1.027
3	R-134a/1234yf/134	0.48/0.48/0.04	633	-1.1	0.987	0.975
4	R-134a/1234yf/1234ze(E)#	0.52/0.32/0.16	640	-1.2	0.987	0.989
5	R-134a/1234yf	0.52/0.48	640	-1.2	0.989	1.029
6	R-134a/1234yf/134	0.4/0.44/0.16	665	-1.3	0.986	0.958
7	R-134a/125/1234yf	0.44/0.04/0.52	676	-1.5	0.985	1.049
8	R-134a/227ea/1234yf	0.40/0.04/0.56	681	-1.5	0.984	1.007
9	R-134a/1234ze(E)	0.60/0.40	745	-2.4	0.988	0.908
10	R-134a/1234yf	0.60/0.40	745	-2.4	0.990	1.031
11	R-134a/1234ze(E)/1243zf	0.60/0.36/0.04	750	-1.5	0.990	0.966
12	R-134a/1234yf/1234ze(E)	0.64/0.2/0.16	799	-3.0	0.990	0.986
13	R-134a/152a/1234yf	0.64/0.04/0.32	817	-1.8	0.993	1.023
14	R-134a/1234yf/134	0.52/0.32/0.16	824	-3.2	0.990	0.966
15	R-134a/1234ze(E)	0.68/0.32	852	-3.7	0.991	0.929
16	R-134a/1234yf/1243zf	0.68/0.2/0.12	870	-1.1	0.994	1.020
<i>Class 2L flammable (predicted)</i>						
17	R-152a/1234yf	0.08/0.92	8	7.7	0.980	0.957
18	R-134a/1234yf	0.20/0.80	238	2.8	0.980	0.996
19	R-134a/152a/1234yf	0.20/0.16/0.64	270	8.7	0.987	0.984
20	R-152a/1234yf/134	0.16/0.48/0.36	417	7.5	0.984	0.900
21	R-134a/1234yf	0.36/0.64	436	1.0	0.985	1.018
22	R-134a/1234yf/1243zf	0.36/0.44/0.20	451	5.2	0.988	1.004
23	R-134a/152a/1234yf	0.36/0.20/0.44	496	8.3	0.994	0.994

*Normalized flammability index [7,13] (negative values indicate non-flammable)

** Designated by ASHRAE Std. 34 as R-513A; safety classification: A1

Referred to as Tern-1

4. Results and Discussion

4.1. Task 1: Experimental Measurements of Blend Properties and Development of Mixture Equation of State

4.1.1. Purpose and Approach.

A mixture equation of state (EOS) providing validated thermodynamic properties and separate transport property models are needed for conducting the MBHP tests (Task 3), refrigerant two-phase heat-transfer tests (Task 4), and ECU tests (Task 7). Updated properties will also be implemented in the NIST heat exchanger and ECU simulation models (Task 7).

The simulation of cycle performance, the analysis of laboratory measurements in equipment, and heat-transfer experiments in support of cycle simulation modeling require thermodynamic and transport properties of the blends. The thermodynamic properties are expressed in terms of an “equation of state,” which is a mathematical model representing all thermodynamic properties of a pure fluid or blend. The properties of a refrigerant blend are given by a combination of the constituent pure fluids in the blend plus additional terms representing the mixture. The transport properties of thermal conductivity and viscosity are represented by separate models, also by combining pure-fluid models with mixture terms.

Any equation of state or transport property model (for a pure fluid or mixture) requires experimental data to fit adjustable parameters and validate its accuracy. While pure-fluid EOS are available and generally adequate for the new low-GWP refrigerants, this is not the case for refrigerant blends. This task has carried out the measurements necessary to define the mixture terms in the EOS and transport property models. These terms are expressed in terms of binary pairs of components; a mixture of the components A, B, and C, for example, is expressed in terms of the binary pairs A/B, A/C, and B/C. Thus, the present measurements were carried out on binary mixtures, even though ternary (three-component) mixtures are also among the “best” blends. The mixture parameters used in the simulations in the limited-scope study were based on limited experimental data from the literature or, in some cases, were entirely predicted, and this task will improve upon the data situation.

Measurements at two levels of effort were carried out. For three binary pairs that appear in multiple “best” blends, comprehensive measurements were carried out in Subtask 1a. These included vapor-liquid equilibrium (VLE) measurements; pressure-density-temperature-composition (p, ρ, T, x) data in the single-phase and supercritical regions; speed of sound in the single-phase liquid region; viscosity in the single-phase liquid region; and thermal conductivity in the single-phase liquid region. Limited measurements (i.e., only vapor-liquid equilibrium) were carried out on additional binary pairs in Subtask 1b. For each blend, measurements were carried out at nominal compositions of (0.33/0.67) and (0.67/0.33) mole fraction. These measurements allowed fitting mixture EOS and transport property models. The measurements are summarized in Table 4.1-1. The remainder of this section provides an overview of the measurements and modeling results, with details (including uncertainties) given in Appendix A.1.

Table 4.1-1. Refrigerant blend properties measured in the current work

Blend	Composition (mole frac)	<i>T</i>-range (K)	<i>P</i>-range (MPa)	Number of points*
Vapor-Liquid Equilibria (VLE)				
R-1234yf/134a	(0.320/0.680)	270 – 360	0.28 – 3.10	10
R-1234yf/134a	(0.647/0.353)	270 – 360	0.29 – 3.05	10
R-134a/1234ze(E)	(0.334/0.666)	270 – 360	0.22 – 2.61	10
R-134a/1234ze(E)	(0.663/0.337)	270 – 360	0.24 – 2.84	10
R-1234yf/1234ze(E)	(0.324/0.676)	270 – 360	0.23 – 2.56	10
R-1234yf/1234ze(E)	(0.638/0.362)	270 – 360	0.26 – 2.74	10
R-125/1234yf	(0.349/0.651)	270 – 335	0.39 – 2.21	10
R-125/1234yf	(0.664/0.336)	270 – 335	0.49 – 2.70	10
R-1234ze(E)/227ea	(0.335/0.665)	270 – 360	0.18 – 2.25	10
R-1234ze(E)/227ea	(0.680/0.320)	270 – 360	0.19 – 2.31	10
(<i>P</i>, ρ, <i>T</i>, <i>x</i>)—Liquid and Vapor Phases and Supercritical States				
R-1234yf/134a	(0.3363/0.6637)	230 – 400	0.04 – 11.7	124
R-1234yf/134a	(0.6471/0.3529)	230 – 400	0.04 – 10.6	105
R-134a/1234ze(E)	(0.3325/0.6675)	230 – 400	0.04 – 20.5	94
R-134a/1234ze(E)	(0.6636/0.3364)	230 – 400	0.04 – 21.5	81
R-1234yf/1234ze(E)	(0.3358/0.6642)	230 – 400	0.04 – 11.4	116
R-1234yf/1234ze(E)	(0.6666/0.3334)	230 – 400	0.04 – 10.5	109
Speed of Sound—Liquid Phase				
R-1234yf/134a	(0.3363/0.6637)	230 – 345	0.35 – 13.0	78
R-1234yf/134a	(0.6471/0.3529)	235 – 310	0.66 – 11.6	40
R-134a/1234ze(E)	(0.3292/0.6708)	235 – 345	0.53 – 51.4	141
R-134a/1234ze(E)	(0.6369/0.3631)	230 – 345	0.13 – 50.3	163
R-1234yf/1234ze(E)	(0.3358/0.6642)	230 – 345	0.26 – 11.3	71
R-1234yf/1234ze(E)	(0.6666/0.3334)	230 – 335	0.45 – 12.0	60
Thermal Conductivity—Liquid Phase				
R-1234yf/134a	(0.320/0.680)	200 – 340	0.95 – 12.05	379
R-1234yf/134a	(0.647/0.353)	200 – 340	1.03 – 12.00	403
R-134a/1234ze(E)	(0.334/0.666)	200 – 340	0.96 – 50.32	350
R-134a/1234ze(E)	(0.663/0.337)	200 – 340	0.97 – 50.14	335
R-1234yf/1234ze(E)	(0.323/0.677)	200 – 340	1.02 – 12.33	352
R-1234yf/1234ze(E)	(0.642/0.358)	200 – 340	0.89 – 12.10	341

*Distinct (*T*, *P*) state points; multiple replicate measurements were made at each state point

Table 4.1-1. (continued) Refrigerant blend properties measured in the current work

Blend	Composition (mole frac)	<i>T</i> -range (K)	<i>p</i> -range (MPa)	Number of points*
Viscosity—Liquid Phase				
R-1234yf/134a	(0.3194/0.6806)	273 – 393	1.83 – 12.01	144
R-1234yf/134a	(0.6469/0.3531)	273 – 393	1.84 – 12.00	112
R-134a/1234ze(E)	(0.3330/0.6670)	273 – 393	1.72 – 40.10	142
R-134a/1234ze(E)	(0.6622/0.3378)	273 – 393	1.13 – 40.09	120
R-1234yf/1234ze(E)	(0.3224/0.6776)	273 – 393	1.88 – 12.04	104
R-1234yf/1234ze(E)	(0.6418/0.3582)	273 – 393	1.84 – 12.02	126

*Distinct (*T*, *p*) state points; multiple replicate measurements were made at each state point.

4.1.2. Vapor-Liquid Equilibrium (VLE) Measurements.

The measurement of vapor-liquid equilibrium is the mixture analog of vapor pressure for a pure component. VLE data are the most important type of data needed for fitting a mixture EOS. They indicate, for example, the departure from ideal behavior and the presence or absence of azeotropes. Measurements of the bubble-point pressure as a function of temperature and liquid-phase composition (*p*, *T*, *x*) were made here. Conceptually, the measurement is very simple: load a liquid sample of known composition into a closed volume (i.e., “measuring cell”), bring the measuring cell to some temperature, and when the temperature has stabilized, measure the pressure. The VLE instrument and measurement details are described in Appendix A.1.1.

4.1.3. Pressure-Density-Temperature (*P*, ρ , *T*, *x*) Measurements.

The present measurements utilized a two-sinker densimeter with a magnetic suspension coupling. This type of instrument applies the Archimedes (buoyancy) principle to provide an absolute determination of the density. This general type of instrument is described by Wagner and Kleinrahm [14], and the instrument used here is described in detail by McLinden and L6sch-Will,[15] and only a brief description is given here. Two sinkers of nearly the same mass and same surface area, but very different volumes, were each weighed with a high-precision balance while they were immersed in the sample of unknown density. The basic form of the working equation for this type of instrument gives the fluid density ρ as:

$$\rho = \frac{(m_1 - m_2) - (W_1 - W_2)}{(V_1 - V_2)}, \quad (4.1-1)$$

where *m* and *V* are the mass and volume of the sinkers, *W* are the balance readings, and the subscripts refer to the two sinkers. One sinker was made of tantalum (*m* = 60.094 633 g, *V* = 3.60 872 cm³) and the other of titanium (*m* = 60.075 386 g, *V* = 13.315 284 cm³). (The sinkers are shown in Figure A.1-3.) A magnetic suspension coupling transmitted the gravity and buoyancy forces on the sinkers to the balance, thus isolating the fluid sample from the balance. With the two-sinker method, systematic errors in the weighing and from many other sources approximately cancel. Figure 4.1-1 illustrates the range of the measurements for one blend composition as an example. In addition to the density measurements, vapor-phase (*p*, ρ , *T*, *x*) data were used to determine the dew points of the blends studied, as discussed in Appendix A.1.2.

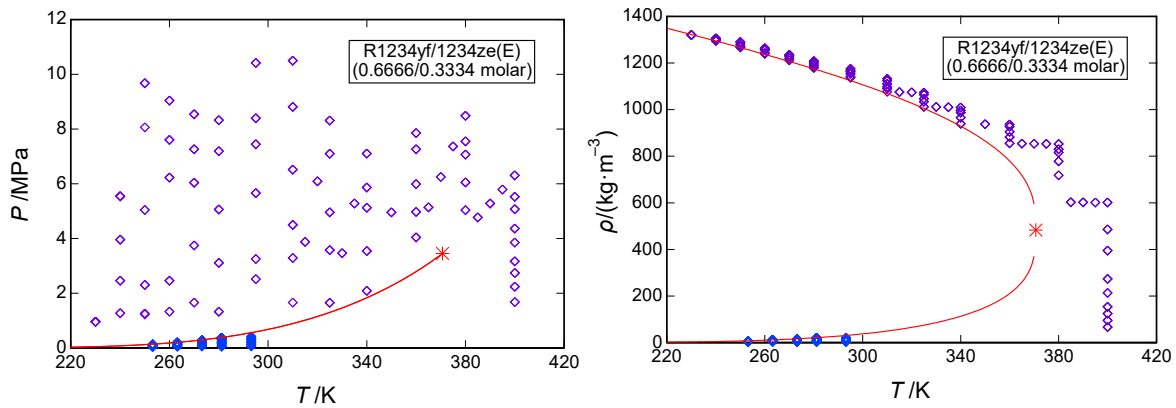


Figure 4.1-1. Measured (P , ρ , T , x) points for the R-1234yf/1234ze(E) blend at a composition of (0.6666/0.3334) molar; left: pressure versus temperature; right: density versus temperature; \diamond , measured points; line, phase boundary; *, critical point

4.1.4. Speed of Sound Measurements.

The speed of sound is closely related to heat capacity, and either speed of sound or heat capacity data are important for obtaining the correct values for enthalpy and entropy, which enter into cycle calculations. Enthalpy and entropy cannot be measured directly, and speed of sound can be measured much more accurately than heat capacity, which was the reason for including speed of sound.

The speed of sound was measured over wide ranges of temperature and pressure in a dual-path, pulse-echo-type instrument. In this technique, a piezoelectric transducer of single-crystal quartz is located within a sample volume of the test fluid. It is excited with a sinusoidal electrical burst, near the crystal resonance frequency, thus emitting ultrasonic pulses from each face of the crystal, which travel through the fluid sample, reflect off planar surfaces at each end of the sample volume, and return to the transducer, which also serves as the detector. The difference in the arrival times of the echo signals give the speed of sound by

$$w = \frac{2(L_2 - L_1)}{\Delta t}, \quad (4.1-2)$$

where w is the speed of sound, L_1 and L_2 are the path lengths, and Δt is the time difference. The differential nature of this technique cancels end effects and improves the accuracy. The instrument, measurement sequence, and uncertainties are described in Appendix A.1.3.

Figure 4.1-2. shows an example of the speed-of-sound measurements carried out. The measured data, as well as the relative, combined, expanded ($k = 2$) uncertainty in the speed of sound for each point, are reported in Appendix A.1.3. For both the (p , ρ , T , x) and sound speed measurements involving blends containing HFO-1234yf, the maximum pressure was restricted to no more than 12 MPa to avoid possible polymerization of HFO-1234yf.

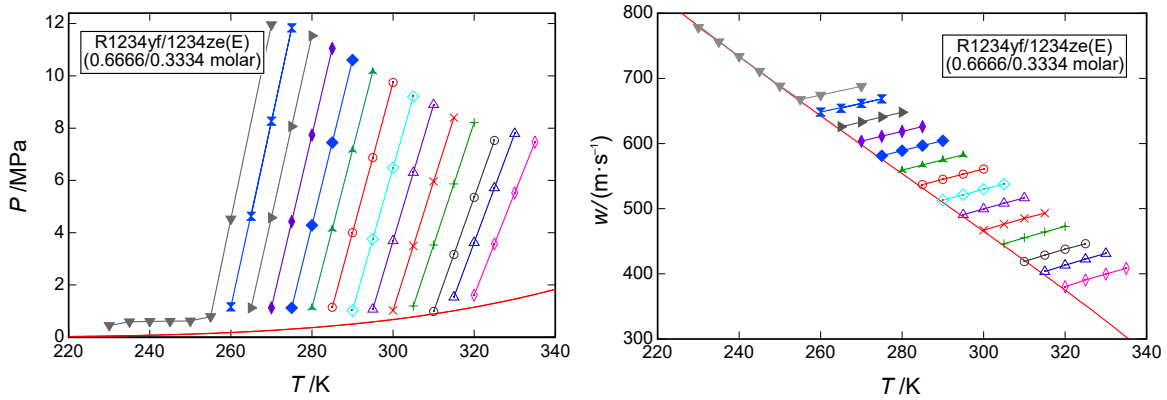


Figure 4.1-2. Measured speed of sound points for the R-1234yf/1234ze(E) blend at a composition of (0.6666/0.3334) mole fraction; left: pressure versus temperature; right: sound speed versus temperature; symbols are measured points and lines connect points along an isochore; red line is phase boundary.

4.1.5. Viscosity Measurements.

Viscosity data cannot be calculated from an equation of state but are important for the analysis of heat-transfer behavior. The dynamic viscosity (η) of three refrigerant blends, at two compositions each, was measured over a range of temperature and pressure using a modified commercial oscillating-piston viscometer. The instrument employs a variation of the falling body technique whereby the alternating motion of the sensing body is driven by electromagnetic induction. Additional details regarding the instrumentation, calibration and measurement protocols, and uncertainty analysis can be found in Appendix A.1.4. An example of measurements for one blend composition are shown in Figure 4.1-

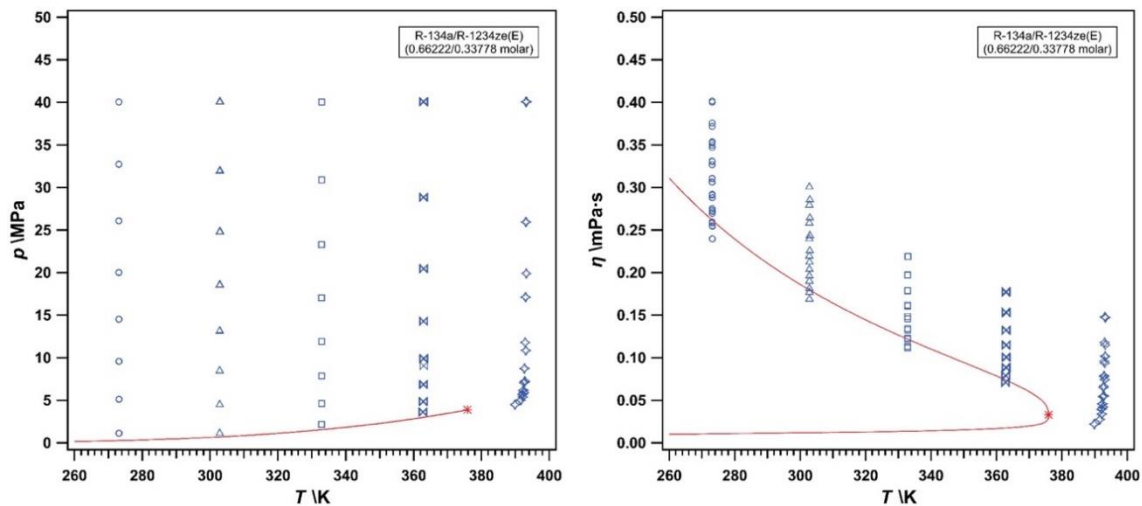


Figure 4.1-3. Measured viscosity points for the R-134a/1234ze(E) blend at a composition of (0.6622/0.3378) mole fraction; left: pressure versus temperature; right: dynamic viscosity versus temperature; the red line indicates the approximate phase boundary; * indicates the critical point.

4.1.6. Thermal Conductivity Measurements.

Thermal conductivity cannot be calculated from an equation of state, but it is important for the analysis of heat-transfer behavior. Here, the thermal conductivity was measured with the transient hot-wire technique, whereby a voltage pulse lasting about 1 s is applied to a fine wire immersed in the fluid under test; this heats the surrounding fluid, and the temperature rise is monitored (using the same wire, which also serves as a resistance thermometer) to extract thermal conductivity. The wire approximates a line source and the ideal temperature rise, ΔT_{id} , is given by

$$\Delta T_{id} = \frac{q}{4\pi\lambda} \left[\ln(t) + \ln\left(\frac{4a}{r_0^2 C}\right) \right] = \Delta T_w + \sum_{i=1}^{10} \delta T_i, \quad (4.1-3)$$

where q is the power applied per unit length, t is the elapsed time, r_0 is the radius of the hot wire, $C = 1.781\dots$ is the exponential of Euler's constant, λ is the thermal conductivity of the fluid, and $a = \lambda/(\rho C_p)$ is the thermal diffusivity of the fluid, where ρ and C_p are the fluid density and isobaric specific heat capacity [16]. The form of Eq. (4.1-3) is that of a line, where the thermal conductivity can be found from the slope and the thermal diffusivity can be found from the intercept. The summation term accounts for deviations from the ideal model. These measurements provided the data necessary for development of a model for the thermal conductivity of refrigerant blends. The instrument, measurement sequence, and uncertainties are described in Appendix A.1.5; the measured data are also tabulated in Appendix A.1.5.

4.1.7. Model Development (Subtask 1c).

The data measured in Subtasks 1a and 1b were fitted to thermodynamic and transport property models with results incorporated into files compatible with the NIST REFPROP database. Data are compared to the developed models using REFPROP.

Mixture EOS for thermodynamic properties. The multi-fluid modeling used in NIST REFPROP yields the most accurate mixture models available today. This approach combines the most accurate pure fluid equations of state with reducing and departure functions to correct for the changes to thermodynamics caused by mixture interactions. The refrigeration industry has been using the multi-fluid modeling approach for many years and will likely do so for many years to come.

In this framework, the equation of state for a pure component is given in terms of the reduced Helmholtz energy, given by $\alpha = a/(RT)$. All the thermodynamic properties are obtained from combinations of the Helmholtz energy and its derivatives. For instance, the pressure is obtained from $p = -\partial\alpha/\partial v$. The total α is given as the sum of ideal-gas (non-interacting) and residual (interacting or real-gas) contributions. These are fitted to experimental data and constrained to have the proper behavior at extremes of temperature and pressure. The residual Helmholtz energy can be expressed generically as

$$\alpha^r = \sum_i n_i \delta^{d_i} \tau^{t_i} \exp(-c_i \delta^{l_i} - \eta_i (\delta - \varepsilon_i)^2 - \beta_i (\tau - \gamma_i)^2) \quad (4.1-4)$$

where $\tau = T_{\text{red}}/T$ and $\delta = \rho/\rho_{\text{red}}$ with T_{red} and ρ_{red} being the reducing temperature and reducing density, respectively. All remaining variables are empirical coefficients fitted to data for a given fluid.

The same thermodynamic identities hold for mixtures as for pure fluids. The Helmholtz energy for a mixture is obtained as the sum of a corresponding states contribution and a departure term

$$\alpha^r = \alpha_{CS}^r(\tau, \delta, \bar{x}) + \alpha_{dep}^r(\tau, \delta, \bar{x}) \quad (4.1-5)$$

which becomes

$$\alpha^r = \sum_{i=1}^N x_i \alpha_{o,i}^r(\tau, \delta) + \sum_{i=1}^N \sum_{j=i+1}^N F_{ij} x_i x_j \alpha_{ij}^r(\tau, \delta), \quad (4.1-6)$$

where the first summation arises from a composition-weighted sum of the pure fluid EOS terms and the double summation is the departure term, with the α_{ij}^r given by

$$\alpha_{ij}^r = \sum_k n_k \tau^{l_k} \delta^{d_k} \exp(-\text{sgn}(l_k) \delta^{l_k}) \quad (4.1-7)$$

where the sgn function is the sign of the value: zero for an argument of zero, and 1 for positive arguments.

For mixtures $\tau = T_{\text{red}}(\bar{x})/T$ and $\delta = \rho/\rho_{\text{red}}(\bar{x})$, and the reducing functions are given by

$$T_{\text{red}}(\bar{x}) = \sum_{i=1}^N \sum_{j=1}^N x_i x_j \beta_{T,ij} \gamma_{T,ij} \frac{x_i + x_j}{\beta_{T,ij}^{x_i + x_j}} (T_{c,i} \cdot T_{c,j})^{0.5} \quad (4.1-8)$$

$$\frac{1}{\rho_r(\bar{x})} = \sum_{i=1}^N \sum_{j=1}^N x_i x_j \beta_{v,ij} \gamma_{v,ij} \frac{x_i + x_j}{\beta_{v,ij}^{x_i + x_j}} \frac{1}{8} \left(\frac{1}{\rho_{c,i}^{1/3}} + \frac{1}{\rho_{c,j}^{1/3}} \right)^3. \quad (4.1-9)$$

Thus the reducing functions have four adjustable parameters per ij binary pair. For mixtures with limited data only (such as the ‘‘VLE-only’’ mixtures measured in this work) only the four adjustable parameters in the reducing functions were fitted, namely $\beta_{T,ij}$, $\beta_{v,ij}$, $\gamma_{T,ij}$, and $\gamma_{v,ij}$; for such mixtures the ‘‘scaling factor’’ F_{ij} of the departure function is set to zero.

For blends where sufficient experimental data are available (such as the blends with ‘‘comprehensive data’’ measured in this work) a departure function, α_{dep}^r , was also fitted, and the F_{ij} of the departure function is set to unity. The fitted parameters are given in Tables 4.1-2 and 4.1-3.

Comparisons of the mixture EOS to the measured data are shown in Figures 4.1-4 and 4.1-5. The average absolute deviations (AAD) of the (p, ρ, T, x) data are comparable to the uncertainty in the experimental data. The AAD of the speed of sound data are within the uncertainty of the data for the R-1234yf/134a blend. For the two blends with R-1234ze(E) as a component, however, the AAD exceeds the experimental uncertainty of the sound speed data by a significant factor; we attribute this to a deficiency in the R-1234ze(E) pure-fluid equation of state in its representation of sound speed, as discussed further by Bell [17]. In any case, the AAD is always less than 0.2 %, and this is quite adequate for the analysis of refrigeration cycles.

Table 4.1-2. Mixture parameters (Eqs. 4.1-6 – 4.1.9) obtained from fitting experimental data. Components in each binary pair are sorted by normal boiling point temperatures, and the order is significant.

Binary Pair	$\beta_{T,ij}$	$\gamma_{T,ij}$	$\beta_{V,ij}$	$\gamma_{V,ij}$	F_{ij}
R-1234yf/1234ze(E)	0.998886	0.993309	0.999302	0.998590	1.0
R-1234yf/134a	1.000026	0.987057	1.000272	1.003747	1.0
R-134a/1234ze(E)	0.998593	0.992009	0.998995	0.998621	1.0
R-125/1234yf*	0.999637	0.999356	1.0	1.0	0.0
R-1234yf/152a*	1.002918	0.983928	1.0	1.0	0.0
R-1234ze(E)/227ea*	1.000895	0.993523	1.0	1.0	0.0

*Only VLE data were measured for these blends, and no departure function was fitted.

Table 4.1-3. Departure functions obtained from fitting experimental speed of sound and density data.

Binary Pair	k	n_k	t_k	d_k	l_k
R-1234yf/1234ze(E)	0	0.051900	2.477314	1	1
	1	-0.011472	0.070541	2	2
R-1234yf/1234ze(E)	0	0.072640	0.012643	1	1
	1	-0.024746	3.992829	2	2
R-134a/1234ze(E)	0	0.068889	3.184446	1	1
	1	-0.004831	2.034344	2	2

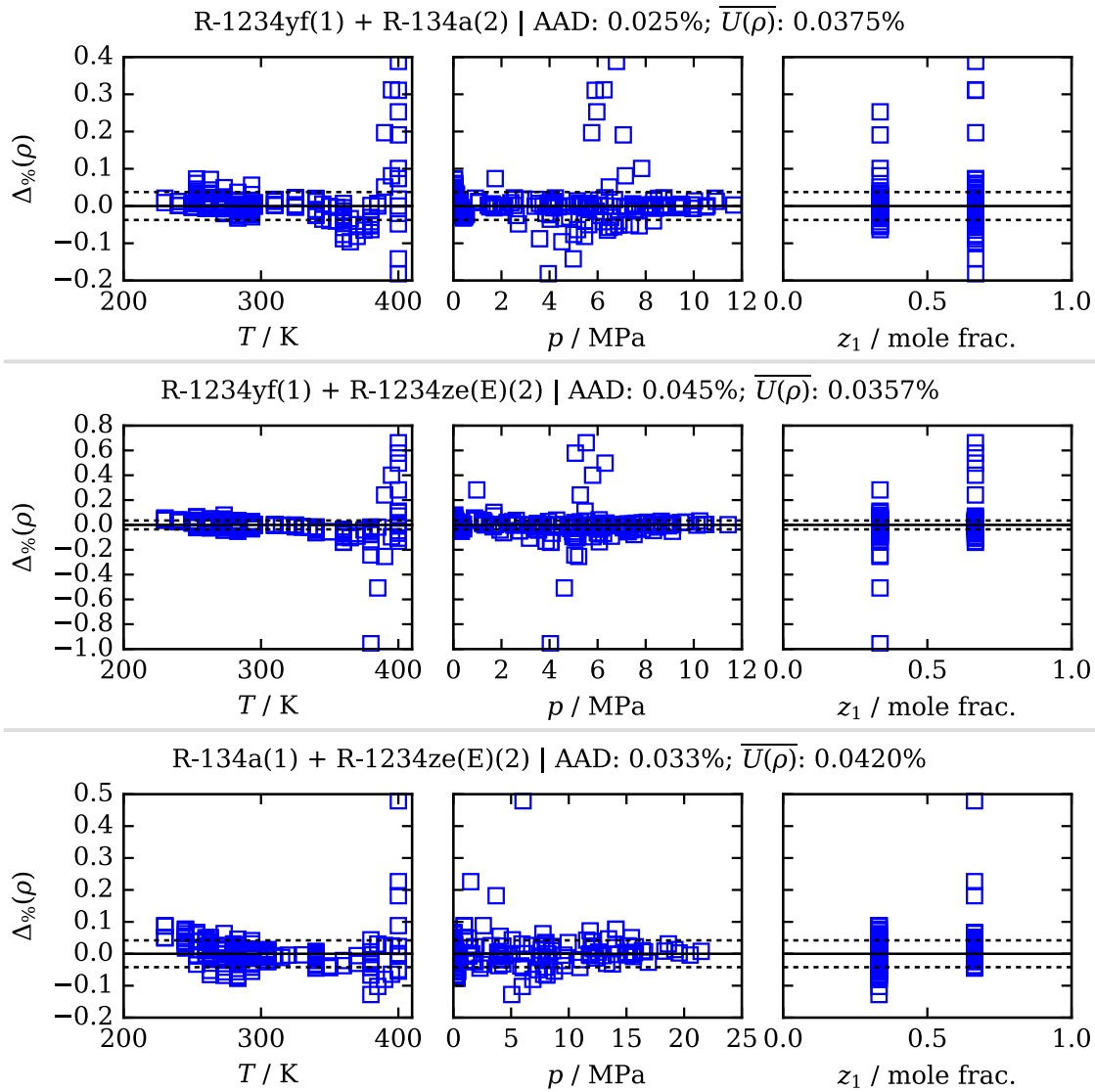


Figure 4.1-4. Relative deviations in measured densities compared to the values predicted by the mixture model. The average combined expanded uncertainty in the experimental data is shown by dashed lines and listed in the figure title.

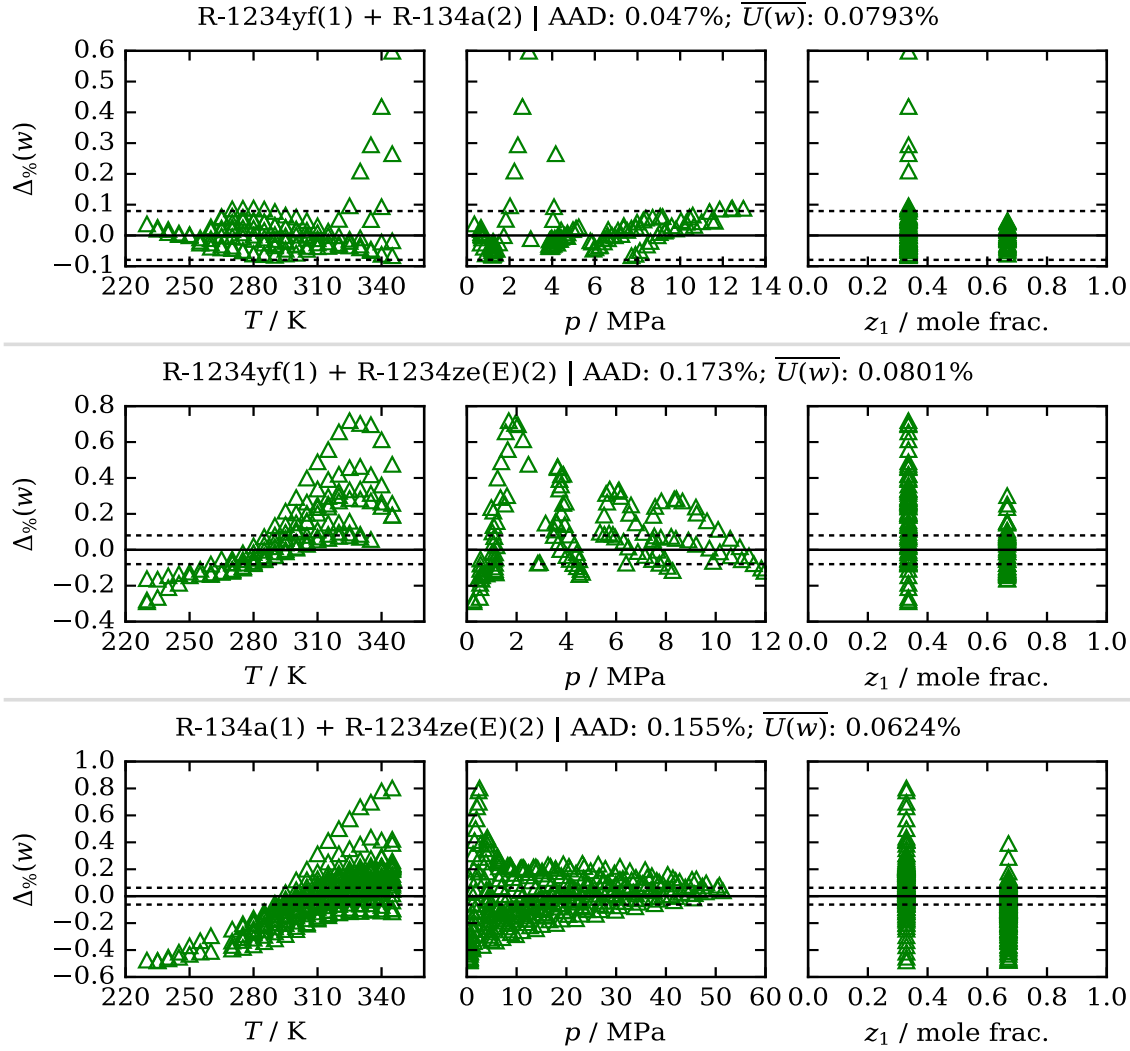


Figure 4.1-5. Relative deviations in measured speed of sound compared to the values predicted by the mixture model. The average combined expanded uncertainty in the measured data is shown by dashed lines and listed in the figure title.

Viscosity model. We fit the mixture viscosity data to the viscosity mixture model implemented in REFPROP; this model is based on the extended corresponding states (ECS) approach. The viscosity of a mixture is treated as a sum of a dilute-gas contribution and a residual contribution with all terms being functions of composition,

$$\eta(\rho, T, x) = \eta_0(T, x) + \Delta\eta(\rho, T, x) \quad (4.1-10)$$

The dilute gas contribution is found from kinetic theory [18-20] assuming a Lennard Jones potential applies with collision integrals based on Neufeld et al.[21]. A scaling factor is used so that in the limit of the pure fluids (i.e., $x = 0$ or $x = 1$), the recommended pure fluid formulation is exactly reproduced.

The residual contribution is modelled using a one-fluid extending corresponding states approach [22-24],

$$\Delta\eta(\rho, T, x) = \Delta\eta_{ref}(T_{ref}, \rho_{ref})F_{\eta}(T, \rho, x), \quad (4.1-11)$$

The mixture is represented by a hypothetical pure fluid, whose properties are found by evaluating a single (“one-fluid”) reference fluid (denoted by subscript ref) that is evaluated not at the mixture T and ρ but rather at a conformal temperature and density T_{ref} and ρ_{ref} ; nitrogen is used as the reference fluid in mixture calculations. The conformal temperature and density are found using the relationships $T_{ref} = T/f_x$ and $\rho_{ref} = \rho h_x$ and the quantities f_x and h_x are determined through the use of mixing and combining rules that involve the individual pure-fluid f_i and h_i . Binary interaction parameters were also used where data are available for a specific binary pair. Further details on the model are given in the Appendix (A1.1.4). This ECS model is adequate for representing the viscosity of many refrigerant and hydrocarbon mixtures, typically representing viscosity of refrigerant mixtures to within about 4% [22]. This model was fitted to data, and the resulting mixture parameters as well as comparisons of the model to the data are given in A1.1.7.

We did not measure the viscosity or thermal conductivity of the R1234ze(E)/227ea blend, but this was one of the blends selected for the ECU testing comprised. (The scope of work called only for the measurement of three binary pairs.) We were unable to locate literature data for thermal conductivity or viscosity of R227ea mixed with R1234ze(E). In fact, we were unable to locate experimental viscosity or thermal conductivity data of R227ea mixed with *any* compound. To provide the data needed for the cycle simulations we estimated the transport properties based on similar blends. There are data for viscosity [25] and thermal conductivity [26] for mixtures of R125 and R1234ze(E), and these data were fitted to obtain binary interaction parameters for R125/R1234ze(E). R227ea (1,1,1,2,3,3,3-heptafluoropropane, C_3HF_7) and R125 (pentafluoroethane, C_2HF_5) are both highly fluorinated n-alkanes that should have similar interaction behavior with R1234ze(E). These parameters should provide a reasonable estimation for the R1234ze(E)/R227ea mixture. We estimate the uncertainty in the liquid phase for viscosity and for thermal conductivity to be 5 – 10%.

Thermal conductivity model (ECS). The model for mixture thermal conductivity is also an ECS model. The treatment is similar to that of viscosity, however the thermal conductivity is first divided [23, 24, 27, 28] into contributions from internal motions of the molecule, λ^{int} , (which are only functions of temperature) and translational contributions, λ^{trans} , which are due to collisions between molecules and are a function of both temperature and density, along with an additional term for the critical enhancement,

$$\lambda(\rho, T, x) = \lambda^{int}(T, x) + \lambda^{trans}(\rho, T, x) + \Delta\lambda_c(\rho, T, x). \quad (4.1-12)$$

The translational contribution is further divided into a dilute gas contribution, λ^* , and a residual contribution λ^r ,

$$\lambda(\rho, T, x) = \lambda^{int}(T, x) + \lambda^*(T, x) + \Delta\lambda^r(\rho, T, x) + \Delta\lambda_c(\rho, T, x). \quad (4.1-13)$$

The final term in Eq. (4.1-13), due to the critical enhancement, is calculated by applying mixing rules to the parameters in the Olchowy-Sengers model [29, 30] as described in Ref. [24]. Further details on the ECS model for thermal conductivity, including details on the mixture terms, are given in the Appendix (A.1.7). This model was fitted to both the thermal conductivity data measured in this work and, where available, the (limited) literature data. The resulting coefficients and comparisons of the model to the data are provided in the Appendix (section A1.1.7). Also given in the Appendix is the mixture data file HMX.BNC for use with REFPROP, which implements the results of both the ECS viscosity and thermal conductivity mixture models.

Thermal conductivity model (Entropy Scaling). In addition to the ECS model, which was used in the cycle simulations (Task 7), we have applied the modified entropy scaling approach to model the measured thermal conductivity data. Entropy scaling is a relatively new approach for the modeling of transport properties that NIST is exploring, and the availability of the high-quality thermal conductivity data measured here allowed us to test this approach on mixtures. Entropy scaling is based on the idea that entropy (a thermodynamic property), when scaled in an appropriate way, is a measure of the structure of the fluid phase. Thus, transport properties can be expressed in terms of this scaled entropy, rather than as a function of, for example, the temperature and density. This approach connects the transport properties (e.g., thermal conductivity and viscosity) to the thermodynamic properties (which are represented by an equation of state). The power of entropy scaling is that it allows an accurate representation of the transport properties with far fewer experimental data needed as input to the model compared to traditional models.

This approach and its application to the mixture thermal conductivity data are detailed in Appendix A1.1.7. The result is a representation of the data that is comparable to the ECS model, but with a single set of four adjustable coefficients (fitted to the experimental data) for the three binary pairs studied. This compares to the separate sets of adjustable coefficients fitted to each binary pair in the ECS approach.

4.2. Task 2: Flammability Testing

4.2.1. Introduction

It is essential that any low-GWP replacement for HFC-134a be non-flammable. This is challenging, however, since for molecules containing only hydrogen, fluorine, and carbon, there is a trade-off between GWP and flammability. The common changes to the molecules (adding hydrogen atoms or double bonds) to make them more reactive in the troposphere and hence lower their atmospheric lifetime (which lowers GWP), also makes them more flammable. Thus, one desires to make the molecules, or mixtures of compounds, have the lowest GWP possible while still maintaining non-flammable behavior. A further challenge arises, however, in that flammable behavior is not a distinct boundary, but depends upon the environment to which the refrigerant is exposed. As described by Williams [31], flame stabilization requires that the characteristic chemical reaction rate be fast enough to keep up with the flow/transport field in which the refrigerant is reacting. For compounds that are clearly flammable or non-flammable, for example methane or CO₂, their behavior in air is consistent among common configurations. But for compounds of intermediate flammability, for example mixtures of CO₂ and CH₄, or pure HFO-1234yf, their behavior will be very sensitive to the flame/fire configuration. For example, in recent full-scale tests in a 50 m³ module [32], stable flames of HFO-1234yf and air could not be initiated with a high-voltage spark ignition system typical of that used in the small-scale E681 test[33]. In contrast, using a glow-plug ignition source, turbulent flames of HFO-1234yf and air in an HVAC duct were achieved by Papas et al. [34], with turbulent flame speeds much higher than previously reported laminar burning velocities.

There are two goals of the present refrigerant flammability work. The first is to assess experimentally the flammability of the candidate blends predicted to be non-flammable (as determined by ASHRAE Standard 34 [33]) in the previous limited-scope project. In the preliminary work, an empirical model of flammability based on the adiabatic flame temperature and the fluorine to hydrogen ratio of the reactants was used to create a flammability index [9] and rank a list of candidate blends with regard to their flammability. All of the candidate blends selected for further study in the MBHP or ECU were predicted to be non-flammable. Nonetheless, it is essential that the candidate blends be tested in experiments to verify that the predictions were accurate. It is expected, however, that the fire threats in the DOD applications will be much more aggressive than in typical HVAC applications, and a more conservative flammability test would be desirable.

The second goal of the present work is to use the experimental flammability test results, together with flame modeling, to predict, for a given blend, if it will be flammable in the fire threats of interest to the DOD. Researchers at the Army Research Laboratory (ARL) have developed a representative scenario, in which an incendiary projectile impacts a coil filled with refrigerant. In such a test, ignition sources are abundant, and it is required that the resulting refrigerant-air cloud not support a self-propagating flame. Predicting the behavior of candidate lower-GWP refrigerant blends in that test is challenging. Of course, all candidate blends could be tested at full-scale, but this would be prohibitively expensive and time consuming. It is desired to predict the full-scale behavior based on laboratory-scale test results. While challenging, such a prediction is not unprecedented. For example, the behavior of HFC fire suppressant agents in the FAA Aerosol Can Test [35] has many similarities as will be discussed below.

The approach for flammability assessment is as follows. First, the flammability of the candidate blends must be experimentally tested. Since the empirical model for refrigerant flammability in the limited-scope project was developed based upon the data in the ASHRAE Standard 34 database, the modified ASTM E681 specified in Standard 34 is used to experimentally verify the predicted performance of the candidate blends. Next, a more stringent test is applied. For this purpose we adopt a modified version of the Japanese High-Pressure Gas Law (JHPGL) test [36], as described below. Development of the kinetic model of combustion of the refrigerant-air flames is discussed, and the model is used to interpret the experimental data available to date. Finally, an approach for connecting the small-scale tests to the full-scale live-fire tests to be conducted at the Army Research Laboratory (ARL) is described, with the goal of properly interpreting those results and minimizing the number of tests necessary to ensure non-flammable behavior of the selected blends.

4.2.2. E681 tests and Japanese High-Pressure Gas Law tests

E681: Experimental Results. For HVAC applications, the flammability of a refrigerant is assessed via ANSI/ASHRAE Standard 34 [37] or the very similar ISO Standard 817 [38]. A flammability rating of Class “1” to “3” is assigned, based on its heat of combustion, lower flammability limit, and laminar burning velocity. In the ASHRAE standard, Class 3 fluids, termed “higher flammability,” exhibit flame propagation at 60 °C and 101.3 kPa and have a heat of combustion greater than 19 MJ/kg *or* a lower flammability limit (LFL) less than 0.10 kg/m³. Class 2 fluids, “lower flammability” have a heat of combustion less than 19 MJ/kg *and* an LFL greater than 0.10 kg/m³. Class 1 fluids exhibit “no flame propagation” when tested at 60 °C and 101.3 kPa. Class “2L” fluids also have a maximum burning velocity less than 10 cm/s. For the present discussion, we focus on the distinction between Class 1 and Class 2L.

Flame propagation and the lower flammability limit in ASHRAE Standard 34 are determined by the test method specified in ASTM E681 [39], with slight modifications. A schematic of the E681 test vessel is shown in Figure 4.2-1. In the test, the refrigerant and air are introduced into a 12 L glass sphere, which is closed by a spring-loaded stopper at the top. A 15 kV AC source provides a spark (spark duration 0.4 s) to tungsten electrodes (1 mm diameter, 6.4 mm gap) located 1/3 diameter from the bottom of the vessel. If a flame forms and extends upwards and outwards from the spark to the walls of the flask and subtends an angle equal to or greater than 90° as measured from the point of ignition, there is “flame propagation.” Tests are conducted at 60 °C with air at 50 % relative humidity (r.h.) at 23 °C (0.0088 g H₂O/g air).



Figure 4.2-1. Left image: schematic of ASTM 681 test vessel; Right two images: visual images from HFC-32/HFC-134a blend (0.35 /0.65 mass fraction) below and above the lean flammability limit [40, 41].

The ASHRAE Standard 34/ASTM E681 tests for the present work were performed by an outside testing laboratory under contract to NIST. This contractor was selected because they have extensive experience with the test [41] and have provided a substantial number of the data in the ASHRAE Standard 34 database. Considering that there is significant variability in the test approaches that can affect the quantitative results [41, 42], it was useful to select a contractor likely to provide a test approach consistent with the existing database. This was important since the present test results are being compared to flammability predictions from our earlier work [6, 9], which was developed based on the existing ASHRAE Standard 34 database.

It was originally expected that all mixtures selected for further study would need to be tested by the outside contractor. However, over the course of the project, it was apparent that several of the candidate blends were very close in composition to existing compounds for which applications to ASHRAE 34 had recently been made, so those similar blends (R-450A, R-513A, and R-515B) were adopted. A side benefit is that they would not need to be tested again via the contracted E681 experiments, freeing up some of those tests for other compounds of interest.

The results of the contracted E681 tests are listed in Section A.2.1 of Appendix A. Table 4.2-1 below summarizes the results of the E681 tests and lists the existing flammability ratings [9] for R-513A, R-450A, and R-515B from the ASHRAE Standard 34 database (P_{max} and ω_{psr} are discussed below). All of the candidate blends are flammability Class 1. The last three mixtures, blends of HFO-1234yf and HFC-134a, were tested at increasing concentration of HFC-134a until a Class 1 rating was achieved. These tests will be used to connect E681 experiments, JHPGL experiments, and simulations to full-scale results, as discussed below.

Table 4.2-1. Modeling and test results for candidate blends (reactants at 296 K, 101 kPa, and 50 % r.h.)

Name	Blend (mole%)	Std.34 Class	$\bar{\Pi}$ †	P_{max} [10 ⁻² kPa]	ω_{psr} [s ⁻¹]
Tern-1	R1234yf/134a/1234ze(E) (32/52/16)	1 ^E	-1.2	0.451	86
R-513A	R1234yf/134a (53.2/46.8)	1 *	-0.5	0.474	99
R-450A	R1234ze(E)/134a (53.3/44.7)	1 *	-0.2	0.262	110
R-515B	R1234ze(E)/227ea (93.85/6.15)	1 *	2.0	1.56	166
YF/134a-30	R1234yf/134a (70/30)	1 ^E	1.7	1.27	166
YF/134a-28	R1234yf/134a (72/28)	2L ^{E,e}	1.9	-	169
YF/134a-26	R1234yf/134a (74/26)	2L ^{E,e}	2.1	-	177

* from Std. 34 database

† flammability index from ref. [9]

^E from contracted E681 testing

^e estimate based on E681 testing and consideration of similar compounds

E681: Interpretation of E681 Results in Regard to Large-Scale Behavior. The E681 test, as modified by ASHRAE Standard 34, is widely used in the HVAC industry and is believed to be sufficiently conservative to provide safe application of refrigerants in those settings. It may not, however, be appropriate for the much more stringent non-flammable requirements of DOD applications. As described above, flammability is a continuum, and only becomes a discrete rating when some criterion is applied. As an example, the 90° flame angle criterion is used in the ASHRAE Standard 34 to distinguish between “flame propagating” and “non-flame propagating.” This is illustrated in Figure 4.2-1, in which the left and right flame images (with flame angles of 85° and 95°, respectively) are for refrigerant concentrations in air that are just below and above the lean flammability limit. To an observer, these flames might both appear to be “flammable,” and hence the 90° criterion may not be appropriate for more energetic, turbulent-ignition scenarios such as in the Army Research Laboratory ARL live-fire tests.

The selection of the 90° criterion is informative for the present discussion. Richard and co-workers [43] conducted experiments in larger, 200 L vessels in which the walls did not constrain the effects of buoyancy on the flame propagation. They found that some flames propagated and consumed all the fuel in the vessel while others self-extinguished and failed to propagate. The successful flame propagation in the 200 L vessel correlated with those flames in the 12 L vessel that had a flame angle of 90° or greater, validating the 90° criterion in the ASHRAE Standard 34/E681 test. Note that as an additional measure of safety, the ASHRAE Standard 34 test is conducted with gases at 60 °C, i.e., a more flammable condition, so that a non-flammable rating obtained at the test condition is conservative. Nonetheless, concerns have been raised with regard to the 90° criterion. For example, only two refrigerant blends were used, i.e., R-152a/134a and R-152a/125, and it is unclear if the behavior will be the same for different chemical classes of refrigerants, e.g., HFOs vs HFCs. Also, the stretched burning velocity and critical flame

radius for flame propagation are known to depend on the Lewis number of the mixture [44, 45], which can vary for different blend components.

The challenge in the present work is to find a relevant flammability criterion in small-scale tests that properly captures the important flame dynamics in the full-scale, live-fire tests of interest to the Department of Defense, which is characterized by strong, multiple ignition sites (due to projectile impact), heated product gases from ancillary combustion (from the pyrotechnic charge) and shock-induced heating, and turbulence. The next section presents the rationale for selecting the Japanese High-Pressure Gas Law (JHPGL) test, and some experimental results from it with the candidate blends and R-1234yf/134a mixtures.

Japanese High-Pressure Gas Law Test: Relevance. A modified version of the Japanese High-Pressure Gas Law (JHPGL) test (documented in the appendix of ref. [36]) has been selected to provide a more stringent, reduced-scale flammability test for refrigerants exposed to live-fire tests at full scale. The experiment uses a 2 L stainless steel spherical pressure vessel into which the premixed gases are introduced using the partial pressure method. A thin platinum wire energized by a continuous 100 VAC source provides ignition. The explosion pressure P_{\max} (i.e., the maximum pressure in the vessel for any value of fuel-air equivalence ratio ϕ) provides the metric for flammability. The experiment is described in detail in previous work [36, 46-48] and in Section A.2.2 of Appendix A, and has been used to understand HFC refrigerant flammability [36, 46] as well as HFC fire-suppressant performance in aircraft fire-suppression applications [47, 48]. Modifications from the original standard are the use of pressure rather than temperature as the flammability metric, and a modified ignitor configuration to allow insertion through a single port.

The test indicates wider flammability limits than the ASHRAE Standard 34 E681 test for the following reasons. The exploding platinum wire sprays droplets of molten platinum through the chamber [49], providing numerous ignition sites by catalytic surfaces, and the turbulent flow field accelerates the flame speed and minimizes stretch-induced extinction of the nascent flames [50] at early times. The constant volume combustion chamber also provides compressive heating, which increases reactivity. In previous work, flammability in the JHPGL test was shown to accurately predict flammability of HFC/hydrocarbon/air mixtures in the very intense conditions of the FAA Aerosol Can Test (FAA-ACT). In that test, a 10 m³ pressure vessel is used to mimic the inside of an airliner cargo-bay, in which an aerosol spray can explodes due to the heat of a cargo-bay fire. In the FAA-ACT, a fast-acting valve releases the contents of the simulated aerosol can (454 g of propane, ethanol, and water) across a 15 kV continuous AC spark ignitor, into the chamber which has been prefilled with a mixture of air and an HFC fire suppressant (e.g., HFC-125, 2-BTP, Novec 1230, etc.). The contents of the aerosol can form an intense propane/ethanol/water turbulent spray flame at the ignitor location, and the question is whether the flame propagates into the air/HFC end-gases in the chamber. The pressure rise in the chamber due to reaction of the aerosol can contents (and sometimes HFC suppressant) creates a temperature rise of 100 °C to 250 °C. The similarities with the ARL live-fire refrigerant-coil test include: strong ignition source, temperature rise due to compressive heating, reactive intermediates supplied by strong combustion of an adjacent flame, and basically the same type of reactants (HFCs, HFOs, etc. mixed with air) in the end gases, which may or may not be ignited. The FAA-ACT also provides extra water (i.e., mixed with the fuel), enhancing the reactivity of the HFC compounds. The fact that the JHPGL test could accurately predict which fire

suppressants (and blends) agents would combust in the end-gases of the FAA-ACT [48] gives confidence that it is a good small scale test for predicting the behavior of similar compounds in the ARL live-fire refrigerant tests.

Japanese High-Pressure Gas Law Test: Experimental Results. The JHPGL as used provides the peak pressure rise in the vessel as a function of blend volume fraction in the air. Figure 4.2-2 shows, for the four candidate blends, the measured peak pressure as a function of refrigerant volume fraction in moist (50 % r.h.) air (lower curves) together with the calculated [51] equilibrium explosion pressures for the same mixtures. Equilibrium values are about 10×10^{-2} kPa for all blends, varying about 1% between the candidate blends, and by about 1% for varying water vapor in the air (0 % to 100 % r.h.). The equilibrium value assumes complete reaction to most stable products with no heat losses. For typical fast hydrocarbon flames, 90 % of the equilibrium value can be attained [47]. For slower flames, the pressure rise is a smaller fraction of equilibrium, for example about 50 % for HFO-1234yf. Fusing of the Pt wire causes a pressure rise of $0.033 \cdot 10^{-2}$ kPa \pm $0.013 \cdot 10^{-2}$ kPa [36]. Thus, the candidate blends have pressure rises of 2 % to 13 % of the equilibrium values.

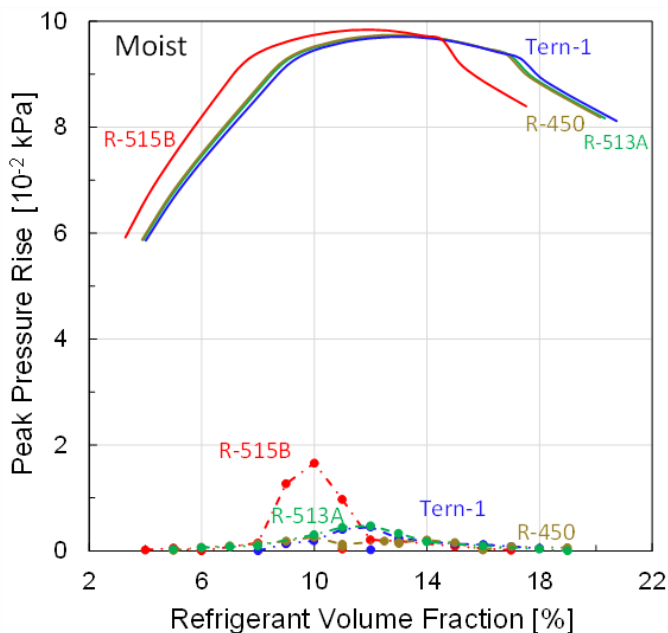


Figure 4.2-2. Equilibrium explosion pressure of candidate blends (Tern-1, R-513A, R-450A, and R-515B) together with experimental results in the JHPGL test as a function of blend volume fraction in air (50 % r.h.)

The experimentally observed peak pressure rise for the four candidate blends is given in Section A.2.2 of Appendix A and shown graphically in Figure 4.2-3 for dry and moist air. Focusing on the moist air results (right frame), the peak pressure for the four agents: R-450A, Tern-1, and R-513A is low (0.262 , 0.451 , and 0.474) $\cdot 10^{-2}$ kPa, but higher for R-515B, about $1.6 \cdot 10^{-2}$ kPa. Details of the results for individual blends are shown in Figure 4.2-4 (note difference in scales). While these data may appear noisy, it is important to keep in mind that these are very low pressure rises, at the lower end of the dynamic range of the piezo-electric dynamic pressure transducer. Also, the stochastic nature of the exploding-wire ignition system creates variability in

the results. The individual results in Figure 4.2-4 illustrate the effects of water vapor, which are small for R-450A and R-515B, and larger for R-513A and the Tern-1 blend.

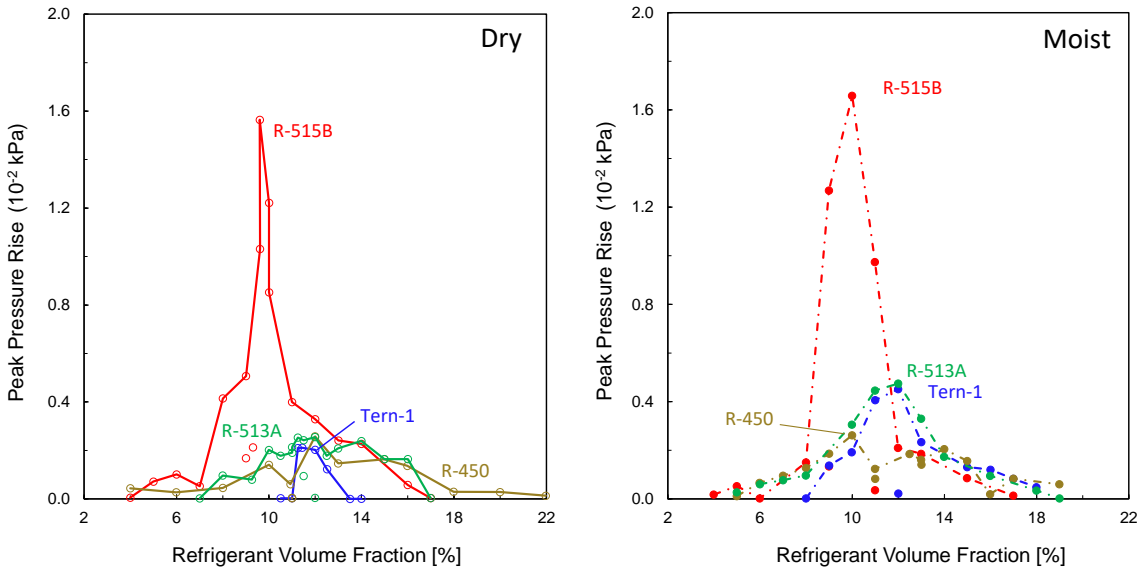


Figure 4.2-3. Explosion pressure of candidate blends in JHPGL test as a function of blend volume fraction in air (left frame: dry air; right, moist)

While the results of the tests for the candidate blends are useful and illuminating, there is value in conducting tests in which the blend components are more systematically varied. To do this, we considered a binary blend of HFC-134a with HFO-1234yf, with increasing mole fraction of the less-flammable component (HFC-134a) up to 100 %. Figure 4.2-5 shows the JHPGL explosion pressure as a function of blend volume fraction in the air; each curve refers to a particular HFC-134a volume fraction in the blend (left frame: dry air; right frame: moist air, 50 % r.h.). Figure 4.2-6 shows the peak values from Figure 4.2-5 as a function of the volume fraction of HFC-134a in the blend. For pure HFO-1234yf flames, moist flames have about 25 % higher peak pressure than do dry flames. For both moist and dry air, the peak pressure drops off steadily until about 50/50 volume fraction, after which the reduction in peak pressure with increasing HFC-134a is small. That is, after about 60 % HFC-134a volume fraction, there appears to be no additional benefit of adding this component to HFO-1234yf, in this experimental configuration.

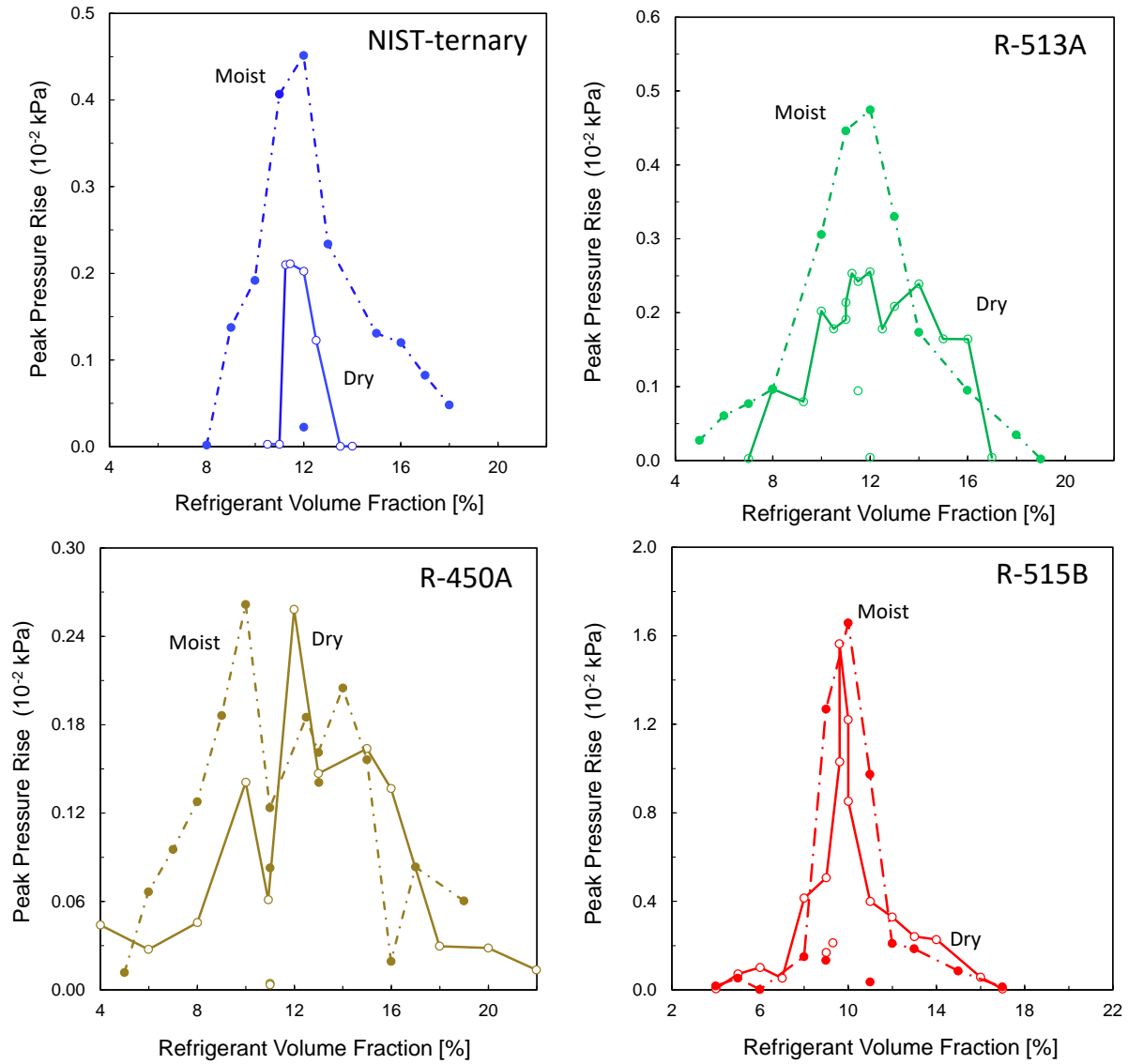


Figure 4.2-4. Explosion pressure of candidate blends (Tern-1, R-513A, R-450A, and R-515B) in JHPGL test as a function of blend volume fraction in air (solid lines: dry air; dashed lines: moist air; note different scales)

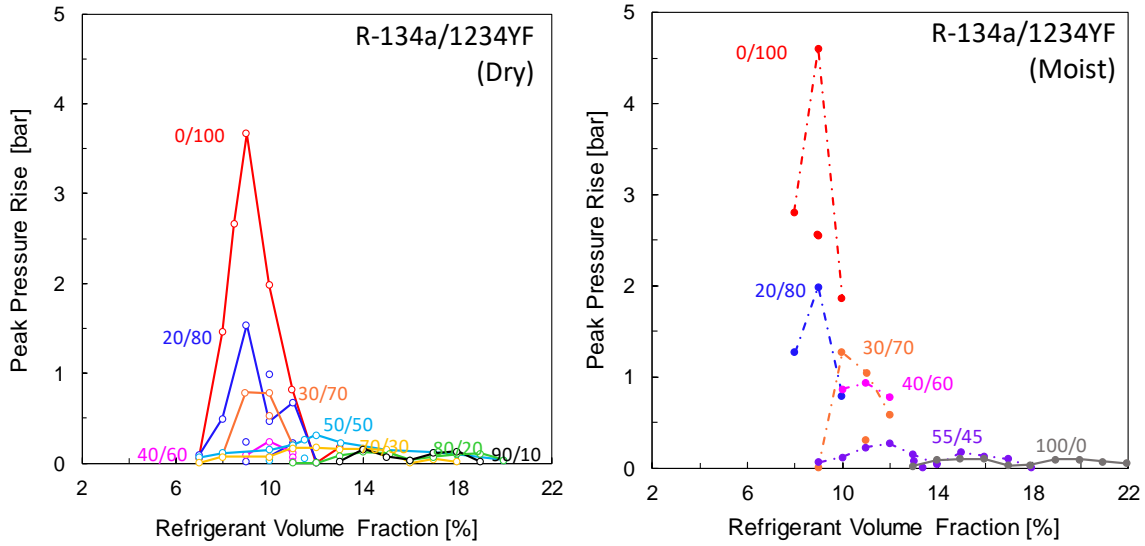


Figure 4.2-5. Explosion pressure in the JHPGL test for binary blends of HFC-134a with HFO-1234yf as function of volume fraction the blend in air. Different curves show results for varying volume fractions of HFC-134a/HFO-1234yf in the blend (left frame: dry air; right: moist).

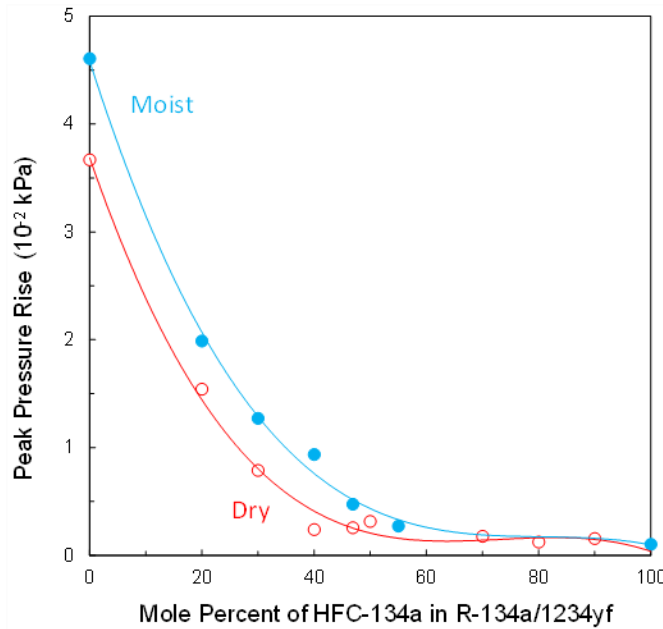


Figure 4.2-6. Peak explosion pressure in the JHPGL test for binary blends of HFC-134a with HFO-1234yf as function the volume fraction of HFC-134a in the blend, for moist (50 % r.h.) and dry (< 2 % r.h.) air

4.2.3. Improvements in Predictive Model

Recent work at NIST has had the goal of developing the predictive capability for flammability. A reasonable surrogate for flammability is the laminar burning velocity S_u^0 , which is defined as the

rate of propagation of a 1-D, planar, adiabatic, combustion wave through a mixture of combustible gases. It is a useful flammability metric since it is a fundamentally based parameter incorporating the effects of overall reaction rate, heat release, and molecular transport for the fuel-oxidizer mixture. It is used as a scaling parameter for turbulent flame speed [52] and as an input to full-scale explosion models [53, 54]. It is correlated with minimum ignition energy, flame quenching diameter, and lean flame extinction, and is a metric used in existing and developing codes and standards for refrigerant flammability [37, 38]. In the present work, we adopt burning velocity, along with the overall chemical rate as determined in a stirred-reactor, since both have proven useful for understanding the behavior of near-limit flames of fluorinated compounds, alone with air, or in hydrocarbon-air mixtures [35, 55-63]. Calculating either the burning velocity or the overall chemical rate requires a detailed kinetic model of the combustion of the fluorinated compounds.

Early work at NIST developed a detailed kinetic model for HFC fire suppressants [64, 65] and recent work has extended it to flames of pure refrigerants and air [66-68]. In the present project, the mechanism was further refined and updated with new rates and thermodynamic data appearing in the literature. As a result, the mechanism can accurately predict the existing experimental burning velocity data in the literature for one- and two-carbon HFCs [67] and fluoropropenes (HFOs) [68]. Since it has not been extensively tested with data for blends of refrigerants, the present work collected new burning velocity data for R-152a/134a, and R-152a/1234yf blends. Also, since the burning velocity of either HFO-1234yf or HFC-134a with air at 298 K is too low to measure in normal-gravity experiments, the addition of a more reactive HFC, in this case HFC-152a, allows one to more readily obtain data on their combustion behavior. The mechanism was then used to calculate the burning velocity *a priori* for the experimental conditions to assess its predictive ability.

Experimental Data for Model Validation. As described in Section A.2.3 of the Appendix, the 2 L chamber was used with a spark ignition system to collect the chamber pressure P as a function of time t , from which the burning velocity is determined using a thermodynamic model [69]. Figure 4.2-7 shows the burning velocity as a function of refrigerant volume fraction [70] (points: experimental data, dotted lines: cubic fit to experimental data, solid lines: numerical predictions). The different curves in each frame are for R-152a/134a blends at (1.00/0.0), (0.80/0.20), (0.50/0.50) volume fractions (left frame), and R-152a/1234yf blends at (1.00/0.0), (0.50/0.50), (0.40/0.60), and (0.30/0.70) volume fraction. The air in these tests was dry ($< 2\%$ r.h. at $23\text{ }^{\circ}\text{C}$) except for the one curve for at R-152a/1234yf (0.40/0.60), for which the r.h. was about 50%. The dotted lines are cubic fits to the experimental data. As indicated, the mechanism does a very good job of predicting the burning velocity for these conditions. A similar comparison has been performed for other refrigerants [66-68]. The different data sets on each frame correspond to different molar ratios of the two constituents, as indicated on the curve labels. The experimental data are the points, the dotted lines cubic fits to the experimental data, and the solid lines the numerical modeling predictions.

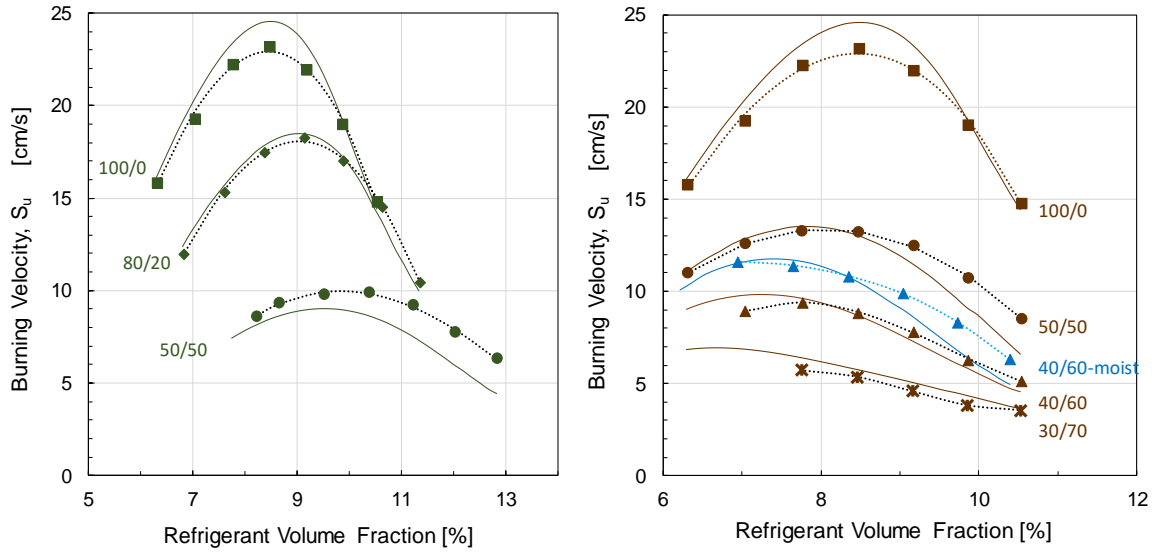


Figure 4.2-7. Laminar burning velocity of R-152a/134a (left frame) and R-152a/1234yf (right frame) mixtures with air as a function of the equivalence ratio

Figure 4.2-8 summarizes the predictions of the present model vs. the experimental results, indicating that the predictive ability of the model is good. Hence, the kinetic model should be a useful tool for understanding the present candidate blends (since all of the constituents of the blends are included in the kinetic model).

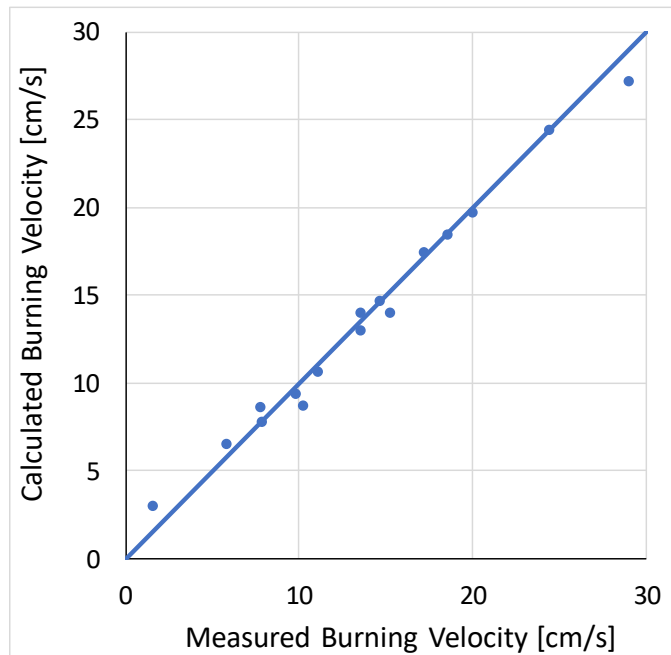


Figure 4.2-8. Calculated vs. measured laminar burning velocity (peak over all ϕ) of twenty-one refrigerant/N₂/O₂ flames for which experimental data are available in the literature [66-68]

4.2.4. Interpretation of E681 and JHPGL Experimental Results

The results in the JHPGL test as well as in the E681 test can be interpreted using the kinetic model as a tool. A useful metric is the overall reaction rate of the mixtures, at the conditions of interest (e.g., initial T , P , humidity, etc.). Simulations (or experiments) of the blow-out condition of a perfectly stirred reactor (PSR) can be used to obtain an estimate of the overall chemical rate ω_{psr} . This rate can be used, among other things, to estimate the laminar burning velocity [71], the flammability limits [36], and the extinction conditions of full-scale fires [59]. For example, in Figure 4.2-9, the overall chemical rate ω_{psr} calculated for the mixture R-1234yf/134a is shown as a function of the volume fraction of the blend (i.e., fuel). Increasing volume fractions of HFC-134a in the blend reduces ω_{psr} , and the effect of humidity is shown by the three frames (0 % r.h., 50 % r.h., and 100 % r.h.). Of particular interest is the peak value of ω_{psr} for each blend. These are shown in Figure 4.2-10 with one curve for each value of the humidity in the air. As indicated, increasing water vapor (0 % to 100 % r.h.) increases the peak overall reactivity by a factor of 2.5 for HFO-1234yf and 1.8 for HFC-134a. Moreover, as shown in Figure 4.2-9, at 50 % r.h. the ω_{psr} has broad plateaus, whereas at 0 and 100 % r.h. there are distinctive peaks. This behavior is expected to be exhibited for all HFC blends.

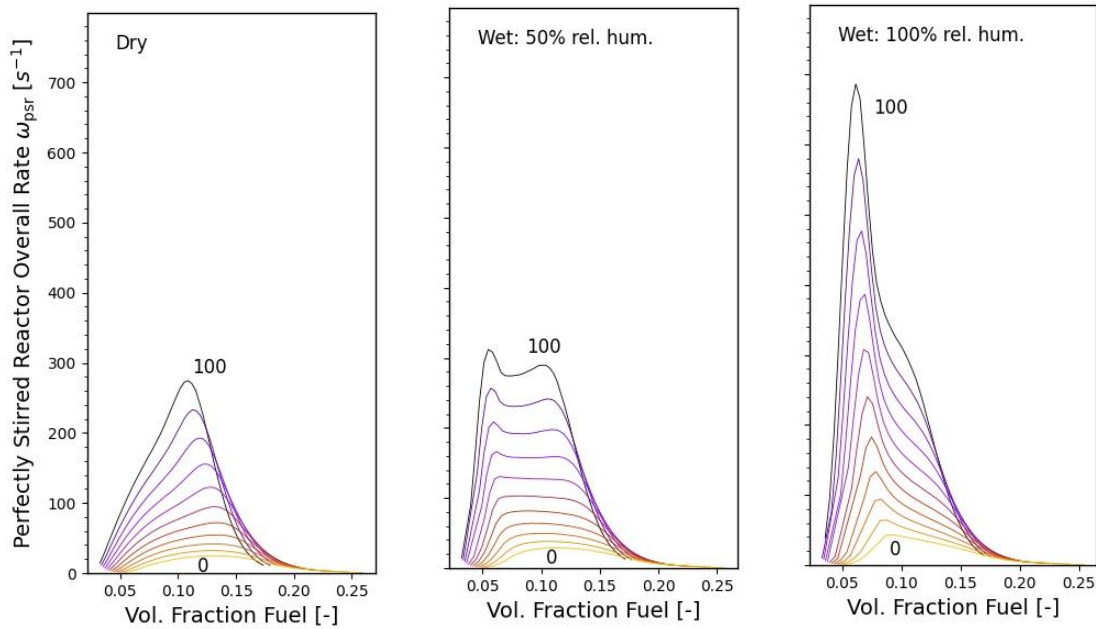


Figure 4.2-9. Overall chemical reaction ω_{psr} as a function of volume fraction in air determined via perfectly stirred reactor simulations for the molar blend R-1234yf/134a. Each curve refers to one blend ratio: top curve, 100% HFO-1234yf, bottom curve 100 % HFC-134a; Frames: 0 % r.h. (dry), 50 % r.h., and 100 % r.h.

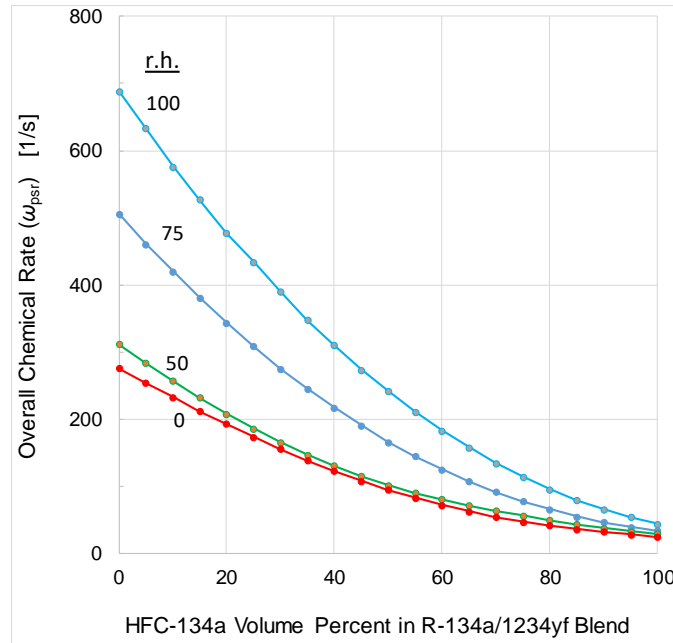


Figure 4.2-10. Peak (over all ϕ for each blend) chemical reaction ω_{psr} as a function of volume fraction of HFC-134a in the blend of R-1234yf/134a. Individual curves are shown for varying water vapor in the air (0 %, 50 %, 75 % and 100 % r.h.)

The overall chemical rate ω_{psr} provides a useful metric for examining the flammability of refrigerant blends. It can be used to compare alternative flame-suppressant agents, examine their flammability with respect to concentration in the air, discern the effects of humidity, and compare with experimental results. It is used in the section below to interpret the experimental results in the E681 and JHPGL tests.

Figure 4.2-11 shows the explosion pressure in the JHPGL test vs. the Overall Chemical Rate ω_{psr} for data from the candidate blends (“×” markers) and the R-1234yf/134a blends (“○” markers) (from Table 4.2-1). Blue points have an ASHRAE Standard 34 Class 1 rating, and the blue box bounds the locus of those mixtures; the orange points are class 2L. As indicated, there is a good correlation between the explosion pressure and ω_{psr} . As described above, the three blends Tern-1, R-513A, and R-450A have about the same explosion pressure and ω_{psr} . The blend R-515B, while it has a Class 1 rating, is likely at the limit of this rating because the 70/30 R1234yf/134a blend is just at the Class 1 limit (i.e., 72/28 and 74/26 had flame angles $> 90^\circ$ and hence were not Class 1). Thus, the three metrics, ASHRAE Standard 34 rating, JHPGL test explosion pressure, and ω_{psr} are related as shown in Figure 4.2-11. For a Class 1 rating, the explosion must be less than $1.41 \cdot 10^{-2}$ kPa $\pm 0.14 \cdot 10^{-2}$ kPa and $\omega_{psr} < 166 \text{ s}^{-1}$. The important point is that ω_{psr} is a parameter based in physics that can be calculated for a mixture and can be used to correlate experimental flammability results between test methods, or with full-scale test results.

Interpretation of Results with Regard to the Full-Scale Live-Fire Tests. As shown in Figure 4.2-11, the JHPGL test explosion pressure and ω_{psr} are useful scales for characterizing blends. The next step is to understand, for the live-fire tests, what degree of flammability is acceptable. A straightforward way to do that would be to do live-fire tests with mixtures of R-1234yf/134a at varying mole fractions of HFC-134a. The mixture ratio that provides non-flammable behavior in

that test can be used with Figure 4.2-11 to quantify the corresponding JHPGL test explosion pressure limit and ω_{psr} limit.

The overall chemical rate ω_{psr} can also be used to explore other features of the blends. For example, Figure 4.2-12 shows ω_{psr} for the candidate blends for different levels of water vapor in the air (0 %, 50 %, and 100 % r.h.). Data are shown for the nominal blend (Nom), worst-case fractionation WCF (from uncertainty in the blend components), and worst-case fractionation for flammability WCFF (from different vaporization rates for leaking blend components of liquid agent at the WCF). As indicated, for most blends, the differences in Nom., WCF, and WCFF are small, except for the case of R-450A, for which the WCFF is quite different from the WCF (although the Class 1 rating is still maintained for the WCFF). In the DOD application, the concern is with rapid loss of refrigerant charge, so WCF is the mixture of interest. A humidity level of 50 % r.h. was selected for the JHPGL tests as listed in the comparisons in Table 4.2-1. Nonetheless, as discussed for the R-1324yf/134a blend in Figure 4.2-10, Figure 4.2-12 shows that for the candidate blends, although there is predicted to be a small effect of humidity at 50 % r.h., there is predicted to be a large effect of humidity at 100 % r.h.

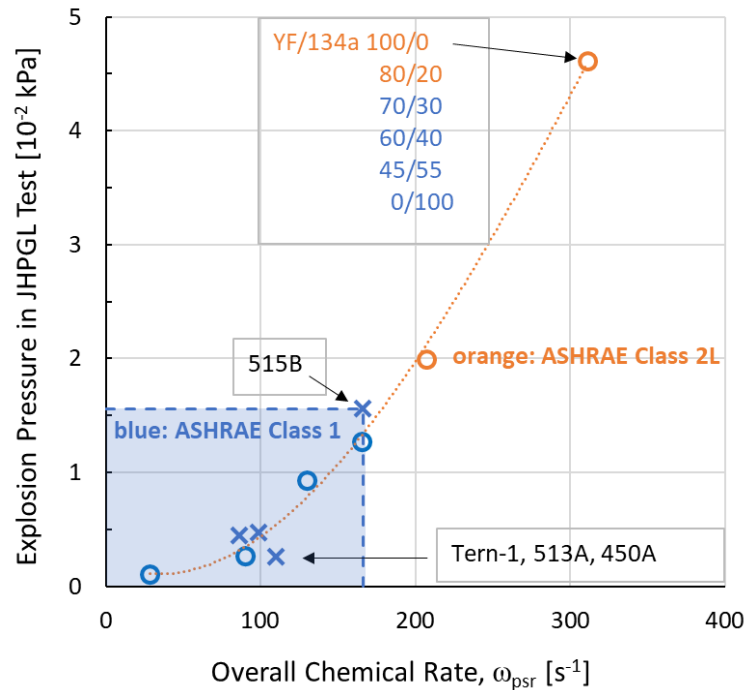


Figure 4.2-11. Explosion pressure in the JHPGL test vs. overall chemical reaction ω_{psr} (both peak over all ϕ) for R-513A, R-450A, R-515B and the Tern-1 blend and the R-1234yf/134a blends at increasing HFC-134a volume fraction. Dotted line is a polynomial fit to all the data to aid in visualization. (Initial conditions: 296 K, 101 kPa, 50 % r.h.)

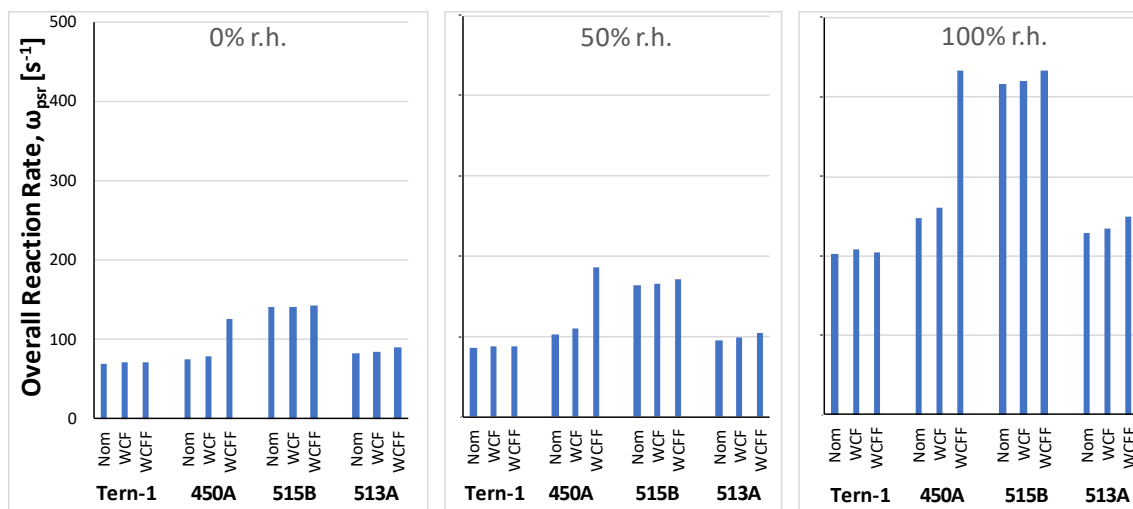


Figure 4.2-12. Peak (over all ϕ for each blend) chemical reaction ω_{psr} for R-513A, R-450A, R-515B and the NIST blend. Data are shown for the Nominal, WCF, and WCFE compositions in air ($T = 296$ K) and 0 %, 50 %, and 100 % r.h.

4.2.5. Coordination with Full-Scale Testing

The live-fire tests at ARL have been delayed due to COVID-19 related shutdowns as well as retirements. NIST has been in communication with James Anderson and Joshua Crookshanks at ARL, and we regularly participate in the Army's LGWP In-Progress Reviews. We had a detailed teleconference on October 13, 2021, in which NIST presented details on the results of this project and what tools and information NIST can provide to ARL. NIST is ready to collaborate with ARL in any way possible as their tests come up to speed. NIST has provided input on potentially useful tests to conduct and plans to provide interpretation using the computational tools that have been developed. For example, based on the results to date:

1. The three blends, Tern-1, R-513A, and R-450A are expected to behave similarly and have the most promising behavior with respect to flammability. R-515B, while nonflammable in the E681 test, it is close to the border of flammability.
2. Levels of humidity above 0.014 moles H₂O/mole air (50 % r.h. at 23 °C) may significantly increase the flammability of the blends.
3. HFC-134a should be tested at high ambient temperature and high humidity as a benchmark. Following that, tests with increasing amounts of added HFO-1234yf would be very valuable.

Recommendations concerning a proposed test matrix with ARL engineers can be discussed. The results of the present tests and calculations will be used as input. The goal is to minimize the number of full-scale tests while extracting as much information as possible from the tests. It is possible that the ASHRAE Standard 34 Class 1 flammability rating will be sufficient to ensure non-flammability in the live-fire tests. It is also possible that a more stringent criterion, for example something close to the behavior of Tern-1, R-513A and R-450A in Figure 4.2-11 ($P_{max} < 0.3 \cdot 10^{-2}$ kPa and $\omega_{psr} < 110$ s⁻¹) will be required. With a few live-fire tests, it should be possible to bound and understand the problem, and additional tests would provide higher levels of confidence in the findings and conclusions.

4.2.6. Summary of Flammability

All four candidate blends are non-flame propagating in the modified E681 test specified in ASHRAE Standard 34. In a more stringent test, the Japanese high-pressure gas law test (JHPGL), the explosion pressure in a 2 L combustion chamber with a fused platinum wire ignition source, is used as a metric for flammability. Three of four candidate blends (Tern-1, R-513A, R-450A) had similar pressure rise ($0.451 \cdot 10^{-2}$, $0.474 \cdot 10^{-2}$, and $0.262 \cdot 10^{-2}$ kPa), while one (R-515B) had a higher pressure rise ($1.56 \cdot 10^{-2}$ kPa). Tests with binary blends of HFC-134a and HFO-1234yf with increasing fraction of HFC-134a showed that an HFC-134a mole fraction of 0.30 was required to pass the E681 tests, and at this composition, the explosion pressure in the JHPGL test was $1.27 \cdot 10^{-2}$ kPa. Hence, it appears that the R-515B blend is close to the edge of passing the E681 test, while the other blends pass the test more easily.

A recently developed and validated kinetic model of combustion for one-, two-, and three-carbon HFC and HFO refrigerants was further improved and validated. For this purpose, burning velocity data were obtained in the 2 L chamber from the rate of pressure rise (using a spark ignition system). For binary blends of R-152a/134a and R-152a/1234yf, the experimentally derived burning velocity agreed well with the predictions from detailed numerical simulations. This adds confidence to the kinetic model.

The kinetic model was subsequently used to estimate the overall chemical reaction rate of the candidate blends. Both the E681 flame propagating/non-propagating boundary, as well as the JHPGL test explosion pressure were well correlated with the calculated overall reaction rate for each blend. The overall reaction rate is easily calculated for any arbitrary mixtures of interest. It is a fundamentally based parameter that can be used to correlate experimental flammability results between test methods, or with full-scale test results.

An important question is how well the live-fire tests at the Army Research Laboratory will compare with the small-scale E681, the JHPGL tests, and the calculated overall rate. It is unclear *a priori* if the live-fire tests will require lower or higher levels of flammability than the E681. For example, turbulence can increase flame speed of premixed flames, but high velocities can strain flames and extinguish them. If live-fire tests can be conducted for the mixtures of HFC-134a/HFO-1234yf at increasing mole fraction of HFC-134a until acceptable flammability occurs, it will presumably be possible to correlate the behavior in the three metrics (E681, JHPGL test, and calculated overall reaction rate), greatly reducing the number of required tests and increasing the information available from each test.

At the time of closing this report, NIST has been in discussion with ARL regarding the most recent live-fire test results performed at ARL. Based on those results, future tests were discussed and recommendations made concerning possible next tests. NIST will continue their collaboration in support of the work being done at ARL, including interpretation of the test results as well as input into the test matrix. This collaboration will include both the live fire test results as well as the laboratory scale tests, and comparative assessment of NIST and ARL test equipment and procedures.

4.3. Task 3: Testing of Selected Blends in a Mini-Breadboard Heat Pump

The Mini-Breadboard Heat Pump (MBHP) was used to experimentally evaluate HFC-134a and four candidate low-GWP blends: R-513A, R-450A, R-515B, and Tern-1. Section 4.5.2 details how these blends were selected. The purpose of these tests was to validate the CYCLE_D-HX simulation model [10,11] used in the limited-scope project [6] and qualify the three “best” blends for testing in a military ECU (Task 7).

Note the MBHP measurements were de facto “drop-in” tests and do *not* show the absolute performance potential for each fluid, since the MBHP hardware was not optimized for each fluid. The limited-scope project simulations included hardware optimized for each fluid, and thus provide a more equitable fluid comparison.

4.3.1. Test Apparatus

The NIST MBHP is a laboratory, modular heat-pump system for measuring performance of refrigerants. This system is extensively instrumented. The refrigerant circuit includes a variable-speed, oil-lubricated, reciprocating compressor powered by an electric motor and inverter, where the speed controls cooling/heating capacity. The evaporator and condenser are single circuits (no parallel tube branches). The heat exchangers’ size can be adjusted by changing the number of active refrigerant tubes, which enables control of the heat flux. The evaporator and condenser are of the annular design arranged in the counter-current configuration; the refrigerant flows in the enhanced inner tube (copper), while the heat-transfer fluid (HTF) flows in the smooth annular space. An electronic expansion valve (EEV) regulates the evaporator-exit superheat. A liquid-line/suction-line heat exchanger (LLSL-HX) can be optionally included in the refrigerant circuit. The small internal volume of this apparatus facilitates testing fluids that are only available in small quantities. A chiller removes heat from the condenser, and a water heater applies a load to the evaporator. More details about the test apparatus are available in [72].

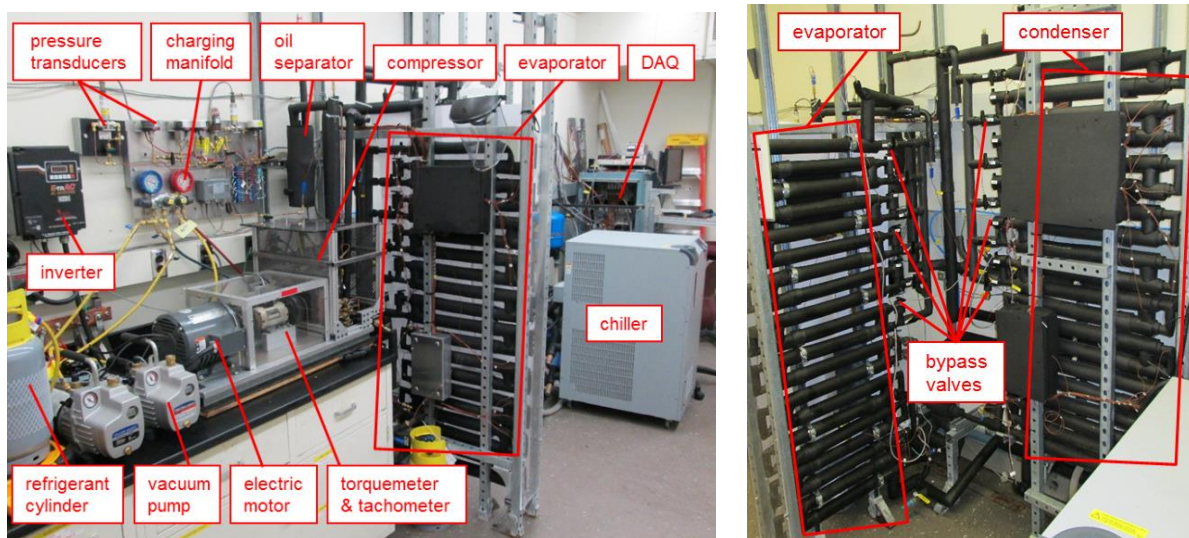


Figure 4.3-1. Photos of the MBHP test apparatus

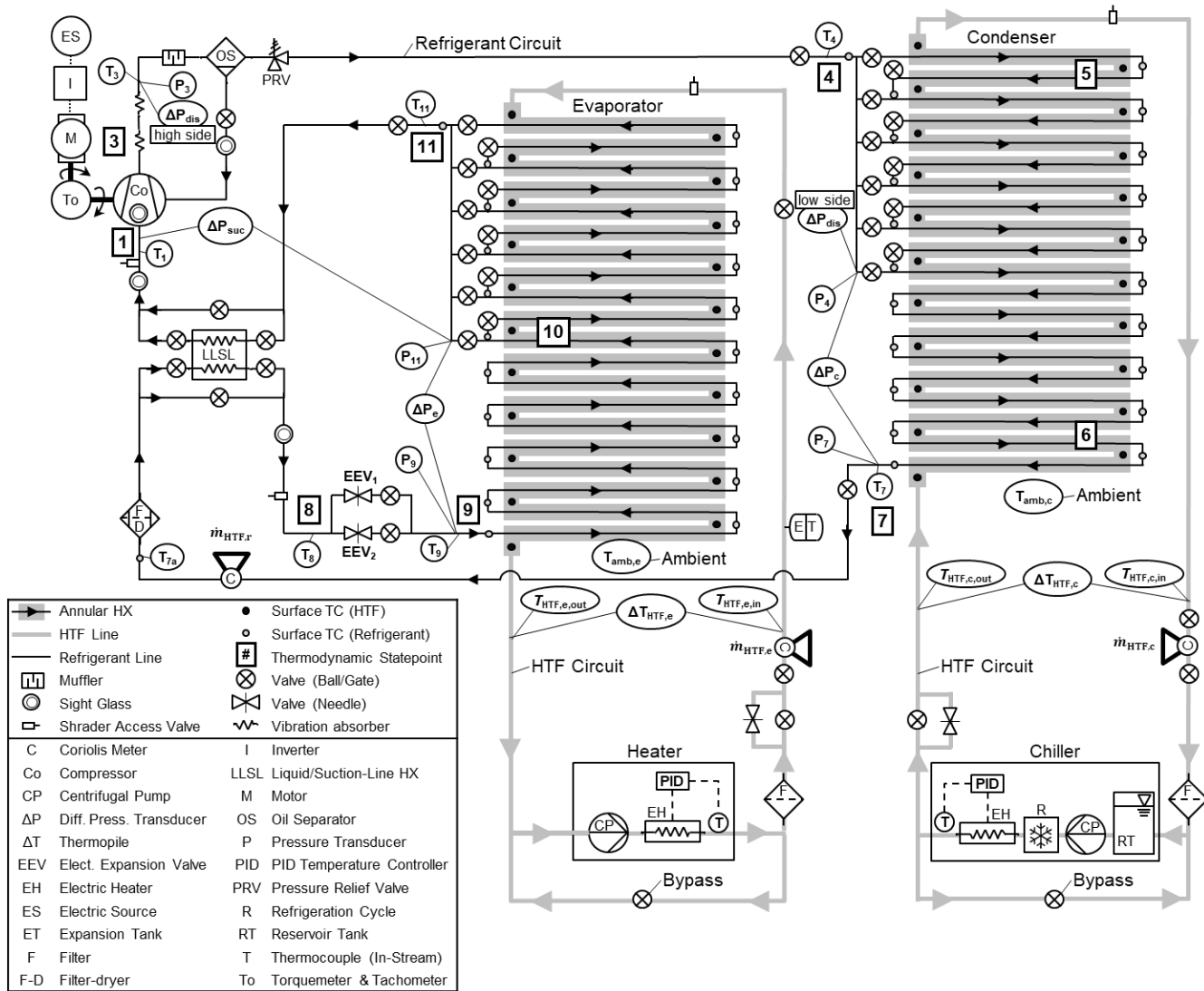


Figure 4.3-2. Schematic of the MBHP test apparatus

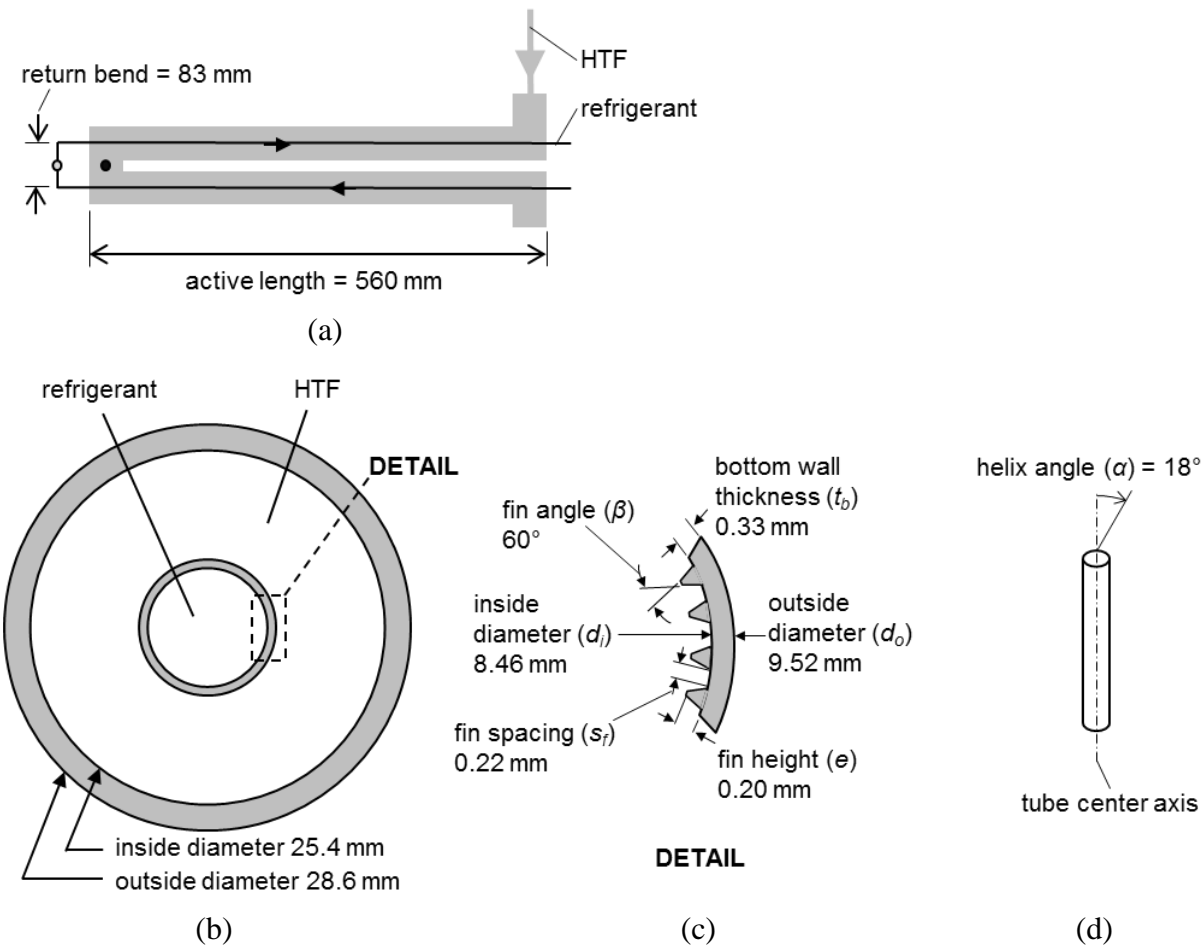


Figure 4.3-3. MBHP: Schematics of annular heat exchanger including (a) refrigerant tube lengths, (b) cross section of annular heat exchanger, (c) detailed cross-section of microfin tube, and (d) helix angle of microfins

4.3.2. Test Protocol

The first baseline tests with HFC-134a established the control parameter settings required to reach the operating targets listed in Table 4.3-1. The HTF inlet temperatures were set to achieve refrigerant average saturation temperatures of 40 °C in the condenser and 8 °C in the evaporator, which are typical for air-source heat pumps operating at the Cooling A rating test [73]. The compressor speed was controlled to generate a cooling capacity of 1.5 kW. Condenser and evaporator dewpoint temperature drops of 2 K were targeted since the CYCLE_D-HX model showed that the COP was maximized under these conditions (HFC-134a mass flux was high enough for good heat transfer but with only moderate pressure drop penalty) [11]. These dewpoint temperature drops were also used in the limited-scope project [6]. These dewpoint temperature changes were obtained using 10 evaporator tubes and 16 condenser tubes. A refrigerant charge of 1420 g produced the targeted subcooling of 5 K. Extensive tests showed that an evaporator-exit superheat of 15 K yielded the best repeatability for the system without the LLSL-HX. A lower evaporator-exit superheat of 8 K was used with the LLSL-HX to achieve nominally equivalent compressor suction superheat (which correlated to repeatability), and because the lower superheat resulted in lower LLSL-HX energy imbalance. The condenser HTF

was distilled water and the evaporator HTF was a potassium formate brine (Dynalene HC40) whose capacitance was measured and reported in Skye et al., 2015 [72].

After establishing the baseline conditions and heat exchanger sizes, HFC-134a and the four replacement candidates were tested at varied capacity (Table 4.3-2, Table 4.3-3) to quantify performance over a range of heat and mass fluxes, for a total of 121 tests. Test conditions were repeated to quantify representative average performance and to bring the 95 % confidence for COP vs. capacity linear regression to the (0.5 to 1.0) % range, where the variation was largely driven by test-to-test differences in compressor efficiency (more details given in Section 4.3.4). The tests were primarily carried out at (1.3, 1.5 and 1.7) kW capacity. Additional tests at higher capacities of (1.9 and 2.0) kW were also performed for HFC-134a, R-513A, and R-450A, but these two test points were abandoned for Tern-1 and R-515B because it became clear that the refrigerant mass flux and pressure drop were too high to represent realistic conditions for a system with optimized evaporator and condenser refrigerant tube circuitry.

The targeted capacities were achieved by adjusting the compressor speed. The condenser and evaporator HTF inlet temperatures, HTF flowrates, and number of active tubes were fixed for all tests at the values established in the baseline tests. The fixed HTF flowrates and number of heat exchanger tubes were necessary for validating CYCLE_D-HX because the model assumes a fixed HTF-side thermal resistance. Further, refrigerant comparisons are most fair when done with equal capacity per heat exchange area [74], Q/A , (ideally the compressor efficiency would also be the same, but that was not possible in these tests). For each test the refrigerant charge was adjusted to achieve the target subcooling. All fluids were tested with and without the LLSL-HX. Energy imbalance between the refrigerant and HTF in the condenser and evaporator was less than 5 %.

Table 4.3-1. MBHP: HFC-134a baseline test operating targets and control parameters.

#	Operating parameter target	Value	Control Parameter	Value
1	Avg. saturation temp - cond.	40 °C	HTF inlet temp: cond.	32.7 °C
2	Avg. saturation temp - evap.	8 °C	HTF inlet temp: evap.	28.0 °C
3a	Cooling capacity (w/o LLSL-HX)	1.5 kW	Compressor speed (w/o LLSL-HX)	14.5 Hz
3b	Cooling capacity (w/ LLSL-HX)	1.5 kW	Compressor speed (w/ LLSL-HX)	13.5 Hz
4	Dewpoint temp. drop - cond.	2 K	Number of tubes: cond.	16
5	Dewpoint temp. drop – evap.	2 K	Number of tubes: evap.	10
6	Subcooling	5 K	Refrigerant charge	1420 g
7a	Superheat – w/o LLSL-HX	15 K	EEV opening	--
7b	Superheat – w/ LLSL-HX	8 K	EEV opening	--

Table 4.3-2. MBHP: Test targets and parameters

Parameter	Unit	Tol.	Value				
Cooling capacity	kW	±2 %	1.3	1.5	1.7	1.9	2.0
HTF temperature change: evap.	K	±0.02	8.67	10.00	11.33	12.67	13.33
HTF inlet temp: cond.	°C	±0.2	32.7				
HTF inlet temp: evap.	°C	±0.3	27.9				
HTF flowrate: cond.	g/s	±0.3	97.6				
HTF flowrate: evap.	g/s	±0.3	56.3				
Number of tube circuits: cond.	--	--	1				
Number of tube circuits: evap.	--	--	1				
Number of tubes: cond.	--	--	16				
Number of tubes: evap.	--	--	10				
Subcooling: cond. out	K	±0.5	5				
Superheat: evap. out (w/ LLSL-HX)	K	±1.0	15				
Superheat: evap. out (w/o LLSL-HX)	K	±1.0	8				
Energy imbalance: cond.	%	±5	0				
Energy imbalance: evap.	%	±5	0				

Table 4.3-3. MBHP: Executed test matrix

Fluid	Cooling capacity [kW]				
	1.3	1.5	1.7	1.9	2.0
	Number of tests: without (with) LLSL-HX				
HFC-134a	4 (4)	4 (4)	4 (4)	4 (4)	3 (2)
R-513A	3 (2)	3 (2)	3 (2)	3 (2)	--
R-450A	4 (3)	4 (3)	4 (3)	1 (0)	--
Tern-1	4 (3)	4 (3)	4 (3)	--	--
R-515B	4 (3)	4 (3)	4 (3)	--	--

4.3.3. Model simulation of tests

CYCLE_D-HX is a semi-theoretical model that simulates performance of a vapor-compression cycle for specified temperature profiles of the heat source and heat sink. The evaporator and condenser refrigerant saturation conditions (e.g., temperature, pressure) can optionally be predicted based on physical models of the two-phase heat transfer and pressure drop. To utilize this feature, CYCLE_D-HX requires, as a preliminary step, simulating of a “reference case” to calculate the thermal resistance on the HTF side and to establish correlations for refrigerant heat

transfer and pressure drop in the heat exchangers [10, 11]. The inputs for the reference case simulation are based on measured data for the reference fluid and also include the geometry parameters characterizing the evaporator and condenser: refrigerant tube inner diameter and length, number of tubes, number of circuits, and indication of whether the tube inside surface is smooth or enhanced (e.g., the microfins shown in Figure 4.3-3). Further, the model can leverage this feature to optimize refrigerant tube circuitry for each fluid, enabling the equitable comparison of fluid performance potential shown in the limited-scope project [6].

Each experimental test was simulated using CYCLE_D-HX to verify the model's predictive capability. Model inputs included measurements for: HTF inlet and outlet temperatures, refrigerant superheat and subcooling, compressor volumetric and isentropic efficiencies, pressure drops in the suction and discharge lines, and the target cooling capacity. The model then predicted the cycle thermodynamic states and the resulting COP and volumetric capacity (Q_{vol}). The model's tube circuit optimization feature was not used for simulation of the experimental tests since the tests had fixed evaporator and condenser tube circuitry (Table 4.3-2).

The baseline tests listed in Table 4.3-1 were the basis for two 'reference cases', one each for the cycle with and without the LLSL-HX. The use of two 'reference cases' was necessitated by the different superheats, 15 K and 8 K, respectively, used in the cycle without and with LLSL-HX. Relying on a single 'reference case' could result in inadequate performance predictions because CYCLE_D-HX, as a simplification, estimates the pressure drop and heat transfer in the superheat section based on the values calculated for the two-phase section. The effect of the superheat section is partially corrected for in the 'reference' HTF-side thermal resistance and refrigerant-side pressure drop multiplication factor. However, the accuracy of this correction diminishes if the superheat is different than that used to establish the 'reference', so we created two unique 'references' for tests with and without the LLSL-HX.

4.3.4. Test Results and CYCLE D-HX Model Validation

It is critical to note that the MBHP measurements reported here were taken primarily for validating the CYCLE_D-HX simulation results from the limited-scope project [6], rather than to provide the absolute performance potential of the candidate low-GWP fluids. While the MBHP tests were controlled to achieve a similar heat flux through the evaporator (a key requirement for a fair experiment-based comparison of different fluids [74]), all MBHP hardware was fixed for all tests, which constituted 'drop-in' testing. Such testing may not affect the results significantly for fluids having similar volumetric capacities, however, its effect on results may increase exponentially for large disparities in Q_{vol} . In such a case, the system performance can be impacted to a significant degree through a performance degradation of the compressor and heat exchangers, which were optimized for the reference refrigerant. The CYCLE_D-HX validation concept relies on the assumption that if the model can correctly predict the MBHP 'drop-in' test results, its predictions from the limited-scope project for optimized systems can be considered as verified.

Test Results. The HFC-134a replacement candidate's performances were evaluated based on cooling COP (Figure 4.3-4) and Q_{vol} (Figure 4.3-5). The COP and Q_{vol} data were correlated to capacity with a linear regression, and the figures show the individual measurements (symbols), curve fits (short-dashed lines), 95 % confidence intervals of the fit (long-dashed lines). When fluid is described here as having higher tested COP (or Q_{vol}) than another fluid, the curve fit

value is higher, and the confidence intervals don't overlap. If the confidence intervals overlap, the average performances of the fluids have no statistical difference (NSD).

The following results summary applies to both tests without and with the LLSL-HX:

- COP (Figure 4.3-4)
 - HFC-134a had higher COP than all replacement candidates for all capacities.
 - R-515B had lower COP than all other fluids for all capacities.
 - At 1.3 kW, R-513A, R-450A, and Tern-1 had NSD in COP.
 - At (1.5 and 1.7) kW, R-513A and Tern-1 had NSD in COP, but both had higher COP than R-450A.
- Q_{vol} (Figure 4.3-5)
 - HFC-134a and R-513A had the highest Q_{vol} (NSD between them), followed by Tern-1, R-450A, and R-515B.

For all tests the LLSL-HX increased COP and Q_{vol} by about (8 to 10) %.

The lower performance of R-450A and R-515B can be mostly related to their lower Q_{vol} , 13.3 % and 26.2 %, respectively, in relation to HFC-134a. The COP lines for R-450A and R-515B (Figure 4.3-4) reflect the trends in compressor isentropic efficiency (Figure 4.3-6). The lower Q_{vol} , and sometimes lower compressor volumetric efficiency (Figure 4.3-7), required higher compressor speeds for R-450A and R-515B (Figure 4.3-8). The associated increase in frictional losses caused the compressor isentropic efficiency to be low. The MBHP measurements also showed a larger pressure drop for these two blends compared to the other fluids tested, especially in the evaporator. Note these data do not constitute the absolute potential for R-450A and R-515B since the MBHP hardware was not optimized for these fluids. The approach used in the limited scope simulation study [6] gave a more fair comparison of fluid performance potential, since all fluids were evaluated with the same compressor isentropic efficiency and the heat exchanger circuitry was optimized for each fluid. Figure 4.3-7 shows significant differences in compressor efficiency, but plotted vs. compressor speed (not shown) the values are very similar. Therefore, it is reasonable to assume that with proper design the compressor efficiencies would be equal for all these refrigerants.

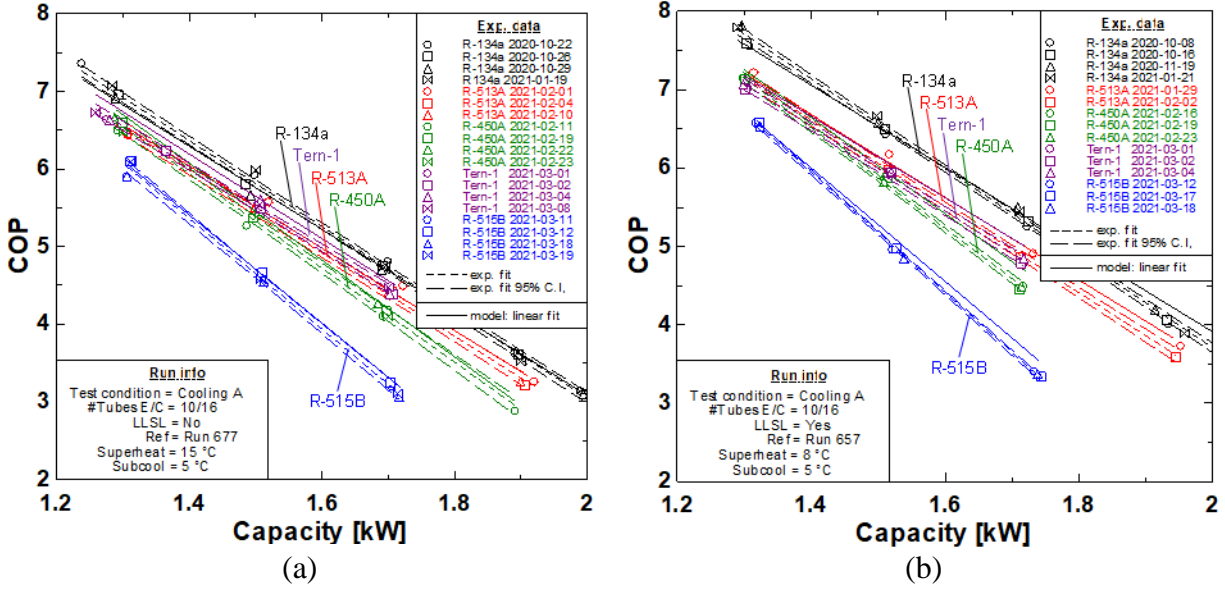


Figure 4.3-4. Cooling COP for HFC-134a and the replacement candidates (a) without LLSL-HX and (b) with LLSL-HX.

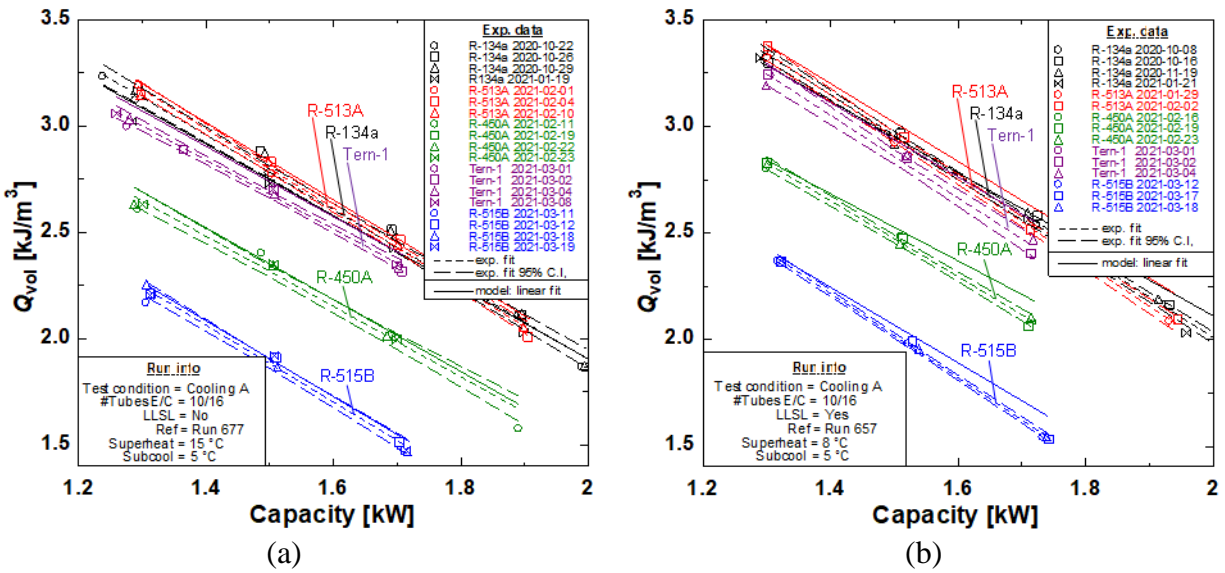


Figure 4.3-5. Cooling volumetric capacity for HFC-134a and the replacement candidates (a) without LLSL-HX and (b) with LLSL-HX

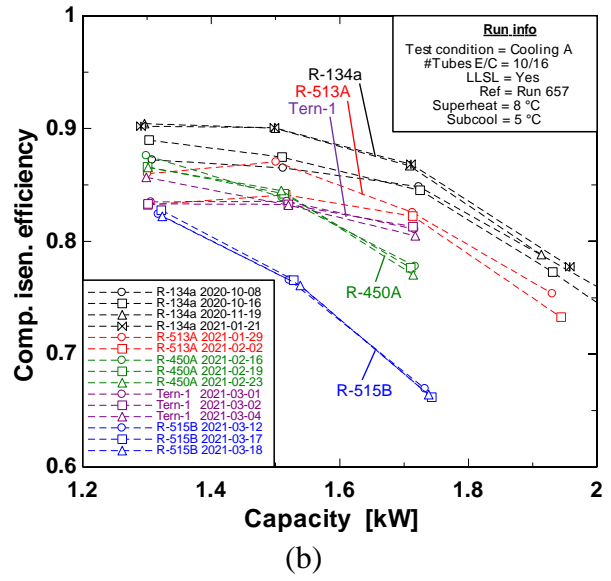
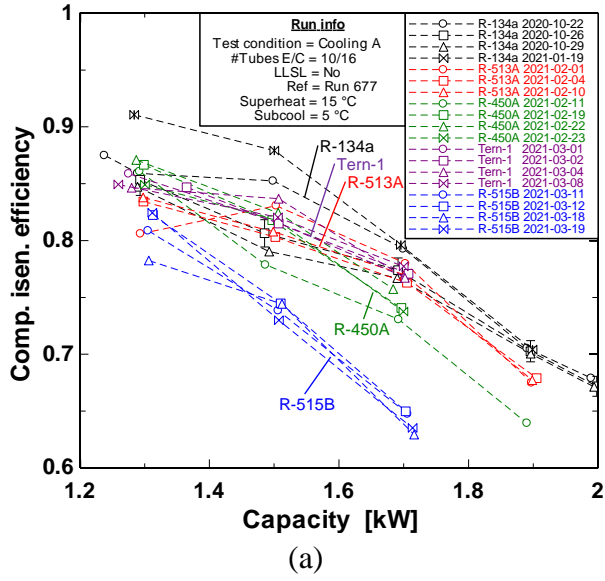


Figure 4.3-6. Compressor isentropic efficiency (a) without LLSL-HX and (b) with LLSL-HX.

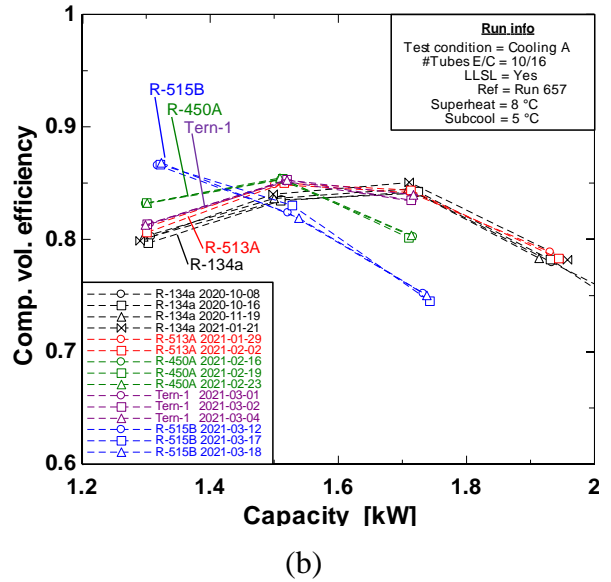
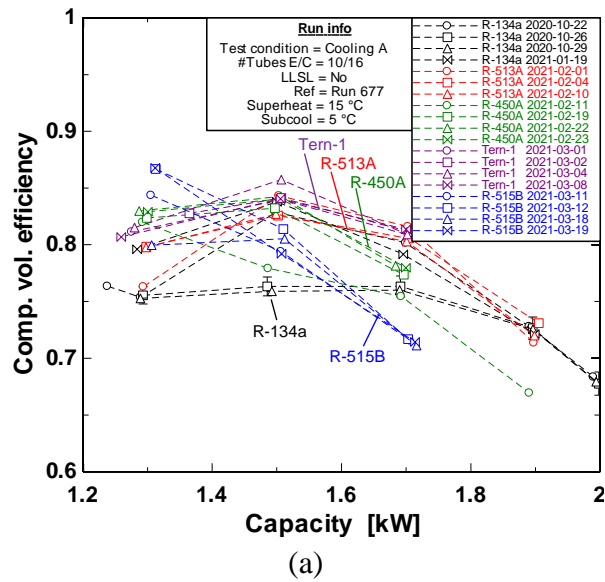


Figure 4.3-7. Compressor volumetric efficiency (a) without LLSL-HX and (b) with LLSL-HX

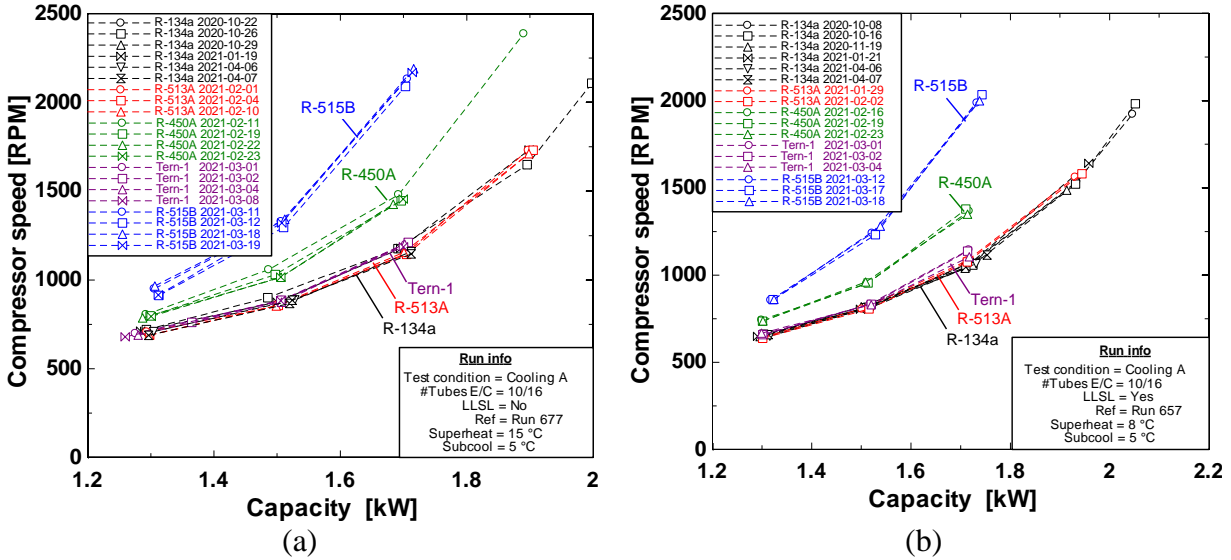


Figure 4.3-8. Compressor speed (a) without LLSL-HX and (b) with LLSL-HX

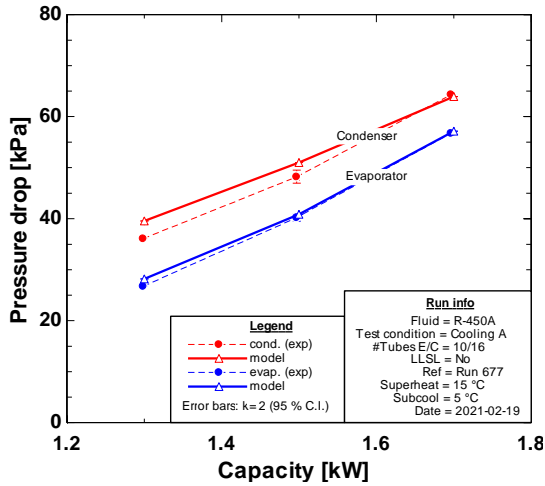
Model Validation. The CYCLE_D-HX simulation COP and Q_{vol} predictions were also correlated to capacity using linear regression (solid lines on Figure 4.3-4 and Figure 4.3-5). For the tests without the LLSL-HX, the model-predicted values were within the confidence intervals of the experimental results, within about $\pm 1.5\%$ of the curve fit. The predictions for Tern-1 were an exception, where the model over-predicted the experimental data by about 3%. For the tests with the LLSL-HX, the CYCLE_D-HX predicted the COP and Q_{vol} within the confidence intervals at 1.3 kW capacity. At 1.5 kW, the COP and Q_{vol} were overpredicted by (0 to 3)%, and at 1.7 kW the COP and Q_{vol} were overpredicted by (1 to 5) %.

Differences between the test data and the CYCLE_D-HX prediction are primarily attributed to the refrigerant heat transfer and pressure drop in the condenser and evaporator, since the thermodynamic property data for the tested fluids are well established and the other hardware performance parameters are input to the model based on each experimental test (including compressor efficiency, LLSL-HX effectiveness, suction & discharge line pressure drop, HTF temperatures, see Section 4.3.3). Using the R-450A tests without the LLSL-HX as an example, the pressure drop in the condenser and evaporator were predicted within about $\pm 5\%$ (Figure 4.3-8(a1)), the condenser saturation and outlet temperatures were underpredicted by about 0.3 °C (Figure 4.3-8(b1)), and the evaporator saturation and outlet temperatures were overpredicted by about 0.6 °C (Figure 4.3-8(c1)). Overpredicted evaporator temperatures indicate an underestimation of overall heat transfer resistance between the HTF and the refrigerant. The error is not likely in the thermal resistances of the tube wall conduction and HTF convection, since the heat exchanger size and flow were fixed and empirically determined from the baseline tests and included in the model ‘reference case’ data. So, we infer the culprit was an underpredicted refrigerant flow-boiling heat transfer resistance. The overpredicted condenser saturation temperature was attributed to an underprediction of refrigerant condensation heat transfer resistance, for similar reasons given for the evaporator. Some of the condenser saturation temperature difference is related to the difference in measured and predicted COP (which determines the amount of heat rejected in the condenser), though this effect appears to be small

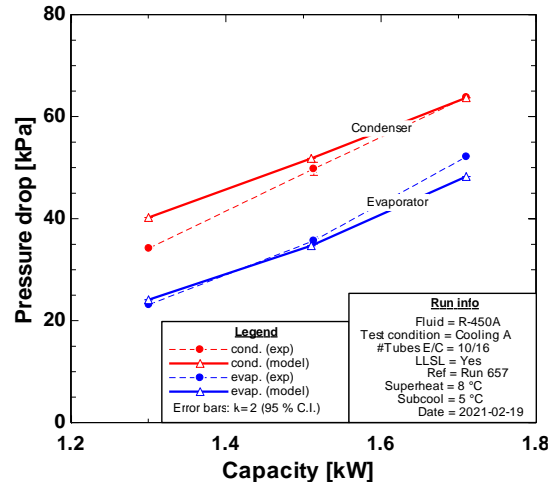
since for R-450A the underpredicted condenser saturation temperature persists despite the nearly exact prediction of COP at 1.5 kW (Figure 4.3-4(a)).

The R-450A tests with the LLSL-HX highlight the effects of an underprediction in evaporator pressure drop. The evaporator pressure drop is predicted within ± 1 % at (1.3 and 1.5) kW (Figure 4.3-5(a2)), and the evaporator saturation temperature was overpredicted by 0.6 °C (Figure 4.3-5(b2)). In contrast, at 1.7 kW capacity the pressure drop was underpredicted by 10 %, and the evaporator saturation temperature was overpredicted by 1.2 °C. Pressure drop in the evaporator causes a reduction in saturation temperature that is unfavorable to countercurrent heat exchange, requiring a lower saturation temperature to drive the heat transfer. So underpredicting pressure drop results in overpredicted saturation temperature and a subsequent overprediction of COP (Figure 4.3-4(b)) as expected from the Carnot efficiency of a heat pump operating with a underpredicted temperature lift. This overprediction of COP occurred despite an overprediction of condenser pressure drop of (0 to 15) %, indicating the evaporator pressure drop is more important for determining the cycle COP.

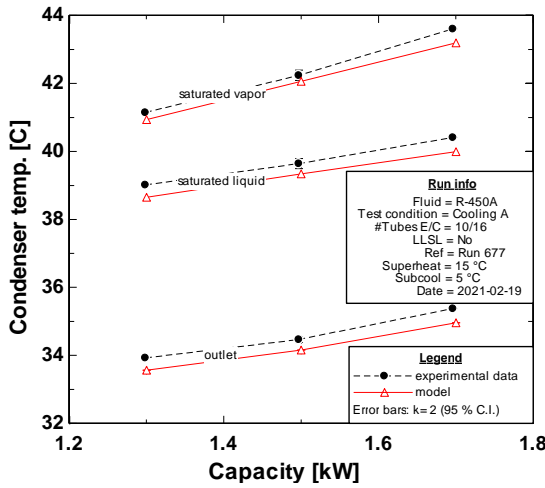
In summary, the CYCLE_D-HX model predicted the same relative COP and Q_{vol} ranking as the experimental data, giving confidence to the HFC-134a replacement candidate screening performed in the limited-scope project. All four low-GWP candidates are acceptable for testing in the ECU as none had significant deviations from modeled performance, excessive discharge temperatures, or other hardware-related problems.



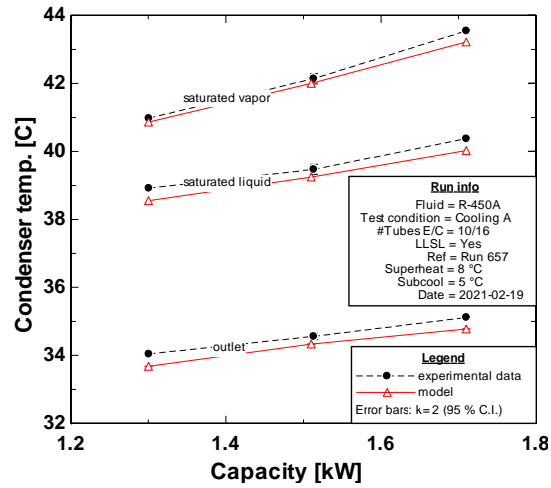
(a1) - without LLSL-HX



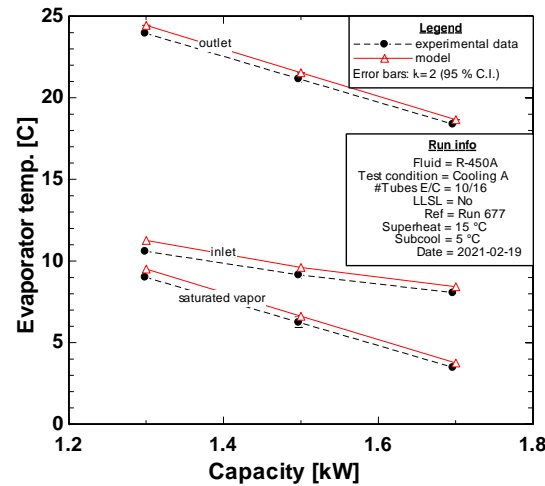
(a2) - with LLSL-HX



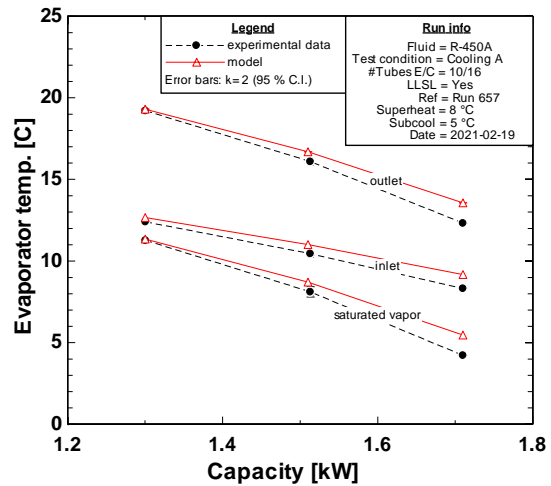
(b1) - without LLSL-HX



(b2) - with LLSL-HX



(c1) - without LLSL-HX



(c2) - with LLSL-HX

Figure 4.3-9. R-450A measurement and model prediction of: (a) evaporator and condenser refrigerant pressure drop, (b) condenser temperatures, and (c) evaporator temperatures

4.4. Task 4: Refrigerant Forced-Convection Heat-Transfer Testing

Measured refrigerant flow boiling heat-transfer coefficients within a micro-fin tube are presented in this section for three low-GWP HFC/HFO refrigerant blends, R-513A, R-450A, and R-515B. A new correlation of the flow boiling heat-transfer coefficient, including data for previously measured HFC-134a [75], is presented. The micro-fin tube is a good choice for experimentation because this type of enhancement is ubiquitous in unitary equipment. Measurements were made to validate and improve the existing NIST evaporation correlation to include HFC/HFO blends for application in heat exchanger and air-conditioning system simulation tools.

4.4.1. Test Apparatus

Figure 4.4-1 shows a schematic of the experimental apparatus used to establish and measure convective boiling heat transfer coefficients. The experimental test facility consisted of two main systems: the refrigerant loop and the water loop. The refrigerant flow rate, pressure, and quality were fixed at the inlet to the test section. The water flow rate and the inlet temperature were fixed to establish the overall refrigerant quality change in the test section. The water temperature drop, the tube wall temperature, the refrigerant temperatures, pressures, and pressure drops were measured at several axial locations along the test section. These measurements were used to calculate the local heat-transfer coefficient for the micro-fin tube.

The test section consisted of a pair of 3.34 m long, horizontal tubes connected by a U-bend. A fixed test pressure was maintained by balancing the refrigerant duty between the subcooler, the test section, the preheater, and the condensers. A magnetically coupled gear pump delivered the test refrigerant to the test section as saturated, near zero quality liquid. Another magnetically coupled gear pump supplied a steady flow of water to the annulus of the test section. The inlet temperature of the water loop was held constant for each test with a water-chilled heat exchanger and variable electric heaters. The refrigerant and water flow rates were controlled by varying the pump speeds using frequency inverters. Redundant flow rate measurements were made with Coriolis flowmeters and with turbine flowmeters for both the refrigerant and water sides.

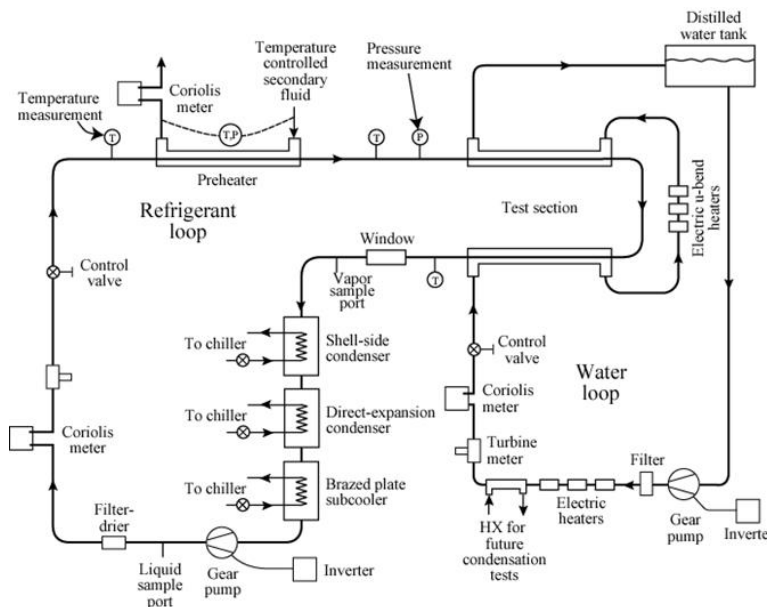


Figure 4.4-1. Schematic of flow boiling test apparatus

Figure 4.4-2 shows a cross section of the test section with a detail of the micro-fin tube geometry. The test refrigerant flowed inside a micro-fin tube, while distilled water flowed either in parallel flow or counterflow to the refrigerant in the annulus that surrounded the micro-fin tube. Conducting some tests in parallel flow and others in counterflow (as shown in Figure 4.4-3) produced a broad range of heat fluxes at both low and high flow qualities. The annulus gap was 2.2 mm, and the micro-fin tube wall thickness was 0.3 mm. The micro-fin tube had 60, 0.2 mm high fins that rifled down the axis of the tube at a helix angle (α) of 18° with respect to the tube axis. For this geometry, the cross-sectional flow area was 60.8 mm^2 , giving an equivalent smooth diameter (D_e) of 8.8 mm. The root diameter of the micro-fin tube was 8.91 mm. The inside-surface area per unit length of the tube was estimated to be 44.6 mm . The hydraulic diameter (D_h) was measured with a polar planimeter from a scaled drawing of the tube cross section and determined to be approximately 5.45 mm. The ratio of the inner surface area of the micro-fin tube to the surface area of a smooth tube of the same D_e was 1.6.

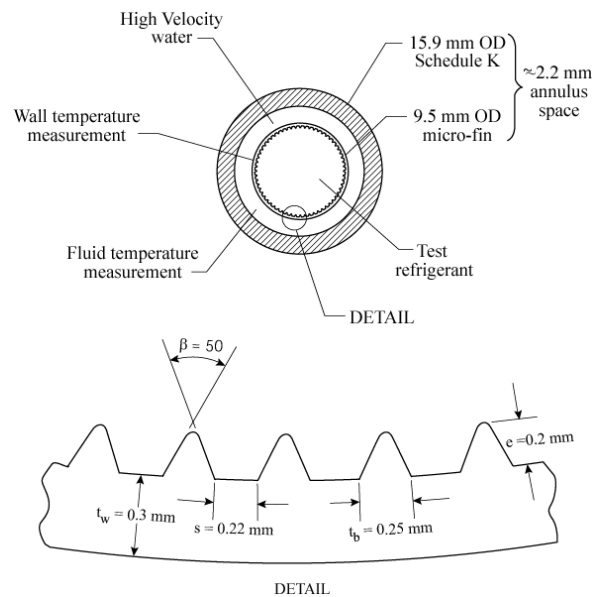


Figure 4.4-2. Cross section of flow-boiling test section

Figure 4.4-3 provides a detailed schematic of the test section. The annulus was constructed by connecting a series of tubes with 14 pairs of stainless-steel flanges. This construction permitted the measurement of both the outer micro-fin wall temperature and the water temperature drop as discussed in the following two paragraphs. The design also avoided abrupt discontinuities such as unheated portions of the test section and tube-wall “fins” between thermopile ends.

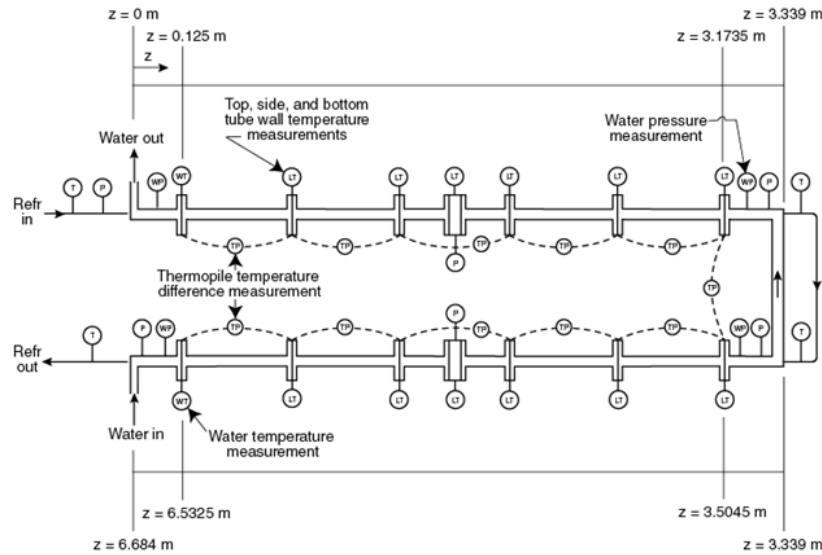


Figure 4.4-3. Detailed schematic of test section (counterflow)

Figure 4.4-3 shows that thermocouple wires pass between 12 of the gasketed flange pairs to measure the refrigerant-tube wall temperature at ten locations on the top, side, and bottom of the tube wall. These locations were separated by 0.6 m on average, and they were located near the intersection of the shell flanges. In addition to these, thermocouples were also mounted next to the pressure taps near the middle of each test section length. The thermocouple junction was soldered to the outside surface and was sanded to a thickness of approximately 0.5 mm. The leads were strapped to a thin non-electrically-conducting epoxy layer on the wall for a distance of 14.3 mm before they passed between a pair of the shell flanges. The wall temperature was corrected for a heat flux dependent fin effect. The correction was typically 0.05 K. Figure 4.4-3 also shows that a chain of thermopiles was used to measure the water temperature drop between each flange location. Each thermopile consisted of ten thermocouples in series, with the ten junctions at each end evenly spaced around the circumference of the annulus. Because the upstream junctions of one thermopile and the downstream junctions of another enter the annulus at the same axial location (except at the water inlet and outlet), the junctions of the adjacent piles were alternated around the circumference. A series of Teflon half-rings attached to the inner refrigerant tube centered the tube in the annulus. The half-rings were circumferentially baffled to mix the water flow. Mixing was further ensured by a turbulent water Reynolds number [76].

As shown in Figure 4.4.3, six refrigerant pressure taps along the test section allowed the measurement of the upstream absolute pressure and five pressure drops along the test section. Two sets of two water pressure taps were used to measure the water pressure drop along each tube. Also, a sheathed thermocouple measured the refrigerant temperature at each end of the two refrigerant tubes, with the junction of each centered radially. Only the thermocouple at the inlet of the first tube was used in the calculations. The entire test section was wrapped with 5 cm of foam insulation to minimize heat transfer between the water and the ambient.

4.4.2. Data Analysis and Correlation Development

The convective boiling heat-transfer coefficient based on the actual inner surface area ($h_{2\phi}$) was calculated as:

$$h_{2\phi} = \frac{q''}{T_w - T_s} \quad (4.4-1)$$

where the measured wall temperatures (T_w) were fitted to their axial position (distance along the test section) to reduce the uncertainty in the measurement.

The average estimated expanded uncertainty of the wall temperature fit for all the measurements at the 95 % confidence level, was approximately 0.42 K and 0.36 K, for the counterflow and the parallel flow data, respectively. The median of the uncertainty in T_w was approximately 0.4 K.

The water temperature (T_f) was determined from the measured temperature change obtained from each thermopile and the inlet water temperature measurement. The water temperature gradient (dT_f/dz) was calculated with second-order finite difference equations using the measured water temperatures and their locations along the tube length z . The water temperature gradients were then fitted with respect to the tube length. The measured water temperatures typically agreed with the integrated fit of the water temperature gradient to within 0.2 K.

The fitted, local, axial water temperature gradient (dT_f/dz), the measured water mass flow rate (\dot{m}), and the properties of the water were used to calculate the local heat flux (q'') to the micro-fin tube based on the actual inner surface area:

$$q'' = \frac{\dot{m}_f}{p} \left(c_{pf} \frac{dT_f}{dz} + v_f \frac{dP_f}{dz} \right) \quad (4.4-2)$$

where p is the wetted perimeter of the inside of the micro-fin tube. The specific heat (c_{pf}) and the specific volume (v_f) of the water were calculated locally as a function of the water temperature. The water pressure gradient (dP_f/dz) was linearly interpolated between the pressure taps to the location of the wall thermocouples. The pressure gradient term was typically less than 3 % of the temperature gradient term. The heat flux obtained by Eq. (4.4-2) was reduced by the amount of heat lost to the surroundings. The heat loss to the surroundings was obtained by calibration of single-phase heat-transfer tests, and it was based on the temperature difference between the room and the test fluid. Typically, the heat loss correction was less than a 0.1 % of that obtained from Eq. (4.4-2). The relative uncertainty of the heat flux measurement was less than 40 % of the measured value, while the average uncertainty for the counterflow and the parallel flow data was approximately 7 % and 20 % of the measured value, respectively.

The local Nusselt number (Nu) was calculated using the hydraulic diameter and the heat-transfer coefficient based on the actual inner surface area of the tube as:

$$\text{Nu} = \frac{h_{2\phi} D_h}{k_l} \quad (4.4-3)$$

The uncertainty of Nu was between roughly 10 % and 40 %. Measurements of Nu with uncertainties greater than 30 % were discarded. Reduction in the uncertainty can be achieved with repeat measurements for the same operating conditions. However, repeat measurements are

difficult to obtain due to the chaotic nature of two-phase flow and the many fixed parameters that need to be matched between measurements.

The 432 measured local convective boiling Nusselt numbers (Nu) for R-515B, R-450A, R-513A, and HFC-134a were compared to the pure and azeotropic refrigerant (Nu_p) version of the Hamilton et al. correlation [77]:

$$Nu_p = 482.18 Re^{0.3} Pr^{C_1} \left(\frac{P_s}{P_c} \right)^{C_2} Bo^{C_3} \left(-\log_{10} \frac{P_s}{P_c} \right)^{C_4} M_w^{C_5} \quad (4.4-4)$$

where

$$C_1 = 0.51x_q$$

$$C_2 = 5.57x_q - 5.21x_q^2$$

$$C_3 = 0.54 - 1.56x_q + 1.42x_q^2$$

$$C_4 = -0.81 + 12.56x_q - 11.00x_q^2$$

$$C_5 = 0.25 - 0.035x_q^2$$

Here, the all-liquid Reynolds number (Re), the Boiling number (Bo), the liquid Prandtl number (Pr), the reduced pressure (P_s/P_c), and the quality (x_q) are all evaluated locally at the saturation temperature. The all-liquid Reynolds number and the Nusselt number are based on the hydraulic diameter (D_h). The Nusselt number is also based on the actual inner surface area of the tube.

Figure 4.4-4 plots the present measurements versus predicted values of the Nusselt number for R-515B, R-450A, and R-513A. Previously made measurements for R-450A [78], R-513A [75] and HFC-134a [75] are also included in the comparison. The Hamilton et al. correlation [77] predicts approximately 43 % measurements to within $\pm 20\%$.

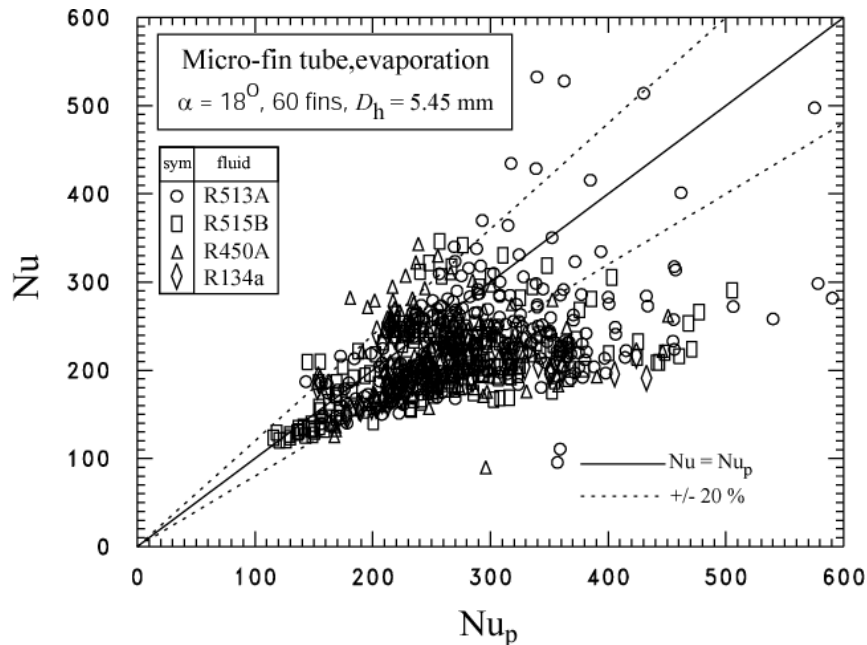


Figure 4.4-4. Comparison between measured Nusselt numbers and those predicted by the Hamilton et al. correlation [77]

A new correlation was developed to more accurately represent the current flow-boiling heat-transfer measurements:

$$Nu_p = 242.5 Re^{0.26(1-x_q)} Bo^{0.28} B_{nd}^{-0.61x_q} \quad (4.4-5)$$

The new correlation (Eq. 4.4-5) predicts approximately 71 % of the measured convective boiling Nusselt numbers for R-515B, R-450A, R-513A, and HFC-134a to within approximately $\pm 20\%$ (Figure 4.4-5). B_{nd} is the dimensionless Bond number [79], which includes fin geometry parameters and the surface tension as defined in the Nomenclature. The correlation is valid for Re between 1000 and 14000, Bo between 0.000002 and 0.001, and B_{nd} between 0.002 and 0.05. Equation (4.4-5) was developed with data where the refrigerant reduced temperature ranged between approximately 0.71 and 0.94.

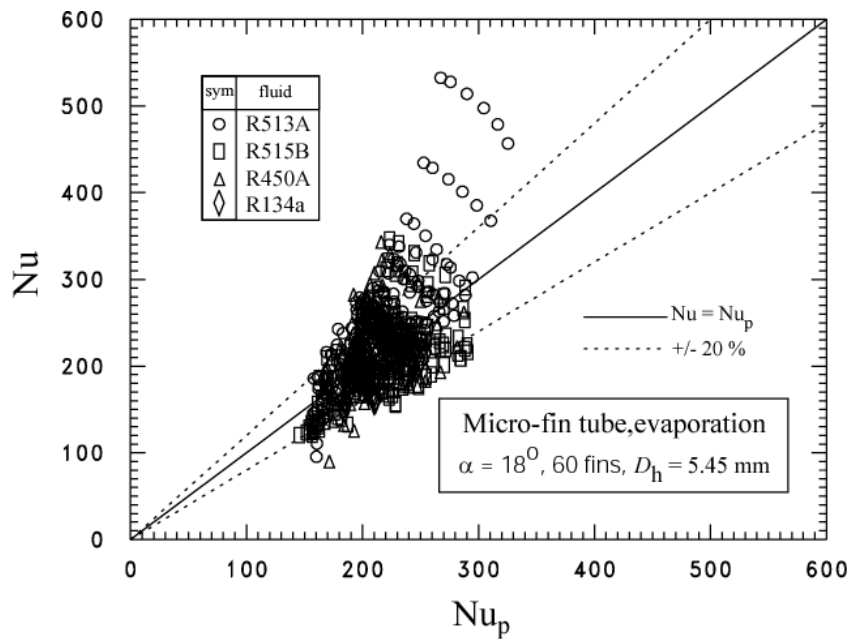


Figure 4.4-5. Comparison between measured Nusselt numbers and those predicted by the new correlation given by Eq. (4.4-5)

4.5. Task 5: Selection of Final Blends for Testing in Military ECU

4.5.1. Preliminary Selection of Four Blends

Before carrying out full-scale ECU tests in environmental chambers, we validated the limited-scope simulation results by measurements taken in the NIST Mini-Breadboard Heat Pump. For this validation we identified four blends judged to be most ‘promising’ with a plan to select three of them for the ECU tests. This preliminary selection also considered thermophysical properties, flammability, and heat transfer measurements. The criteria for blend selection consisted of the following parameters:

- Non-flammability ($\bar{I} < 0$)
- Minimum GWP
- Maximum coefficient of performance (COP)
- The volumetric capacity (Q_{vol}) matching that of the baseline HFC-134a.

We also considered market availability as a practical attribute influencing our decision. The following four blends, based on HFC-134a, HFO-1234yf, HFO-1234ze(E) and HFC-227ea, were selected:

- **R-513A:** [R-134a/1234yf (44/56^{*})], GWP = 573. R-513A was identified in our limited-scope study (blend # 2). A1 ASHRAE safety classification.
- **R-450A:** [R-134a/1234ze(E) (42/58^{*})], GWP = 547. R-450A was not specifically identified in the limited-scope study; however, its make-up and performance are similar to those for blend # 9. A1 ASHRAE safety classification.
- **Tern-1:** [R-134a/1234yf/1234ze(E) (49.2/33.9/16.9^{*})], GWP = 640. This blend was identified in our limited-scope study (blend #4). The Tern-1 name adopted for convenience.
- **R-515B:** [R-1234ze(E)/227ea (91.1/8.9^{*})], GWP = 344. R-515B was not identified in the limited-scope study. A1 ASHRAE safety classification. Significantly lower GWP than those of other fluids. According to our detailed cycle simulations, the COP of R-515B is within 2.6 % of HFC-134a. The volumetric capacity is 27 % lower.

4.5.2. Evaluation of “New” Fluids

While carrying out measurements and analysis of thermophysical properties, flammability, heat transfer, and mini-breadboard heat pump tests, we continually monitored technical developments in low-GWP fluids to make sure that we did not overlook any promising new refrigerants.

A review of ASHRAE Standard 34 showed three new single-compound refrigerants that were classified since the completion of the analysis for the limited-scope project in 2017:

- HFO-1336mzz(E) ($\text{CF}_3\text{CH}=\text{CHCF}_3$), safety classification A1, NBP = 7.4 °C
- HFO-1132a ($\text{CF}_2=\text{CH}_2$), safety classification A2, NBP = -83 °C
- R-131I (CF_3I), safety classification A1, NBP = -21.9 °C

As indicated by its relatively high NBP, HFO-1336mzz(E) is a low-pressure refrigerant and not suitable for application in medium-pressure AC equipment, even as a blend component. The very

* Composition stated in mass fraction (%)

low NBP of HFO-1132a, on the other hand, makes it unsuitable at the other extreme; in a blend it would result in high pressures and a significant temperature glide. HFO-1132a is also flammable.

Consideration of CF₃I. The NBP of CF₃I, on the other hand, is close to that of HFC-134a (– 26.1 °C), which makes CF₃I, thermodynamically at least, a fluid warranting consideration. Its GWP is also very low; a relatively old study characterized its GWP as “likely to be very small, less than 5.” [80] The appeal of CF₃I is further increased by its flame-suppression characteristics. A drawback of CF₃I is its reactivity, which would require the application of proprietary chemical stabilizers not available on the open market.

We spent a considerable analytical effort to formulate, within the constraints of publicly available data, a state-of-the-art representation of thermodynamic properties of both the pure fluid and blends containing CF₃I. This effort was summarized by Bell and McLinden [81]. We also added CF₃I to the screening developed under the limited-scope project in a search for the best performing CF₃I-based blends. Although the COP and volumetric capacity of the pure CF₃I was poor compared to HFC-134a, these simulations identified some blends of CF₃I with HFC-152a and HFC-32 as having potentially favorable performance. The high-performing blends, however, contained a low fraction of CF₃I. Specifically, for R-152a/CF₃I blends a mole fraction of HFC-152a of 0.80 (mass fraction of 0.57) yielded the same COP as HFC-134a. For blends with HFC-32, the corresponding mole fraction was 0.75 (mass fraction of 0.32). This led us to question whether such blends were still nonflammable.

The flame inhibition characteristics of CF₃I have been studied. We could find no information on the specific mixture of HFC-152a/CF₃I, but Yang et al.[82] report that CF₃I is substantially more effective than HFC-125 in inhibiting the flammability of HFC-32 (a minimum concentration of 0.0536 kg·m⁻³ for CF₃I versus 0.0984 kg·m⁻³ for HFC-125). We can use information on the blend R-410A (the blend of HFC-32 and HFC-125 at a mass composition of (50.0/50.0) and the blend R-466A (the blend of HFC-32, HFC-125, and CF₃I at a mass composition of (49.0/11.5/39.5)) to formulate an informed guess on the flammability of HFC-152a/CF₃I) with the following reasoning. Both R-410A and R-466A are classified as A1 (i.e., nonflammable) and contain about 50 % of the flammable HFC-32 with a 50 % content of flame suppressing agents (i.e., HFC-125 and/or CF₃I). In the detailed report of flammability testing contained in the application to the Standard 34 committee [83] it is seen that R-466A exhibits a flame angle as large as 40° in the ASTM E681 test protocol under some conditions. This is “not flammable” under the E681 protocol (which defines “flammable” as a flame angle of 90° or larger), but it does indicate that R-466A was formulated close to the border of flammability. Given that HFC-152a is more flammable than HFC-32, a CF₃I fraction greater than 50 % would likely be required to suppress flammability, i.e., compositions that showed lower performance in the simulations.

There are also stability and toxicity concerns around CF₃I. Although having a safety classification of A1, CF₃I has a relatively low “refrigerant concentration limit” (RCL) of 2000 ppm (i.e., a concentration in air of 0.2 % by volume) [84]. This compares to an RCL of 50 000 ppm for HFC-134a [33]. The RCL considers a range of hazards and is “intended to reduce the risks of acute toxicity, asphyxiation, and flammability hazards in normally occupied, enclosed spaces” [33]. The RCL impacts the maximum charge allowed in a particular system. We also note that in a review of the toxicity of CF₃I, the National Research Council

recommended that it be used (as a fire suppressant) only in unoccupied spaces [85]. The chemical stability of the CF₃I molecule is substantially lower than typical HFC refrigerants, and it would require stabilizers for use in a refrigeration system. Such stabilizers have been developed, but they are proprietary. NIST engaged with a refrigerant manufacturer that was pursuing the development of CF₃I-containing refrigerant blends, such as R-466A, in an attempt to obtain samples of CF₃I and the necessary stabilizers. These negotiations were not successful.

A “roundtable discussion” published in the March 2021 issue of *ASHRAE Journal* [86] illustrates that industry disagreed about the future of CF₃I and CF₃I blends. One company stated that “An emerging nonflammable (ASHRAE class A1) <750 GWP candidate, R-466A, is under heavy consideration by a number of manufacturers.” And that “R-466A would be an ideal interim solution ... until further innovation could lead to even lower GWP nonflammable alternatives.” In contrast, a second company stated that R-466A was “in our opinion, questionable for stability and for compatibility with materials as a result of potential acid formation. This can lead to reliability, durability and performance problems over time.” And “No major North American equipment or compressor manufacturers have announced or shared that they are developing equipment and component parts around this refrigerant. This suggests it is not presently viewed as a viable candidate.”

We also noted a conference paper published in June 2021 [87], which reported results from chemical stability tests of R-466A with optimized materials and additives. The paper concluded that this blend is a viable option for use. However, the availability of CF₃I and chemical stabilizers remained an issue. Taking all the above in its totality, we concluded that it was not feasible to include a blend containing CF₃I in the ECU testing. At the time of writing of this final report we are still not aware about any announcements regarding prospective use of R-466A. The ultimate utility of CF₃I as a refrigerant remains an open research question.

Consideration of HFO-1132(E). In addition to the fluids noted above that were added to the ASHRAE standard another isomer of difluoroethene is currently being studied for use as a refrigerant:

- HFO-1132(E) (*trans*-1,2-difluoroethene), safety classification not assigned, NBP = -53 °C

The -53 °C boiling point of HFO-1132(E) is similar to that of R-410A (-51.5 °C), making it of high commercial interest. Limited data on this fluid are now becoming available [88] [89]. HFO-1132(E) was one of the fluids identified in the comprehensive screening of McLinden et al.[90] that was in the category of “novel molecules” for which “few data could be found.” The analysis of McLinden et al. was based on a predicted critical temperature of 370.5 K, which resulted in a low volumetric capacity relative to R-410A (which was the baseline for that study); this contrasts the recently measured critical temperature of 348.8 K [89], which is similar to R-410A. Much of the research on HFO-1132(E) remains proprietary, making detailed simulations of its performance impossible at this time. Furthermore, it is flammable (likely ASHRAE classification of “2”) and not commercially available. For these reasons, HFO-1132(E) was dropped from further consideration in this project.

4.5.3. Selection of Three Blends for Testing in ECU

The tests conducted in the mini-breadboard heat pump on HFC-134a and the four blends validated the prediction capability of the CYCLE_D-HX model used in the limited-scope project

thus confirming the relative performance of blends established earlier. Lacking new low-GWP options, the selection of the three blends centered on the four blends tested in the mini-breadboard heat pump.

Regarding safety characteristics, R-513A, R-450A, and R-515B have the ASHRAE safety designation A1 (low toxicity, no flame propagation). While Tern-1 does not have ASHRAE classification, it can also be considered an A1 blend, since its ‘non-flammability’ was confirmed by the ASTM E861 test prescribed in ASHRAE Standard 34, and its three components are classified as ‘low-toxicity’ fluids by this standard. It is uncertain at this time whether the ASTM E861 test is stringent enough for military requirements; since this issue has not been determined yet, we decided to use the ASHRAE flammability criteria in this study.

Ultimately, we selected R-513A, Tern-1, and R-515B for testing in the ECU. Table 4.5-1 provides selected properties of the selected blends. The presented ratios of COP/COP_{R-134a} and $Q_{vol}/Q_{vol, R-134a}$ were obtained from CYCLE_D-HX simulations with optimized heat exchangers.

Table 4.5-1. Selected properties of blends tested in ECU

Blend	NBP (°C)	COP/ COP _{R-134a}	$Q_{vol}/$ $Q_{vol, R-134a}$	GWP	$C_{p,l}$ [*] (J/mol ⁻¹ K ⁻¹)	k_l [*] (W m ⁻¹ K ⁻¹)	μ_l [*] (mPa·s)
HFC-134a	-26.1	1	1	1300	136.8	0.092	0.266
R-513A	-29.6	0.988	1.027	573	142.3	0.067	0.226
Tern-1	-27.8	0.987	0.989	640	143.8	0.079	0.239
R-515B	-19.0	0.974	0.738	344	152.8	0.080	0.250

* at 0.0 °C from REFPROP [8]

R-513A [R-134a/1234yf (44/56)^{*}] possesses a very good combination of three important attributes: its GWP is second to the lowest on our list (Table 3.1-1); its COP is 1.2 % below COP_{R-134a}, which makes it the second top COP of blends with GWP < 750; and its volumetric capacity is the highest on our list, 2.7 % better than that of HFC-134a. In addition, this blend is an azeotrope and is commercially available.

Tern-1 [R-134a/1234yf/1234ze(E) (49.2/33.9/16.9)^{*}], compared to R-513A, comprises 5.2 % more HFC-134a and includes 16.9 % HFO-1234ze(E), which is less flammable (lower burning velocity) than HFO-1234yf. As a result, Tern-1 is expected to be farther away from the flammability boundary than R-513A (see Section 4.2.4) and is a more conservative choice should military criteria with respect to flammability become more rigorous (see Section 4.2.5). The simulated COP of Tern-1 is 1.3 % below COP_{R-134a}. The 1.1 % lower volumetric capacity than that for HFC-134a is a trivial difference.

R-515B [R-1234ze(E)/227ea (91.1/8.9)^{*}] was selected because of its significantly lower GWP than those of other blends chosen. Per CYCLE_D-HX simulations with optimized heat exchangers, the COP of this blends is lower than COP_{R-134a} by 2.6 %, and the volumetric capacity is lower than $Q_{vol, R-134a}$ by 26.2 %, which will have to be mitigated by a larger compressor and some efficiency enhancing features. The data presented in Section 4.2.4 indicate that R-515B is closer to the flammability boundary than the other blends. Despite these shortfalls, it is of

*Composition stated as mass fraction (%)

interest to explore the performance potential of this low-pressure blend in case lower-GWP fluids become strongly preferred in the future. R-515B is an azeotrope and is commercially available.

Table 4.5-1 provides selected thermophysical data, which complement the COP and Q_{vol} information. The normal boiling point correlates with Q_{vol} : R-515B has the highest NBP and the lowest volumetric capacity. The molar heat capacity of liquid ($C_{p,l}$) affects the shape of the two-phase dome and the slope of the saturated liquid line on the temperature-entropy diagram, and higher values of $C_{p,l}$ correspond to a less steep slope and larger throttling losses in the expansion device. In this respect, HFC-134a has a slight advantage over the blends. Regarding thermal conductivity and viscosity, HFC-134a also has an advantage in a better conductivity although its higher viscosity is a disadvantage.

By the above selection of three blends we dropped R-450A from further testing. The volumetric capacity of R-450A is about half the way between $Q_{vol, R-134a}$ and $Q_{vol, R-515B}$, 13.3 % lower than $Q_{vol, R-134a}$. However, testing R-515B instead of R-450A provides more useful data for validating the ECU model with a broad spectrum of measurements (performance of a low-pressure fluid). The model then can be used for predicting performance of other fluids that were not included in the ECU tests.

4.6. Experimental Evaluation of Blend Performance in ECU

4.6.1. Military ECU Specifications and Operation

The tested system was a military HFC-134a air conditioner with a 19.9 kW (68000 Btu/h) rated cooling capacity (Figure 4.6-1). It was comprised of a 208 VAC, 3-phase, scroll compressor, finned-tube evaporator and blower, microchannel condenser and fan, and controls, all tightly packaged in one assembly. The unit was designed to run continuously at part load by modulating its capacity using a hot-gas bypass with a tempering expansion valve and an evaporator pressure regulating valve (Figure 4.6-2). This arrangement of components and controls would have made it impossible to execute a test program with different refrigerants. Therefore, for the purpose of this study, we disabled the hot-gas bypass and fully opened the evaporator-pressure-regulator (EPR) valve to produce a basic vapor-compression cycle, as shown in Figure 4.6-2. We made these modifications in consultation with the ECU manufacturer.

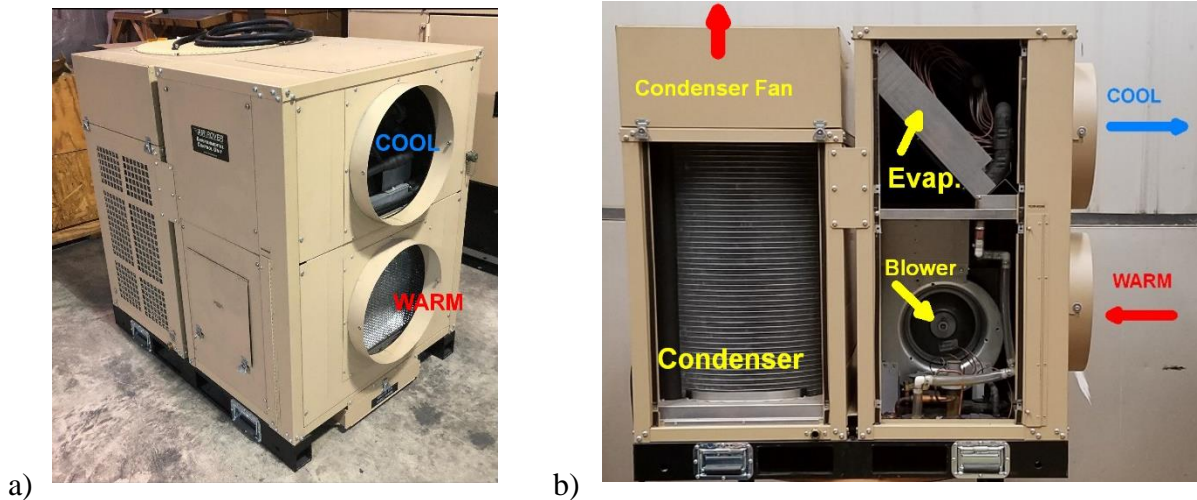


Figure 4.6-1. ECU before installation (a). The condenser protective grid and the covers for evaporator coil and blower were removed on the unit's left-side in picture (b).

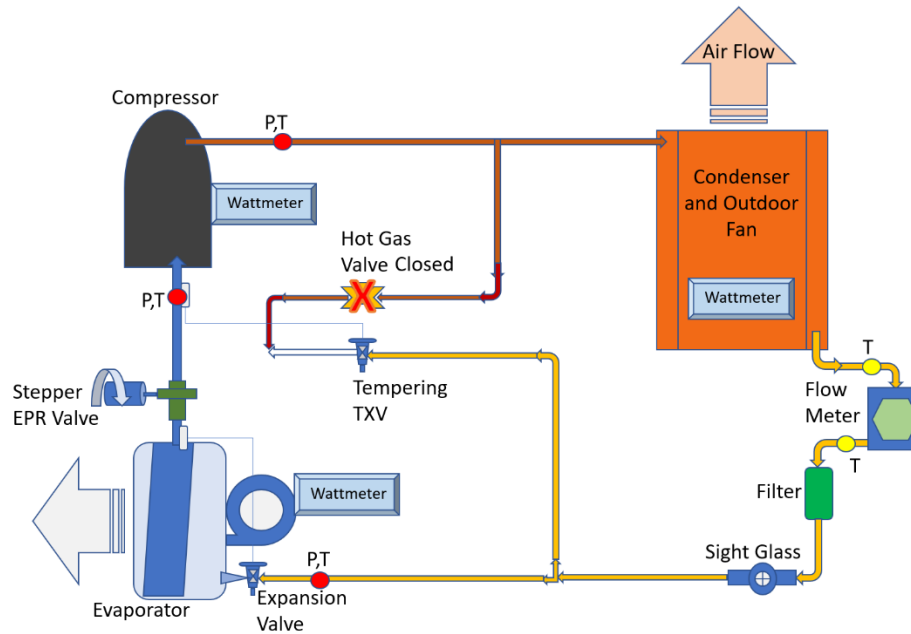


Figure 4.6-2. ECU schematic with installed instrumentation. Symbol **X** designates the disabled valve on the hot-gas bypass. P and T designate pressure and temperature sensors.

4.6.2. Test Facility

The test facility consisted of a system of two adjacent environmental chambers (Figure 4.6-3). The ECU was installed in the outdoor chamber and supplied the conditioned air to the indoor chamber through the attached ductwork. Figure 4.6-4 shows the nozzle chamber setup used to measure the volumetric flow rate of air. A constant static pressure was maintained in the air supply duct at the inlet to the nozzle chamber by using the nozzle chamber booster fan, which was powered by a variable frequency drive. The ECU pulled return air from the indoor chamber and back through its evaporator before expelling the conditioned air into the indoor chamber's nozzle air measurement apparatus. The measurements were performed according to the applicable standards [ANSI/ASHRAE Standard 51 (111); AHRI 210-240 (112)].

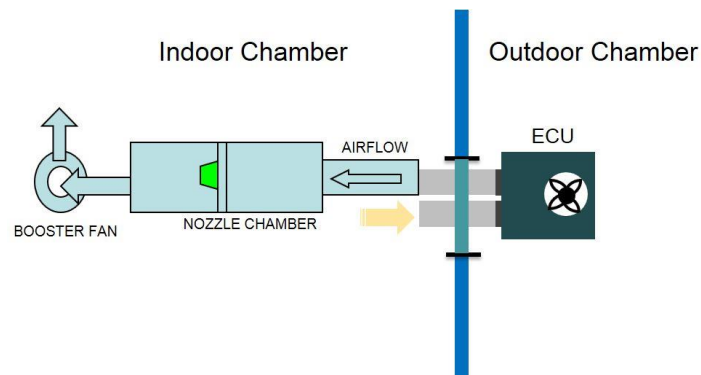


Figure 4.6-3. Schematic of ECU installation in environmental chambers



Figure 4.6-4. Connecting ducts and nozzle chamber located in the indoor environmental chamber

The primary measurement of ECU capacity was the air enthalpy method, and the refrigerant enthalpy method served as the secondary measurement. The air enthalpy method relied on measurements of the entering and exiting air's drybulb and dewpoint temperatures along with airflow rate measured in the nozzle chamber. The inlet and exit air streams' drybulb and dewpoint temperatures were measured with T-type thermocouple grids (5x5) and chilled mirror hygrometers, respectively. The conditioned supply air passed through mixers and straighteners before entering the thermocouple grid to ensure no stratification and an accurate measurement of the average temperature. All ductwork was thoroughly insulated, and leak tested before testing began.

On the refrigerant side, pressure transducers and T-type thermocouples were attached at the inlet and exit of every ECU component to measure refrigerant pressure and temperature (Figure 4.6-2). The refrigerant mass flow rate was also measured using a Coriolis-type flow meter; mass flow rate combined with pressure and temperature measurements before and after the evaporator allowed refrigerant-side capacity calculation as a secondary check on the air-side capacity. Additionally, outdoor fan power, indoor blower power and total power were measured for calculation of the coefficient of performance (COP).

All measurements were recorded by a data acquisition system, which allowed real-time monitoring of collected measurements (Figure 4.6-5).

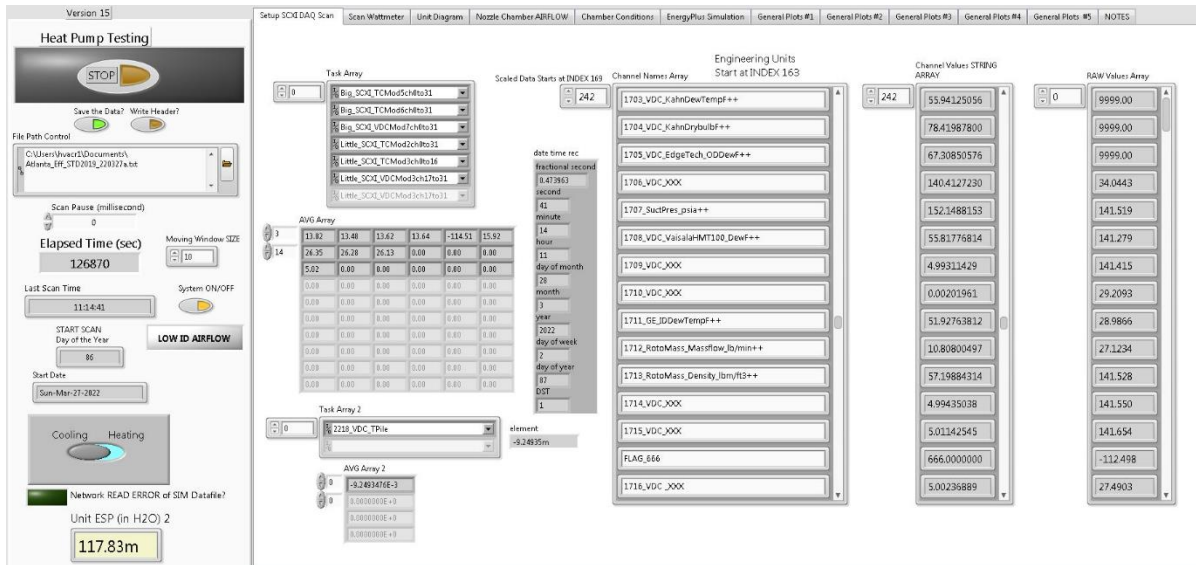


Figure 4.6-5. Data acquisition screen for data monitoring

Table 4.6-1 lists uncertainties of the major quantities measured during this work. Reported values and uncertainties with an (XXX±YY) representation indicate an average of multiple measurements with the variation given as two standard deviations of the measurement (k=2 coverage factor).

Table 4.6-1. Measurement uncertainties

Measurement	Range	Total Uncertainty at the 95 % Confidence Level
Individual Temperature	-18 °C to 93 °C (0 °F to 200 °F)	±0.44 °C (±0.8 °F)
Temperature Difference	0 °C to 28 °C (0 °F to 50 °F)	±0.44 °C (±0.8 °F)
Air Nozzle Pressure	0 Pa to 1245 Pa (0 in H ₂ O to 5.0 in H ₂ O)	±1.0 Pa (±0.004 in H ₂ O)
Refrigerant Mass Flow Rate	136 kg/h to 544 kg/h (5 lb/min to 20 lb/min)	±0.10 %
Dewpoint Temperature	0 °C to 38 °C (32 °F to 100 °F)	±0.4 °C (0.72 °F)
Drybulb Temperature	2 °C to 49 °C (35 °F to 120 °F)	±0.44 °C (0.8 °F)
Power Demand	0 W to 8 000 W	0.5 %
Total Cooling Capacity	(15 000 Btu/h to 60 000 Btu/h)	4.0 %
Latent Cooling Capacity	(3 000 Btu/h to 12 000 Btu/h)	8.5 %
COP	2.0 to 6.0	5.5 %

4.6.3. Test Protocol and Metrics

Break-in Tests

Once the ECU was installed in the environmental chamber, the refrigerant circuit was modified to prevent hot-gas bypass and evaporator pressure control, and all instrumentation was installed. At the outset, we verified the air-side sensible capacity calculations involving nozzle chamber air flow and thermocouple grids measurements by operating the ECU's electric resistance heater and measuring its power. The heat balance between these measurements was within ±3 % at the

outdoor condition of 35.0 °C (95 °F), Also, we checked dewpoint sensors by placing them in one location (return duct) and verifying their readings at the dewpoint condition of 15.8 °C (60.5 °F). This was done to ensure proper calculation of latent capacity, which uses dewpoint temperature measurements.

After break-in tests, the testing program started with HFC-134a, followed by Tern-1 and R-515B tests, and a re-test with HFC-134a to verify the stability of the measurement setup. Then we proceeded to tests with R-513A, for which it was necessary to install a larger size TXV; R-513A has a higher ratio of vapor density at the compressor suction to liquid density at the TXV inlet, and the original TXV was too restrictive for the R-513A flow rate delivered by the ECU compressor.

For each refrigerant, the ECU was charged with refrigerant per the manufacturer's recommended charging process while operating at 26.7 °C (80.0 °F) indoor drybulb, 15.8 °C (60.5 °F) indoor dewpoint, and 35.0 °C (95.0 °F) outdoor drybulb. In this process, the TXV and refrigerant charge were adjusted to produce an evaporator exit superheat and condenser subcooling per manufacturer's instruction. We refer to these tests as 'drop-in' tests.

Test Metrics

The project plan stipulated evaluation of ECU performance at four tests points prescribed by the indoor condition of 26.7 °C (80.0 °F) drybulb and 15.8 °C (60.5 °F) dewpoint and four outdoor conditions:

- 27.8 °C (82 °F)
- 35.0 °C (95.0 °F)
- 46.1 °C (115.0 °F)
- 51.7 °C (125.0 °F).

The repeatability of tests at a given outdoor condition was used to determine the combined total uncertainty (measurement uncertainty and repeatability uncertainty) as reported in later figures.

4.6.4. ECU Test Results

ECU Performance at Test Conditions

Tables 4.6-2 to 4.6-5 show representative test data for each of the refrigerants. These are average values of each parameter measured over a steady-state test period for one test at a given outdoor ambient temperature. The total capacity (Q_{air}) is the measured capacity on the air side, which includes the heat added by the blower. Refrigerant-side capacity (Q_{ref}) has also been adjusted for the blower's heat (the electrical energy delivered to the blower is transformed to heat).

Table 4.6-2. Representative ECU test data for HFC-134a at four outdoor temperatures

HFC-134a				
Parameter	27.8 °C (82 °F)	35.0 °C (95 °F)	46.1 °C (115 °F)	51.7 °C (125 °F)
Total Capacity, W (Btu/h)	12644 (43166)	11664 (39821)	9323 (31829)	7500 (25605)
Latent Capacity, W (Btu/h)	2723 (9296)	2290 (7816)	1386 (4733)	876 (2991)
Compressor Power, W	5139	6038	7687	8572
Indoor Blower Power, W	1965	1922	1970	1952
Condenser Fan Power, W	355	352	343	336
COP	1.685	1.402	0.936	0.692
Evaporator Exit Refrigerant Pressure, kPa (psia)	298.9 (43.4)	311.8 (45.2)	335.0 (48.6)	360.9 (52.3)
Evaporator Exit Refrigerant Temperature, °C (°F)	8.7 (47.6)	8.3 (47.0)	13.7 (56.7)	14.8 (58.7)
Evaporator Exit Refrigerant Sat. Temperature, °C (°F)	0.6 (33.0)	1.8 (35.2)	3.8 (38.8)	5.9 (42.6)
Evaporator Exit Refrigerant Superheat, °C (°F)	8.1 (14.6)	6.6 (11.9)	10.0 (17.9)	8.9 (16.1)
Condenser Inlet Refrigerant Pressure, kPa (psia)	1388.6 (201.4)	1650.9 (239.4)	2130.0 (308.9)	2374.5 (344.4)
Condenser Inlet Refrigerant Temperature, °C (°F)	75.4 (167.8)	83.3 (181.9)	108.6 (227.5)	121.2 (250.2)
Condenser Inlet Refrigerant Sat. Temperature, °C (°F)	52.1 (125.8)	59.2 (138.6)	70.3 (158.5)	75.2 (167.4)
Condenser Inlet Superheat, °C (°F)	24.0 (43.2)	24.4 (44.0)	37.8 (68.1)	45.1 (81.1)
Condenser Exit Refrigerant Pressure, kPa (psia)	1274.6 (184.9)	1537.0 (222.9)	2042.1 (296.2)	2290.6 (332.2)
Condenser Exit Refrigerant Temperature, °C (°F)	41.3 (106.3)	48.6 (119.5)	57.3 (135.2)	61.9 (143.5)
Condenser Exit Refrigerant Sat. Temperature, °C (°F)	48.7 (119.6)	56.2 (133.2)	68.4 (155.1)	73.6 (164.4)
Condenser Exit Refrigerant Subcooling, °C (°F)	7.4 (13.3)	7.6 (13.7)	11.1 (19.9)	11.6 (20.9)
Indoor Air Volumetric Flow Rate, m ³ /h (scfm)	3060 (1801)	2948 (1735)	3034 (1786)	3020 (1777)
Refrigerant Mass Flow Rate, g/s (lb/min)	97.025 (12.83)	100.50 (13.29)	96.10 (12.71)	92.97 (12.30)
Q_{ref} , W (Btu/h)	12386 (42263)	11756 (40113)	10225 (34889)	9221 (31464)
$(Q_{air} - Q_{ref})/Q_{ref}$	0.021	-0.008	-0.089	-0.187

Table 4.6-3. Representative ECU test data for R-515B at four outdoor temperatures

R-515B				
Parameter	27.8 °C (82 °F)	35.0 °C (95 °F)	46.1 °C (115 °F)	51.7 °C (125 °F)
Total Capacity, W (Btu/h)	10635 (36312)	9315 (31807)	7403 (25277)	6479 (22122)
Latent Capacity, W (Btu/h)	1525 (5207)	1027 (3505)	1116 (3809)	767 (2618)
Compressor Power, W	3762	4354	5459	6130
Indoor Blower Power, W	1962	1974	1904	1901
Condenser Fan Power, W	358	352	346	340
COP	1.735	1.391	0.965	0.778
Evaporator Exit Refrigerant Pressure, kPa (psia)	233.7 (33.9)	243.4 (35.3)	263.4 (38.2)	278.5 (40.4)
Evaporator Exit Refrigerant Temperature, °C (°F)	14.1 (57.3)	15.7 (60.3)	8.8 (47.8)	10.2 (50.3)
Evaporator Exit Refrigerant Sat. Temperature, °C (°F)	2.3 (36.2)	3.4 (38.2)	5.6 (42.1)	7.2 (45.0)
Evaporator Exit Refrigerant Superheat, °C (°F)	11.8 (21.2)	12.3 (22.1)	3.2 (5.7)	3.0 (5.4)
Condenser Inlet Refrigerant Pressure, kPa (psia)	992.8 (144.0)	1169.4 (169.6)	1478.9 (214.5)	1687.1 (244.7)
Condenser Inlet Refrigerant Temperature, °C (°F)	65.8 (150.4)	74.8 (166.7)	81.1 (178.0)	88.8 (191.8)
Condenser Inlet Refrigerant Sat. Temperature, °C (°F)	50.1 (122.1)	56.6 (133.9)	66.5 (151.7)	72.3 (162.2)
Condenser Inlet Superheat, °C (°F)	15.7 (28.2)	18.2 (32.8)	14.9 (26.9)	16.6 (29.9)
Condenser Exit Refrigerant Pressure, kPa (psia)	880.5 (127.7)	1066.0 (154.6)	1372.1 (199.0)	1581.7 (229.4)
Condenser Exit Refrigerant Temperature, °C (°F)	37.2 (98.9)	45.0 (113.0)	59.4 (138.9)	65.2 (149.4)
Condenser Exit Refrigerant Sat. Temperature, °C (°F)	45.4 (113.7)	52.8 (127.1)	63.3 (145.9)	69.4 (157.0)
Condenser Exit Refrigerant Subcooling, °C (°F)	8.3 (14.9)	7.9 (14.2)	3.9 (7.0)	4.2 (7.6)
Indoor Air Volumetric Flow Rate, m ³ /h (scfm)	3041 (1790)	3036 (1787)	3019 (1777)	3021 (1778)
Refrigerant Mass Flow Rate, g/s (lb/min)	86.66 (11.463)	88.03 (11.644)	95.22 (12.596)	98.15 (12.983)
Q_{ref} , W (Btu/h)	10206 (34824)	9516 (32469)	7865 (26835)	7385 (25199)
$(Q_{air} - Q_{ref})/Q_{ref}$	0.042	-0.021	-0.059	0.122

Table 4.6-4. Representative ECU test data for Tern-1 at four outdoor temperatures

Tern-1 [R-134a/1234yf/1234ze(E) (49.2/33.9/16.9) mass %]				
Parameter	27.8 °C (82 °F)	35.0 °C (95 °F)	46.1 °C (115 °F)	51.7 °C (125 °F)
Total Capacity, W (Btu/h)	13508 (46123)	12526 (42769)	10485 (35799)	9253 (31594)
Latent Capacity, W (Btu/h)	2585 (8825)	1970 (6728)	1120 (3825)	674 (2303)
Compressor Power, W	5037	5952	7575	8534
Indoor Blower Power, W	1963	1963	1961	1957
Condenser Fan Power, W	356	350	341	336
COP	1.822	1.513	1.064	0.857
Evaporator Exit Refrigerant Pressure, kPa (psia)	302.0 (43.8)	322.0 (46.7)	346.8 (50.3)	366.1 (53.1)
Evaporator Exit Refrigerant Temperature, °C (°F)	12.9 (55.3)	13.3 (56.0)	16.7 (62.1)	17.9 (64.2)
Evaporator Exit Refrigerant Sat. Temperature, °C (°F)	-0.2 (31.7)	1.7 (35.0)	3.8 (38.9)	5.4 (41.8)
Evaporator Exit Refrigerant Superheat, °C (°F)	13.1 (23.6)	11.7 (21.0)	12.9 (23.3)	12.4 (22.4)
Condenser Inlet Refrigerant Pressure, kPa (psia)	1377.6 (199.8)	1644.4 (238.5)	2120.8 (307.6)	2391.1 (346.8)
Condenser Inlet Refrigerant Temperature, °C (°F)	73.2 (163.7)	81.4 (178.6)	101.9 (215.5)	112.0 (233.6)
Condenser Inlet Refrigerant Sat. Temperature, °C (°F)	51.8 (125.2)	59.2 (138.6)	70.4 (158.7)	75.9 (168.7)
Condenser Inlet Superheat, °C (°F)	21.3 (38.4)	22.2 (40.0)	31.5 (56.7)	36.1 (65.0)
Condenser Exit Refrigerant Pressure, kPa (psia)	1245.9 (180.7)	1521.0 (220.6)	2013.3 (292.0)	2287.0 (331.7)
Condenser Exit Refrigerant Temperature, °C (°F)	39.9 (103.9)	47.8 (118.0)	56.9 (134.5)	62.3 (144.1)
Condenser Exit Refrigerant Sat. Temperature, °C (°F)	47.4 (117.4)	55.7 (132.2)	67.8 (154.1)	73.7 (164.6)
Condenser Exit Refrigerant Subcooling, °C (°F)	7.5 (13.5)	7.8 (14.1)	10.9 (19.6)	11.4 (20.5)
Indoor Air Volumetric Flow Rate, m ³ /h (scfm)	3041 (1790)	3045 (1792)	3038 (1788)	3038 (1788)
Refrigerant Mass Flow Rate, g/s (lb/min)	102.65 (13.578)	107.06 (14.162)	105.41 (13.944)	105.46 (13.950)
Q_{ref} , W (Btu/h)	12178 (41553)	11518 (39301)	10112 (34502)	9296 (31718)
$(Q_{air} - Q_{ref})/Q_{ref}$	0.109	0.088	0.037	-0.005

Table 4.6-5. Representative ECU test data for R-513A at four outdoor temperatures

R-513A				
Parameter	27.8 °C (82 °F)	35.0 °C (95 °F)	46.1 °C (115 °F)	51.7 °C (125 °F)
Total Capacity, W (Btu/h)	12833 (43817)	11583 (39548)	9459 (32298)	8587 (29320)
Latent Capacity, W (Btu/h)	3217 (10984)	2647 (9038)	1539 (5256)	1263 (4314)
Compressor Power, W	5508	6511	7971	8907
Indoor Blower Power, W	1970	1911	1953	1944
Condenser Fan Power, W	363	346	347	341
COP	1.637	1.324	0.924	0.770
Evaporator Exit Refrigerant Pressure, kPa (psia)	313.0 (45.4)	328.9 (47.7)	373.0 (54.1)	386.1 (56.0)
Evaporator Exit Refrigerant Temperature, °C (°F)	9.7 (49.4)	10.8 (51.4)	11.6 (52.8)	15.0 (59.0)
Evaporator Exit Refrigerant Sat. Temperature, °C (°F)	-1.1 (30.1)	0.3 (32.6)	4.1 (39.3)	5.1 (41.2)
Evaporator Exit Refrigerant Superheat, °C (°F)	10.7 (19.3)	10.4 (18.8)	7.5 (13.5)	9.9 (17.8)
Condenser Inlet Refrigerant Pressure, kPa (psia)	1452.7 (210.7)	1766.4 (256.2)	2200.1 (319.1)	2466.9 (357.8)
Condenser Inlet Refrigerant Temperature, °C (°F)	73.7 (164.6)	84.8 (184.7)	96.1 (205.0)	108.4 (227.1)
Condenser Inlet Refrigerant Sat. Temperature, °C (°F)	52.2 (126.0)	60.6 (141.0)	70.4 (158.8)	75.8 (168.5)
Condenser Inlet Superheat, °C (°F)	21.9 (39.5)	24.4 (43.9)	25.5 (45.9)	31.9 (57.5)
Condenser Exit Refrigerant Pressure, kPa (psia)	1334.8 (193.6)	1654.7 (240.0)	2079.5 (301.6)	2357.3 (341.9)
Condenser Exit Refrigerant Temperature, °C (°F)	38.7 (101.6)	45.2 (113.4)	58.4 (137.1)	63.2 (145.8)
Condenser Exit Refrigerant Sat. Temperature, °C (°F)	48.7 (119.7)	57.7 (135.9)	67.8 (154.1)	73.7 (164.6)
Condenser Exit Refrigerant Subcooling, °C (°F)	10.1 (18.1)	12.6 (22.6)	9.4 (17.0)	10.4 (18.8)
Indoor Air Volumetric Flow Rate, m ³ /h (scfm)	3079 (1812)	2978 (1753)	3077 (1811)	3062 (1802)
Refrigerant Mass Flow Rate, g/s (lb/min)	110.10 (14.564)	112.43 (14.872)	122.33 (16.182)	119.55 (15.814)
Q_{ref} , W (Btu/h)	12518 (42713)	11875 (40520)	10515 (35878)	9670 (32996)
$(Q_{air} - Q_{ref})/Q_{ref}$	0.025	-0.025	-0.100	-0.112

The tables include the energy balance between Q_{air} and Q_{ref} . In a typical setup for testing an air conditioner, the refrigerant-side capacity measured across the evaporator is somewhat higher (typically within 5 %) than the air-side capacity due to the heat gain in the ductwork. In our tests the energy balance was affected by the outdoor temperature (temperature in the outdoor chamber

where the ECU was installed) showing a significant reduction of the air-side capacity with respect to refrigerant-side capacity at increased outdoor temperatures.

To verify the effect of ambient temperature on the energy balance, we performed energy balance tests on the ECU and its ductwork in the outdoor chamber (where the ECU was located). We operated the blower and the unit’s electric resistance heat at a constant power at different outdoor temperatures of 27.8 °C (82 °F), 35.0 °C (95 °F), 46.1 °C (115 °F), and 51.7 °C (125 °F), while supplying air from the indoor chamber at 26.7 °C (80 °F) drybulb.

These tests showed that heat transfer between the outdoor ambient and the unit’s interior and ductwork was occurring (Figure 4.6-6). The ductwork was insulated with 100 mm fiberglass insulation while the unit’s supply and return sections were insulated with 25 mm of foam and 12 mm of fiberglass. The heat transfer effect was magnified during the cooling mode operation at high ambient test conditions, which affected heat balance between the refrigerant side and the air side during ECU performance tests.

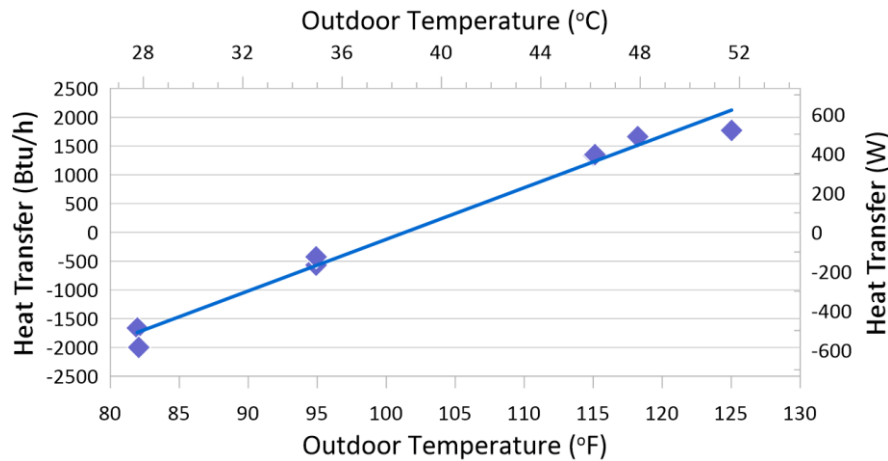


Figure 4.6-6. Heat transfer to the ECU and ductwork at different outdoor air temperatures

We also obtained atypical energy balance for ECU measurements with the Tern-1 showing higher air-side capacity than the refrigerant-side calculations (Table 4.6-4). It was hypothesized that composition shifting could have occurred due to solubility of the blend in the compressor polyolester (POE) oil. Discussions with other researchers revealed that HFO-1234ze(E) has a higher solubility with POE oil than other blend components. To evaluate this effect we used a theoretical CYCLE_D cycle model [91] to investigate a possible change in refrigerant-side capacity due to HFO-1234ze(E) being preferentially dissolved in the POE oil. Simulations were run with the nominal mass fraction of HFO-1234ze(E) and with a 6 % reduced mass fraction (an estimated reasonable value for this analysis). The volumetric capacity of the circulating refrigerant increases by 1.4 % thus increasing refrigerant-side capacity. This change is consistent with the observed trend in energy balance though it does not fully explain the magnitude of the heat balance reported in Table 4.6-4.

Figures 4.6-7 to 4.6-10 show absolute values of ECU total cooling capacity (air side), latent cooling capacity, total power demand, and COP for the tested refrigerants. The error bars indicate the combined total uncertainty at a 95 % confidence level of the shown measurements including test-to-test repeatability.

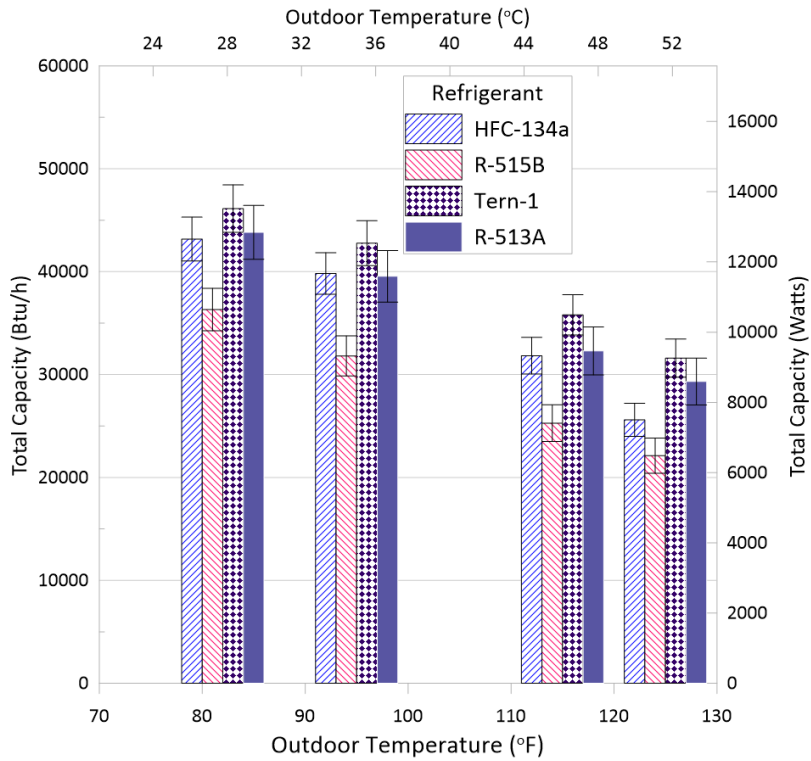


Figure 4.6-7. ECU total air-side capacity at outdoor temperatures 27.8 °C (82 °F), 35.0 °C (95 °F), 46.1 °C (115 °F), and 51.7 °C (125 °F) (center of bars)

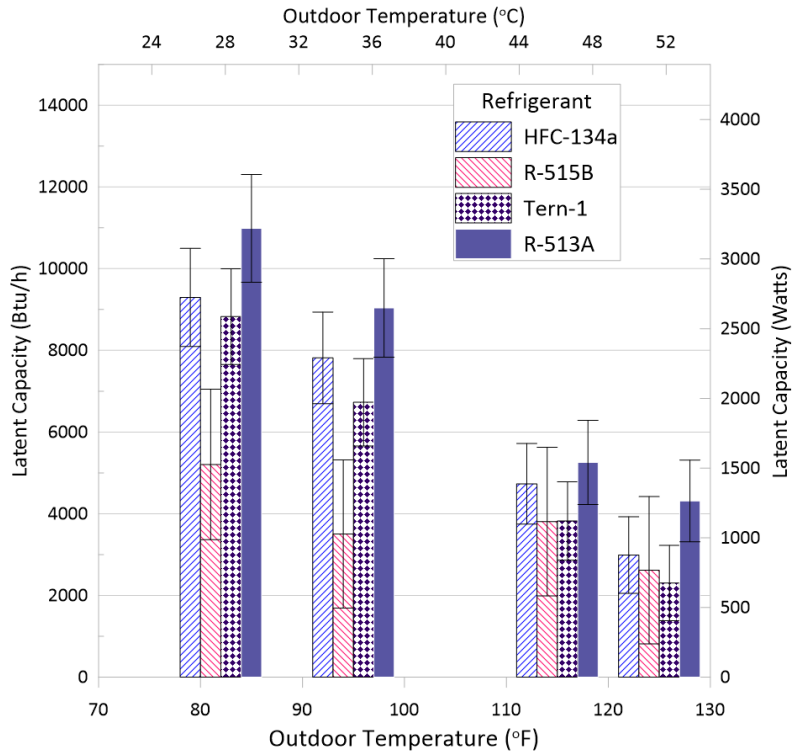


Figure 4.6-8. ECU latent capacity at outdoor temperatures 27.8 °C (82 °F), 35.0 °C (95 °F), 46.1 °C (115 °F), and 51.7 °C (125 °F) (center of bars)

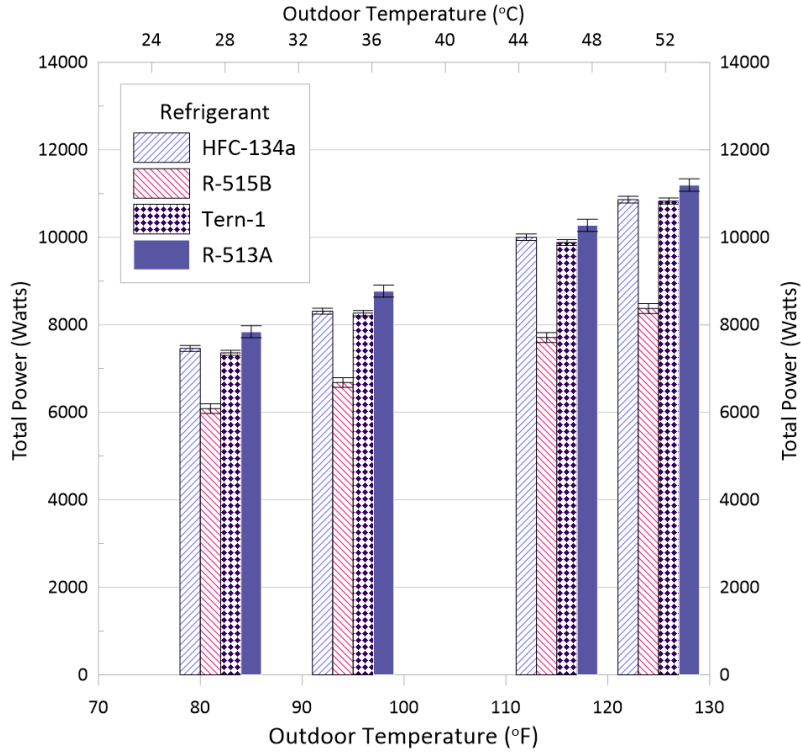


Figure 4.6-9. ECU total power at outdoor temperatures 27.8 °C (82 °F), 35.0 °C (95 °F), 46.1 °C (115 °F), and 51.7 °C (125 °F) (center of bars)

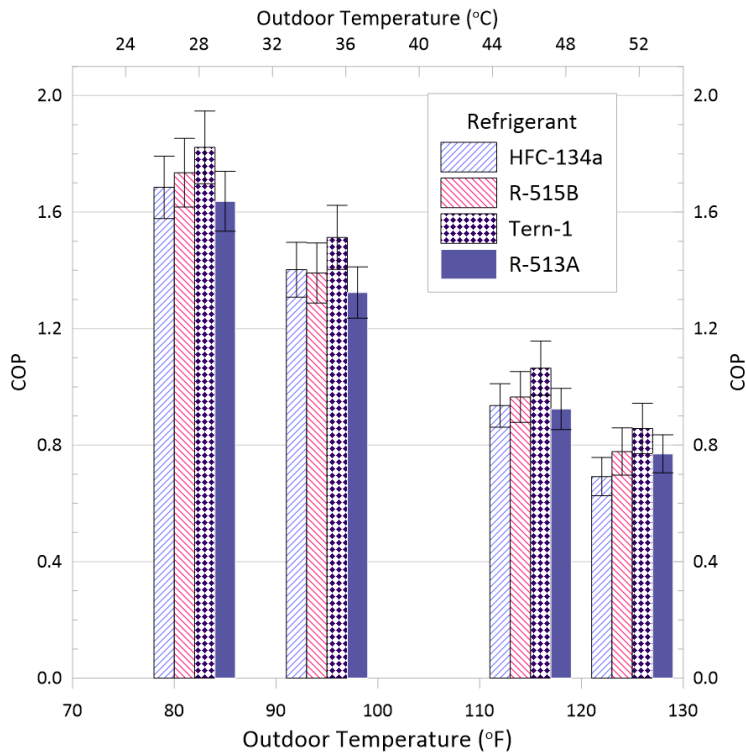


Figure 4.6-10. ECU COP at outdoor temperatures 27.8 °C (82 °F), 35.0 °C (95 °F), 46.1 °C (115 °F), and 51.7 °C (125 °F) (center of bars)

4.7. Modeling of Blend Performance in an Optimized ECU

The ECU tests conducted in the environmental chambers provided information on the ECU performance with tested refrigerants producing different capacities. To determine performance merits equitably for each fluid, performance comparisons need to be carried out at the same capacity produced by each fluid [74]. It would be a rather complex task to carry out experimentally, but it is practical to execute it using simulation models. In this work, we used the heat exchanger model EVAP-COND [92] and a system model ACSIM with the same capacity imposed at the 35.0 °C (95 °F) rating point. Compressor isentropic efficiencies for these simulations were calculated by the HFO-134a compressor map using the suction and discharge saturation temperatures established in a cycle for a given individual blend.

EVAP-COND is a software package that contains NIST's simulation models EVAP and COND for finned-tube evaporators and condensers. The “tube-by-tube” simulation scheme used in these models allows for specifying complex refrigerant circuits, modeling refrigerant distribution between these circuits, and accounting for one-dimensional air maldistribution. EVAP-COND includes a computational intelligence-based module for optimizing a heat exchanger’s refrigerant circuitry. ACSIM is the NIST in-house model of an air conditioner. It includes models of a compressor, evaporator, condenser, TXV, and connecting tubing. It uses the EVAP-COND routines for simulating performance of the evaporator and condenser.

4.7.1. Modeling Methods

Compressor

The compressor was modeled using compressor map correlations in the format defined by the ANSI/AHRI Standard 540:

$$X = B1 + B2 \cdot T_s + B3 \cdot T_d + B4 \cdot T_s^2 + B5 \cdot T_s \cdot T_d + B6 \cdot T_d^2 + B7 \cdot T_s^3 + B8 \cdot T_d \cdot T_s^2 + B9 \cdot T_s \cdot T_d^2 + B10 \cdot T_d^3$$

where:

X = designated performance parameter (e.g., power consumption, mass flow, etc.)

B1-B10 = correlation coefficients

T_s = compressor suction dew-point temperature (°F)

T_d = compressor discharge dew-point temperature (°F)

Compressor map coefficients are derived from calorimeter tests and correlate the compressor performance at prescribed values of the suction superheat and condenser subcooling used during the calorimeter test. To allow simulations at different conditions, the following assumptions and steps were employed:

- It was assumed that the isentropic efficiency is not affected by the level of suction vapor superheat. The compressor isentropic efficiency was calculated using the compressor map correlations for saturation temperatures in the compressor suction and discharge and at the superheat and subcooling levels used during the calorimeter tests.
- When calculating the refrigerant mass flow rate, it was assumed that the compressor volumetric efficiency and speed (revolutions per minute) are not affected by the suction vapor superheat. Consequently, the refrigerant mass flow rate at a given suction superheat equals the

value of mass flow rate at the superheat set during the calorimeter tests adjusted for a different specific volume of the suction vapor due to a different superheat.

The maps for the HFC-134a compressor used in the ECU were provided by the compressor manufacturer. These maps served as the reference performance characteristics for the compressors simulated with all four fluids. We implemented two options to the compressor simulation module for the purpose of this study:

- Use of the HFC-134a compressor performance maps for other refrigerants. Under this option, the compressor simulation module calculates the isentropic efficiency and volumetric flow rate for HFC-134a using the compressor saturation suction and discharged temperatures established during the cycle simulation for the new refrigerant. Then, using these values, the compressor power and mass flow rate for the new refrigerant is calculated using its thermodynamic properties.
- A multiplying parameter for modifying the refrigerant mass flow rate pumped by the compressor. With this adjustment we could match HFC-134a capacity at a selected rating point with each alternative fluid.

The ECU test matrix included two extreme outdoor temperatures, 46.1 °C (115 °F) and 51.7 °C (125 °F), which were outside the compressor maps developed by the manufacturer. For this reason, we evaluated predictions of compressor power input and refrigerant mass flow rate against those measured during system tests in the environmental chambers. The predictions of refrigerant mass flow rate were consistent through the whole operation range covered by the compressor maps; however, the prediction of compressor power was overpredicted by as much as 26 % at the two highest outdoor temperatures. By applying a multiplier y to the compressor-map predicted value, where $y = (0.0044 \cdot T_s (\text{°F}) + 0.0066(T_d - T_s))$, the discrepancy was reduced to within 2.1 % over the tested range of operating conditions. This multiplier was developed by fitting the compressor map predictions and the laboratory measurements.

Evaporator

The evaporator was oriented at 45 ° angle relative to the ground (Figure 4.7-1). It was a finned-tube heat exchanger consisting of 72 copper tubes placed in four depth rows, 18 tubes per depth row. The tube spacing and the depth row spacing were 25.4 mm (1 inch). The tubes were of the microfin type with an outside diameter of 7.9 mm (5/16 in) and a wall thickness of 0.3 mm (0.012 in). The tube length was 700 mm (27.6 in), and the coil finned height was 460 mm (18.1 in). The heat exchanger used wavy-lanced aluminum fins spaced at 2.5 mm (11 fins/in) with a thickness of 0.075 mm (0.003 in) (Figure 4.7-2).

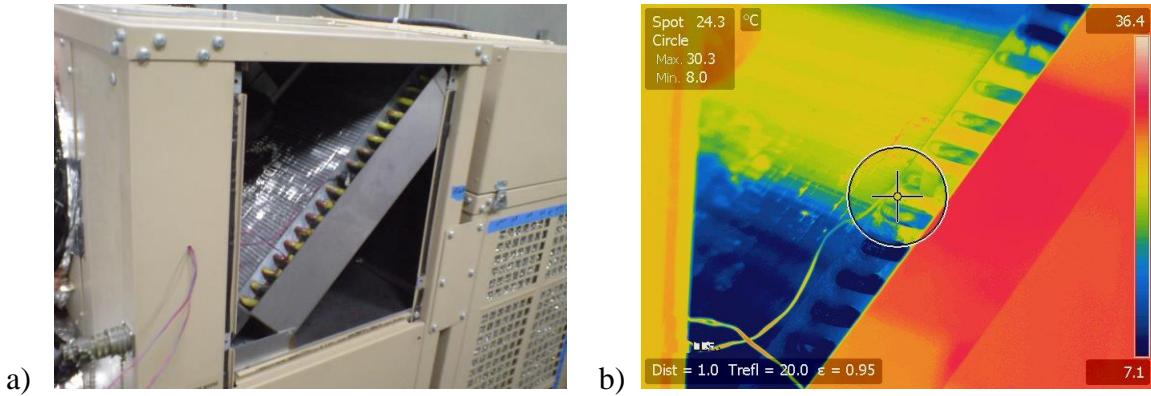


Figure 4.7-1. Right side of the evaporator in the ECU package (a) with infrared image (b)

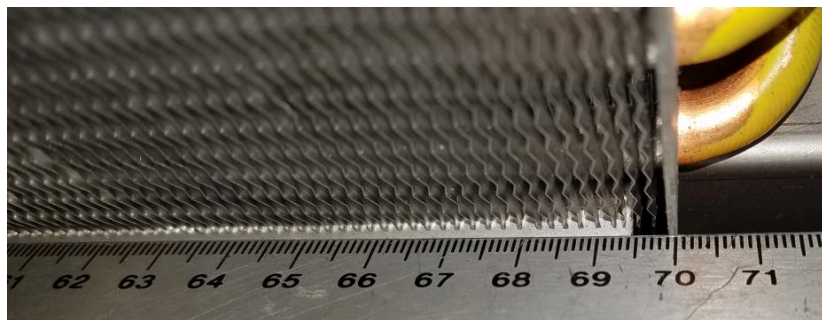


Figure 4.7-2. Evaporator fin spacing (cm scale)

The coil had a symmetrical refrigerant circuitry arrangement. It used 18 parallel refrigerant circuitry branches, each consisting of four tubes located in four depth rows, one tube after another to produce a cross-counter flow with the indoor air moving up from the bottom face (inlet) of the evaporator. The refrigerant was delivered to the coil by 18 feeding tubes connecting the thermostatic expansion valve (TXV) with the inlet tube of each individual circuit (Figure 4.7-3). The indicated coil tubes (tubes 1, 2, 3 and 4) comprise one of the eighteen circuits. Refrigerant entered by Tube 1 and left by Tube 4. The air flow was from the bottom to the top.



Figure 4.7-3. Evaporator refrigerant circuitry

Figure 4.7-4 shows an infrared image of the air-exit side of the evaporator. The image was taken looking down on the image shown in Figure 4.7-1 and 4.7-3. The colors are white/red (hottest @ 26.8 °C) to coolest (blue @ 21.5 °C). The inlet air temperature was 26.7 °C (80 °F). The pictures

were taken for the system charged with HFC-134a, but they are expected to represent the evaporator operation with other tested refrigerants as well.

The variation of colors shown by the infrared image indicates significant differences in temperatures in the tubes of the top depth row. Since the entry refrigerant condition and mass flow rate in these tubes can be assumed to be similar (fed by identical distributor tubes), the infrared image indicates a significant maldistribution of air in the evaporator.

Air velocity profile measurements verified the maldistribution of the inlet air, as shown in Figure 4.7-5. The measurements were taken 1.5 cm from the coil face. The measurements were taken 1.5 cm from the coil face in an evenly divided 5 x 5 grid, whose corners were 2.5 cm away from horizontal and vertical edges of the finned face. A hot wire anemometer with a single hot wire sensor was used to measure the air speed; total uncertainty of this instrument was $\pm 5\%$ of the reading. The average air velocity was 528 cm/s (1039 ft/min) with a standard deviation of 267 cm/s (526 ft/min). The maximum velocity occurred near the geometric center with a value of 1389 cm/s (2734 ft/min); the minimum velocity occurred at the edges and was 203 cm/s (400 ft/min). The air in the center was moving 6.8 times faster than the air at the edges. This significant two-dimensional air maldistribution is a combined effect of the compact installation of the evaporator slab in the package and the upstream location of the blower in the proximity of the slab. The significantly different amounts of air seen by different refrigerant circuits had a detrimental effect on the evaporator performance, i.e., poorly matched refrigerant distribution and air flow makes some tubes have long sections with superheated vapor with little heat transfer and high pressure drop, and other tubes, with two-phase refrigerant exiting the evaporator, representing a loss in capacity. The net effect is a loss in capacity and lower efficiency.

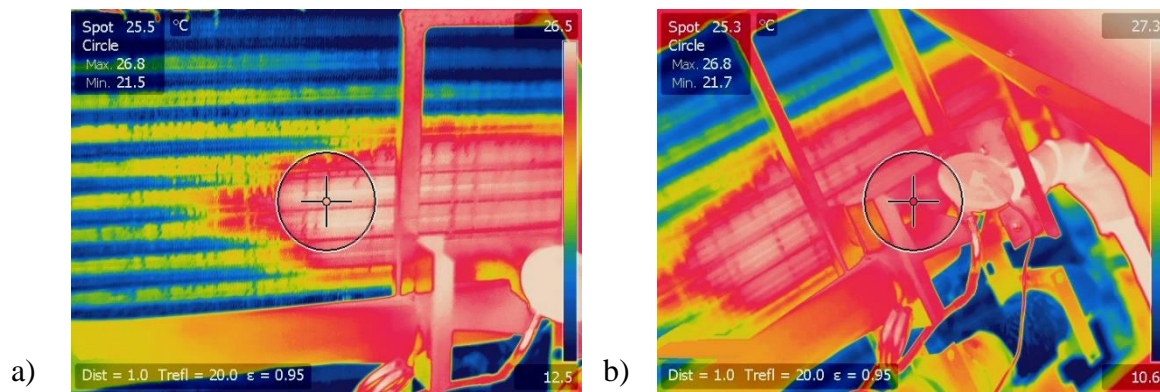


Figure 4.7-4. Infrared image of evaporator air side exit (view from the top, looking down). The left side of the image (a) corresponds to the near-side edge of the coil shown in Figure 4.7-1, (b) shows further right in the same picture.

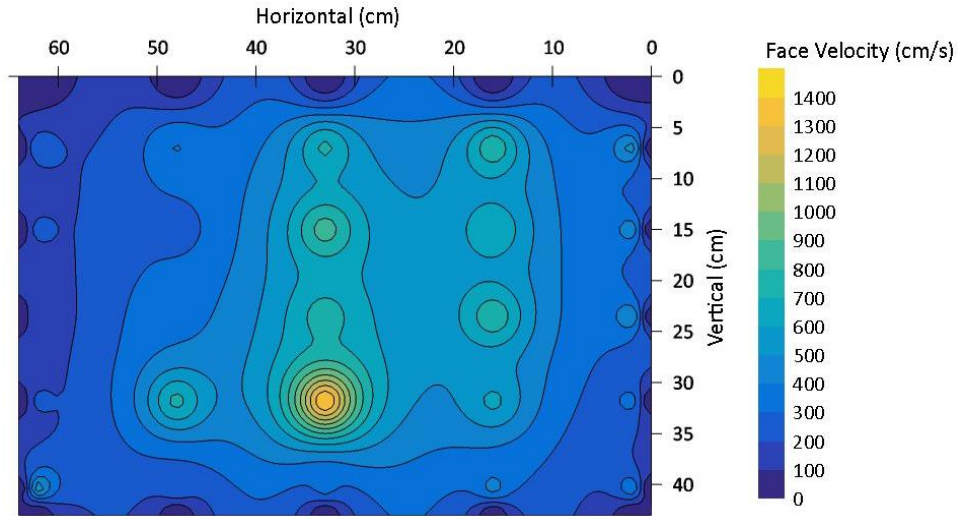


Figure 4.7-5. Evaporator air velocity profile measured at air inlet to coil. Refrigerant feeding tubes are on the right side. The grid origin is at the top of the coil.

Figure 4.7-6 shows the conceptual representation of a finned-tube heat exchanger in EVAP-COND. The red and blue circles denote the inlet and outlet tubes, respectively, the solid connecting lines denote return bends on the near side, and the broken lines denote return bends on the far (hidden) side. On the right of the heat exchanger schematic is a one-dimensional inlet air distribution.

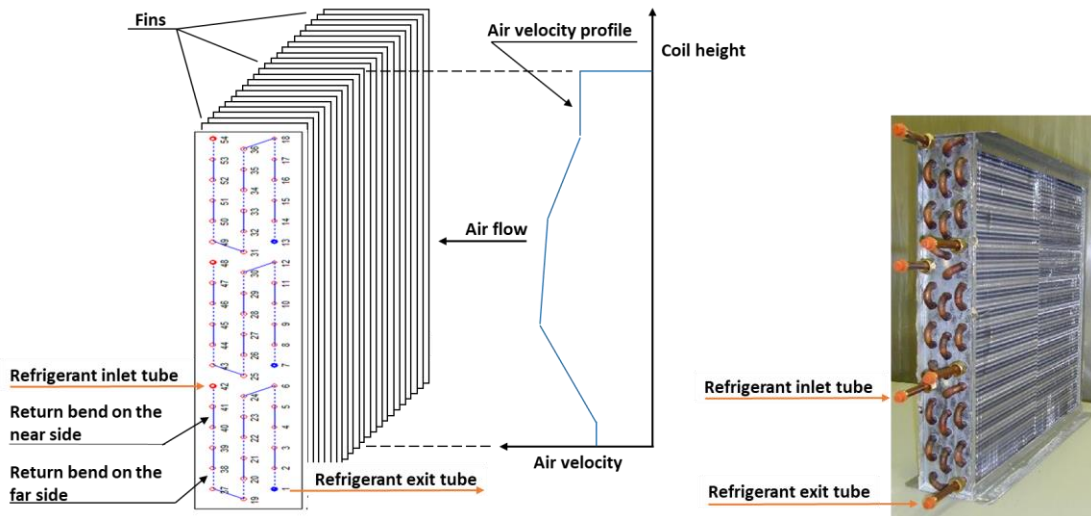


Figure 4.7-6. Conceptual representation of a heat exchanger in EVAP-COND

Figure 4.7-7 shows a graphical representation of the ECU evaporator with one-dimensional inlet air velocity profile approximating the two-dimensional air maldistribution of Figure 4.7-5. This inlet air velocity profile was used in ECU simulations.

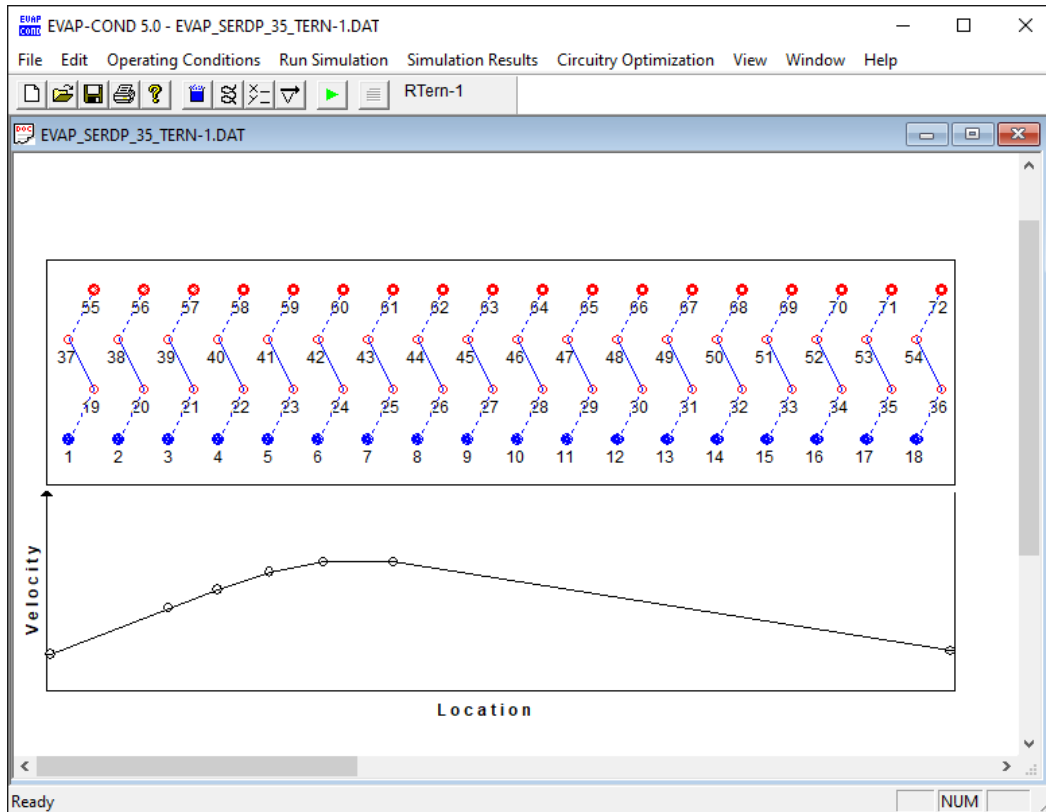


Figure 4.7-7. EVAP-COND side-view representation of the ECU evaporator with one-dimensional inlet air velocity profile

Condenser

The condenser consisted of 51 aluminum microchannel tubes, which were 1473 mm (58 inch) long, 27 mm (1.1 inch) wide, 3 mm (0.12 inch) thick, and were spaced vertically by 12 mm (0.5 inch). The vertical spacing between tubes was filled with wavy-lanced aluminum fins, which were solder-bonded to the flat microchannel tubes. The condenser was formed in a U-shape (Figure 4.7-8) and fitted tightly in the package. The fan, located at the top, pulled the ambient air into the condenser through two identical openings on two opposite sides of the ECU package. This air was then exhausted through a vertical opening.

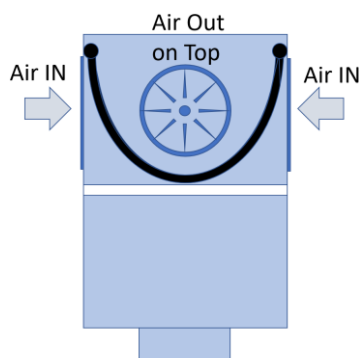


Figure 4.7-8. Configuration of the condenser (view from the top)

Figure 4.7-9 shows the left-side opening in the package with the air inlet face of the condenser and its infrared image, which reflects the refrigerant flow path. The hot refrigerant vapor entered the condenser through a manifold, which distributed the refrigerant to the top microchannel tubes while flowing from right to left (shown by the red arrows) and back left to right (orange arrows). Then, the partially condensed or subcooled refrigerant entered the remaining bottom microchannel tubes (yellow arrows) and continued to the exit. The infrared image implies that the microchannels located at the very bottom of the heat exchanger may not fully condense the refrigerant while the other exit microchannels have a different level of subcooling. The temperature scale goes from the hottest (red @ 42.8 °C) to the coolest (blue @ 36 °C). Resolution in this image is approximately 0.2 °C. The ambient was at 35 °C (95 °F). The ECU was charged with HFC-134a.

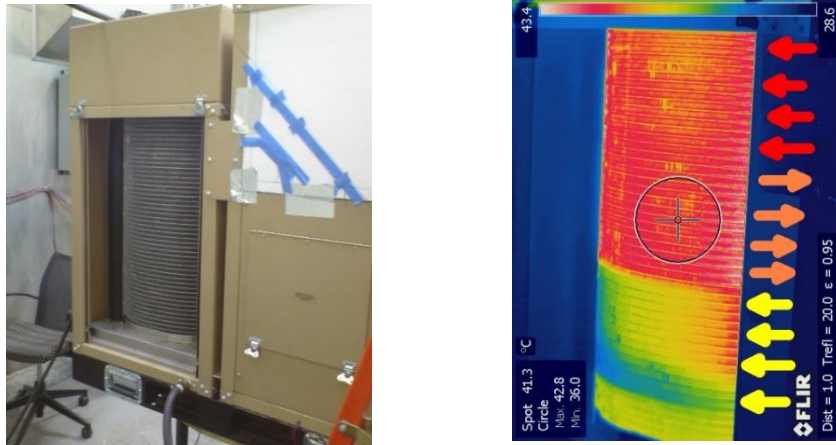


Figure 4.7-9. Infrared image of condenser air side inlet

Air velocity measurements with a hot wire anemometer were taken 1.5 cm above the surface of the protective grid at the air inlet to the condenser. Besides the spaces obstructed by the protective grid (see Figure 4.6-1, grid in place), the air distribution at the inlet to the condenser cage was relatively uniform with slightly higher air velocity at the top louvered entrances and the lowest at the bottom of the coil due to the relative distances from the suction action of the condenser fan (Figure 4.7-10). On the left condenser side, the velocity averaged 292 cm/s (574.8 ft/min) with a standard deviation of 27 cm/s (53.1 ft/min). On the opposite (right) side, the air velocity averaged 292 cm/s (574.8 ft/min) with a standard deviation of 31 cm/s (61.0 ft/min). Based on these measurements, the air flow through the condenser was estimated to be $2718.3 \pm 85 \text{ m}^3/\text{h}$ ($1600 \pm 50 \text{ cfm}$).

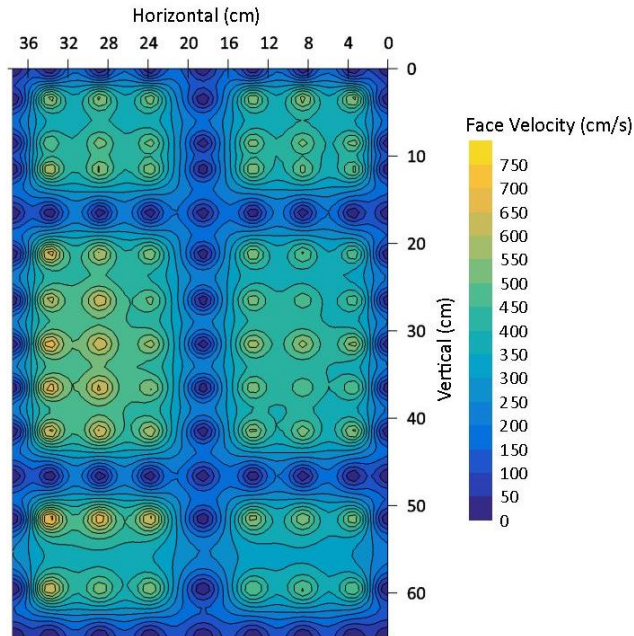


Figure 4.7-10. Condenser right-side air velocity measured at the protective grid

The air distribution at the inlet face of the condenser could not be measured because of space constraints. The air distribution was expected to be symmetric between the left and right sides of the heat exchanger with the air flow at the center part of the heat exchanger being significantly reduced due to proximity of the wall separating the condenser section and the compressor located within the “U” space of the condenser. Regardless of the maldistributed air in the horizontal plane (along the tubes, which were laid out horizontally), there was no significant air maldistribution in the vertical plane, i.e., each tube saw a similar amount of air flow.

Since EVAP-COND does not have the capability to model microchannel heat exchangers, we designed a finned-tube condenser, which had similar performance characteristics as microchannel condenser used in the ECU. This was accomplished by selecting the tube and fin material (aluminum), tube diameter, tube pattern, and iteratively selecting the number of tubes in a row, tube length, and fin spacing. The performance similarity was confirmed by validating the finned-tube condenser against the measurements taken on the ECU with the four tested refrigerants.

The designed finned-tube condenser consisted of two tube rows with 60 tubes per row. Since a uniform air distribution between tubes could be assumed and the design was symmetrical, we used the EVAP-COND option allowing to simulate a subsection of the heat exchanger assembly, in this case one third of the heat exchanger, as shown in Figure 4.7-11. Figure 4.7-12 is an EVAP-COND screenshot with the condenser design data.

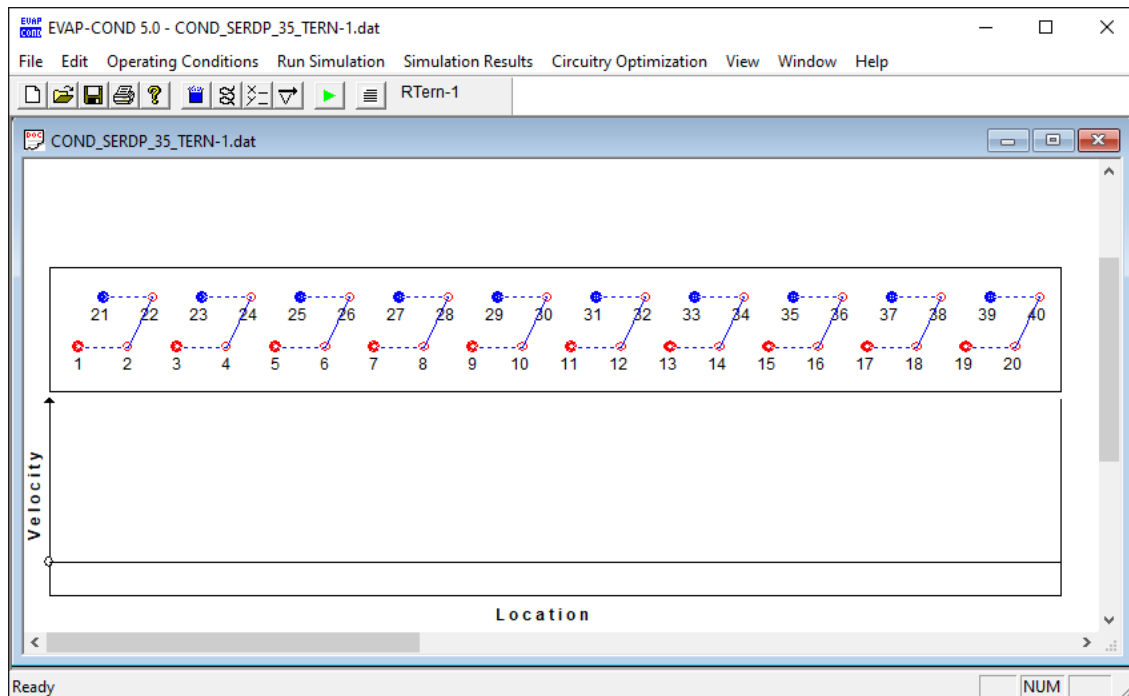


Figure 4.7-11. EVAP-COND side-view representation of the equivalent finned-tube condenser used in ECU simulations

Coil Design Data	
Data for a section	
No. of tubes in depth row #1:	20
No. of tubes in depth row #2:	20
No. of tubes in depth row #3:	0
No. of tubes in depth row #4:	0
No. of tubes in depth row #5:	0
Tube data	
Tube length	mm 1773
Inner diameter	mm 3.7
Outer diameter	mm 5.7
Tube pitch	mm 15
Depth row pitch	mm 18
Inner surface	Smooth
Material	Aluminum
Thermal conductivity	kW/(m.C) 0.237
ECU condenser	
Units	
<input checked="" type="checkbox"/> SI Units	<input type="checkbox"/> British Units
Number of slabs	3
Fin data	
Thickness	mm 0.6
Pitch	mm 1.5
Type	Lanced
Material	Aluminum
Thermal conductivity	kW/(m.C) 0.237
Volumetric flow rate	m ³ /min 45.3052
Fan power	W 0
<input type="button" value="Cancel"/> <input type="button" value="OK"/>	

Figure 4.7-12. Design data of the of the equivalent finned-tube condenser used in ECU simulations

4.7.2. Modeling Procedure

Modeling objectives

A given refrigerant can provide a range of COP values depending on the relative size of the compressor compared to the sizes of the evaporator and condenser as this affects saturation temperatures in the heat exchangers and the pressure lift against which the compressor operates.

In general, for given sizes of the evaporator and compressor, employing a larger compressor will result in a higher capacity and a lower COP, and vice versa. Because of this capacity vs. COP fundamental trade-off, the objective of this simulation task was to generate performance data in a modified ECU for each fluid so they would provide the same capacity as HFC-134a at the 35 °C rating point.

Considering fixed sizes of the heat exchangers, in our simulations we adjusted the size of the compressor for each fluid to achieve a match with the HFC-134a capacity. This resulted in the same heat flux in the evaporator for both fluids. Adjusting the size of the compressor to achieve the target evaporator capacity did not exactly achieve the matching of heat flux in the condenser; however, a small mismatch would have a negligible effect. Matching the heat flux in the evaporator is more important from thermodynamic considerations.

The following is the outline of the applied simulation process:

1. Tune EVAP-COND to the experimental measurements taken on the ECU evaporator and condenser during ECU tests at four ECU operating conditions (27.8 °C, 35.0 °C, 46.1 °C, and 51.7 °C outdoor temperatures). The tuning depended on adjusting parameters for air-side heat transfer, refrigerants heat transfer and pressure drop for the evaporator and condenser to achieve best (close) predictions of capacity of these heat exchangers as measured during the tests. Once a set of adjusting parameters was selected for each heat exchanger working with each fluid, these sets were used in the following system simulations.
2. Use ACSIM to simulate the ECU performance for each fluid (HFC-134a, R-515B, Tern-1, and R-513A) at each test condition reported in Tables 4.6-2 to 4.6-5. Use the measured performance parameter values and corresponding simulation predictions to determine correction parameters for the ACSIM simulation results at all individual test conditions. Tables A.4-1 to A.4-4 list the measured values, simulated values, and the discrepancy between them.
3. Perform ECU simulations for each fluid at the 35.0 °C test condition using the HFC-134a compressor isentropic efficiency at this condition and adjusting the displacement of the compressor to match the HFC-134a capacity. These simulations established the size of the compressor used for each fluid.
4. Perform ECU simulations for each fluid at the remaining test conditions using the compressor size determined at the 35.0 °C test condition. Use the isentropic efficiency of HFC-134a at each condition.

We applied this simulation process to develop capacity and COP values for the four operating conditions for R-515B, Tern-1, and R-513A, which we then related them to the capacity and COP of HFC-134a. The listed values were obtained from ACSIM simulations and adjusted by correction parameters obtained in step 2 (Table A.4-6).

4.7.3. Optimization of Heat Exchangers

We explored the possibility to improve the performance of the ECU through optimization of refrigerant circuitry in the heat exchangers, i.e., by modifying the path the refrigerant flows from inlet to outlet to achieve a higher capacity. There are three considerations related to refrigerant circuitry, which can improve the heat exchanger performance.

- For heat exchangers with multiple parallel circuits and several exit tubes, it is beneficial to ensure that refrigerant leaves each exit tube with a similar degree of vapor superheat. If the overall superheat (needed to protect the compressor) is achieved by mixing highly superheated vapor with two-phase refrigerant leaving different tubes, the portion of tubes with superheated vapor do not transfer much heat and contribute little to the heat exchanger capacity. A common cause for uneven refrigerant superheat is uneven distribution of air over the face of the heat exchanger, which was not addressed by the circuitry design.
- Selection of the number of parallel circuits affects the refrigerant mass flux. A higher mass flux enhances the refrigerant heat transfer coefficient but brings a penalty of additional pressure drop. With an optimized circuitry design, an optimum mass flux can be achieved where capacity of the heat exchanger is enhanced with acceptable pressure drop penalty.
- It is beneficial to establish a semi-counterflow alignment between the temperature of the air flowing through the heat exchanger and the temperature of the refrigerant in the tubes the air flows over. The temperature of air changes as it exchanges heat with the coil. Within the two-phase region, refrigerant temperature changes due to pressure drop. For zeotropic mixtures, it also changes as a result of a phase change. Typically, this third consideration has the smallest effect in air-to-refrigerant heat exchangers.

EVAP-COND is equipped with a machine-learning-based module for optimization of refrigerant circuitry. It is based on the evolutionary principle and involves genetic algorithms and symbolic learning sub-modules. We used this optimization capability to develop new circuit designs that would offer a higher capacity compared to the original ECU designs. We set the evolutionary process to consist of 400 generations with 20 members (designs) per a generation following earlier computational experiments and recommendations [93]. Hence, in each optimization run EVAP-COND evaluated 8000 circuitry architectures.

Optimization of evaporator

Figure 4.7-13 shows the best refrigerant circuitry obtained from multiple optimization runs for R-515A, Tern-1, and R-513A evaporators. This design maintained the same number and locations for inlet and outlet tubes and used several long tube-to-tube connections to provide most circuits with a balanced exposure to coil areas with high air velocity and low air velocity. This eliminated significant flooding that existed in the original design at the exit tubes 1 and 18.

Medium-pressure refrigerants, such as HFC-134a and the candidate replacement blends, have a larger drop in saturation temperature for a given pressure drop than high-pressure refrigerants, e.g., propane or R-410A. It appears that this increased penalty prevented the optimization scheme from finding a good circuit architecture with a smaller number of parallel circuits.

The improvement of capacity at a fixed evaporator saturation temperature was 1.8 % for R-515B, 2.1 % for Tern-1, 1.9 % for R-513A, and 1.3 % for HFC-134a. When installed in a system, these evaporators would operate at a somewhat higher saturation temperature than the original evaporator providing about 1/3 of the capacity improvement shown by simulations at the fixed saturation temperature. Considering the small impact on system capacity of the more complex circuitry and its higher manufacturing cost, we decided to use the original evaporator in system simulations; mostly because the effect of the optimized circuitry was very similar for the three candidate blends and would not affect their relative ranking.

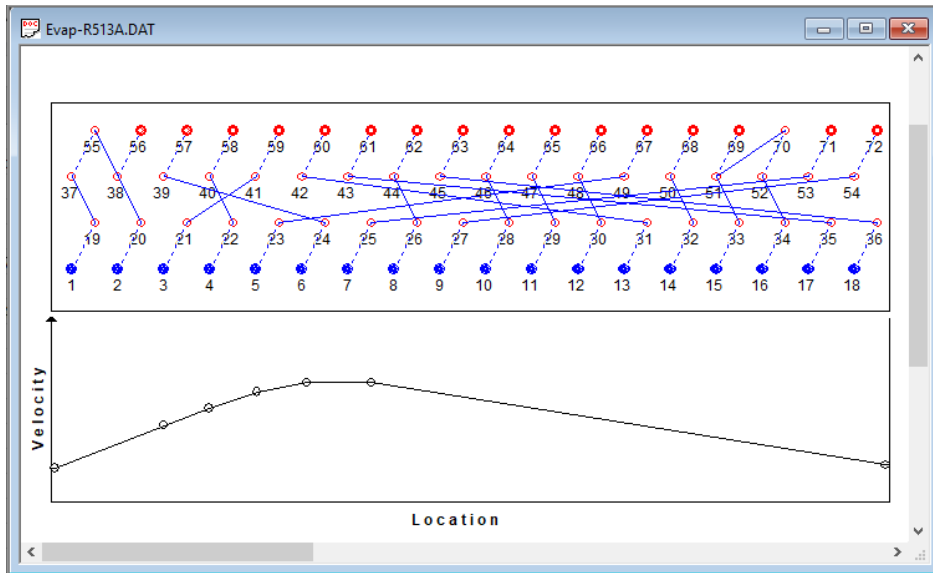


Figure 4.7-13. Optimized refrigerant circuitry designs for R-515B, Tern-1, R-513A and HFC-134a evaporator

Our analytical evaluation also included CO₂ (see Section 4.8.3). For this reason, we performed optimization of refrigerant circuitry for CO₂ evaporator as well (Figure 4.7-14). In this case, the optimization module returned a design with seven parallel circuits (instead of 18 in the case of R-515B, Tern-1, and R-513A). The improvement of capacity at a fixed evaporator saturation temperature was 6.0 %. We implemented this circuitry design in CO₂ ECU simulations.

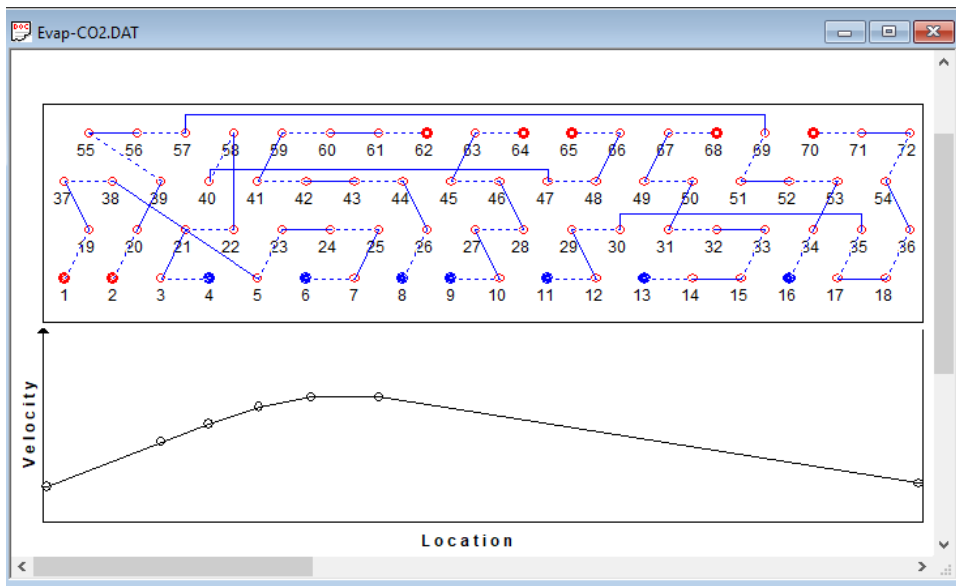


Figure 4.7-14. Optimized refrigerant circuitry design for CO₂ evaporator

Optimization of Condenser

Our optimization runs yielded circuitry designs with capacities that were just a fraction of a percent better than that of the current condenser while being much more complex for manufacturing. Consequently, we opted to use the current condenser in ECU simulations. The condenser used in the ECU was significantly oversized compared to conventional designs, and for this reason the attempts to optimize it were ineffective.

4.8. Comparison of Performance of Alternative Fluids

Here we present two comparative performance evaluations of the tested refrigerants by two evaluation scenarios. Section 4.8.1 contains results from laboratory “drop in” measurements of the acquired ECU where the tested refrigerants produced different capacities. In a contrast, Section 4.8.2 presents performance in a modified ECUs where each refrigerant matched the capacity of HFC-134a at the 35.0 °C (95 °F) rating point. These results were obtained through simulations.

While ECU laboratory measurements produce performance results on the air side and the refrigerant side, ECU simulations are based on the refrigerant side only. For this reason, to avoid the uncertainty associated with heat transfer between the unit’s interior, ductwork and the outdoor ambient, all results presented here are based on the refrigerant side data.

4.8.1. Performance of Three Blends in Original ECU (“drop-in” tests in environmental chambers)

Figure 4.8-1 and Figure 4.8-2 show differences in capacity and COP for the tested blends with respect to the values for HFC-134a (Table A.4-5). R-513A is a somewhat higher-pressure fluid than HFC-134a and provides a higher capacity at all test conditions. Its COP is lower than that of HFC-134a COP at 27.8 °C and 35.0 °C outdoor temperature; however, it is better at the 51.7 °C outdoor temperature even as R-513A delivers a higher capacity.

Tern-1 performance is similar to that of HFC-134a, both in terms of capacity and COP; they are within 2.6 % of the HFC-134a values. On the other hand, R-515B is a much lower-pressure fluid and provides significantly lower capacity by as much as 23 %. In this drop-in application with a much lower capacity, the COP of R-515B is comparable to that of HFC-134a.

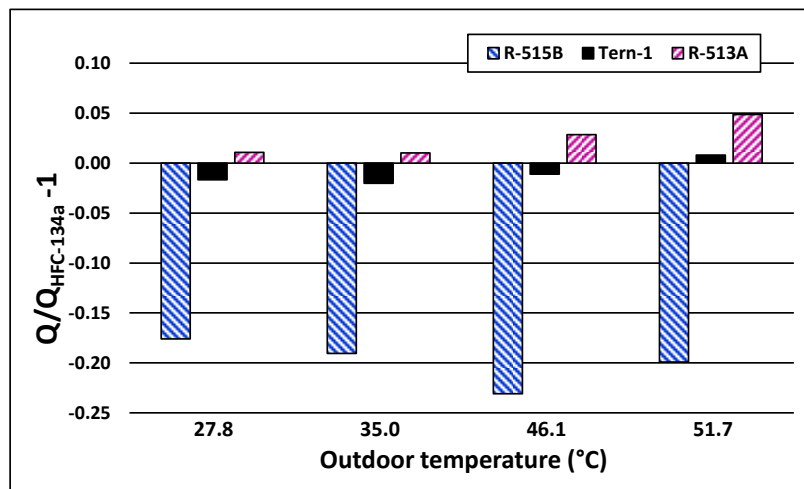


Figure 4.8-1. Capacity difference for R-515B, Tern-1, and R-513A versus HFC-134a, referenced to HFC-134a capacity, based on ECU tests at outdoor temperatures 27.8 °C, 35.0 °C, 46.1 °C, and 51.7 °C

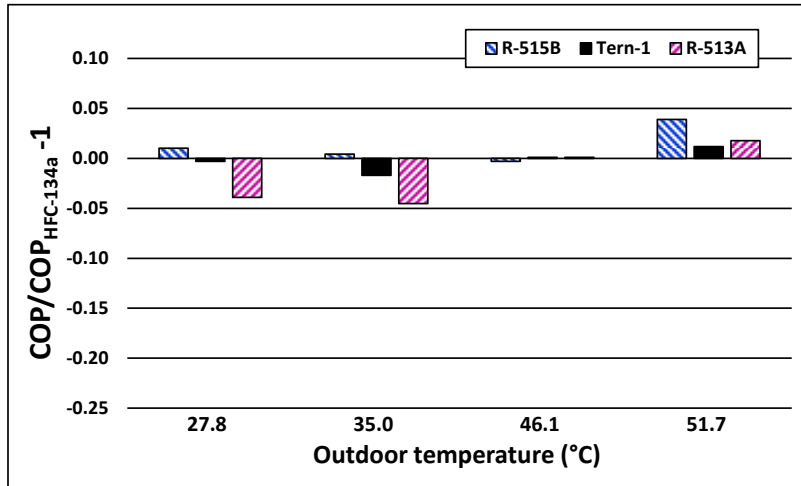


Figure 4.8-2. COP difference for R-515B, Tern-1, and R-513A versus HFC-134a, referenced to HFC-134a COP, based on ECU tests at outdoor temperatures 27.8 °C, 35.0 °C, 46.1 °C, and 51.7 °C

4.8.2. Performance of Three Blends in Modified ECUs Matching HFC-134a Capacity at 35 °C Test

In this evaluation scenario, R-513A requires a bit smaller compressor to match the capacity of HFC-134a. For a lower refrigerant mass flux, the dew-point temperature in the evaporator increased and the dew-point temperature in the condenser decreased, which resulted in an increased COP above the ‘drop-in’ evaluation case. Overall, R-513A is an attractive alternative, in particular for application in hotter climates: it has a competitive performance at 27.8 °C and 35.0 °C conditions and has better capacity and COP at higher ambient temperatures.

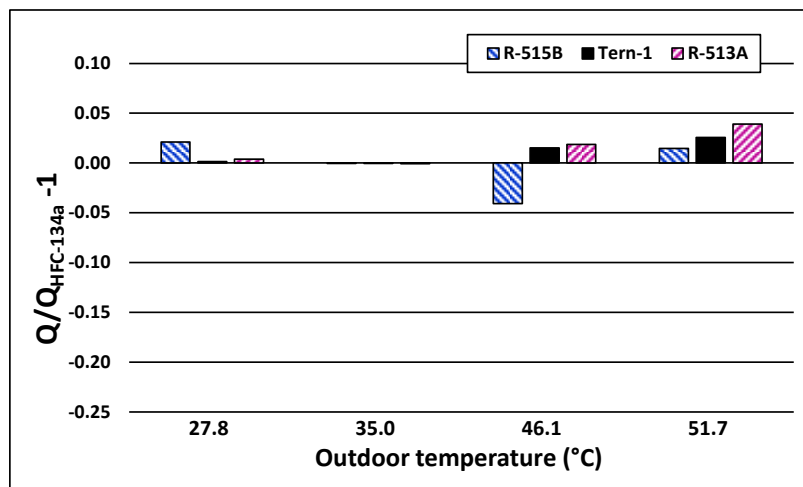


Figure 4.8-3. Capacity difference for R-515B, Tern-1, and R-513A versus HFC-134a, referenced to HFC-134a capacity, for ECUs with capacity matching that of HFC-134a at the 35.0 °C test condition; based on ACSIM simulations at outdoor temperatures 27.8 °C, 35.0 °C, 46.1 °C, and 51.7 °C

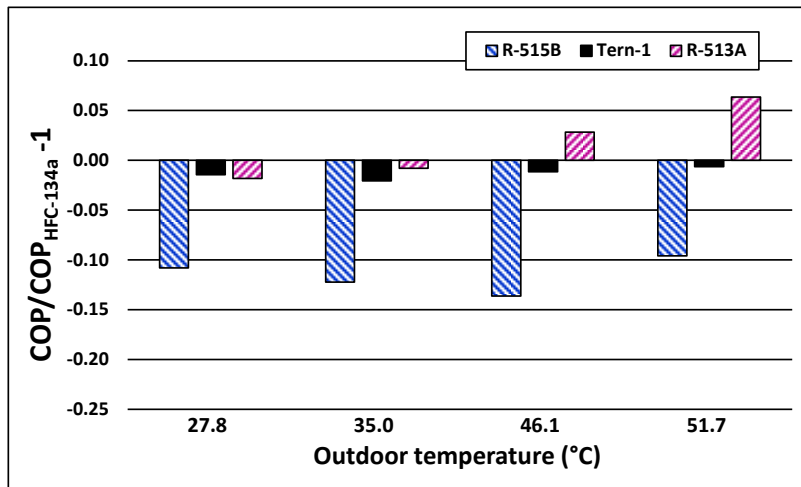


Figure 4.8-4. COP difference for R-515B, Tern-1, and R-513A versus HFC-134a, referenced to HFC-134a COP, for ECUs with capacity matching that of HFC-134a at the 35.0 °C test condition; based on ACSIM simulations at outdoor temperatures 27.8 °C, 35.0 °C, 46.1 °C, and 51.7 °C

Tern-1 capacity is at least equal to that of HFC-134a; the simulations show that it can provide a few percentages higher capacity at high outdoor temperatures than HFC-134a. Regarding COP, Tern-1 lags behind HFC-134a by 1 % or 2 % over the whole testing range.

The low-pressure R-515B can provide HFC-134a capacity if equipped with a large compressor; however, its COP would be at least 10 % below that of HFC-134a. Clearly, R-515B would require significant efficiency improvement measures to be competitive COP- wise while providing the target capacity.

4.8.3. Performance Carbon Dioxide in ECU Having HFC-134a Capacity at 35 °C Test Condition

In response to a recommendation of the committee reviewing the project proposal, we conducted an exploratory evaluation of carbon dioxide (CO₂). Since CO₂ has a low critical temperature (30.1 °C) and much higher pressure than HFC-134a, we could not carry out ECU tests with CO₂. We limited our assessment to analytical evaluation using EVAP-COND and a modified ACSIM model, which we will refer to as ACSIM.CO₂.

For this evaluation, we modified ACSIM to model a transcritical cycle, in which the high-pressure heat exchanger (condenser) operates above the critical point and becomes a gas cooler. To account for a substantial changes in CO₂ properties, ACSIM.CO₂ includes a CO₂ specific correlation for heat transfer above the critical point [94]. Another important change to ACSIM was the incorporation of an iteration scheme for optimizing pressure in the gas cooler while seeking the best coefficient of performance of the transcritical cycle. Notwithstanding the above modifications, we need to emphasize the exploratory character of this CO₂ evaluation.

We considered a basic ECU and an ECU equipped with a LLSL-HX of 60 % effectiveness. For both systems the compressor size was adjusted to provide cooling capacity matching that of the HFC-134a ECU at the 35.0 °C test condition. We included a system with a LLSL-HX in

recognition of significant throttling irreversibilities in the basic cycle and the need to provide some measures to reduce them. The simulation results with the LLSL-HX indicate what efficiency improvements can be achieved. Most likely, a LLSL-HX will not be viable due to the resulting high discharge temperatures; however, comparable efficiency improvements possibly can be achieved with other measures, e.g., a two-phase ejector.

The simulations indicate that the CO₂ system requires considerable research and development to bring its COP to the level of the HFC-134a ECU.

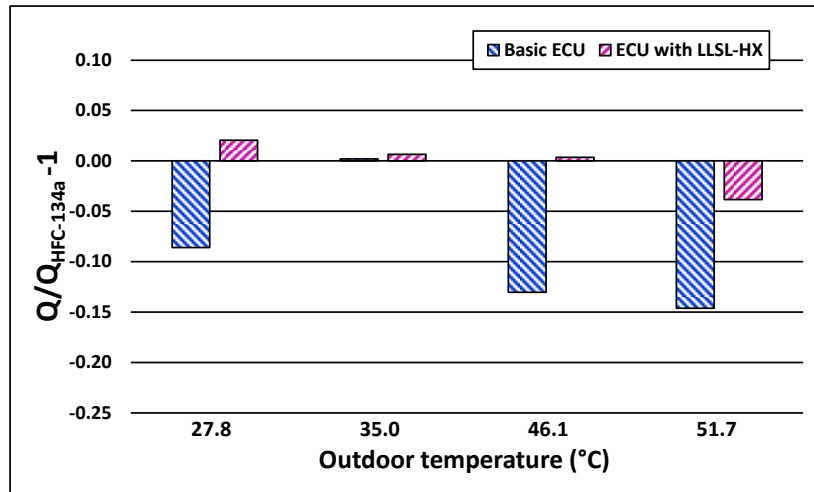


Figure 4.8-5. Capacity difference of CO₂ in basic ECU and ECU with LLSL-HX versus capacity of HFC-134a, referenced to HFC-134a capacity, for ECUs with capacity matching that of HFC-134a at the 35.0 °C test condition; based on ACSIM.CO₂ simulations at outdoor temperatures 27.8 °C, 35.0 °C, 46.1 °C, and 51.7 °C

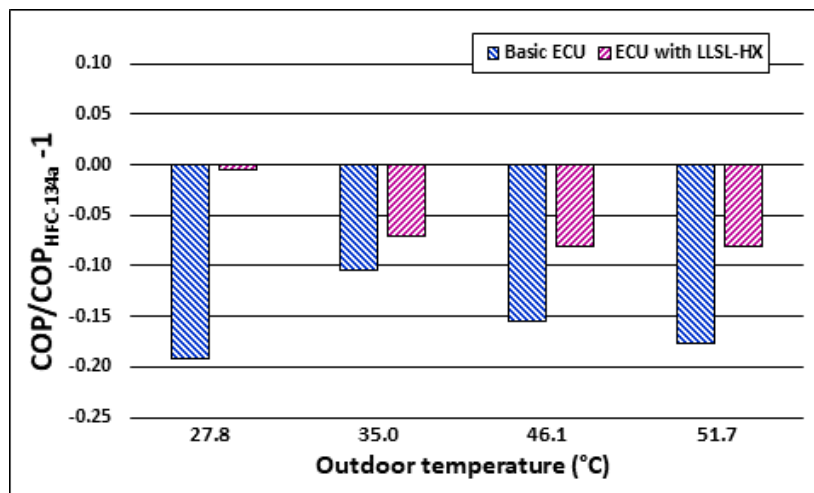


Figure 4.8-6. COP difference of CO₂ in basic ECU and ECU with LLSL-HX versus COP of HFC-134a, referenced to HFC-134a COP, for ECUs with capacity matching that of HFC-134a at the 35.0 °C test condition; based on ACSIM.CO₂ simulations at outdoor temperatures 27.8 °C, 35.0 °C, 46.1 °C, and 51.7 °C

5. Conclusions and Implications for Future Research/Implementation

Task 1. Experimental Measurements of Blend Properties and Development of Mixture Equation of State

We have carried out measurements on the thermophysical properties of refrigerant blends identified in the limited-scope project [6] and of interest in the current project. Accurate property data are the backbone of any project to identify and verify new refrigerants; they are essential for cycle analysis, heat transfer analysis, and the analysis of system tests. The new data have allowed us to improve the refrigerant mixture models needed for conducting the mini-breadboard heat pump tests (Task 3), refrigerant two-phase heat-transfer tests (Task 4), and ECU tests and detailed simulations (Task 7). While the improved property models were important for these tasks, no major deficiencies were identified in the models used in the limited-scope project; in other words, the selection of “best” blends made in the limited-scope project remains valid. All data taken under this project will be incorporated into future versions of REFPROP [8] and, thus, be made available to the entire HVAC industry.

Task 2. Flammability Testing

The four candidate HFC-134a replacement blends, R-513A, R-450A, R-515B, and Tern-1, were non-flammable by the ASTM E-681 test. While R-515B is non-flammable by the E681 test, it is close to the border of flammability in that test. If a Class 1 flammability rating via ASHRAE Standard 34 (i.e., based on the ASTM E681 test) is acceptable, then R-515B may be of great interest since it has the lowest GWP. Tern-1, R-513A, and R-450A are of similar flammability and are farther from the border of flammability. Thus, if a more stringent flammability test than the E681 test is required, then Tern-1, R-450A, or R-513A would be more promising candidates. This depends upon how the live-fire test compares to the E681 test.

A new parameter has been developed for characterizing the flammability. The overall reaction rate is a fundamentally based parameter that can be used to correlate experimental flammability results between test methods, or with full-scale test results. It is easily calculated for any arbitrary mixtures of interest and can be used to predict their flammability. In the present work, a detailed kinetic model has been developed and validated, and used to estimate the overall chemical reaction rate of the candidate blends. Both the E681 flame propagating/non-propagating boundary, as well as the JHPGL test explosion pressure were well correlated with the calculated overall reaction rate for each blend. The calculated overall reaction rate predicts that, for the candidate blends, the effect of humidity in the air will be small for an increase from 0 to 50 % r.h., but large for 50 % r.h. to 100 % r.h. Thus, levels of humidity above 0.014 moles H₂O/mole air (50 % r.h. at 23 °C) may have large effects on the flammability of the blends.

HFC-134a should be tested at high ambient temperature and high humidity as a benchmark.

We suggest live-fire tests of HFC-134a with increasing amounts of added HFO-1234yf to enable correlation to the small-scale experimental and numerical results. Once that is done, either explosion pressure tests or numerical calculations of overall reaction rate can be used for the candidate blends tested here (or new blends) to predict their behavior in the live-fire experiments. Finally, these candidate blends should be tested in the live-fire tests.

Task 3. Testing of Selected Blends in a Mini-Breadboard Heat Pump

The Mini-Breadboard Heat Pump (MBHP) was used to experimentally evaluate HFC-134a and four candidate low-GWP blends: R-513A, R-450A, R-515B, and Tern-1. The purpose of these tests was to: (1) validate the CYCLE_D-HX simulation model [10, 11] used in the limited-scope project [6], and (2) qualify the three “best” blends for testing in a military ECU (Task 7). Cycle performance of each fluid was measured over a range of capacity including (1.3, 1.5, and 1.7) kW, where 1.5 kW was the rating point. The varying capacity provided measurements to verify the model’s prediction ability over a range of mass and heat fluxes in the condenser and evaporator. Each capacity point was tested both without and with a liquid-line/suction-line heat exchanger (LLSL-HX). The test-to-test variation, largely driven by compressor efficiency, yielded representative average COP and Q_{vol} values with (0.5 to 1.0) % confidence intervals. No tests had excessive discharge temperatures or other hardware-related problems.

All 121 experimental tests were then simulated using CYCLE_D-HX. For R-513A, R-450A, and R-515B in the basic cycle (tests without the LLSL-HX), the model-predicted values were within the confidence intervals of the experimental results, within about ± 1.5 % of the curve fit. For Tern-1, the model overpredicted the experimental data by about 3 %. For the tests with the LLSL-HX, at 1.5 kW, the COP and Q_{vol} were overpredicted by (0 to 3) %. Importantly, the model provided the same relative COP and Q_{vol} ranking as the experimental data, giving confidence to the screening study performed in the limited-scope project.

Task 4. Refrigerant Forced-Convection Heat-Transfer Testing

An experimental apparatus was used to measure convective-boiling heat-transfer coefficients at 432 conditions for R-515B, R-450A, R-513A, and HFC-134a in a micro-fin tube. The measurements were used to develop an improved correlation for the local Nusselt number for the micro-fin tube. The new correlation predicted 82.8 % of the measured convective boiling Nusselt numbers for R-515B, R-450A, R-513A, and HFC-134a to within ± 20 %. The data taken and the new correlation were tailored for use in Task 7 of the project for simulations of the ECU system.

Task 5. Selection of three blends for testing in military ECU

We selected R-513A [R-134a/1234yf (44/56)*], Tern-1 [R-134a/1234yf/1234ze(E) (49.2/33.9/16.9)*], and R-515B [R-1234ze(E)/227ea (91.1/8.9)*] for ECU testing in the NIST environmental chambers. Each of these blends has the potential of being a fluid of choice depending on the weights applied to the selection criteria (GWP, COP, Q_{vol} , flammability characteristics). The main merits of R-513A (GWP = 573) and Tern-1 (GWP = 640) was their performance. For R-515B (GWP = 344), we made its selection based on its low GWP, which may gain in significance should fluids with a lower-GWP become mandated. In the above blend selection, we adopted the ASTM E681 test method as stipulated by ASHRAE Standard 34 for qualifying ‘non-flammability’ of refrigerants.

Task 7. Examination of Blend Performance in ECU

This task included experimental and simulation components. In the experimental effort, NIST procured, installed, and instrumented a 3-ton military ECU in the NIST environmental chambers and conducted performance tests according to the AHRI Standard 210/240 [73]. HFC-134a, R-513A, Tern-1, and R-515B were tested at the indoor condition of 26.7 °C drybulb and 15.8 °C dewpoint and four outdoor temperatures of 27.8 °C, 35.0 °C, 46.1 °C and 51.7 °C. These tests,

* Compositions stated as mass fraction (%)

referred to as “drop-in” tests, were conducted with the same heat exchangers and compressor for all fluids but included “soft optimization” of the ECU, which entailed a modification of the expansion device and optimization of the refrigerant charge.

Within the simulation effort, we extrapolated “drop-in” test results to evaluation of performance in a system with a compressor size adjusted for each fluid to achieve the same capacity at the rating point of 35.0 °C outdoor temperature. Compressor isentropic efficiencies for these simulations were calculated by the HFO-134a compressor map using the suction and discharge saturation temperatures established in a cycle for a given individual blend.

Based on laboratory measurements in the environmental chambers, Tern-1 and R-513A showed comparable performance to HFC-134a, with Tern-1 having 1 % to 2 % lower capacity and very close COP, within 2 %. R-513A had capacity higher than HFC-134a by 1 % to 5 %, and COP 4 % lower to 2% higher. R-515B provided lower capacity by as much as 17 % to 24 % and comparable COP to that of HFC-134a.

For ECUs equipped with a compressor to match the HFC-134a capacity at 35.0 °C, the performance of Tern-1 paralleled that of HFC-134a, with a small COP degradation of 1 % to 2 %. R-513A provided a similar performance at 27.8 °C, 35.0 °C outdoor temperatures and higher capacities at higher outdoor temperatures with a better COP than that of HFC-134a. R-515B provided a comparable capacity, but its COP was degraded by at least 10 %. Hence, the tested fluids present a range of choices which can be made depending on the importance of the low-GWP criteria. The above three blends provide the following approximate GWP reduction with respect to HFC-134a: Tern-1 – 51 %; R-513A – 66 %; R-515B – 74 %.

In conclusion, R-513A and Tern-1 are good replacement blends for HFC-134a offering GWP reduction of 66 % and 51 %, respectively. They do not present significant application difficulties.

If a greater reduction in GWP is desirable, R-515B (74 % GWP reduction) can be considered but it requires further research and developmental work. Exploratory simulations with carbon dioxide also indicated a need for significant developmental work to deliver competitive performance.

While all tested blends passed the ASTM E681 test method as stipulated by ASHRAE Standard 34 for qualifying “non-flammability” of refrigerants, some pass more easily than others, as determined from the other tests and modeling. There is a trade-off between “non-flammability” and GWP. If military requirements for “non-flammability” are more stringent than the E681 standard, the less flammable of the three (Tern-1 and R-513A) might still pass a more stringent criterion while R-515B would likely fail. Nonetheless, if the ASHRAE flammability criterion also meets the needs of the military, R-515B would be acceptable. If better flammability behavior than Tern-1 and R-513A is required, the less flammable blends identified in the earlier phase of the project would need to be selected and then tested experimentally to verify their performance and flammability; these compounds would have a smaller reduction of GWP although the GWP would still be about a factor of two lower than R-134a.

A live-fire test program in conjunction with modeling should be carried out to establish a representative test for assessing “non-flammability” for the military environment.

Literature Cited

- [1] EU (2014) Regulation (EU) No 517/2014 of the European Parliament and of the Council of 16 April 2014 on fluorinated greenhouse gases and repealing Regulation (EC) No 842/2006.
- [2] UNEP (2019) Handbook for the Montreal Protocol on Substances that Deplete the Ozone Layer. Ozone Secretariat United Nations Environment Programme 2019.
- [3] UN (2016) Kigali Amendment to the Montreal Protocol.
(<https://iifir.org/en/fridoc/amendment-to-the-montreal-protocol-on-substances-that-deplete-the-142049>).
- [4] US Congress (*American Manufacturing and Competitiveness (AIM), Section 103 of H.R. 133 (116th)*)
(AIM_Act_Section_103_of_H.R._133_Consolidated_Appropriations_Act_2021 (pdf), in Consolidated Appropriations Act 2021 (pp.1074-1090)).
- [5] McLinden MO, Brown JS, Brignoli R, Kazakov AF, Domanski PA (2017) Limited options for low-global-warming-potential refrigerants. *Nat Commun* 8.
<https://doi.org/https://doi.org/10.1038/ncomms14476>
- [6] Domanski PA, McLinden MO, Bell IH, Linteris GT (2018) Low-GWP Alternative Refrigerant Blends for HFC-134a. (NIST Technical Note 2014; National Institute of Standards and Technology, Gaithersburg, MD).
- [7] Bell IH, Domanski PA, McLinden MO, Linteris GT (2019) The hunt for nonflammable refrigerant blends to replace R-134a. *Int J Refrig* 104:484-495.
<https://doi.org/10.1016/j.ijrefrig.2019.05.035>
- [8] Lemmon E, Bell IH, Huber M, McLinden M (2018) NIST Standard Reference Database 23: Reference Fluid Thermodynamic and Transport Properties-REFPROP, Version 10.0, National Institute of Standards and Technology. *Standard Reference Data Program, Gaithersburg*.
- [9] Linteris G, Bell I, McLinden M (2019) An Empirical Model for Refrigerant Flammability Based on Molecular Structure and Thermodynamics. *International Journal of Refrigeration* 104:144-150. <https://doi.org/https://doi.org/10.1016/j.ijrefrig.2019.05.006>
- [10] Brown JS, Brignoli, R., Domanski, P.A., Yoon, Y.J. (2021) CYCLE_D-HX: NIST Vapor Compression Cycle Model Accounting for Refrigerant Thermodynamic and Transport Properties; Version 2.0 (National Institute of Standards and Technology, Gaithersburg, MD. <https://www.nist.gov/services-resources/software/cycled-hx-nist-vapor-compression-cycle-model-accounting-refrigerant-0>)
- [11] Brignoli R, Brown JS, Skye HM, Domanski PA (2017) Refrigerant performance evaluation including effects of transport properties and optimized heat exchangers. *Int J Refrig* 80:52-65. <https://doi.org/10.1016/j.ijrefrig.2017.05.014>
- [12] IPCC (2013) Climate Change 2013: The Physical Science Basis, Fifth Assessment Report of the Intergovernmental Panel on Climate Change. *Cambridge University Press, Cambridge*.
- [13] Linteris GT, Bell IH, McLinden MO (2019) An empirical model for refrigerant flammability based on molecular structure and thermodynamics. *International Journal of Refrigeration* 104:144-150.
- [14] Wagner W, Kleinrahm R (2004) Densimeters for very accurate density measurements of fluids over large ranges of temperature, pressure, and density. *Metrologia* 41:S24-S39.
- [15] McLinden MO, Lösch-Will C (2007) Apparatus for wide-ranging, high-accuracy fluid (p, ρ , T) measurements based on a compact two-sinker densimeter. *J Chem Thermodyn* 39:507-530.
- [16] Healy J, DeGroot JJ, Kestin J (1976) The theory of the transient hot-wire method for measuring the thermal conductivity. *Physica* C82:392-408.
- [17] Bell I, H. (2022) Mixture Models for Refrigerants R-1234yf/134a, R-1234yf/1234ze(E), and R-134a/1234ze(E) and Interim Models for R-125/1234yf, R-1234ze(E)/227ea, and

- R-1234yf/152a. *J Phys Chem Ref Data* 51:013103.
<https://doi.org/https://doi.org/10.1063/5.0086060>
- [18] Kestin J, Knierim K, Mason EA, Najafi B, Ro ST, Waldman M (1984) Equilibrium and Transport Properties of the Noble Gases and Their Mixtures at Low Density. *J Phys Chem Ref Data* 13:229-303. <https://doi.org/http://dx.doi.org/10.1063/1.555703>
- [19] Vesovic V, Wakeham WA (1989) Prediction of the viscosity of fluid mixtures over wide ranges of temperature and pressure. *Chem Eng Science* 44:2181-2189.
- [20] Di Pippo R, Dorfman R, Kestin J, Khalifa HE, Mason EA (1977) Composition dependence of the viscosity of dense gas mixtures. *Physica A* 86:205-223.
[https://doi.org/https://doi.org/10.1016/0378-4371\(77\)90029-2](https://doi.org/https://doi.org/10.1016/0378-4371(77)90029-2)
- [21] Neufeld PD, Janzen AR, Aziz RA (1972) Empirical equations to calculate 16 of the transport collision integrals $\Omega(l,s)^*$ for the Lennard-Jones (12-6) potential. *J Chem Phys* 57:1100-1102.
- [22] Klein SA, McLinden MO, Laesecke A (1997) An improved extended corresponding states method for the estimation of viscosity of pure refrigerants and mixtures. *Int J Refrig* 20(3):208-217.
- [23] Huber ML, Laesecke A, Perkins RA (2003) Model for the Viscosity and Thermal Conductivity of Refrigerants, Including a New Correlation for the Viscosity of R134a. *Ind Eng Chem Res* 42(13):3163-3178. <https://doi.org/doi:10.1021/ie0300880>
- [24] Chichester JC, Huber ML (2008) Documentation and Assessment of the Transport Property Models for Mixtures Implemented in NIST REFPROP (Version 8.0), NISTIR 6650. (National Institute of Standards and Technology), June 2008 Ed.
- [25] Akhfash M, Al Ghafri SZS, Rowland D, Hughes TJ, Tsuji T, Tanaka Y, Seiki Y, May EF (2019) Liquid and Vapor Viscosities of Binary Refrigerant Mixtures Containing R1234yf or R1234ze(E). *J Chem Eng Data* 64(3):1122-1130.
<https://doi.org/10.1021/acs.jced.8b01039>
- [26] Mylona SK, Hughes TJ, Saeed AA, Rowland D, Park J, Tsuji T, Tanaka Y, Seiki Y, May EF (2019) Thermal conductivity data for refrigerant mixtures containing R1234yf and R1234ze(E). *J Chem Thermodyn* 133:135-142. <https://doi.org/10.1016/j.jct.2019.01.028>
- [27] McLinden MO, Klein SA, Perkins RA (2000) An extended corresponding states model for the thermal conductivity of refrigerants and refrigerant mixtures. *Int J Refrig* 23:43-63.
- [28] Ely JF, Hanley HJM (1983) Prediction of transport properties. 2. Thermal conductivity of pure fluids and mixtures. *Ind Eng Chem Fundam* 22(1):90-97.
- [29] Olchowy GA, Sengers JV (1989) A Simplified Representation for the Thermal Conductivity of Fluids in the Critical Region. *Int J Thermophys* 10:417-426.
<https://doi.org/doi:10.1007/BF01133538>
- [30] Perkins RA, Sengers JV, Abdulagatov IM, Huber ML (2013) Simplified model for the critical thermal-conductivity enhancement in molecular fluids *Int J Thermophys* 34(2):191-212. <https://doi.org/doi:10.1007/s10765-013-1409-z>
- [31] Williams FA (1974) A unified view of fire suppression. *J Fire Flamma* 5:54-63.
- [32] Davis SG, Pagliaro JL, Debold TF, van Wingerden M, van Wingerden K (2017) Flammability and explosion characteristics of mildly flammable refrigerants. *Journal of Loss Prevention in the Process Industries* 49:662-674.
<https://doi.org/https://doi.org/10.1016/j.jlp.2017.05.019>
- [33] ASHRAE (2019)– *ANSI/ASHRAE Standard 34-2019, Designation and Safety Classification of Refrigerants* (American Society of Heating, Refrigerating and Air-Conditioning Engineers, Atlanta, GA).
- [34] Papas P, Verma P, Lord R, Burns L (2019) Turbulent deflagrations of mildly flammable refrigerant-air mixtures. *Journal of Loss Prevention in the Process Industries* 61:255-261.
<https://doi.org/https://doi.org/10.1016/j.jlp.2019.07.005>
- [35] Linteris GT, Babushok VI, Pagliaro JL, Burgess JDR, Manion JA, Takahashi F, Katta VR, Baker PT (2016) Understanding overpressure in the FAA aerosol can test by

- $C_3H_2F_3Br$ (2-BTP). *Combust Flame* 167:452-462.
<https://doi.org/http://dx.doi.org/10.1016/j.combustflame.2015.10.022>
- [36] Linteris G, Pagliaro JL, Sunderland PB (2016) Test Results Prepared for Honeywell: Igniter Material Effects in the Japanese High Pressure Gas Law Test. (National Institute of Standards and Technology, Gaithersburg, MD), NIST Technical Note 1902.
<https://doi.org/http://dx.doi.org/10.6028/NIST.TN.1902>
- [37] ASHRAE (2019) ANSI/ASHRAE Standard 34-2019, Designation and Safety Classification of Refrigerants. (American Society of Heating, Refrigerating and Air-Conditioning Engineers, Atlanta, GA).
- [38] ISO (2017) International Organization for Standardization (ISO-817): Refrigerants—Designation and safety classification. (Geneva, Switzerland).
- [39] ASTM (2015) ASTM E681-09: Standard test method for concentration limits of flammability of chemicals (vapors and gases). *ASTM Fire Standards*, (American Society of Testing and Materials, West Conshohocken, PA), Sixth Ed.
- [40] Richard RG (2011) *Personal Communication*.
- [41] Richard RG, Kannoy D, Kusmierz A (2017) Binary Refrigerant Flame Boundary Concentrations (ASHRAE Research Project 1507-RP Final Report). (ASHRAE, Atlanta, GA).
- [42] Kim DK, Klieger AE, Lomax PQ, McCoy CG, Reymann JY, Sunderland PB (2018) An improved test method for refrigerant flammability limits in a 12 L vessel. *Sci Technol Built Environ* 24(8):861-866. <https://doi.org/10.1080/23744731.2018.1434381>
- [43] Richard RG (1998) Refrigerant flammability testing in large volume vessels. (Allied Signal Buffalo Research Laboratories, Buffalo, NY), DOE/CE/23810-87, March 1998.
- [44] Kelley AP, Jomaas G, Law CK (2009) Critical radius for sustained propagation of spark-ignited spherical flames. *Combust Flame* 156(5):1006-1013.
- [45] Berger L, Hesse R, Kleinheinz K, Hegetschweiler MJ, Attili A, Beeckmann J, Linteris GT, Pitsch H (2020) A DNS study of the impact of gravity on spherically expanding laminar premixed flames. *Combust Flame* 216:412-425.
<https://doi.org/https://doi.org/10.1016/j.combustflame.2020.01.036>
- [46] Pagliaro JL (2015) Inhibition of laminar premixed flames by Halon 1301 alternatives. (University of Maryland, College Park, MD), Ph.D. Thesis, 2015.
<https://doi.org/https://doi.org/10.13016/M27W7F>
- [47] Pagliaro JL, Linteris GT, Sunderland PB, Baker PT (2015) Combustion inhibition and enhancement of premixed methane-air flames by halon replacements. *Combust Flame* 162(1):41-49. <https://doi.org/10.1016/j.combustflame.2014.07.006>
- [48] Linteris GT, Pagliaro JL (2016) Burning Velocity Measurements and Simulations for Understanding the Performance of Fire Suppressants in Aircraft. (National Institute of Standards and Technology, Gaithersburg, MD), NIST TN 1904, 2016.
<https://doi.org/http://dx.doi.org/10.6028/NIST.TN.1904>
- [49] Linteris GT, Pagliaro JL (2011) Test results prepared for Honeywell: Flammability of refrigerants in the Japanese high pressure gas law test. (Gaithersburg MD), NISTIR 7178, 10/05/2011.
- [50] Chen Z, Burke MP, Ju Y (2011) On the critical flame radius and minimum ignition energy for spherical flame initiation. *Proc Combust Inst* 33(1):1219-1226.
<https://doi.org/https://doi.org/10.1016/j.proci.2010.05.005>
- [51] Goodwin DG, Moffat HK, Speth RL (2016) Cantera: An object-oriented software toolkit for chemical kinetics, thermodynamics, and transport processes. <http://www.cantera.org>, Version 2.1.1. (California Institute of Technology, Pasadena, CA), Vol. 2016.
- [52] Peters N (2000) *Turbulent Combustion* (Cambridge University Press, Cambridge).
- [53] Hansen OR, Hinze P, Engel D, Davis S (2010) Using computational fluid dynamics (CFD) for blast wave predictions. *Journal of Loss Prevention in the Process Industries* 23(6):885-906. <https://doi.org/10.1016/j.jlpi.2010.07.005>

- [54] Hisken H, Enstad G, Middha P, van Wingerden K (2015) Investigation of concentration effects on the flame acceleration in vented channels. *Journal of Loss Prevention in the Process Industries* 36:447-459.
- [55] Linteris GT, Burgess DR, Babushok V, Zachariah M, Tsang W, Westmoreland P (1998) Inhibition of premixed methane-air flames by fluoroethanes and fluoropropanes. *Combust Flame* 113(1-2):164-180.
- [56] Linteris GT, Truett L (1996) Inhibition of premixed methane-air flames by fluoromethanes. *Combust Flame* 105(1-2):15-27. [https://doi.org/Doi.10.1016/0010-2180\(95\)00152-2](https://doi.org/Doi.10.1016/0010-2180(95)00152-2)
- [57] Katta VR, Takahashi F, Linteris GT (2006) Fire-suppression characteristics of CF₃H in a cup burner. *Combust Flame* 144(4):645-661. <https://doi.org/10.1016/j.combustflame.2005.09.006>
- [58] Babushok VI, Linteris GT, Meier O (2012) Combustion properties of halogenated fire suppressants. *Combust Flame* 159:3569-3575.
- [59] Linteris GT, Burgess DR, Takahashi F, Katta VR, Chelliah HK, Meier O (2012) Stirred reactor calculations to understand unwanted combustion enhancement by potential halon replacements. *Combust Flame* 159(3):1016-1025. <https://doi.org/10.1016/j.combustflame.2011.09.011>
- [60] Pagliaro JL, Bouvet N, Linteris GT (2016) Premixed flame inhibition by CF₃Br and C₃H₂F₃Br (2-BTP). *Combust Flame* 169:272-286. <https://doi.org/http://dx.doi.org/10.1016/j.combustflame.2016.04.017>
- [61] Takahashi F, Katta VR, Linteris GT, Babushok VI (2015) Combustion inhibition and enhancement of cup-burner flames by CF₃Br, C₂HF₅, C₂HF₃Cl₂, and C₃H₂F₃Br. *Proc Combust Inst* 35:2741-2748. <https://doi.org/10.1016/j.proci.2014.05.114>
- [62] Takahashi F, Katta VR, Linteris GT, Meier OC (2013) Cup-burner flame structure and extinguishment by CF₃Br and C₂HF₅ in microgravity. *Proc Combust Inst* 34:2707-2717.
- [63] Linteris GT, Babushok VI, Sunderland PB, Takahashi F, Katta VR, Meier O (2013) Unwanted combustion enhancement by C₆F₁₂O fire suppressant. *Proc Combust Inst* 34:2683-2690. <https://doi.org/10.1016/j.proci.2012.06.050>
- [64] Burgess Jr DR, Zachariah MR, Tsang W, Westmoreland PR (1995) Thermochemical and Chemical Kinetic Data for Fluorinated Hydrocarbons. (National Institute of Standards and Technology, Gaithersburg, MD), NIST Technical Note 1412.
- [65] Burgess DR, Babushok VI, Linteris GT, Manion JA (2015) A Chemical Kinetic Mechanism for 2-Bromo-3,3,3-trifluoropropene (2-BTP) Flame Inhibition. *Int J Chem Kinet* 47(9):533-563. <https://doi.org/doi:10.1002/kin.20923>
- [66] Babushok VI, Burgess DR, Kim DK, Hegetschweiler MJ, Linteris GT (2021) Kinetic Model for Refrigerant-Air Flames. (National Institute of Standards and Technology, Gaithersburg, MD), NIST Technical Note xxxx, 2021.
- [67] Linteris GT, Babushok VI (2020) Laminar burning velocity predictions for C₁ and C₂ hydrofluorocarbon refrigerants with air. *J Fluorine Chem* 230. <https://doi.org/https://doi.org/10.1016/j.jfluchem.2019.05.002>
- [68] Babushok VI, Burgess DR, Hegetschweiler MJ, Linteris GT (2020) Flame propagation in the mixtures of O₂/N₂ oxidizer with fluorinated propene refrigerants (CH₂CFCF₃, CHFCHCF₃, CH₂CHCF₃). *Combust Sci Technol*:1-24. <https://doi.org/10.1080/00102202.2020.1720663>
- [69] Hegetschweiler MJ, Linteris GT (2021) Data Reduction Tool for Spherical Constant Volume Flame Experiments. (National Institute of Standards and Technology, Gaithersburg, MD), NIST Technical Note in preparation.
- [70] Kim DK, Babushok VI, Burgess DR, Hegetschweiler MJ, Linteris GT (2020) Burning Velocity of Blends of R-152a with R-134a or R-1234yf and air. *Combust Sci Technol*:to be submitted.
- [71] Barat RB (2001) Correlating laminar burning velocities using perfectly stirred reactor theory. *Chem Eng Sci* 56:2761-2766.

- [72] Skye HM (2015) Heat Pump Test Apparatus for the Evaluation of Low Global Warming Potential Refrigerants. (NIST Technical Note 1895, National Institute of Standards and Technology, Gaithersburg, MD). <https://doi.org/https://doi.org/10.6028/NIST.TN.1895>
- [73] AHRI (2017)– *210/240-2017 Standard for Performance Rating of Unitary A/C and Air Source Heat Pump Equipment* (Arlington, VA).
- [74] McLinden MO , Radermacher R (1987) Methods for comparing the performance of pure and mixed refrigerants in the vapour compression cycle. *International Journal of Refrigeration* 10(6):318-325.
- [75] Kedzierski MA , Park KJ (2013) Horizontal Convective Boiling of R134a, R1234yf/R134a, and R1234ze(E) within a Micro-Fin Tube. *J Enhanc Heat Transf* 20(4):333-346. <https://doi.org/DOI.10.1615/JEnhHeatTransf.2014010579>
- [76] Kattan N, Thome JR, Favrat D (1995) R-502 and two near-azeotropic alternatives. Part 1: In-tube flow-boiling tests. *ASHRAE Transactions* 101(1):491-508.
- [77] Hamilton L, Kedzierski M, Kaul M (2008) Horizontal convective boiling of pure and mixed refrigerants within a micro-fin tube. *J Enhanc Heat Transf* 15(3).
- [78] Kedzierski MA , Kang D (2018) Horizontal convective boiling of R1234yf, R134a, and R450A within a micro-fin tube. *Int J Refrig* 88:538-551. <https://doi.org/10.1016/j.ijrefrig.2018.02.021>
- [79] Kedzierski MA, Lin L, Kang D (2018) Pool Boiling of Low-Global Warming Potential Replacements for R134a on a Reentrant Cavity Surface. *J Heat Trans-T Asme* 140(12). <https://doi.org/https://doi.org/10.1115/1.4040783>
- [80] Solomon S, Burkholder JB, Ravishankara AR, Garcia RR (1994) Ozone depletion and global warming potentials of CF₃I. *J Geo Res Atmospheres* 99:20929-20935. <https://doi.org/https://doi.org/10.1029/94JD01833>
- [81] Bell IH , McLinden MO (2020) The status of thermodynamic data and models for CF₃I and its mixtures. *Int J Thermopysics* 41:134. <https://doi.org/10.1007/s10765-020-02712-w>
- [82] Yang Z, Liu H, Wu X (2012) Theoretical and experimental study of the inhibition and inert effect of HFC125, HFC227ea and HFC131I on the flammability of HFC32. *Process Safety and Environmental Protection* 90:311–316.
- [83] Yana Motta SF (2018) Submission to ASHRAE SSPC 34 Committee. Request for Refrigerant Designation and Safety Classification For R-32/R-125/CF₃I (49.0/11.5/39.5 % by mass) Zeotropic Refrigerant Blend. (Honeywell International, Inc., Buffalo, NY).
- [84] ASHRAE (2019)– *Addendum t to Standard 34-2019, Designation and Safety Classification of Refrigerants* (American Society of Heating, Refrigerating and Air-Conditioning Engineers).
- [85] National Research Council (*Iodotrifluoromethane: Toxicity Review (2004)*) (Washington, DC: The National Academies Press).
- [86] Allgood C, Johnston P, Kim S, Kujak S, Yana Motta S (2021) Roundtable: A conversation on refrigerants. *ASHRAE J* March 2021:30-37.
- [87] Kujak S, Sorenson, E. (2021) Accelerated equipment reliability evaluation of R-131I (CF₃I) in R-466A. *2nd IIR Conference on HFOs and Low GWP blends* (Int. Institute of Refrigeration, Paris, France).
- [88] Akasaka R, Fukuda S, Sakoda N, Higashi Y (2020) *pvT* Property measurement and development of an equation of state for new refrigerant HFO1132(E). *Proceedings of the 2020 JSRAE Annual Conference*.
- [89] Perera UA, Miyazaki T, Sakoda N, Higashi Y (2020) Determination of saturation pressure and critical pressure for new refrigerant HFO1132(E). *Proceedings of the 2020 JSRAE Annual Conference*.
- [90] McLinden MO, Brown JS, Brignoli R, Kazakov AF, Domanski PA (2017) Limited options for low-global-warming-potential refrigerants. *Nat Comm* 8:14476. <https://doi.org/10.1038/ncomms14476>

- [91] Domanski PA, Brown JS, Lemmon EW (2018) CYCLE_D: NIST Vapor Compression Cycle Design Program, Version 6.0. (National Institute of Standards and Technology, Gaithersburg, MD).
- [92] Domanski PA, Yashar DA, Wojtusiak J (2021) EVAP-COND, Version 5.0; Simulation Models for Finned-Tube Heat Exchangers with Circuitry Optimization (National Institute of Standards and Technology, Gaithersburg, MD,
- [93] Domanski PA, Yashar DA, Lee S, Wojtusiak J (2011) Practical Aspects of Applying Evolutionary Algorithms for Optimizing Refrigerant Circuitry in Heat Exchangers. *Congres Int Froid* 23:2664-+.
- [94] Yoon SH, Kim JH, Hwang YW, Kim MS, Min K, Kim Y (2003) Heat transfer and pressure drop characteristics during the in-tube cooling process of carbon dioxide in the supercritical region. *International journal of refrigeration* 26(8):857-864.
- [95] Outcalt SL, Lemmon EW (2013) Bubble point measurements of eight binary mixtures for organic rankine cycle applications. *J Chem Engr Data* 58:1853-1860.
- [96] Hust JG, Filla J, Smith DR (1987) A modified digital PID temperature controller for thermal property measurements. *Journal of Thermal Insulation* 11(10):102-107.
- [97] McLinden MO, Kleinrahn R, Wagner W (2007) Force transmission errors in magnetic suspension densimeters. *Int J Thermophys* 28:429-448.
- [98] McLinden MO, Richter M (2016) Application of a two-sinker densimeter for phase-equilibrium measurements: A new technique for the detection of dew points and measurements on the (methane + propane) System. *J Chem Thermodyn* 99:105-115. <https://doi.org/10.1016/j.jct.2016.03.035>
- [99] McLinden MO, Splett JD (2008) A liquid density standard over wide ranges of temperature and pressure based on toluene. *J Res Natl Inst Stand Technol* 113:29-67.
- [100] McLinden MO (2009) Thermodynamic properties of propane. I. p- ρ -T behavior from 265 K to 500 K with pressures to 36 MPa. *J Chem Eng Data* 54:3181-3191.
- [101] Lemmon EW, McLinden MO, Wagner W (2009) Thermodynamic properties of propane. III. A Reference Equation of State for Temperatures from the Melting Line to 650 K and Pressures up to 1000 MPa. *Journal of Chemical and Engineering Data* 54:3141-3180.
- [102] Meier K, Kabelac S (2012) Thermodynamic Properties of Propane. IV. Speed of Sound in the Liquid and Supercritical Regions. *J Chem Engr Data* 57:3391-3398. <https://doi.org/10.1021/je300466a>
- [103] Dealy JM (1982) *Rheometers for Molten Plastics* (Van Norstrand Reinhold, New York, NY).
- [104] Laesecke A, Junker C, Lauria DS (2018) Viscosity Measurements of Three Base Oils and One Fully Formulated Lubricant and New Viscosity Correlations for the Calibration Liquid Squalane. *J Res NIST* (submitted).
- [105] Huber ML, Laesecke A, Perkins RA (2003) Model for the viscosity and thermal conductivity of refrigerants, including a new correlation for the viscosity of R134a. *Ind Eng Chem Res* 42:3163-3178.
- [106] Roder HM (1981) A transient hot wire thermal conductivity apparatus for fluids. *J Res Natl Bur Stand* 86(5):457-493.
- [107] Healy JJ, de Groot JJ, Kestin J (1976) The theory of the transient hot-wire method for measuring thermal conductivity. *Physica* 82:392-408.
- [108] Rowane AJ, Bell IH, Huber ML, Perkins RA (2022) Thermal conductivity of binary mixtures of 1,1,1,2-tetrafluoroethane, 2,3,3,3-tetrafluoropropene, and 1,3,3,3-tetrafluoropropene refrigerants. *Ind Eng Chem Res* (submitted).
- [109] Harris GL, Torres JA (2003) Selected laboratory and measurement practices and procedures, to support basic mass calibrations. (National Institute of Standards and Technology), NISTIR 6969.
- [110] Richter M, McLinden MO (2014) Vapor-phase (p, ρ , T, x) behavior and virial coefficients for the (methane + propane) system. *J Chem Eng Data* 59:4151-4164. <https://doi.org/10.1021/je500792x>

- [111] Bell IH, Lemmon EW (2016) Automatic Fitting of Binary Interaction Parameters for Multi-fluid Helmholtz-Energy-Explicit Mixture Models. *J Chem Eng Data* 61(11):3752–3760–3752–3760.
- [112] Ely JF, Hanley HJM (1981) Prediction of transport properties. 1. Viscosity of fluids and mixtures. *Ind Eng Chem Fundam* 20(4):323–332.
- [113] Ely JF (1984) Application of the Extended Corresponding States Model to Hydrocarbon Mixtures. *Proceedings of the 63rd Annual Gas Processors Association Meeting*, pp 9–22.
- [114] Hirschfelder JO, Curtiss CF, Bird RB (1964, 1954) *Molecular theory of gases and liquids* (Wiley, New York), Corr. print. with notes attached Ed., p 1249.
- [115] Bi S, Cui J, Zhao G, Wu J (2016) Surface tension and liquid viscosity measurement for binary mixtures of R134a with R1234yf and R1234ze(E). *Fluid Phase Equilib* 414:60–64.
- [116] Yang X, Arami-Niya A, Xiao X, Kim D, Al Ghafri SZS, Tsuji T, Tanaka Y, Seiki Y, May EF (2020) Viscosity Measurements of Binary and Multicomponent Refrigerant Mixtures Containing HFC-32, HFC-125, HFC-134a, HFO-1234yf, and CO₂. *J Chem Eng Data* 65:4252–4262.
- [117] Liang X, Sun Q, Meng X, Wu J (2022 (in press)) Liquid Viscosity Measurements for the Binary and Ternary Refrigerant Mixtures of R134a, R1234ze(E), and R1234yf. *J Chem Eng Data*.
- [118] Kim D, Yang X, Arami-Niya A, Rowland D, Xiao X, Al Ghafri SZS, Tsuji T, Tanaka Y, Seiki Y, May EF (2020) Thermal conductivity data for refrigerant mixtures containing R1234yf and R1234ze(E). *J Chem Thermodyn* 133:135–142.
- [119] Mylona SK, Hughes TJ, Saeed AA, Rowland D, Park J, Tsuji T, Tanaka Y, Seiki Y, May EF (2019) Thermal conductivity data for refrigerant mixtures containing R1234yf and R1234ze(E). *J Chem Thermodyn* 133:135–142. <https://doi.org/10.1016/j.jct.2019.01.028>
- [120] Akhflash M, Al Ghafri SZS, Rowland D, Hughes TJ, Tsuji T, Tanaka Y, Seiki Y, May EF (2019) Liquid and Vapor Viscosities of Binary Refrigerant Mixtures Containing R1234yf or R1234ze(E). *J Chem Eng Data* 64(3):1122–1130. <https://doi.org/10.1021/acs.jced.8b01039>
- [121] Rosenfeld Y (1977) Relation between the transport coefficients and the internal entropy of simple systems. *Phys Rev A* 15:2545–2549–2545–2549.
- [122] Bell IH, Messerly R, Thol M, Costigliola L, Dyre J (2019) Modified Entropy Scaling of the Transport Properties of the Lennard-Jones Fluid. *J Phys Chem B* 123(29):6345–6363–6345–6363.
- [123] Bell IH (2020) Entropy Scaling of Viscosity – I: A Case Study of Propane. *J Chem Eng Data*:3203–3215–3203–3215.
- [124] Bell IH (2020) Entropy Scaling of Viscosity—II: Predictive Scheme for Normal Alkanes. *J Chem Eng Data* 65(11):5606–5616–5606–5616.
- [125] Yang X, Xiao X, May EF, Bell IH (2021) Entropy Scaling of Viscosity—III: Application to Refrigerants and Their Mixtures. *J Chem Eng Data*.
- [126] Liu H, Yang F, Yang Z, Duan Y (2020) Modeling the viscosity of hydrofluorocarbons, hydrofluoroolefins and their binary mixtures using residual entropy scaling and cubic-plus-association equation of state. *J Mol Liq* 308:113027–113027.
- [127] Lötgering-Lin O, Gross J (2015) Group Contribution Method for Viscosities Based on Entropy Scaling Using the Perturbed-Chain Polar Statistical Associating Fluid Theory. *Ind Eng Chem Res* 54(32):7942–7952–7942–7952.
- [128] Lötgering-Lin O, Fischer M, Hopp M, Gross J (2018) Pure Substance and Mixture Viscosities Based on Entropy Scaling and an Analytic Equation of State. *Ind Eng Chem Res* 57(11):4095–4114–4095–4114.
- [129] Fouad WA, Alasiri H (2020) Molecular dynamic simulation and SAFT modeling of the viscosity and self-diffusion coefficient of low global warming potential refrigerants. *J Mol Liq* 317:113998–113998.
- [130] Bell IH, Dyre JC, Ingebrigtsen TS (2020) Excess-entropy scaling in supercooled binary mixtures. *Nature Communications* 11(1).

- [131] Kondo S, Takizawa K, Takahashi A, Tokuhashi K, Sekiya A (2009) Flammability limits of five selected compounds each mixed with HFC-125. *Fire Saf J* 44(2):192-197. <https://doi.org/DOI.10.1016/j.firesaf.2008.06.001>
- [132] Shebeko YN, Azatyan VV, Bolodian IA, Navzenya VY, Kopyov SN, Shebeko DY, Zamishevski ED (2000) The influence of fluorinated hydrocarbons on the combustion of gaseous mixtures in a closed vessel. *Combust Flame* 121(3):542-547.
- [133] Pagliaro JL, Linteris GT, Babushok VI (2016) Premixed flame inhibition by C₂HF₃Cl₂ and C₂HF₅. *Combust Flame* 163:54-65. <https://doi.org/http://dx.doi.org/10.1016/j.combustflame.2015.08.015>
- [134] Shephard JE, Krok JC, Lee JJ (1999) Spark Ignition Energy Measurements in Jet A. (Calif. Inst. Tech).
- [135] Metghalchi M, Keck JC (1980) Laminar burning velocity of propane-air mixtures at high temperature and pressure. *Combust Flame* 38:143-154.
- [136] Metghalchi M, Keck JC (1982) Burning velocities of mixtures of air with methanol, isooctane, and indolene at high pressure and temperature. *Combust Flame* 48:191-210.
- [137] Hill PG, Hung J (1988) Laminar Burning Velocities of Stoichiometric Mixtures of Methane with Propane and Ethane Additives. *Combustion Science and Technology* 60:7-30.
- [138] Takizawa K, Takahashi A, Tokuhashi K, Kondo S, Sekiya A (2005) Burning velocity measurement of fluorinated compounds by the spherical-vessel method. *Combust Flame* 141(3):298-307. <https://doi.org/10.1016/j.combustflame.2005.01.009>
- [139] Lewis B, von Elbe G (1961) *Combustion, Flames, and Explosions of Gases*.
- [140] Saeed K, Stone CR (2004) Measurements of the laminar burning velocity for mixtures of methanol and air from a constant-volume vessel using a multizone model. *Combustion and Flame* 139(1-2):152-166. <https://doi.org/10.1016/j.combustflame.2004.08.008>
- [141] Eisazadeh-Far K, Moghaddas A, Al-Mulki J, Metghalchi H (2011) Laminar burning speeds of ethanol/air/diluent mixtures. *Proc Combust Inst* 33(1):1021-1027. <https://doi.org/10.1016/j.proci.2010.05.105>
- [142] Williams FA (1975) A review of some theoretical considerations of turbulent flame structure. *AGARD Conference Proceeding*.
- [143] Takizawa K, Takahashi A, Tokuhashi K, Kondo S, Sekiya A (2006) Burning velocity measurement of HFC-41, HFC-152a, and HFC-161 by the spherical-vessel method. *J Fluorine Chem* 127(12):1547-1553. <https://doi.org/10.1016/j.jfluchem.2006.07.013>
- [144] Marshall SP, Taylor S, Stone CR, Davies TJ, Cracknell RF (2011) Laminar burning velocity measurements of liquid fuels at elevated pressures and temperatures with combustion residuals. *Combustion and Flame* 158(10):1920-1932. <https://doi.org/10.1016/j.combustflame.2011.02.016>
- [145] Babushok VI, Burgess Jr DR, Kim DK, Hegetschweiler MJ, Linteris GT (2021) Modeling of Combustion of Fluorine-Containing Refrigerants. (National Institute of Standards and Technology, Gaithersburg, MD), NIST Technical Note in preparation.

Appendix A: Details of Experiments and Modeling

A.1. Task 1 - Details of Thermophysical Properties Measurements and Modeling

A schematic of the instrument used to make the measurements is shown in Figure A.1-1; it is an updated version of the instrument described by Outcalt and Lemmon.[95] The heart of the instrument was a cylindrical stainless steel measuring cell with a sapphire window on each end so that the liquid level in the cell was visible. The cell had an internal volume of approximately 30 mL. The operating range of the apparatus was 270 K to 360 K, with pressures to 7 MPa.

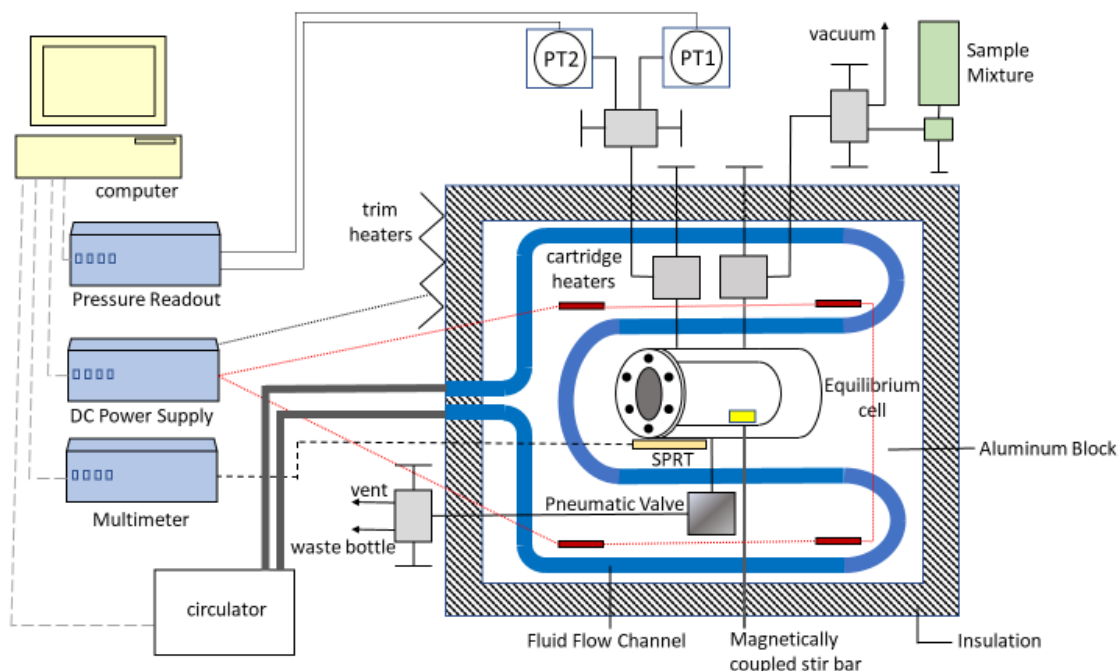


Figure A.1-1. Schematic of instrument for vapor liquid equilibria measurements. Main components include a stainless steel equilibrium cell housed in a thermostated aluminum block, standard platinum resistance thermometer (SPRT), and two oscillating quartz crystal pressure transducers (PT1 and PT2) with maximum pressure ranges of 0.7 MPa and 7 MPa.

The cell was fitted inside a temperature-controlled, insulated aluminum block. The valves for filling the system were installed in the aluminum block to limit the sample volume outside the temperature-controlled zone. Cooling fluid from an external refrigerated circulator flowed through channels drilled into the aluminum block. Cartridge heaters installed in the aluminum block provided heat for operation above ambient temperature. Thin-film type heaters were adhered to the outside of the block for fine control of the temperature. Temperature control was automated with the modified PID algorithm of Hust et al.[96]

Temperature was measured with a standard platinum resistance thermometer (SPRT) installed in a thermowell adjacent to the measuring cell. The pressure was measured with one of two oscillating-quartz-crystal pressure transducers connected to the system through one of the ports at the top of the cell. These transducers had full-scale ranges of 0.7 MPa and 7.0 MPa; the low-

range transducer had the higher sensitivity, and it was used whenever possible. The transducers were thermostatted in separate thermostats maintained at 313 K.

For loading, the sample bottle was connected to the system in an inverted position so that the liquid phase was loaded into the cell. Prior to loading a sample into the system, the system was evacuated and cooled to approximately 270 K, and the pressure reading under vacuum was recorded. The sample was then quickly loaded into the system until only a small vapor space remained in the equilibrium cell. Stirring of the sample was effected by a stir bar inside the cell that was magnetically coupled to an external motor.

By loading the sample from the liquid phase of the sample bottle and filling the measuring cell nearly full, the liquid-phase composition in the cell was nearly that of the bulk composition of the sample bottle. Small corrections to the composition were made using the mixture model in REFPROP and assuming equilibrium between the liquid and vapor phases in both the sample bottle and measuring cell.

Measurements commenced at 270 K. After temperature and pressure equilibrium were obtained, the conditions were recorded. The temperature was then increased by an increment of 10 K. As the temperature was increased, the liquid expanded, eventually filling the cell with compressed liquid. As a result it was necessary to periodically release a small amount of liquid from the bottom of the cell to maintain a vapor space; this was done by opening a pneumatically actuated valve. Repeat measurements were conducted at a minimum of two temperatures. These repeats established the repeatability of the measurements and also helped to determine whether the loss of small amounts of the liquid phase affected the sample composition to the extent that duplicate measurements at a given temperature yielded different bubble-point pressures. In almost all instances this was not the case.

The principal sources of uncertainty in these measurements arose from the measurement of temperature, pressure, and sample composition as well as repeatability of the measurements. The SPRT was calibrated with fixed-point cells, and the standard ($k = 1$) uncertainty in temperature, including calibration, repeatability and possible temperature gradients was estimated to be 20 mK. The pressure transducers were calibrated with a piston gage, and the zero of the transducers was regularly checked. The uncertainty in the pressure was 0.005 % of the full-scale pressure (i.e., 0.035 kPa or 0.35 kPa for the two transducers). As described in section A.1.6, the uncertainty in the composition due to the weighings was less than 0.0001 mole fraction. Because of the two-phase nature of the liquid-phase samples and because the weighings could determine only the overall (bulk) composition of the sample, it was necessary to estimate the change in composition caused by the liquid/vapor fractionation inside the cylinder. This change was less than 0.0005 mole fraction, and its standard uncertainty was estimated to be less than 0.0001 mole fraction. Thus, the combined, expanded uncertainty in composition of the liquid-phase samples was estimated to be less than 0.00028 mole fraction. In addition to these uncertainties, the standard deviation in repeat measurements were added in quadrature to arrive at the overall uncertainty, which is stated in the tables of VLE data presented below.

For all of the property measurements presented here deviations of the experimental data from the models developed in this project are expressed as relative deviations:

$$\Delta x = 100 \cdot (x_{\text{exp}} - x_{\text{EOS}}) / x_{\text{EOS}} \quad (\text{A.1-1})$$

where Δx is the relative deviation, x_{exp} is a measured property, and x_{EOS} is the value predicted by the model.

Table A.1-1. Measured vapor-liquid equilibria (VLE) data for the system R-1234yf/134a at a molar composition of (0.320/0.680)

Listed for Tables A.1-1 through A.1-12 are temperature T , bubble-point pressure p_{bub} , combined expanded ($k = 2$) state point uncertainty in the bubble-point pressure U_c , and relative deviation from the mixture EOS Δp_{bub} . The standard uncertainty in temperature is 20 mK, and the standard uncertainty in composition is 0.00028 mole fraction. Two replicate measurements are given for most temperatures.

T/K	$p_{\text{bub}}/\text{kPa}$	$U_c/\%$	$\Delta p_{\text{bub}}/\%$
269.99	282.7	0.83	-0.108
279.99	399.3	0.61	-0.152
279.99	399.6	0.61	-0.077
289.99	549.3	0.47	-0.204
289.99	549.6	0.47	-0.150
299.99	739.7	0.36	-0.080
299.99	739.8	0.36	-0.067
309.99	975.1	0.29	-0.057
309.99	974.5	0.29	-0.118
319.99	1262.0	0.23	-0.085
319.99	1261.8	0.23	-0.101
329.99	1609.3	0.19	-0.028
329.99	1608.6	0.19	-0.072
339.99	2024.3	0.16	0.028
339.99	2023.2	0.16	-0.026
349.99	2516.9	0.11	0.097
349.99	2515.1	0.11	0.026
359.99	3098.6	0.10	0.139
359.99	3095.7	0.10	0.045

Table A.1-2. Measured vapor-liquid equilibria (VLE) data for the system R-1234yf/134a at a molar composition of (0.647/0.353)

T/K	$p_{\text{bub}}/\text{kPa}$	$U_{\mathcal{L}}/\%$	$\Delta p_{\text{bub}}/\%$
269.99	289.9	0.28	-0.219
269.99	290.0	0.28	-0.185
279.99	406.9	0.22	-0.234
279.99	407.0	0.22	-0.209
289.99	557.8	0.17	-0.042
289.99	556.5	0.17	-0.275
289.99	556.5	0.17	-0.275
299.99	745.2	0.17	-0.175
299.99	745.2	0.17	-0.175
309.99	977.0	0.15	-0.212
309.99	976.8	0.15	-0.232
319.99	1259.8	0.15	-0.171
319.99	1259.3	0.15	-0.211
329.99	1599.0	0.13	-0.186
339.99	2005.3	0.11	-0.074
339.99	2003.8	0.11	-0.149
349.99	2482.2	0.10	-0.130
349.99	2482.9	0.10	-0.101
359.99	3047.8	0.09	-0.075
359.99	3047.6	0.09	-0.082

Table A.1-3. Measured vapor-liquid equilibria (VLE) data for the system R-134a/1234ze(E) at a molar composition of (0.334/0.666)

T/K	$p_{\text{bub}}/\text{kPa}$	$U_{\mathcal{L}}/\%$	$\Delta p_{\text{bub}}/\%$
269.99	222.3	0.35	-1.312
279.99	318.1	0.26	-1.178
289.99	442.8	0.20	-1.052
299.99	601.4	0.16	-0.951
299.99	601.1	0.16	-0.990
309.99	799.6	0.17	-0.828
319.99	1043.7	0.17	-0.676
319.99	1043.0	0.17	-0.745
329.99	1339.6	0.15	-0.540
339.99	1694.3	0.13	-0.405
349.99	2115.3	0.17	-0.293
359.99	2614.9	0.11	-0.071

Table A.1-4. Measured vapor-liquid equilibria (VLE) data for the system R-134a/1234ze(E) at a molar composition of (0.663/0.337)

T/K	$p_{\text{bub}}/\text{kPa}$	$U_{\mathcal{L}}/\%$	$\Delta p_{\text{bub}}/\%$
269.99	244.0	0.29	-0.806
279.99	348.6	0.22	-0.736
289.99	484.6	0.18	-0.669
289.99	484.3	0.18	-0.738
299.99	657.0	0.15	-0.669
309.99	872.8	0.15	-0.574
309.99	872.5	0.15	-0.608
319.99	1138.3	0.16	-0.447
329.99	1460.0	0.14	-0.334
339.99	1846.1	0.12	-0.199
349.99	2304.5	0.11	-0.090
359.99	2843.2	0.10	-0.080

Table A.1-5. Measured vapor-liquid equilibria (VLE) data for the system R-1234yf/1234ze(E) at a molar composition of (0.324/0.676)

T/K	$p_{\text{bub}}/\text{kPa}$	$U_{\mathcal{L}}/\%$	$\Delta p_{\text{bub}}/\%$
270.00	229.5	0.36	-0.439
270.00	229.5	0.36	-0.439
280.00	325.4	0.27	-0.386
280.00	325.5	0.27	-0.355
290.00	449.1	0.21	-0.374
290.00	449.2	0.21	-0.352
300.00	605.7	0.17	-0.334
300.00	605.4	0.17	-0.383
310.00	799.6	0.17	-0.382
310.00	799.1	0.17	-0.444
320.00	1038.6	0.18	-0.240
320.00	1037.1	0.18	-0.384
330.00	1325.4	0.15	-0.269
330.00	1324.7	0.15	-0.321
340.00	1669.5	0.13	-0.195
340.00	1667.8	0.13	-0.297
340.00	1668.5	0.13	-0.255
350.00	2077.0	0.11	-0.132
350.00	2076.2	0.11	-0.171
360.00	2556.7	0.10	-0.076
360.00	2557.1	0.10	-0.060

Table A.1-6. Measured vapor-liquid equilibria (VLE) data for the system
R-1234yf/1234ze(E) at a molar composition of (0.638/0.362)

T/K	$p_{\text{bub}}/\text{kPa}$	$U_{\text{L}}/\%$	$\Delta p_{\text{bub}}/\%$
270.00	258.9	0.58	0.448
270.00	258.0	0.58	0.098
280.00	363.5	0.42	0.282
280.00	362.9	0.42	0.117
280.00	362.8	0.42	0.089
290.00	497.8	0.31	0.202
290.00	497.1	0.31	0.061
290.00	497.0	0.31	0.041
300.00	666.3	0.24	0.097
300.00	665.7	0.24	0.007
300.00	665.6	0.24	-0.008
310.00	874.6	0.21	0.032
310.00	873.8	0.21	-0.060
310.00	873.7	0.21	-0.071
320.00	1128.8	0.20	0.030
320.00	1127.8	0.20	-0.058
320.00	1127.7	0.20	-0.067
330.00	1435.4	0.16	0.085
330.00	1434.0	0.16	-0.012
330.00	1434.0	0.16	-0.012
340.00	1800.0	0.14	0.098
340.00	1798.8	0.14	0.031
340.00	1799.1	0.14	0.048
350.00	2229.1	0.12	0.033
350.00	2231.3	0.12	0.131
360.00	2734.0	0.11	-0.009
360.00	2738.9	0.11	0.170

Table A.1-7. Measured vapor-liquid equilibria (VLE) data for the system R-125/1234yf at a molar composition of (0.349/0.651)

T/K	$p_{\text{bub}}/\text{kPa}$	$U_{\text{L}}/\%$	$\Delta p_{\text{bub}}/\%$
270.00	393.4	0.27	0.005
270.00	393.8	0.27	0.106
280.00	542.2	0.21	0.057
290.00	729.5	0.20	0.098
300.00	959.9	0.16	0.013
300.00	960.4	0.16	0.065
310.00	1240.8	0.14	-0.010
315.00	1401.0	0.15	-0.093
315.00	1401.8	0.15	-0.036
320.00	1577.9	0.14	-0.051
325.00	1770.1	0.13	-0.050
330.00	1979.7	0.12	-0.020
330.00	1980.8	0.12	0.036
335.00	2206.6	0.11	-0.020

Table A.1-8. Measured vapor-liquid equilibria (VLE) data for the system R-125/1234yf at a molar composition of (0.664/0.336)

T/K	$p_{\text{bub}}/\text{kPa}$	$U_{\text{L}}/\%$	$\Delta p_{\text{bub}}/\%$
270.00	494.0	0.37	-0.062
270.00	494.6	0.37	0.059
280.00	677.4	0.28	0.083
290.00	905.9	0.23	0.058
290.00	907.0	0.23	0.179
300.00	1186.1	0.19	-0.045
310.00	1525.9	0.16	-0.120
310.00	1527.6	0.16	-0.009
315.00	1721.4	0.16	-0.099
320.00	1935.0	0.14	-0.072
325.00	2167.5	0.13	-0.054
330.00	2421.0	0.12	-0.007
330.00	2423.6	0.12	0.101
335.00	2695.5	0.12	0.012

Table A.1-9. Measured vapor-liquid equilibria (VLE) data for the system
R-1234ze(E)/227ea at a molar composition of (0.3347/0.6653)

T/K	$p_{\text{bub}}/\text{kPa}$	$U_{\mathcal{L}}/\%$	$\Delta p_{\text{bub}}/\%$
270.00	183.2	0.36	-0.323
280.00	264.2	0.26	-0.190
280.00	264.4	0.26	-0.114
290.00	370.0	0.21	-0.125
300.00	505.5	0.17	-0.027
300.00	506.0	0.17	0.072
310.00	674.8	0.14	-0.045
320.00	884.2	0.20	0.012
320.00	883.9	0.20	-0.022
330.00	1139.5	0.17	0.109
340.00	1445.8	0.14	0.138
340.00	1445.5	0.14	0.117
350.00	1812.4	0.12	0.251
360.00	2249.2	0.11	0.453

Table A.1-10. Measured vapor-liquid equilibria (VLE) data for the system
R-1234ze(E)/227ea at a molar composition of (0.680/0.320)

T/K	$p_{\text{bub}}/\text{kPa}$	$U_{\mathcal{L}}/\%$	$\Delta p_{\text{bub}}/\%$
270.00	189.7	0.33	-0.450
270.00	190.0	0.33	-0.292
280.00	273.3	0.25	-0.249
290.00	382.3	0.19	-0.158
290.00	382.5	0.19	-0.106
300.00	521.8	0.16	-0.036
310.00	695.9	0.17	-0.047
310.00	696.0	0.17	-0.032
320.00	911.4	0.19	0.050
330.00	1173.5	0.16	0.136
330.00	1173.3	0.16	0.119
340.00	1488.9	0.13	0.236
340.00	1488.3	0.13	0.196
350.00	1863.7	0.12	0.279
360.00	2309.0	0.10	0.402

Table A.1-11. Measured vapor-liquid equilibria (VLE) data for the system R-1234yf/152a at a molar composition of (0.3653/0.6347)

T/K	$p_{\text{bub}}/\text{kPa}$	$U_c/\%$	$\Delta p_{\text{bub}}/\%$
270.00	268.2	0.26	-0.290
270.00	268.3	0.26	-0.253
280.00	378.2	0.20	-0.121
290.00	519.2	0.17	-0.066
290.00	519.4	0.17	-0.027
300.00	697.3	0.17	0.054
310.00	917.0	0.15	0.062
310.00	916.8	0.15	0.040
320.00	1185.7	0.15	0.134
330.00	1508.8	0.13	0.155
330.00	1509.5	0.13	0.201
340.00	1895.1	0.11	0.233
350.00	2352.5	0.10	0.323
360.00	2889.9	0.09	0.376

Table A.1-12. Measured vapor-liquid equilibria (VLE) data for the system R-1234yf/152a at a molar composition of (0.6851/0.3149)

T/K	$p_{\text{bub}}/\text{kPa}$	$U_c/\%$	$\Delta p_{\text{bub}}/\%$
270.00	283.3	0.24	-0.318
270.00	283.4	0.24	-0.283
280.00	397.5	0.19	-0.141
290.00	543.2	0.16	-0.075
290.00	543.3	0.16	-0.056
300.00	726.2	0.16	0.018
310.00	951.1	0.14	0.009
320.00	1225.3	0.15	0.069
320.00	1225.6	0.15	0.094
330.00	1555.0	0.13	0.134
340.00	1947.4	0.11	0.189
340.00	1947.0	0.11	0.168
350.00	2411.0	0.10	0.232
360.00	2956.9	0.09	0.264

A.1.2. Density (p, ρ, T, x) Measurements

Instrument description. The present measurements utilized a two-sinker densimeter with a magnetic suspension coupling. This type of instrument applies the Archimedes (buoyancy) principle to provide an absolute determination of the density. This general type of instrument is described by Wagner and Kleinrahm,[14] and our instrument is described in detail by McLinden and Lösch-Will.[15] Briefly, two sinkers of nearly the same mass (~60 g) and same surface area (~41.5 cm²), but very different volumes, were each weighed with a high-precision balance while they were immersed in the sample of unknown density. The basic form of the working equation for this type of instrument gives the fluid density ρ as:

$$\rho = \frac{(m_1 - m_2) - (W_1 - W_2)}{(V_1 - V_2)}, \quad (\text{A.1-2})$$

where m and V are the mass and volume of the sinkers, W are the balance readings, and the subscripts refer to the two sinkers. One sinker was made of tantalum ($m = 60.094\ 633\ \text{g}$, $V = 3.60\ 872\ \text{cm}^3$) and the other of titanium ($m = 60.075\ 386\ \text{g}$, $V = 13.315\ 284\ \text{cm}^3$). A magnetic suspension coupling transmitted the gravity and buoyancy forces on the sinkers to the balance, thus isolating the fluid sample from the balance. With the two-sinker method, systematic errors in the weighing and from other sources approximately cancel. Figure A.1-2 shows the entire instrument and Figure A.1-3 shows the two sinkers inside the cell.



Figure A.1-2. Two-sinker densimeter

The main part of the instrument is to the right of center with the vacuum thermostat below and balance above; the instruments are on the left side; a vacuum system for both evacuating the measuring cell and maintaining the vacuum thermostat is on the right. A separate system for calibrating sinker volumes sits to the right of the instrument rack.



Figure A.1-3. Sinkers in the two-sinker densimeter (shown removed from the measuring cell)

The titanium sinker is on the bottom, with the tantalum sinker above. The magnetic suspension coupling is at the top of the image; this comprises the electromagnet, which hangs from the balance; and the permanent magnet, which picks up the sinkers via “lifting forks;” the top of the measuring cell passes between the electromagnet and permanent magnet. In this photo, the titanium sinker is suspended off of its rest and is being weighed.

In addition to the sinkers, two calibration masses (designated m_{cal} and m_{tare}) were also weighed by placing them directly on the balance pan. This provided a calibration of the balance and also the information needed to correct for magnetic effects as described by McLinden et al.[97] The four weighings (two sinkers and two calibration masses) yield a set of four equations that were solved to yield a balance calibration factor α and a parameter ϕ characterizing the efficiency of the magnetic suspension coupling. With these additional terms, the fluid density is:

$$\rho_{\text{fluid}} = \left\{ \left[(m_1 - m_2) - \frac{(W_1 - W_2)}{\alpha\phi} \right] / (V - V_2) \right\} - \rho_0 \quad (\text{A.1-3})$$

where ρ_0 is the indicated density when the sinkers are weighed in vacuum. In other words, ρ_0 is an “apparatus zero.” The density given by Eq. (A.1-3) compensates for the magnetic effects of both the apparatus and the fluid being measured. The difference of the value of ϕ from 1 indicates the magnitude of the force transmission error.[97]

The densimeter was thermostated by means of a multi-layer, vacuum-insulated thermostat. A copper shield with heaters at the top and side surrounded the measuring cell. An additional isothermal shield with heaters at the top and sides and a fluid cooling channel at the top

surrounded the “inner shield”; it was maintained at a temperature approximately 1 K below the measuring-cell temperature. A chiller that circulated ethanol was used at temperatures below room temperature.

The temperature was measured with a 25 Ω standard platinum resistance thermometer (SPRT) and an AC resistance bridge referenced to a thermostated standard resistor. The temperature inside the measuring cell was constant within 5 mK. Pressures were measured with one of three vibrating-quartz-crystal type pressure transducers having full-scale pressure ranges of 2.8 MPa, 13.8 MPa, or 69 MPa. The transducers and pressure manifold were thermostated at $T = 313.15$ K to minimize the effects of variations in laboratory temperature.

Density measurement sequence—liquid and supercritical states. A combination of measurements along isochores and along isotherms was carried out. The evacuated measuring cell was cooled and then the gas-phase sample from the sample bottle was condensed into the measuring cell; higher pressures were obtained by closing the valve to the sample bottle and then increasing the cell temperature in steps along a pseudoisochore. Once a new setpoint temperature and pressure was reached an additional equilibration time of 30–60 minutes was allowed; four replicate density determinations were then carried out. When the maximum desired pressure along a pseudoisochore was reached, a portion of the sample was vented into a waste bottle to decrease the pressure; measurements were made in this manner along an isotherm to a minimum pressure of approximately 1 MPa or slightly above the bubble-point pressure, whichever was higher. Measurements then resumed at increasing temperatures along the next, lower-density pseudoisochore. This procedure did not require any pump and thus avoided any sample contamination that a pump might introduce.

Between each of the measured blend compositions and also before and after all of the testing, the densimeter cell was evacuated for a minimum of 36 h. This was done to clear the previously measured sample and to check the zero of the pressure transducers and the ρ_0 of the apparatus (Eq. A.1-3). The ρ_0 varied by less than $0.0011 \text{ kg}\cdot\text{m}^{-3}$. These data are presented in Tables A.1-13 through A.1-18.

Vapor-phase (p, ρ, T, x) and dew point. The density in the vapor phase was measured along isotherms at temperatures from 253.15 K to 283.15 K. Each isotherm started at a low pressure (40 to 100 kPa); the pressure was increased in steps by cycling two pneumatic valves piped in series to introduce additional gaseous sample. The dew point was determined by continuing the vapor-phase isotherms into the two-phase region. As the pressure reached the dew point the value of the coupling parameter ϕ in Eq. (A.1-3) increased dramatically because of adsorption and condensation onto the sinkers; the intersection of lines fitted to the single-phase and two-phase data yielded the dew point. This effect and its exploitation for the measurement of dew points is discussed by McLinden and Richter.[98] With this technique the filling/pressure line was completely vapor filled up to the dew-point pressure, minimizing uncertainties in the composition. Each isotherm started with fresh sample. The dew points determined in this manner are presented in Table A.1-19.

(p, ρ, T, x) measurement uncertainties. The measurement uncertainty of the experimental density data measured with the two-sinker densimeter has been evaluated in previous works.[15] [99] [100] Only a brief description of the main uncertainty sources is given here. The main sources of

the uncertainty in density, in order of significance, arose from the sinker volumes (V_1, V_2), the weighings of the sinkers and calibration masses ($W_1, W_2, W_{\text{cal}}, W_{\text{tare}}$) and their masses ($m_1, m_2, m_{\text{cal}}, m_{\text{tare}}$), and the apparatus zero ρ_0 . The variance in the replicate balance readings was also included. The standard uncertainty in the density measurement is given by

$$u(\rho)/\text{kg} \cdot \text{m}^{-3} = [\{28\}^2 + \{0.2(T/\text{K} - 293)\}^2 + \{0.63p/\text{MPa}\}^2]^{1/2} \cdot 10^{-6} \rho/\text{kg} \cdot \text{m}^{-3} + 0.0010 \quad (\text{A.1-4})$$

where the term in brackets is from the uncertainty in the sinker volumes, and the final, constant term includes all other uncertainties.

The SPRT used to measure the temperature of the mixture was calibrated in our laboratory on ITS-90 from 83 K to 505 K by use of fixed-point cells. The standard uncertainty of the temperature, including the uncertainty in the fixed point cells, drift in the SPRT and in the standard resistor, and any temperature gradients, is 3 mK. The pressure transducers were calibrated with one of two gas-operated piston gages. We estimated the standard uncertainty in pressure to be $(20 \times 10^{-6} \cdot p + 0.03 \text{ kPa})$ for the vapor-phase measurements and $(26 \times 10^{-6} \cdot p + 1.0 \text{ kPa})$ for the liquid-phase measurements. To the above uncertainty estimates we added the standard deviations actually observed in the multiple temperature, pressure, and balance readings made over the 12 minutes necessary to complete a single density determination.

For mixtures a considerable fraction of the overall density uncertainty was due to uncertainty in the composition. This arose from the gravimetric preparation of the gas mixture used to charge the densimeter, but a larger contribution arose from possible adsorption of sample onto the inner walls of the sample cylinder, filling lines, measuring cell, etc. In other words, the composition in the measuring cell was not necessarily a simple ratio of the component masses loaded into the sample cylinder.

For purposes of comparing (p, ρ, T, x) measurements to a model, it is customary to assume that the temperature, pressure, and composition are known exactly, and to lump all uncertainties into a single value for the density, a so-called state-point uncertainty. This value is tabulated in the data tables for each measured point.

Table A.1-13. Measured (p, ρ, T, x) data for the system R-1234yf/134a at a molar composition of (0.33634/0.66366)

Listed for Tables A.1.13 through A.1.18 are temperature T , pressure p , density ρ , standard uncertainty in pressure $u(p)$, relative combined, expanded ($k = 2$) state-point uncertainty in the density U_c , and relative deviation from the mixture EOS $\Delta\rho$. The standard uncertainty in temperature is 3 mK. Data are presented in the sequence measured. Average values for the replicate measurements at each (T, p) state point are given.

T/K	p/MPa	$\rho/\text{kg}\cdot\text{m}^{-3}$	$u(p)/\text{kPa}$	$U_c/\%$	$\Delta\rho/\%$
Vapor-phase					
293.154	0.0645	2.847	0.03	0.139	0.009
293.156	0.1202	5.369	0.03	0.078	-0.040
293.156	0.1813	8.215	0.03	0.054	-0.030
293.156	0.2435	11.203	0.03	0.037	-0.008
293.156	0.3038	14.196	0.03	0.031	0.016
293.154	0.3601	17.079	0.03	0.027	0.009
293.157	0.4207	20.292	0.03	0.024	0.008
293.157	0.4801	23.564	0.03	0.021	0.011
293.157	0.5407	27.045	0.03	0.020	0.019
293.154	0.5781	29.102	0.53	0.172	-0.558
283.158	0.0616	2.819	0.03	0.154	0.063
283.158	0.1024	4.733	0.03	0.086	-0.003
283.156	0.1513	7.084	0.03	0.057	0.008
283.155	0.1844	8.710	0.03	0.047	-0.018
283.156	0.2242	10.712	0.03	0.039	0.021
283.159	0.2682	12.975	0.03	0.036	-0.007
283.159	0.3068	15.018	0.03	0.031	0.003
283.158	0.3406	16.850	0.03	0.027	0.007
283.157	0.3810	19.100	0.03	0.025	0.024
283.158	0.4105	20.780	0.03	0.024	0.004
273.156	0.0591	2.806	0.03	0.145	-0.012
273.157	0.0854	4.087	0.03	0.099	0.028
273.158	0.1103	5.314	0.03	0.079	-0.053
273.157	0.1557	7.609	0.03	0.055	-0.018
273.156	0.1557	7.609	0.03	0.055	-0.019
273.157	0.1864	9.198	0.03	0.052	-0.025
273.158	0.2055	10.205	0.03	0.042	-0.016
273.158	0.2323	11.640	0.03	0.038	-0.016
273.156	0.2569	12.982	0.03	0.034	-0.014
273.155	0.2866	14.639	0.03	0.031	0.007
273.157	0.3006	15.435	0.03	0.030	0.019

Table A.1-13. Measured (p, ρ, T, x) data for the system R-1234yf/134a at a molar composition of (0.33634/0.66366) (continued)

T/K	p/MPa	$\rho/\text{kg}\cdot\text{m}^{-3}$	$u(p)/\text{kPa}$	$U_c/\%$	$\Delta\rho/\%$
Vapor-phase					
273.156	0.3038	15.614	0.03	0.029	-0.007
273.154	0.3099	15.790	0.57	0.364	-1.093
263.157	0.0460	2.260	0.03	0.197	-0.144
263.158	0.0604	2.986	0.03	0.136	-0.006
263.157	0.0803	3.993	0.03	0.103	-0.078
263.160	0.1010	5.060	0.03	0.083	-0.040
263.157	0.1207	6.089	0.03	0.072	-0.041
263.159	0.1410	7.166	0.03	0.061	-0.024
263.159	0.1603	8.206	0.03	0.057	-0.014
263.157	0.1800	9.285	0.03	0.047	0.007
263.155	0.2014	10.472	0.03	0.042	-0.024
263.155	0.2082	10.855	0.03	0.040	-0.021
253.155	0.0439	2.247	0.03	0.188	-0.086
253.157	0.0615	3.169	0.03	0.140	-0.079
253.156	0.0764	3.964	0.03	0.104	0.030
253.155	0.0908	4.738	0.03	0.089	0.016
253.157	0.1064	5.585	0.03	0.083	-0.021
253.157	0.1214	6.410	0.03	0.105	-0.065
253.158	0.1310	6.949	0.03	0.065	-0.014
Liquid-phase and supercritical states					
230.018	1.0576	1377.826	1.15	0.015	-0.010
240.013	4.0960	1357.442	1.88	0.020	-0.002
240.015	2.5156	1353.415	1.77	0.019	-0.002
240.017	1.4521	1350.630	2.11	0.021	-0.002
249.999	10.5097	1346.407	1.72	0.018	0.002
250.005	8.7756	1341.986	1.63	0.018	0.002
250.005	7.1237	1337.663	1.67	0.018	0.002
250.007	5.5507	1333.409	1.34	0.016	0.002
250.008	4.0542	1329.242	1.48	0.017	0.002
250.007	1.5142	1321.869	1.60	0.018	0.002
260.006	9.9755	1318.072	1.88	0.019	0.006
260.007	9.9631	1318.033	1.31	0.015	0.006
260.009	8.4079	1313.584	1.72	0.018	0.006
260.006	5.5221	1304.933	1.65	0.018	0.005
260.008	4.1796	1300.704	1.54	0.017	0.005
260.007	1.6895	1292.499	1.40	0.016	0.005
269.996	9.5068	1288.959	1.36	0.015	0.004
269.999	8.1305	1284.487	1.30	0.015	0.003

Table A.1-13. Measured (p, ρ, T, x) data for the system R-1234yf/134a at a molar composition of (0.33634/0.66366) (continued)

T/K	p/MPa	$\rho/\text{kg}\cdot\text{m}^{-3}$	$u(p)/\text{kPa}$	$U_c/\%$	$\Delta\rho/\%$
Liquid-phase and supercritical states					
269.998	5.5605	1275.750	1.47	0.016	0.003
270.000	4.3640	1271.459	1.24	0.015	0.002
269.999	2.1260	1263.066	1.52	0.016	0.002
280.001	9.3445	1259.774	1.45	0.016	0.002
280.002	8.1204	1255.273	1.53	0.016	0.001
280.004	6.9504	1250.820	1.56	0.017	0.000
280.002	4.7596	1242.075	1.53	0.016	0.000
280.002	3.7348	1237.760	1.38	0.015	-0.001
280.002	1.8254	1229.313	1.40	0.016	-0.001
295.002	11.6641	1224.821	1.70	0.017	-0.003
295.004	9.4725	1215.562	1.44	0.016	-0.005
295.002	7.4648	1206.491	1.39	0.015	-0.006
295.005	5.6265	1197.556	1.45	0.016	-0.008
295.003	3.9356	1188.754	1.27	0.015	-0.009
295.006	2.3904	1180.086	1.23	0.015	-0.009
309.994	10.9362	1175.984	1.56	0.016	-0.013
309.995	10.0282	1171.275	1.39	0.015	-0.014
309.994	8.3387	1162.044	1.43	0.016	-0.015
309.994	6.0523	1148.363	1.38	0.015	-0.017
309.994	4.0423	1134.895	1.32	0.015	-0.018
309.994	3.4279	1130.444	1.18	0.014	-0.018
325.000	10.8843	1126.954	1.30	0.015	-0.021
325.003	8.7589	1112.710	1.35	0.015	-0.022
325.000	6.3017	1093.916	1.22	0.015	-0.023
325.000	4.2422	1075.416	1.35	0.016	-0.022
325.002	2.5328	1057.236	1.17	0.015	-0.022
339.995	8.5374	1054.188	1.26	0.015	-0.021
339.995	6.7027	1035.338	1.25	0.015	-0.018
339.996	5.1479	1016.459	1.15	0.015	-0.014
339.998	4.1584	1002.423	1.10	0.015	-0.013
339.995	2.5732	974.714	1.19	0.015	-0.018
344.995	4.1226	973.807	1.12	0.015	-0.006
349.993	5.6823	972.933	1.13	0.015	0.001
354.997	7.2507	972.074	1.12	0.015	0.003
359.997	8.8219	971.227	1.16	0.015	0.004
359.997	7.5859	952.038	1.09	0.015	0.013
359.998	6.1084	923.683	1.10	0.015	0.025
360.000	4.8366	890.821	1.11	0.015	0.030

Table A.1-13. Measured (p, ρ, T, x) data for the system R-1234yf/134a at a molar composition of (0.33634/0.66366) (continued)

T/K	p/MPa	$\rho/\text{kg}\cdot\text{m}^{-3}$	$u(p)/\text{kPa}$	$U_c/\%$	$\Delta\rho/\%$
Liquid-phase and supercritical states					
359.998	3.5802	839.396	1.05	0.015	-0.008
364.997	4.5968	838.736	1.05	0.016	0.033
369.997	5.6301	838.098	1.05	0.016	0.050
375.000	6.6755	837.453	1.08	0.016	0.055
379.995	7.7284	836.812	1.06	0.016	0.053
379.996	6.8786	805.893	1.10	0.016	0.050
379.996	6.2346	774.666	1.05	0.016	0.042
379.997	5.1658	681.598	1.05	0.017	0.063
384.996	5.8202	681.229	1.04	0.017	-0.001
389.995	6.4842	680.854	1.05	0.017	-0.051
394.995	7.1547	680.450	1.05	0.017	-0.082
400.001	7.8310	680.027	1.05	0.017	-0.101
400.000	7.0690	616.988	1.06	0.018	-0.190
399.998	5.9665	460.146	1.05	0.021	-0.254
400.000	5.0347	305.067	1.07	0.028	-0.001
400.000	3.8496	183.201	1.09	0.043	0.019
400.000	2.9176	121.603	1.10	0.043	-0.017
400.003	1.7421	63.903	1.12	0.127	-0.110

Table A.1-14. Measured (p, ρ, T, x) data for the system R-1234yf/134a at a molar composition of (0.66759/0.33241)

T/K	p/MPa	$\rho/\text{kg}\cdot\text{m}^{-3}$	$u(p)/\text{kPa}$	$U_c/\%$	$\Delta\rho/\%$
Vapor-phase					
293.156	0.0660	3.024	0.03	0.126	0.232
293.155	0.1241	5.762	0.03	0.074	0.224
293.154	0.1874	8.833	0.03	0.047	0.218
293.155	0.2418	11.555	0.03	0.037	0.244
293.157	0.3059	14.865	0.03	0.030	0.257
293.155	0.3654	18.045	0.03	0.026	0.247
293.155	0.4237	21.280	0.03	0.023	0.266
293.155	0.4801	24.530	0.03	0.021	0.286
283.154	0.0625	2.968	0.03	0.134	0.239
283.155	0.1042	4.999	0.03	0.081	0.183
283.156	0.1422	6.894	0.03	0.060	0.212

Table A.1-14. Measured (p , ρ , T , x) data for the system R-1234yf/134a at a molar composition of (0.66759/0.33241) (continued)

T/K	p/MPa	$\rho/\text{kg}\cdot\text{m}^{-3}$	$u(p)/\text{kPa}$	$U_c/\%$	$\Delta\rho/\%$
Vapor-phase					
283.158	0.1879	9.226	0.03	0.045	0.215
283.157	0.2286	11.356	0.03	0.037	0.216
283.157	0.2648	13.299	0.03	0.033	0.238
283.156	0.3048	15.499	0.03	0.029	0.256
283.155	0.3462	17.841	0.03	0.026	0.269
283.155	0.3815	19.892	0.03	0.024	0.273
283.155	0.4209	22.247	0.03	0.022	0.278
273.153	0.0674	3.327	0.03	0.121	0.163
273.152	0.0932	4.638	0.03	0.088	0.193
273.153	0.1291	6.498	0.03	0.063	0.237
273.152	0.1513	7.670	0.03	0.055	0.249
273.151	0.1823	9.331	0.03	0.046	0.218
273.152	0.2106	10.885	0.03	0.040	0.256
273.151	0.2449	12.804	0.03	0.035	0.235
273.151	0.2755	14.567	0.03	0.031	0.271
273.152	0.2965	15.794	0.03	0.029	0.245
263.156	0.0442	2.252	0.03	0.182	0.086
263.156	0.0696	3.581	0.03	0.114	0.214
263.156	0.0818	4.224	0.03	0.097	0.156
263.156	0.1050	5.469	0.03	0.076	0.216
263.155	0.1269	6.663	0.03	0.063	0.229
263.155	0.1476	7.807	0.03	0.054	0.209
263.156	0.1671	8.903	0.03	0.049	0.205
263.154	0.1854	9.953	0.03	0.044	0.258
253.154	0.0413	2.189	0.03	0.191	0.054
253.153	0.0569	3.040	0.03	0.137	0.238
253.155	0.0718	3.859	0.03	0.108	0.239
253.153	0.0861	4.650	0.03	0.090	0.168
253.154	0.1014	5.514	0.03	0.076	0.229
253.154	0.1161	6.352	0.03	0.066	0.228
253.153	0.1302	7.164	0.03	0.060	0.194
Liquid-phase and supercritical states					
230.002	0.9128	1336.222	2.22	0.023	-0.194
239.998	1.0653	1309.005	1.27	0.016	-0.185
239.998	1.0651	1309.002	1.19	0.016	-0.185
249.997	5.6266	1294.295	1.88	0.020	-0.175
249.998	4.1645	1290.030	1.93	0.020	-0.177
249.999	1.6129	1282.245	1.77	0.019	-0.179

Table A.1-14. Measured (p, ρ, T, x) data for the system R-1234yf/134a at a molar composition of (0.66759/0.33241) (continued)

T/K	p/MPa	$\rho/\text{kg}\cdot\text{m}^{-3}$	$u(p)/\text{kPa}$	$U_c/\%$	$\Delta\rho/\%$
Liquid-phase and supercritical states					
259.997	9.4759	1278.562	1.63	0.018	-0.167
259.999	7.9770	1274.037	1.50	0.017	-0.169
259.997	5.2635	1265.460	1.30	0.016	-0.172
260.000	3.9996	1261.256	1.28	0.015	-0.173
259.999	1.6694	1253.139	1.43	0.017	-0.175
269.994	8.9006	1249.632	1.88	0.019	-0.166
269.997	7.5847	1245.109	1.42	0.016	-0.167
269.997	6.3403	1240.695	1.54	0.017	-0.168
269.998	4.0550	1232.170	1.49	0.017	-0.171
269.998	1.9836	1223.903	1.44	0.016	-0.174
280.001	8.6323	1220.574	1.52	0.017	-0.165
280.001	7.4700	1216.029	1.43	0.016	-0.166
280.001	5.3396	1207.255	1.40	0.016	-0.169
280.003	3.4024	1198.696	1.27	0.015	-0.172
280.003	1.6537	1190.428	1.49	0.016	-0.174
295.003	10.5573	1185.253	1.40	0.016	-0.163
295.004	9.5150	1180.602	1.42	0.016	-0.164
295.003	7.5910	1171.564	1.33	0.015	-0.167
295.006	5.8284	1162.653	1.37	0.015	-0.170
295.003	4.2089	1153.864	1.55	0.017	-0.173
295.003	2.0563	1141.048	1.29	0.015	-0.177
309.994	9.9069	1137.041	1.29	0.015	-0.164
309.999	8.2737	1127.710	1.36	0.015	-0.167
309.996	6.0974	1114.100	1.39	0.016	-0.171
309.997	4.1899	1100.709	1.35	0.015	-0.175
309.995	2.0299	1083.314	1.55	0.017	-0.182
325.002	8.6630	1079.822	1.25	0.015	-0.163
325.003	8.0388	1075.113	1.26	0.015	-0.164
325.001	5.8320	1056.789	1.30	0.015	-0.168
325.002	3.9881	1038.780	1.29	0.015	-0.172
325.002	2.1196	1016.673	1.29	0.016	-0.181
339.997	7.5364	1013.684	1.22	0.015	-0.149
339.997	5.9387	995.131	1.11	0.015	-0.149
339.997	4.0328	967.738	1.17	0.015	-0.150
339.996	2.6131	940.709	1.12	0.015	-0.161
344.995	4.0305	939.822	1.08	0.015	-0.137
349.994	5.4565	938.943	1.13	0.015	-0.121
354.994	6.8882	938.074	1.11	0.015	-0.110

Table A.1-14. Measured (p, ρ, T, x) data for the system R-1234yf/134a at a molar composition of (0.66759/0.33241) (continued)

T/K	p/MPa	$\rho/\text{kg}\cdot\text{m}^{-3}$	$u(p)/\text{kPa}$	$U_c/\%$	$\Delta\rho/\%$
Liquid-phase and supercritical states					
359.998	8.3244	937.210	1.13	0.015	-0.102
359.998	6.4863	904.331	1.14	0.015	-0.089
359.998	5.0076	867.437	1.07	0.015	-0.075
359.999	3.5874	807.728	1.05	0.016	-0.073
364.998	4.5146	807.093	1.04	0.016	-0.041
369.998	5.4569	806.464	1.05	0.016	-0.038
374.998	6.4088	805.823	1.06	0.016	-0.041
379.998	7.3671	805.162	1.06	0.016	-0.044
379.997	6.5403	772.196	1.07	0.016	-0.049
379.998	5.5548	711.581	1.05	0.017	-0.026
384.998	5.2432	595.068	1.04	0.018	0.254
389.997	5.7522	594.705	1.04	0.018	0.023
394.997	6.2656	594.329	1.05	0.018	-0.117
399.999	6.7830	593.964	1.05	0.018	-0.209
400.002	5.8987	475.041	1.05	0.021	0.143
400.001	4.9852	322.447	1.07	0.027	0.698
400.001	3.9472	203.238	1.09	0.040	0.603
400.001	2.7048	115.490	1.10	0.040	0.368
400.003	1.7401	66.680	1.11	0.117	0.204

Table A.1-15. Measured (p, ρ, T, x) data for the system R-134a/1234ze(E) at a molar composition of (0.33250/0.66750)

T/K	p/MPa	$\rho/\text{kg}\cdot\text{m}^{-3}$	$u(p)/\text{kPa}$	$U_c/\%$	$\Delta\rho/\%$
Vapor-phase					
293.156	0.0577	2.640	0.03	0.160	-0.008
293.156	0.0577	2.640	0.03	0.136	-0.008
293.157	0.1025	4.739	0.03	0.086	-0.033
293.159	0.1415	6.606	0.03	0.057	-0.018
293.159	0.1817	8.574	0.03	0.045	0.036
293.157	0.2212	10.545	0.03	0.038	0.029
293.158	0.2624	12.649	0.03	0.033	0.032
293.157	0.3013	14.681	0.03	0.028	0.022
293.157	0.3417	16.848	0.03	0.027	0.049
293.159	0.3807	18.993	0.03	0.024	0.061
283.155	0.0603	2.864	0.03	0.129	0.000
283.156	0.0947	4.540	0.03	0.082	0.012

Table A.1-15. Measured (p, ρ, T, x) data for the system R-134a/1234ze(E) at a molar composition of (0.33250/0.66750) (continued)

T/K	p/MPa	$\rho/\text{kg}\cdot\text{m}^{-3}$	$u(p)/\text{kPa}$	$U_c/\%$	$\Delta\rho/\%$
Vapor-phase					
283.157	0.1255	6.070	0.03	0.062	0.036
283.155	0.1532	7.466	0.03	0.051	0.007
283.155	0.1838	9.042	0.03	0.043	0.050
283.157	0.2107	10.449	0.03	0.038	0.044
283.158	0.2430	12.172	0.03	0.034	0.042
283.157	0.2700	13.645	0.03	0.031	0.072
283.156	0.3015	15.394	0.03	0.029	0.065
283.157	0.3218	16.544	0.03	0.027	0.072
283.157	0.3241	16.674	0.03	0.027	0.063
273.158	0.0496	2.438	0.03	0.154	-0.064
273.155	0.0751	3.720	0.03	0.108	-0.057
273.155	0.1059	5.298	0.03	0.072	-0.028
273.154	0.1269	6.393	0.03	0.060	-0.026
273.155	0.1524	7.744	0.03	0.056	-0.004
273.155	0.1754	8.986	0.03	0.044	0.036
273.158	0.2011	10.397	0.03	0.040	0.057
273.160	0.2238	11.666	0.03	0.039	0.063
263.161	0.0376	1.917	0.03	0.235	0.072
263.161	0.0628	3.225	0.03	0.122	-0.059
263.158	0.0860	4.454	0.03	0.086	-0.048
263.156	0.1004	5.231	0.03	0.082	0.016
263.156	0.1206	6.333	0.03	0.062	0.047
263.158	0.1452	7.697	0.03	0.052	0.038
263.160	0.1565	8.337	0.03	0.054	0.085
253.167	0.0361	1.913	0.03	0.202	-0.061
253.163	0.0455	2.419	0.03	0.159	-0.107
253.163	0.0606	3.244	0.03	0.125	-0.031
253.163	0.0760	4.094	0.03	0.102	-0.047
253.164	0.0905	4.906	0.03	0.081	-0.025
Liquid-phase and supercritical states					
230.011	0.9398	1379.400	2.12	0.021	-0.087
230.011	0.9410	1379.400	2.10	0.021	-0.087
230.010	0.9419	1379.406	1.66	0.018	-0.087
245.008	14.0799	1368.702	1.80	0.018	-0.077
245.008	14.0811	1368.706	1.76	0.018	-0.077
245.013	11.8531	1364.114	1.63	0.017	-0.072
245.011	7.7630	1355.310	1.92	0.019	-0.063
245.012	4.0499	1346.804	1.78	0.018	-0.055

Table A.1-15. Measured (p, ρ, T, x) data for the system R-134a/1234ze(E) at a molar composition of (0.33250/0.66750) (continued)

T/K	p/MPa	$\rho/\text{kg}\cdot\text{m}^{-3}$	$u(p)/\text{kPa}$	$U_c/\%$	$\Delta\rho/\%$
Liquid-phase and supercritical states					
245.015	1.3039	1340.152	1.63	0.017	-0.048
259.998	15.4284	1335.162	1.96	0.019	-0.051
260.001	13.4515	1330.555	1.46	0.016	-0.047
260.000	11.5563	1326.008	1.68	0.017	-0.043
260.000	8.0156	1317.092	1.35	0.015	-0.035
260.001	3.2734	1304.149	1.75	0.018	-0.025
260.002	1.8344	1299.957	1.25	0.015	-0.022
279.999	18.6289	1294.065	1.58	0.016	-0.031
280.001	15.1498	1284.619	1.56	0.016	-0.025
280.002	11.9530	1275.346	1.40	0.015	-0.019
280.002	7.6361	1261.735	1.47	0.016	-0.012
280.002	3.8418	1248.486	1.55	0.016	-0.005
280.004	1.5807	1239.867	1.48	0.016	0.000
304.997	19.1999	1233.418	1.48	0.015	-0.013
304.998	16.3852	1223.766	1.64	0.016	-0.009
304.998	12.5771	1209.525	1.39	0.015	-0.005
304.997	8.1740	1190.906	1.50	0.016	0.000
304.997	4.4491	1172.670	1.63	0.016	0.004
304.997	1.3206	1154.826	1.48	0.016	0.007
309.996	4.0730	1153.572	1.41	0.015	0.006
319.988	9.5781	1151.337	1.38	0.015	0.004
329.988	15.0585	1149.270	1.26	0.015	0.003
339.994	20.5178	1147.397	1.50	0.016	0.004
339.994	15.6051	1122.887	1.48	0.016	0.009
339.994	12.3123	1103.560	1.40	0.015	0.013
339.994	8.2775	1074.984	1.43	0.016	0.021
339.997	4.2837	1037.485	1.12	0.015	0.032
339.994	2.4419	1014.334	1.20	0.015	0.033
349.993	6.0374	1012.627	1.14	0.015	0.044
359.995	9.6560	1011.043	1.10	0.015	0.037
369.995	13.2786	1009.529	1.13	0.015	0.030
379.994	16.8942	1008.053	1.16	0.016	0.026
379.994	13.7847	978.472	1.20	0.016	0.032
379.994	10.9640	944.282	1.17	0.016	0.043
379.996	8.1076	895.878	1.09	0.016	0.067
379.996	5.0537	795.139	1.09	0.016	0.128
384.994	5.9657	794.626	1.06	0.016	0.102
389.994	6.8886	794.099	1.06	0.016	0.080

Table A.1-15. Measured (p, ρ, T, x) data for the system R-134a/1234ze(E) at a molar composition of (0.33250/0.66750) (continued)

T/K	p/MPa	$\rho/ \text{kg}\cdot\text{m}^{-3}$	$u(p)/\text{kPa}$	$U_c/\%$	$\Delta\rho/\%$
Liquid-phase and supercritical states					
394.993	7.8191	793.564	1.06	0.016	0.064
399.997	8.7563	793.013	1.07	0.017	0.054
399.998	7.2821	727.654	1.08	0.017	0.050
399.998	6.1369	629.406	1.08	0.018	0.001
399.998	5.0684	399.697	1.10	0.022	-0.003
399.998	3.8715	206.293	1.12	0.037	0.008
399.998	2.5928	110.897	1.13	0.037	-0.087

Table A.1-16. Measured (p, ρ, T, x) data for the system R-134a/1234ze(E) at a molar composition of (0.66356/0.33644)

T/K	p/MPa	$\rho/ \text{kg}\cdot\text{m}^{-3}$	$u(p)/\text{kPa}$	$U_c/\%$	$\Delta\rho/\%$
Vapor-phase					
293.154	0.0537	2.364	0.03	0.152	-0.022
293.157	0.1002	4.458	0.03	0.083	-0.041
293.158	0.1512	6.808	0.03	0.059	-0.035
293.160	0.2037	9.290	0.03	0.042	-0.030
293.159	0.2550	11.783	0.03	0.034	-0.023
293.159	0.3029	14.175	0.03	0.030	-0.008
293.158	0.3501	16.597	0.03	0.026	-0.006
293.157	0.4017	19.330	0.03	0.024	0.017
293.159	0.4503	21.986	0.03	0.023	0.023
293.158	0.4808	23.697	0.03	0.021	0.019
283.154	0.0511	2.329	0.03	0.175	-0.124
283.155	0.1060	4.903	0.03	0.078	-0.075
283.157	0.1536	7.203	0.03	0.054	0.006
283.157	0.2028	9.644	0.03	0.041	0.007
283.158	0.2510	12.108	0.03	0.034	0.020
283.158	0.3013	14.762	0.03	0.029	0.023
283.158	0.3528	17.573	0.03	0.026	0.004
273.158	0.0489	2.313	0.03	0.168	-0.125
273.156	0.0815	3.895	0.03	0.101	-0.076
273.156	0.1208	5.844	0.03	0.067	-0.053
273.155	0.1640	8.046	0.03	0.048	-0.019
273.157	0.2017	10.021	0.03	0.048	-0.008
273.158	0.2410	12.141	0.03	0.035	0.019
263.158	0.0468	2.302	0.03	0.168	-0.094

Table A.1-16. Measured (p, ρ, T, x) data for the system R-134a/1234ze(E) at a molar composition of (0.66356/0.33644) (continued)

T/K	p/MPa	$\rho/\text{kg}\cdot\text{m}^{-3}$	$u(p)/\text{kPa}$	$U_c/\%$	$\Delta\rho/\%$
Vapor-phase					
263.157	0.0780	3.880	0.03	0.105	-0.029
263.156	0.1066	5.359	0.03	0.073	0.018
263.154	0.1329	6.745	0.03	0.058	0.008
263.154	0.1571	8.047	0.03	0.055	0.017
263.154	0.1722	8.874	0.03	0.046	0.036
253.162	0.0449	2.301	0.03	0.205	-0.021
253.159	0.0651	3.361	0.03	0.129	-0.085
253.158	0.0933	4.875	0.03	0.091	-0.034
253.155	0.1108	5.835	0.03	0.077	-0.007
Liquid-phase and supercritical states					
230.010	0.9663	1402.623	4.57	0.037	-0.050
230.008	0.9667	1402.628	5.59	0.044	-0.051
230.009	0.9687	1402.626	4.20	0.034	-0.051
245.011	12.0546	1386.704	1.59	0.017	-0.039
245.011	12.0502	1386.694	1.78	0.018	-0.039
245.015	9.9508	1382.143	1.49	0.016	-0.035
245.013	7.9659	1377.720	1.51	0.017	-0.032
245.012	4.2868	1369.139	1.61	0.017	-0.024
245.015	1.4248	1362.070	1.84	0.018	-0.018
260.002	15.7691	1356.809	1.70	0.017	-0.022
260.003	14.0267	1352.679	1.40	0.016	-0.020
260.005	12.1367	1348.071	1.71	0.017	-0.016
260.003	8.6023	1339.042	1.84	0.018	-0.010
260.004	3.8613	1325.928	1.66	0.017	-0.001
260.007	1.3603	1318.456	1.17	0.015	0.005
280.000	18.3310	1312.269	1.91	0.018	-0.009
280.001	14.9348	1302.734	1.58	0.016	-0.004
280.003	11.8171	1293.387	1.54	0.016	0.000
280.002	7.6042	1279.684	1.55	0.016	0.007
280.003	3.8966	1266.338	1.45	0.016	0.015
280.008	1.6837	1257.638	1.28	0.015	0.020
304.999	19.5685	1250.996	1.42	0.015	-0.003
304.999	15.4975	1236.449	1.53	0.016	0.001
304.999	11.8883	1222.160	1.32	0.015	0.005
304.999	7.7059	1203.446	1.40	0.015	0.012
304.999	4.1635	1185.110	1.32	0.015	0.019
304.999	1.8789	1171.601	1.17	0.014	0.025
314.993	7.4883	1169.120	1.19	0.014	0.011

Table A.1-16. Measured (p, ρ, T, x) data for the system R-134a/1234ze(E) at a molar composition of (0.66356/0.33644) (continued)

T/K	p/MPa	$\rho/\text{kg}\cdot\text{m}^{-3}$	$u(p)/\text{kPa}$	$U_c/\%$	$\Delta\rho/\%$
Liquid-phase and supercritical states					
339.999	21.4741	1164.055	1.37	0.015	-0.008
339.996	15.6947	1134.447	1.48	0.016	-0.003
339.996	11.8006	1110.170	1.28	0.015	0.003
339.998	8.0476	1081.430	1.19	0.015	0.016
339.998	3.9440	1038.952	1.15	0.015	0.037
339.997	2.3054	1015.611	1.16	0.015	0.045
349.993	5.8381	1013.890	1.09	0.015	0.038
359.998	9.4056	1012.324	1.09	0.015	0.021
369.995	12.9837	1010.853	1.18	0.015	0.006
379.996	16.5642	1009.426	1.14	0.016	-0.006
379.997	14.1225	984.560	1.21	0.016	0.002
379.997	11.0710	945.135	1.11	0.016	0.018
379.998	7.9933	886.503	1.08	0.016	0.042
379.998	5.1088	765.284	1.07	0.016	-0.043
384.995	5.9414	764.838	1.05	0.016	-0.030
389.995	6.7865	764.396	1.06	0.016	-0.026
394.995	7.6408	763.955	1.06	0.017	-0.024
399.999	8.5025	763.500	1.07	0.017	-0.022
399.998	6.0366	536.798	1.78	0.026	-0.474
400.003	3.7066	175.446	1.12	0.042	-0.180
400.001	1.5024	54.037	1.14	0.131	-0.222

Table A.1-17. Measured (p, ρ, T, x) data for the system R-1234yf/1234ze(E) at a molar composition of (0.33584/0.66416)

T/K	p/MPa	$\rho/\text{kg}\cdot\text{m}^{-3}$	$u(p)/\text{kPa}$	$U_c/\%$	$\Delta\rho/\%$
Vapor-phase					
293.153	0.1061	5.092	0.03	0.075	-0.018
293.154	0.1509	7.323	0.03	0.060	-0.054
293.158	0.2004	9.856	0.03	0.042	-0.022
293.159	0.2535	12.651	0.03	0.035	-0.017
293.158	0.3023	15.303	0.03	0.029	0.011
293.156	0.3517	18.067	0.03	0.026	0.005
293.156	0.3755	19.431	0.03	0.025	0.001
293.156	0.4052	21.172	0.03	0.023	0.029
293.158	0.4144	21.715	0.03	0.023	0.026
293.159	0.4193	22.010	0.03	0.023	0.040

Table A.1-17. Measured (p, ρ, T, x) data for the system R-1234yf/1234ze(E) at a molar composition of (0.33584/0.66416) (continued)

T/K	p/MPa	$\rho/\text{kg}\cdot\text{m}^{-3}$	$u(p)/\text{kPa}$	$U_c/\%$	$\Delta\rho/\%$
Vapor-phase					
283.150	0.0765	3.784	0.03	0.104	0.018
283.150	0.1235	6.190	0.03	0.064	-0.001
283.150	0.1635	8.289	0.03	0.049	-0.040
283.150	0.2026	10.400	0.03	0.040	0.015
283.150	0.2436	12.667	0.03	0.034	0.008
283.150	0.2626	13.743	0.03	0.032	0.028
283.152	0.2826	14.887	0.03	0.031	0.018
283.153	0.3025	16.048	0.03	0.028	0.051
283.153	0.3172	16.913	0.03	0.027	0.047
283.154	0.3319	17.791	0.03	0.026	0.065
273.157	0.0565	2.884	0.03	0.143	-0.098
273.156	0.0813	4.182	0.03	0.098	-0.111
273.156	0.1041	5.396	0.03	0.076	-0.068
273.158	0.1251	6.533	0.03	0.068	-0.021
273.157	0.1506	7.934	0.03	0.055	-0.003
273.157	0.1789	9.520	0.03	0.045	0.009
273.158	0.2038	10.942	0.03	0.041	0.016
273.159	0.2259	12.228	0.03	0.036	0.019
263.155	0.0592	3.149	0.03	0.129	-0.048
263.153	0.0824	4.421	0.03	0.093	-0.016
263.154	0.1038	5.616	0.03	0.077	0.010
263.155	0.1236	6.739	0.03	0.063	0.033
263.156	0.1420	7.797	0.03	0.054	0.017
253.155	0.0395	2.173	0.03	0.191	-0.067
253.152	0.0631	3.506	0.03	0.119	-0.018
253.153	0.0849	4.760	0.03	0.091	-0.044
253.153	0.1050	5.942	0.03	0.071	0.002
Liquid-phase and supercritical states					
230.007	0.8784	1338.848	1.23	0.016	-0.054
230.004	0.8783	1338.855	1.25	0.016	-0.054
240.002	6.0634	1325.128	2.10	0.022	-0.042
240.004	4.2970	1321.033	1.40	0.017	-0.039
240.008	2.6142	1317.007	1.46	0.017	-0.037
240.003	1.2209	1313.598	1.48	0.017	-0.035
240.001	1.2191	1313.601	1.61	0.018	-0.035
250.000	10.2447	1310.027	1.48	0.017	-0.032
250.002	8.6454	1306.194	1.48	0.017	-0.030
250.001	5.2840	1297.786	2.08	0.021	-0.025

Table A.1-17. Measured (p, ρ, T, x) data for the system R-1234yf/1234ze(E) at a molar composition of (0.33584/0.66416) (continued)

T/K	p/MPa	$\rho/\text{kg}\cdot\text{m}^{-3}$	$u(p)/\text{kPa}$	$U_c/\%$	$\Delta\rho/\%$
Liquid-phase and supercritical states					
250.001	2.2462	1289.697	1.78	0.019	-0.021
250.001	1.2160	1286.830	1.75	0.019	-0.020
259.997	9.4609	1283.176	1.74	0.018	-0.019
259.999	7.8656	1278.858	1.38	0.016	-0.017
259.999	6.3383	1274.596	1.54	0.017	-0.016
259.997	3.4945	1266.270	1.65	0.018	-0.013
259.999	1.2243	1259.202	1.74	0.019	-0.010
269.995	8.9145	1255.977	1.66	0.017	-0.011
269.996	7.4945	1251.634	1.30	0.015	-0.009
269.999	6.1360	1247.333	1.48	0.016	-0.008
269.995	3.5968	1238.910	1.52	0.017	-0.006
269.998	1.3080	1230.781	1.45	0.016	-0.003
280.000	8.3907	1227.760	1.35	0.015	-0.005
280.003	7.1400	1223.389	1.35	0.015	-0.004
280.002	4.7940	1214.791	1.48	0.016	-0.002
280.004	2.6525	1206.367	1.24	0.015	0.000
280.004	1.6537	1202.235	1.43	0.016	0.001
295.003	11.4293	1198.217	1.32	0.015	-0.002
295.003	9.1249	1189.218	1.32	0.015	-0.001
295.005	6.0230	1175.988	1.24	0.015	0.000
295.006	4.1645	1167.315	1.20	0.014	0.001
295.005	1.6701	1154.569	1.25	0.015	0.001
310.001	10.1305	1150.870	1.28	0.015	0.002
310.003	8.2970	1141.824	1.12	0.014	0.002
310.002	5.8188	1128.430	1.21	0.015	0.001
310.005	4.3376	1119.616	1.20	0.015	0.001
310.000	1.7391	1102.274	1.25	0.015	-0.003
314.997	4.1433	1101.096	1.16	0.014	0.001
319.994	6.5521	1100.014	1.10	0.014	0.004
324.992	8.9552	1098.971	1.16	0.014	0.007
324.993	6.8863	1085.356	1.13	0.014	0.007
324.994	5.0663	1071.889	1.17	0.014	0.007
324.994	3.4730	1058.570	1.17	0.015	0.006
324.995	1.6643	1041.020	1.09	0.014	0.002
329.991	3.6505	1040.015	1.12	0.014	0.012
334.990	5.6441	1039.089	1.14	0.015	0.018
339.997	7.6437	1038.200	1.15	0.015	0.020
339.998	6.1682	1024.498	1.10	0.014	0.025

Table A.1-17. Measured (p, ρ, T, x) data for the system R-1234yf/1234ze(E) at a molar composition of (0.33584/0.66416) (continued)

T/K	p/MPa	$\rho/\text{kg}\cdot\text{m}^{-3}$	$u(p)/\text{kPa}$	$U_c/\%$	$\Delta\rho/\%$
Liquid-phase and supercritical states					
339.999	4.8763	1010.886	1.11	0.014	0.029
340.000	3.4110	992.892	1.10	0.015	0.035
339.999	1.9412	970.611	1.15	0.015	0.041
349.995	5.1155	968.963	1.09	0.015	0.054
359.999	8.3222	967.480	1.08	0.015	0.045
360.000	7.2697	953.571	1.11	0.015	0.055
360.001	6.0691	935.147	1.08	0.015	0.073
360.002	5.0693	916.771	1.07	0.015	0.097
360.001	4.0665	893.911	1.08	0.015	0.138
370.001	6.5744	892.621	1.06	0.015	0.090
379.996	9.1111	891.418	1.07	0.015	0.051
379.997	7.5159	858.682	1.10	0.016	0.077
380.000	6.0718	816.850	1.07	0.016	0.136
379.998	5.0507	770.576	1.07	0.016	0.242
380.000	4.0343	659.766	1.07	0.017	0.965
384.996	4.6155	659.407	1.05	0.017	0.507
389.997	5.2102	659.054	1.05	0.017	0.254
394.994	5.8136	658.681	1.05	0.017	0.095
400.001	6.4252	658.305	1.08	0.018	-0.007
400.001	5.4776	532.489	1.06	0.019	-0.113
400.002	4.1094	250.120	1.09	0.033	0.069
399.997	2.7673	127.701	1.10	0.033	0.048
400.005	1.6855	67.553	1.11	0.115	-0.100
400.002	0.9735	36.215	1.52	0.405	-0.281

Table A.1-18. Measured (p, ρ, T, x) data for the system R-1234yf/1234ze(E) at a molar composition of (0.66660/0.33340)

T/K	p/MPa	$\rho/\text{kg}\cdot\text{m}^{-3}$	$u(p)/\text{kPa}$	$U_c/\%$	$\Delta\rho/\%$
Vapor-phase					
293.149	0.0630	2.989	0.03	0.129	-0.086
293.149	0.1234	5.943	0.03	0.066	-0.039
293.150	0.1856	9.084	0.03	0.051	-0.002
293.150	0.2442	12.136	0.03	0.035	-0.032
293.151	0.3014	15.222	0.03	0.031	-0.004
293.153	0.3596	18.472	0.03	0.025	0.003
293.153	0.4200	21.977	0.03	0.025	0.003

Table A.1-18. Measured (p, ρ, T, x) data for the system R-1234yf/1234ze(E) at a molar composition of (0.66660/0.33340) (continued)

T/K	p/MPa	$\rho/\text{kg}\cdot\text{m}^{-3}$	$u(p)/\text{kPa}$	$U_c/\%$	$\Delta\rho/\%$
Vapor-phase					
281.157	0.0508	2.512	0.03	0.194	-0.029
281.157	0.1027	5.151	0.03	0.089	-0.040
281.157	0.1533	7.806	0.03	0.052	-0.016
281.156	0.2005	10.359	0.03	0.040	0.009
281.158	0.2515	13.204	0.03	0.038	-0.017
281.161	0.3025	16.160	0.03	0.032	0.016
281.160	0.3251	17.506	0.03	0.027	0.027
281.160	0.3451	18.717	0.03	0.025	0.034
273.156	0.0564	2.879	0.03	0.173	-0.039
273.155	0.0900	4.640	0.03	0.088	-0.084
273.156	0.1201	6.254	0.03	0.069	-0.050
273.156	0.1595	8.420	0.03	0.050	0.009
273.155	0.1933	10.320	0.03	0.048	-0.026
273.158	0.2131	11.461	0.03	0.039	0.019
273.153	0.2310	12.503	0.03	0.038	0.009
273.154	0.2511	13.692	0.03	0.033	0.011
263.154	0.0523	2.775	0.03	0.149	-0.010
263.155	0.0770	4.120	0.03	0.099	-0.039
263.155	0.1069	5.786	0.03	0.077	0.025
263.154	0.1207	6.567	0.03	0.063	0.027
263.152	0.1401	7.678	0.03	0.055	0.009
263.152	0.1637	9.054	0.03	0.049	0.006
263.151	0.1799	10.015	0.03	0.043	0.010
253.155	0.0368	2.019	0.03	0.212	-0.170
253.152	0.0614	3.408	0.03	0.126	0.001
253.152	0.0842	4.714	0.03	0.095	-0.078
253.152	0.1051	5.941	0.03	0.071	-0.013
253.154	0.1102	6.246	0.03	0.074	0.027
253.157	0.1202	6.842	0.03	0.063	0.025
Liquid-phase and supercritical states					
230.014	0.9578	1320.352	1.63	0.019	-0.040
230.012	0.9575	1320.359	1.50	0.018	-0.040
230.010	0.9583	1320.366	1.67	0.019	-0.040
240.008	5.5444	1305.661	1.48	0.017	-0.030
240.011	5.5463	1305.663	1.34	0.016	-0.030
240.013	3.9585	1301.686	2.17	0.023	-0.028
240.011	2.4590	1297.830	1.40	0.017	-0.026
240.010	1.2698	1294.682	4.02	0.038	-0.025

Table A.1-18. Measured (p, ρ, T, x) data for the system R-1234yf/1234ze(E) at a molar composition of (0.66660/0.33340) (continued)

T/K	p/MPa	$\rho/\text{kg}\cdot\text{m}^{-3}$	$u(p)/\text{kPa}$	$U_c/\%$	$\Delta\rho/\%$
Liquid-phase and supercritical states					
250.004	9.6755	1290.781	1.79	0.019	-0.023
250.006	8.0610	1286.603	1.34	0.016	-0.022
250.004	5.0435	1278.444	1.66	0.018	-0.019
250.007	2.3030	1270.555	1.40	0.017	-0.016
250.007	1.2491	1267.385	2.25	0.023	-0.015
260.000	9.0427	1263.765	1.52	0.017	-0.015
260.001	7.6043	1259.563	1.21	0.015	-0.014
260.004	6.2283	1255.416	1.37	0.016	-0.012
260.002	2.4583	1243.330	1.86	0.019	-0.009
260.003	1.3290	1239.466	1.25	0.015	-0.008
269.998	8.5423	1236.120	1.58	0.017	-0.010
269.999	7.2638	1231.889	1.38	0.016	-0.008
270.001	6.0400	1227.696	1.54	0.017	-0.007
269.997	3.7481	1219.475	1.49	0.017	-0.005
270.002	1.6598	1211.443	1.28	0.015	-0.003
279.999	8.3244	1208.371	1.50	0.016	-0.006
280.003	7.1923	1204.103	1.22	0.015	-0.006
280.001	5.0620	1195.688	1.30	0.015	-0.003
280.004	3.1089	1187.411	1.25	0.015	-0.002
280.001	1.3268	1179.339	1.58	0.017	0.000
295.004	10.4177	1175.186	1.34	0.015	-0.005
295.003	8.3964	1166.449	1.41	0.016	-0.003
295.004	7.4455	1162.109	1.23	0.015	-0.003
295.004	5.6599	1153.532	1.25	0.015	-0.001
295.005	3.2518	1140.885	1.25	0.015	0.001
295.004	2.5156	1136.726	1.22	0.015	0.002
309.998	10.5000	1132.914	1.34	0.015	-0.003
310.002	8.8111	1124.052	1.32	0.015	-0.002
310.000	6.5191	1110.918	1.36	0.016	0.000
310.001	4.4981	1097.962	1.23	0.015	0.002
310.004	3.2886	1089.421	1.17	0.015	0.003
310.000	1.6602	1076.765	1.49	0.017	0.003
314.996	3.8770	1075.564	1.36	0.016	0.003
319.993	6.0927	1074.429	1.22	0.015	0.003
324.992	8.3118	1073.367	1.26	0.015	0.002
324.994	7.0981	1064.512	1.35	0.016	0.004
324.994	4.9574	1046.987	1.30	0.015	0.009
324.996	3.5777	1033.973	1.22	0.015	0.012

Table A.1-18. Measured (p, ρ, T, x) data for the system R-1234yf/1234ze(E) at a molar composition of (0.66660/0.33340) (continued)

T/K	p/MPa	$\rho/\text{kg}\cdot\text{m}^{-3}$	$u(p)/\text{kPa}$	$U_c/\%$	$\Delta\rho/\%$
Liquid-phase and supercritical states					
324.994	1.6530	1012.488	1.45	0.017	0.016
329.990	3.4644	1011.475	1.16	0.015	0.019
334.990	5.2816	1010.507	1.16	0.015	0.019
339.996	7.1043	1009.576	1.10	0.014	0.016
339.998	5.8662	996.239	1.10	0.015	0.023
340.000	5.1260	987.381	1.19	0.015	0.028
339.999	3.5439	965.403	1.21	0.015	0.042
339.999	2.0871	939.259	1.15	0.015	0.063
349.997	4.9567	937.639	1.13	0.015	0.056
360.000	7.8541	936.080	1.14	0.015	0.035
360.002	7.2613	927.025	1.13	0.015	0.043
360.001	5.9880	904.517	1.17	0.016	0.064
360.001	4.9740	882.133	1.09	0.015	0.093
360.001	4.0423	855.376	1.06	0.015	0.140
364.999	5.1397	854.591	1.05	0.015	0.103
369.997	6.2494	853.933	1.08	0.016	0.070
374.999	7.3667	853.266	1.06	0.016	0.040
379.996	8.4858	852.569	1.13	0.016	0.017
379.998	7.5529	829.783	1.09	0.016	0.021
380.001	7.0689	815.792	1.05	0.016	0.023
380.000	6.0517	778.564	1.06	0.016	0.035
379.999	5.0385	718.365	1.05	0.017	0.073
384.997	4.7731	602.491	1.05	0.018	0.017
389.997	5.2796	602.119	1.05	0.018	-0.241
394.994	5.7916	601.753	1.05	0.018	-0.399
399.998	6.3086	601.368	1.05	0.018	-0.496
400.002	5.5254	486.233	1.06	0.020	-0.658
400.003	5.0718	394.718	1.07	0.023	-0.575
400.002	4.3633	273.239	1.08	0.031	-0.002
400.004	3.8560	213.394	1.09	0.038	0.133
400.002	3.1672	153.911	1.10	0.039	0.109
400.005	2.7375	124.515	1.10	0.039	0.045
400.004	2.2406	95.385	1.11	0.039	-0.021
400.005	1.6796	67.018	1.11	0.115	-0.072

Table A.1-19. Dew points derived from vapor-phase measurements

For a given blend, with composition in mole fraction, listed are temperature T , dew-point pressure p_{dew} , standard uncertainty in dew-point pressure $u(p_{\text{dew}})$, dew-point density ρ_{dew} , standard uncertainty in dew-point density $u(\rho_{\text{dew}})$, relative deviation of dew-point pressure from the mixture EOS Δp_{dew} , and relative deviation of dew-point density from the mixture EOS $\Delta \rho_{\text{dew}}$.

T (K)	p_{dew} ———— (MPa) ————	$u(p_{\text{dew}})$ ————	ρ_{dew} ———— (kg·m ⁻³) ————	$u(\rho_{\text{dew}})$ ————	Δp_{dew} ———— (%) ————	$\Delta \rho_{\text{dew}}$ ————
<u>R-1234yf/134a at a molar composition of (0.33634/0.66366)</u>						
283.157	0.4464	0.0178	22.597	0.031	0.72	-0.43
273.156	0.3197	0.0095	16.243	0.015	1.17	-0.45
263.158	0.2195	0.0089	11.310	0.017	0.30	-1.30
253.156	0.1484	0.0096	7.774	0.015	1.34	-0.60
<u>R-1234yf/134a at a molar composition of (0.66759/0.33241)</u>						
283.156	0.4540	0.0143	23.951	0.208	0.51	-0.52
273.152	0.3277	0.0116	17.365	0.016	0.99	-0.35
263.155	0.2304	0.0034	12.272	0.009	1.65	-0.53
253.154	0.1574	0.0061	8.453	0.010	2.74	-0.54
<u>R-134a/1234ze(E) at a molar composition of (0.33250/0.66750)</u>						
283.156	0.3452	0.0144	17.895	0.022	-1.27	-1.32
273.156	0.2425	0.0083	12.723	0.018	-1.55	-1.69
263.158	0.1654	0.0099	8.833	0.013	-1.80	-1.91
253.164	0.1088	0.0048	5.946	0.010	-2.08	-2.22
<u>R-134a/1234ze(E) at a molar composition of (0.66356/0.33644)</u>						
281.158	0.3710	0.0088	20.308	0.014	-1.14	-1.28
273.155	0.2825	0.0195	15.564	0.026	-1.40	-1.65
263.152	0.1959	0.0037	10.943	0.007	-1.64	-1.86
253.154	0.1314	0.0126	7.514	0.014	-2.00	-2.32
<u>R-1234yf/1234ze(E) at a molar composition of (0.33584/0.66416)</u>						
283.156	0.3822	0.0119	19.231	0.015	-0.56	-0.71
273.157	0.2693	0.0086	13.687	0.012	-0.68	-0.82
263.155	0.1841	0.0180	9.517	0.020	-0.95	-0.99
253.156	0.1214	0.0047	6.408	0.007	-1.13	-1.29
<u>R-1234yf/1234ze(E) at a molar composition of (0.66660/0.33340)</u>						
281.158	0.3710	0.0088	20.308	0.014	-0.46	-0.51
273.155	0.2825	0.0195	15.564	0.026	-0.63	-0.85
263.152	0.1959	0.0037	10.943	0.007	-0.77	-1.11
253.154	0.1314	0.0126	7.514	0.014	-0.86	-0.94

A.1.3. Liquid-Phase Speed of Sound

Speed of sound instrument description. The speed of sound was measured over wide ranges of temperature and pressure in a dual-path, pulse-echo-type instrument. In this technique, a piezoelectric transducer is located within a sample volume of the test fluid. It is excited with a sinusoidal burst, near the crystal resonance frequency, thus emitting ultrasonic pulses from each face of the crystal, which travel through the fluid sample, reflect off planar surfaces at each end of the sample volume, and return to the transducer, which also serves as the detector. The difference in the arrival times of the echo signals give the speed of sound by

$$w = \frac{2(L_2 - L_1)}{\Delta t} \quad (\text{A.1-5})$$

where w is the speed of sound, L_1 and L_2 are the path lengths, and Δt is the time difference. The differential nature of this technique cancels end effects and improves the accuracy.

A quartz crystal with a diameter of 24 mm, thickness of 0.36 mm, and resonant frequency of 8.000 MHz served as the ultrasonic transducer. The quartz crystal was “X-cut,” which means that its thickness expands and contracts when a voltage is applied to electrodes on opposite faces of the crystal. It was excited with a 10-cycle sinusoidal burst from an arbitrary function generator. The fluid path lengths on the opposite faces of the crystal were 30 mm and 12 mm (ratio of 2.5:1); these separations of the crystal and the reflectors were provided by tubular spacers fabricated of a machinable ceramic. A high-speed switch connected the crystal to the function generator during the input sinusoidal burst and then, after a delay of 6 μs , switched the crystal to the input of a three-stage amplifier ($5\times$ per stage for a total of $125\times$), which then fed into a digital storage oscilloscope. The echo signals were recorded for off-line analysis.



Figure A.1-4. Dual-path, pulse-echo, speed of sound instrument

Shown are the thermostat (left of center, which contains the measuring cell) and the fluid manifold and pressure transducer; a vacuum system for evacuating the measuring cell is to the left of the thermostat.

The measuring cell holding the crystal and fluid sample was contained in a pressure vessel rated to 93 MPa. This, in turn, was held in a thermostated liquid bath operating from $-45\text{ }^{\circ}\text{C}$ to $150\text{ }^{\circ}\text{C}$.

A photo of the bath and associated fluid-handling manifold is shown as Figure A.1-4. A photo of the instruments (which were located in the adjacent room) is shown as Figure A.1-5. A schematic of the measuring cell is shown as Figure A.1-6.

The temperature of the fluid bath was measured with a long-stem 25-ohm standard platinum resistance thermometer (SPRT); the temperature-sensing portion of the SPRT was located immediately adjacent to the pressure vessel, as indicated in Figure A.1-6. The resistance of the SPRT was ratioed to a standard resistor with an AC resistance bridge. The pressure was measured with a vibrating-quartz-crystal pressure transducer with a maximum pressure of 138 MPa. The transducer was held at room temperature.



Figure A.1-5. Instrument rack for the pulse-echo speed of sound instrument

Speed of sound measurement sequence. The entire experiment was controlled by a PC running a custom control program. At each (T, p) state point multiple echo signals were recorded and analyzed. The pressure of the fluid sample and the temperature of the thermostat bath were scanned every 30 s. The approach to equilibrium conditions was determined by monitoring three quantities: (1) the difference of the average temperature computed over the previous eight scans compared to the set-point temperature; (2) the

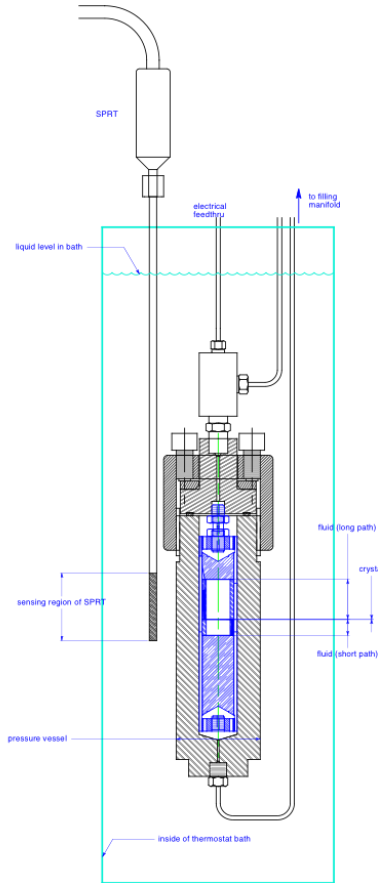


Figure A.1-6. Schematic diagram of the measuring cell inside the pressure vessel

standard deviation of the previous eight temperature scans; (3) the rate of change of pressure with time, computed with a linear fit of the previous eight pressure readings. When all three of these were within preset tolerances a “converged” flag was set in the control program, and measurements commenced following an additional equilibration time of 20 minutes. A single measurement set comprised recording three echo signals and the four temperature and pressure readings made at the start and end of the set and between the recording of the echoes. Four such sets, spaced 10 minutes apart, were recorded before moving to the next (T, p) state point. These raw data were analyzed with a separate program to generate the (T, p, w) data points.

When measurements at the first temperature were completed, the temperature was increased by an increment of 5 K or 10 K; since the cell was completely filled with liquid, the increase in temperature also increased the pressure. Measurements continued along this pseudoisochore (line of nearly constant density) until either the desired maximum temperature or maximum pressure was reached. The bath was then cooled to the starting temperature of the next isochore, and a portion of the sample in the measuring cell was vented to a waste bottle to achieve a starting pressure for the next isochore of 1 MPa or the saturation pressure (whichever was greater). The next isochore then commenced. This process was repeated to cover the liquid surface.

Speed of sound calibrations and measurement uncertainties. The difference of the path lengths in the measuring cell, i.e., $(L_2 - L_1)$ in Eq. (A.1-4), was calibrated as a function of temperature and

pressure with measurements on propane over the temperature range of 260 K to 420 K, with pressures to 56 MPa. The propane speed of sound, as calculated with the equation of state (EOS) of Lemmon et al.[101], was taken as the known quantity in the calibration. The EOS, in turn, represents the high-accuracy propane measurements of Meier and Kabelac [102] with an average absolute deviation of 0.012 %. The RMS deviation of the calibration equation from the measurements was 0.010 %. Combining, in quadrature, the deviation of the EOS from the data of Meier and Kabelac [102] with the deviation of the path-length calibration equation from the present measurements yields an estimated combined standard uncertainty of 0.016 % arising from the calibration.

The SPRT, standard resistor, and resistance bridge were calibrated as a system over the range of 234.316 K to 429.749 K (–38.834 °C to 156.599 °C) with fixed-point cells (mercury triple point, water triple point, and indium freezing point). The standard uncertainty in the SPRT/resistor/bridge system was estimated as 3 mK. The short-term (minute-to-minute) variations in the fluid-bath temperature were 2 mK or less. No long-term (hour-to-hour) variation was observed. The temperature gradients in the bath were less than 2.5 mK over the region of the pressure vessel. The combined standard ($k = 1$) uncertainty in the temperature measurement, including the effects of the SPRT, standard resistor, resistance bridge, calibration standards, stability of the fluid bath, and temperature gradients in the bath was 4 mK.

The pressure transducer was calibrated by the manufacturer with piston gages; this calibration included a temperature-compensation term. The zero of the transducer was checked regularly (while the system was evacuated between samples) and readings were corrected for any drift in the zero. The standard uncertainty in pressure was 0.007 MPa.

When reporting the uncertainties in experimental data it is customary to combine the effects of the state-point uncertainty (i.e., the effects of the uncertainties in temperature, pressure, and composition) with those in the uncertainty of the primary measurand (i.e., the speed of sound):

$$U_c(w) = 2 \times 100 \times \left\{ u^2(w) + \left[\frac{\partial w}{\partial T} \right]^2 u^2(T) + \left[\frac{\partial w}{\partial p} \right]^2 u^2(p) \right\} / w , \quad (\text{A.1-6})$$

where the $u(x)$ are the standard ($k = 1$) uncertainties in the different measurands (temperature, pressure, and speed of sound), the derivatives of the speed of sound with temperature and pressure are computed with an equation of state. The coverage factor of 2 corresponds to a 95 % confidence interval, and the factor of 100 converts the relative deviation to a percentage deviation. The $U_c(w)$ is the relative, combined, expanded ($k = 2$) uncertainty in the speed of sound; it averaged 0.07 % for the present measurements.

Speed of sound results. An example of the measurements carried out are depicted in Figure 3.1-2. The measured data, as well as the relative, combined, expanded ($k = 2$) uncertainty in the speed of sound for each point, are reported in Tables A.1-20 through A.1-25. As indicated above, the data in these tables are the averages of four sets of three replicates each.

Table A.1-20. Measured speed of sound data for the system R-1234yf/134a at a molar composition of (0.33634/0.66366)

Listed for Tables A.1-20 through A.1-25 are temperature T , pressure p , speed of sound w , relative combined, expanded ($k = 2$) state point uncertainty in the speed of sound U_c , and relative deviation from the mixture EOS. Average values for the replicate measurements at each (T, p) state point are given.

T/K	p/MPa	$w/\text{m}\cdot\text{s}^{-1}$	$U_c/\%$	$\Delta w/\%$
230.013	0.353	790.84	0.041	-0.037
235.007	0.658	769.59	0.041	-0.019
240.004	0.678	746.67	0.042	-0.009
245.004	0.690	723.74	0.044	-0.002
250.005	0.704	700.89	0.046	0.002
254.995	1.231	682.11	0.047	0.019
259.987	5.247	689.09	0.045	-0.027
264.996	9.178	695.40	0.044	-0.060
254.993	0.651	677.79	0.048	0.026
259.986	4.420	683.24	0.046	-0.017
264.996	8.392	690.07	0.045	-0.056
269.993	12.399	697.15	0.043	-0.086
259.986	1.278	659.86	0.049	0.025
264.995	5.122	666.92	0.047	-0.023
269.993	9.068	674.67	0.046	-0.062
274.996	12.964	681.96	0.044	-0.088
264.994	1.260	637.06	0.052	0.032
269.991	4.977	644.66	0.050	-0.018
274.995	8.710	652.21	0.048	-0.058
279.999	12.442	659.66	0.046	-0.088
269.991	1.167	613.65	0.055	0.043
274.995	4.716	621.41	0.053	-0.008
280.000	8.276	629.11	0.050	-0.049
285.001	11.853	636.78	0.048	-0.085
274.993	1.193	591.14	0.059	0.049
279.999	4.586	599.13	0.056	0.000
285.000	7.981	606.95	0.053	-0.042
290.003	11.378	614.61	0.051	-0.077
279.998	0.890	565.36	0.064	0.061
285.000	4.124	573.74	0.060	0.009
290.003	7.359	581.87	0.057	-0.032
294.998	10.590	589.77	0.054	-0.065
284.998	1.183	545.28	0.068	0.063

Table A.1-20. Measured speed of sound data for the system R-1234yf/134a at a molar composition of (0.33634/0.66366) (continued)

T/K	p/MPa	$w/m \cdot s^{-1}$	$U_c/\%$	$\Delta w/\%$
290.001	4.259	553.65	0.064	0.014
294.997	7.347	561.90	0.060	-0.026
299.998	10.440	569.91	0.057	-0.059
290.000	1.199	522.32	0.074	0.065
294.997	4.134	531.05	0.069	0.020
299.999	7.087	539.59	0.065	-0.017
304.998	10.041	547.87	0.061	-0.048
294.996	1.213	499.13	0.081	0.061
299.998	4.004	508.17	0.075	0.032
304.998	6.801	516.85	0.070	-0.001
310.000	9.603	525.24	0.066	-0.031
299.997	1.313	476.73	0.089	0.059
304.996	3.957	485.96	0.082	0.036
309.999	6.613	494.84	0.076	0.011
314.995	9.266	503.35	0.071	-0.013
304.995	1.397	453.89	0.099	0.046
309.998	3.908	463.47	0.091	0.037
314.995	6.420	472.55	0.084	0.022
320.004	8.941	481.25	0.078	0.002
309.997	1.503	431.03	0.111	0.025
314.994	3.859	440.71	0.101	0.036
320.004	6.236	450.01	0.092	0.033
325.009	8.608	458.78	0.085	0.020
314.992	1.733	409.82	0.124	0.002
320.002	3.960	419.66	0.112	0.027
325.008	6.201	429.07	0.102	0.035
330.000	8.441	437.99	0.094	0.032
320.002	1.827	386.04	0.142	-0.051
325.008	3.924	396.35	0.127	0.013
330.000	6.023	405.99	0.115	0.041
335.004	8.112	414.85	0.105	0.050
325.006	2.025	363.70	0.164	-0.095
329.999	3.980	374.21	0.145	0.009
335.002	5.935	383.73	0.130	0.045
340.007	7.905	392.88	0.118	0.062
329.998	2.229	341.01	0.191	-0.208
335.002	4.041	351.53	0.167	-0.051
340.007	5.877	361.47	0.148	0.022

Table A.1-20. Measured speed of sound data for the system R-1234yf/134a at a molar composition of (0.33634/0.66366) (continued)

T/K	p/MPa	$w/\text{m}\cdot\text{s}^{-1}$	$U_c/\%$	$\Delta w/\%$
345.013	7.718	370.79	0.134	0.067
335.001	2.392	317.01	0.230	-0.294
340.006	4.087	328.15	0.198	-0.093
345.013	5.792	338.36	0.173	0.018
340.006	2.607	293.45	0.282	-0.418
345.012	4.167	304.49	0.237	-0.265
345.012	2.910	271.59	0.345	-0.597

Table A.1-21. Measured speed of sound data for the system R-1234yf/134a at a molar composition of (0.66759/0.33241)

T/K	p/MPa	$w/m\cdot s^{-1}$	$U_c/\%$	$\Delta w/\%$
235.007	0.663	746.03	0.043	-0.026
240.002	0.672	723.28	0.044	-0.019
245.003	0.694	700.73	0.046	-0.007
250.004	0.708	678.16	0.048	-0.002
254.995	0.720	655.72	0.050	0.008
259.987	2.996	651.70	0.050	0.011
264.997	6.626	658.38	0.048	-0.019
269.993	10.288	665.31	0.046	-0.042
260.001	0.801	633.95	0.053	0.039
264.995	4.338	640.85	0.051	0.002
269.993	7.925	648.05	0.049	-0.027
274.995	11.487	654.98	0.047	-0.048
264.994	1.250	615.38	0.055	0.041
269.992	4.705	622.85	0.053	0.004
274.995	8.164	630.22	0.050	-0.024
280.000	11.622	637.48	0.049	-0.045
269.990	1.132	591.90	0.059	0.035
274.995	4.413	599.48	0.056	0.007
279.999	7.714	607.04	0.053	-0.023
285.001	11.008	614.44	0.051	-0.044
274.994	1.218	570.34	0.062	0.051
279.999	4.366	578.19	0.059	0.014
285.001	7.517	585.89	0.056	-0.016
290.002	10.656	593.38	0.054	-0.032
279.998	1.243	548.15	0.067	0.060
284.999	4.239	556.18	0.063	0.026
290.003	7.244	564.05	0.060	-0.002
294.998	10.251	571.77	0.057	-0.026
284.998	1.205	525.15	0.073	0.061
290.002	4.071	533.56	0.068	0.029
294.998	6.933	541.67	0.064	0.001
299.998	9.802	549.61	0.061	-0.021
290.000	1.169	501.82	0.080	0.034
294.997	3.881	510.45	0.074	0.015
299.999	6.601	518.81	0.070	-0.001
304.997	9.317	526.84	0.066	-0.017
294.995	1.281	480.27	0.087	0.045
299.998	3.860	489.10	0.081	0.029

Table A.1-21. Measured speed of sound data for the system R-1234yf/134a at a molar composition of (0.66759/0.33241) (continued)

T/K	p/MPa	$w/\text{m}\cdot\text{s}^{-1}$	$U_c/\%$	$\Delta w/\%$
304.998	6.446	497.61	0.075	0.010
309.999	9.038	505.86	0.071	-0.009
299.996	0.972	452.68	0.099	0.009
304.996	3.395	461.90	0.091	0.009
309.999	5.829	470.77	0.084	0.001
314.994	8.257	479.23	0.079	-0.005
304.995	1.420	435.21	0.107	-0.003
309.998	3.733	444.58	0.098	0.003
314.994	6.045	453.48	0.091	0.006
320.004	8.354	461.92	0.084	0.015
309.996	1.406	411.00	0.123	-0.011
314.994	3.578	420.69	0.111	0.017
320.003	5.762	429.89	0.101	0.029
325.009	7.944	438.60	0.094	0.031
314.992	1.632	390.16	0.137	-0.035
320.001	3.686	400.08	0.124	0.011
325.008	5.741	409.38	0.112	0.035
329.999	7.794	418.17	0.103	0.042
320.001	1.869	369.14	0.156	-0.114
325.008	3.802	379.36	0.139	-0.033
330.000	5.728	388.77	0.126	0.012
335.006	7.635	397.31	0.115	0.043
325.006	1.989	345.81	0.182	-0.168
329.998	3.782	356.19	0.161	-0.055
335.003	5.578	365.68	0.144	-0.007
340.008	7.384	374.72	0.131	0.022
329.998	2.169	323.07	0.218	-0.266
335.003	3.829	333.61	0.188	-0.083
340.008	5.503	343.40	0.167	-0.004
345.013	7.185	352.57	0.150	0.035
335.001	2.323	299.00	0.266	-0.402
340.004	3.868	309.86	0.226	-0.259
345.013	5.424	320.37	0.197	-0.033
340.005	2.580	277.01	0.327	-0.523
345.013	3.999	288.20	0.272	-0.250

Table A.1-22. Measured speed of sound data for the system R-134a/1234ze(E) at a molar composition of (0.32916/0.67084)

T/K	p/MPa	$w/m\cdot s^{-1}$	$U_c/\%$	$\Delta w/\%$
235.008	0.525	812.57	0.039	0.481
240.003	0.537	789.62	0.040	0.454
245.004	0.541	766.62	0.041	0.417
250.004	0.549	743.64	0.042	0.369
254.994	0.553	720.81	0.044	0.332
259.987	0.559	698.02	0.046	0.295
269.992	1.140	657.06	0.050	0.246
274.995	4.782	663.40	0.048	0.227
280.000	8.458	669.98	0.046	0.200
285.001	12.144	676.62	0.045	0.170
290.003	15.823	683.20	0.044	0.140
294.998	19.487	689.68	0.043	0.110
299.999	23.144	696.07	0.042	0.083
304.997	26.739	702.09	0.041	0.060
310.000	30.316	707.98	0.040	0.039
314.994	33.894	713.91	0.040	0.020
320.004	37.460	719.74	0.039	0.005
325.010	41.009	725.47	0.038	-0.010
330.000	44.515	731.03	0.038	-0.021
335.004	47.984	736.38	0.038	-0.031
340.009	51.440	741.68	0.037	-0.039
274.989	1.010	633.32	0.052	0.206
279.995	4.674	641.29	0.050	0.179
284.997	8.321	649.02	0.048	0.151
290.000	11.947	656.43	0.047	0.117
294.995	15.574	663.80	0.045	0.086
299.996	19.173	670.85	0.044	0.058
304.995	22.769	677.82	0.043	0.032
309.998	26.350	684.61	0.042	0.010
314.993	29.899	691.17	0.041	-0.010
320.005	33.452	697.64	0.040	-0.030
325.008	36.980	703.96	0.040	-0.045
329.999	40.468	710.07	0.039	-0.057
335.004	43.903	715.84	0.039	-0.068
340.008	47.327	721.56	0.038	-0.075
345.014	50.738	727.19	0.038	-0.081
279.994	0.983	610.28	0.056	0.164
284.996	4.446	618.17	0.053	0.134

Table A.1-22. Measured speed of sound data for the system R-134a/1234ze(E) at a molar composition of (0.32916/0.67084) (continued)

T/K	p/MPa	$w/m \cdot s^{-1}$	$U_c/\%$	$\Delta w/\%$
289.998	7.896	625.79	0.051	0.100
294.994	11.388	633.58	0.049	0.061
299.996	14.861	641.10	0.047	0.030
304.995	18.318	648.38	0.046	0.001
309.997	21.756	655.44	0.045	-0.024
314.993	25.181	662.33	0.043	-0.046
320.003	28.593	669.03	0.043	-0.064
325.009	31.978	675.51	0.042	-0.081
330.000	35.346	681.89	0.041	-0.094
335.003	38.647	687.82	0.040	-0.104
340.008	41.950	693.72	0.040	-0.116
345.012	45.243	699.54	0.039	-0.124
284.995	1.030	587.84	0.060	0.116
289.997	4.364	596.15	0.056	0.081
294.994	7.702	604.29	0.054	0.047
299.996	11.081	612.50	0.052	0.008
304.995	14.423	620.29	0.050	-0.019
309.997	17.750	627.78	0.048	-0.049
314.992	21.047	634.96	0.046	-0.071
320.001	24.301	641.73	0.045	-0.087
325.008	27.528	648.23	0.044	-0.107
329.999	30.759	654.73	0.043	-0.124
335.003	33.970	661.02	0.042	-0.139
340.008	37.171	667.20	0.041	-0.151
345.013	40.356	673.25	0.041	-0.161
289.996	1.161	566.13	0.064	0.053
294.992	4.345	574.65	0.060	0.021
299.994	7.543	583.01	0.057	-0.011
304.994	10.731	591.05	0.054	-0.040
309.996	13.911	598.82	0.052	-0.068
314.992	17.077	606.34	0.050	-0.092
320.003	20.248	613.69	0.049	-0.115
325.008	23.442	621.11	0.047	-0.133
329.999	26.574	628.01	0.046	-0.150
335.003	29.665	634.47	0.045	-0.172
340.006	32.755	640.89	0.044	-0.188
345.014	35.827	647.15	0.043	-0.197
294.991	0.899	540.26	0.070	-0.026

Table A.1-22. Measured speed of sound data for the system R-134a/1234ze(E) at a molar composition of (0.32916/0.67084) (continued)

T/K	p/MPa	$w/\text{m}\cdot\text{s}^{-1}$	$U_c/\%$	$\Delta w/\%$
299.994	3.918	549.04	0.065	-0.047
304.993	6.942	557.56	0.062	-0.069
309.996	9.974	565.85	0.059	-0.093
314.991	12.986	573.78	0.056	-0.112
320.001	15.983	581.33	0.054	-0.131
325.007	18.972	588.66	0.052	-0.152
329.999	21.942	595.75	0.050	-0.171
335.003	24.877	602.46	0.048	-0.188
340.007	27.825	609.15	0.047	-0.205
345.013	30.764	615.69	0.046	-0.220
299.991	0.756	515.11	0.077	-0.120
304.993	3.626	524.27	0.072	-0.121
309.995	6.506	533.14	0.067	-0.128
314.991	9.373	541.58	0.063	-0.137
320.001	12.244	549.72	0.060	-0.150
325.007	15.100	557.52	0.057	-0.164
329.998	17.941	565.04	0.055	-0.181
335.002	20.767	572.22	0.053	-0.201
340.008	23.590	579.25	0.051	-0.219
345.013	26.400	586.06	0.049	-0.237
304.991	1.377	498.72	0.081	-0.199
309.994	4.125	507.93	0.076	-0.180
314.990	6.876	516.79	0.071	-0.169
320.001	9.632	525.29	0.067	-0.169
325.007	12.380	533.43	0.063	-0.175
329.998	15.115	541.25	0.060	-0.187
335.003	17.824	548.60	0.057	-0.205
340.008	20.519	555.69	0.055	-0.220
345.013	23.229	562.73	0.053	-0.243
309.993	1.253	473.32	0.091	-0.314
314.989	3.848	482.89	0.084	-0.253
320.000	6.456	492.03	0.078	-0.217
325.006	9.061	500.75	0.073	-0.201
329.997	11.654	509.07	0.069	-0.197
335.002	14.232	516.91	0.065	-0.205
340.007	16.806	524.47	0.062	-0.220
345.012	19.379	531.84	0.059	-0.239
314.990	1.546	453.04	0.100	-0.412

Table A.1-22. Measured speed of sound data for the system R-134a/1234ze(E) at a molar composition of (0.32916/0.67084) (continued)

T/K	p/MPa	$w/m\cdot s^{-1}$	$U_c/\%$	$\Delta w/\%$
319.999	4.024	462.90	0.092	-0.314
325.005	6.490	472.10	0.085	-0.248
329.997	8.953	480.84	0.079	-0.216
335.002	11.402	489.00	0.074	-0.211
340.008	13.858	496.96	0.070	-0.217
345.013	16.312	504.64	0.066	-0.231
319.999	1.756	431.60	0.111	-0.501
325.005	4.078	441.42	0.101	-0.352
329.997	6.412	450.80	0.093	-0.268
335.001	8.742	459.60	0.087	-0.227
340.007	11.076	468.04	0.081	-0.212
345.013	13.404	476.10	0.076	-0.216
325.005	1.948	409.78	0.125	-0.573
329.997	4.146	419.95	0.113	-0.385
335.001	6.350	429.46	0.104	-0.279
340.007	8.553	438.42	0.095	-0.224
345.012	10.760	446.98	0.089	-0.207
329.998	2.044	386.06	0.144	-0.663
335.002	4.096	396.26	0.129	-0.437
340.006	6.157	405.92	0.117	-0.296
345.013	8.225	415.07	0.107	-0.229
335.000	2.385	366.39	0.163	-0.697
340.006	4.329	377.01	0.145	-0.415
345.013	6.278	386.87	0.130	-0.261
340.005	2.348	338.90	0.199	-0.781
345.013	4.140	349.93	0.174	-0.421
345.010	2.550	315.54	0.238	-0.802

Table A.1-23. Measured speed of sound data for the system R-134a/1234ze(E) at a molar composition of (0.67102/0.32898)

T/K	p/MPa	$w/m \cdot s^{-1}$	$U_c/\%$	$\Delta w/\%$
229.997	0.131	829.10	0.039	0.476
235.007	0.589	808.34	0.039	0.478
240.004	0.609	785.19	0.040	0.466
245.006	0.605	761.97	0.041	0.455
250.005	0.609	738.83	0.043	0.433
254.994	0.618	715.85	0.044	0.416
259.988	0.611	692.86	0.046	0.411
269.993	5.812	685.99	0.045	0.335
274.995	9.842	693.24	0.044	0.287
280.000	13.884	700.47	0.043	0.243
285.001	17.913	707.56	0.042	0.204
290.003	21.919	714.46	0.041	0.168
294.998	25.905	721.19	0.040	0.135
299.999	29.876	727.77	0.039	0.106
304.998	33.823	734.20	0.039	0.080
310.000	37.736	740.43	0.038	0.057
314.995	41.622	746.51	0.038	0.034
320.004	45.494	752.47	0.037	0.014
269.993	3.174	666.80	0.048	0.367
274.995	7.130	674.44	0.046	0.309
280.000	11.085	681.95	0.045	0.257
285.001	15.028	689.29	0.043	0.211
290.003	18.959	696.46	0.042	0.170
294.999	22.863	703.42	0.041	0.135
299.999	26.745	710.16	0.040	0.101
304.998	30.611	716.76	0.040	0.072
310.000	34.457	723.21	0.039	0.046
314.993	38.265	729.45	0.039	0.024
320.004	42.025	735.38	0.038	0.003
325.008	45.773	741.24	0.038	-0.018
269.987	1.099	650.78	0.050	0.393
274.991	4.970	658.61	0.048	0.330
279.996	8.848	666.34	0.046	0.272
284.998	12.716	673.89	0.045	0.221
290.001	16.573	681.26	0.044	0.177
294.996	20.399	688.35	0.043	0.137
299.998	24.212	695.26	0.042	0.101
304.997	28.005	702.00	0.041	0.070

Table A.1-23. Measured speed of sound data for the system R-134a/1234ze(E) at a molar composition of (0.67102/0.32898) (continued)

T/K	p/MPa	$w/m \cdot s^{-1}$	$U_c/\%$	$\Delta w/\%$
309.999	31.782	708.59	0.040	0.042
314.996	35.538	715.02	0.039	0.016
320.004	39.328	721.55	0.039	-0.007
325.009	43.044	727.69	0.038	-0.027
330.000	46.700	733.54	0.038	-0.044
335.004	50.316	739.13	0.037	-0.063
274.990	1.038	627.36	0.053	0.382
279.995	4.733	635.34	0.051	0.313
284.997	8.434	643.22	0.049	0.252
290.000	12.131	650.91	0.047	0.198
294.995	15.817	658.41	0.046	0.149
299.997	19.484	665.63	0.044	0.107
304.995	23.137	672.69	0.043	0.071
309.998	26.772	679.54	0.042	0.038
314.994	30.385	686.21	0.041	0.010
320.004	33.986	692.71	0.040	-0.016
325.009	37.562	699.04	0.040	-0.039
330.000	41.101	705.15	0.039	-0.060
335.003	44.595	710.97	0.039	-0.080
340.007	48.088	716.76	0.038	-0.098
279.994	1.100	604.88	0.057	0.363
284.996	4.633	613.08	0.054	0.292
289.999	8.175	621.14	0.051	0.229
294.995	11.707	628.97	0.049	0.174
299.996	15.229	636.54	0.048	0.125
304.996	18.740	643.90	0.046	0.082
309.997	22.215	650.90	0.045	0.045
314.994	25.689	657.82	0.044	0.012
320.003	29.154	664.55	0.043	-0.018
325.009	32.599	671.10	0.042	-0.045
330.000	36.014	677.47	0.041	-0.068
335.004	39.380	683.47	0.040	-0.090
340.008	42.752	689.47	0.040	-0.110
345.013	46.114	695.38	0.039	-0.128
284.995	1.402	584.62	0.060	0.339
289.997	4.794	593.04	0.057	0.267
294.995	8.187	601.25	0.054	0.205
299.996	11.580	609.23	0.052	0.148

Table A.1-23. Measured speed of sound data for the system R-134a/1234ze(E) at a molar composition of (0.67102/0.32898) (continued)

T/K	p/MPa	$w/\text{m}\cdot\text{s}^{-1}$	$U_c/\%$	$\Delta w/\%$
304.994	14.949	616.85	0.050	0.100
309.997	18.320	624.30	0.048	0.057
314.992	21.683	631.61	0.046	0.020
320.002	25.028	638.61	0.045	-0.013
325.009	28.354	645.41	0.044	-0.043
330.000	31.643	651.94	0.043	-0.069
335.003	34.896	658.15	0.042	-0.094
340.009	38.152	664.32	0.041	-0.116
345.013	41.393	670.37	0.041	-0.136
289.996	1.173	559.27	0.065	0.318
294.993	4.392	567.96	0.061	0.249
299.994	7.623	576.43	0.058	0.187
304.994	10.850	584.61	0.055	0.133
309.996	14.070	592.50	0.053	0.084
314.993	17.273	600.08	0.051	0.042
320.002	20.478	607.48	0.049	0.003
325.008	23.661	614.60	0.047	-0.031
330.000	26.822	621.49	0.046	-0.061
335.002	29.939	627.95	0.045	-0.091
340.007	33.106	634.64	0.044	-0.119
345.012	36.236	641.04	0.043	-0.141
294.991	1.056	534.63	0.071	0.286
299.994	4.110	543.54	0.066	0.226
304.993	7.173	552.18	0.063	0.169
309.996	10.239	560.54	0.059	0.118
314.991	13.297	568.59	0.056	0.072
320.003	16.348	576.32	0.054	0.032
325.008	19.388	583.79	0.052	-0.006
329.997	22.381	590.80	0.050	-0.042
335.002	25.368	597.59	0.048	-0.075
340.009	28.359	604.32	0.047	-0.104
345.012	31.341	610.89	0.046	-0.131
299.992	1.274	513.38	0.077	0.249
304.992	4.193	522.57	0.071	0.198
309.995	7.123	531.46	0.067	0.148
314.992	10.048	539.99	0.063	0.105
320.001	12.974	548.17	0.060	0.061
325.007	15.890	556.02	0.057	0.020

Table A.1-23. Measured speed of sound data for the system R-134a/1234ze(E) at a molar composition of (0.67102/0.32898) (continued)

T/K	p/MPa	$w/\text{m}\cdot\text{s}^{-1}$	$U_c/\%$	$\Delta w/\%$
329.999	18.784	563.55	0.055	-0.017
335.002	21.654	570.67	0.052	-0.053
340.007	24.524	577.65	0.051	-0.086
345.013	27.388	584.46	0.049	-0.116
304.992	1.802	495.84	0.082	0.209
309.995	4.602	505.21	0.076	0.171
314.990	7.403	514.17	0.071	0.131
320.001	10.211	522.77	0.067	0.092
325.007	13.007	530.95	0.063	0.053
329.998	15.788	538.80	0.060	0.015
335.002	18.543	546.15	0.057	-0.026
340.008	21.304	553.38	0.055	-0.062
345.013	24.059	560.42	0.053	-0.096
309.994	1.809	472.09	0.091	0.162
314.990	4.450	481.66	0.084	0.146
320.002	7.105	490.82	0.078	0.123
325.006	9.758	499.55	0.073	0.090
329.999	12.400	507.86	0.068	0.057
335.003	15.021	515.63	0.065	0.015
340.007	17.643	523.20	0.061	-0.024
345.013	20.252	530.47	0.059	-0.056
314.990	1.964	449.98	0.101	0.109
319.999	4.471	459.83	0.092	0.125
325.006	6.981	469.12	0.085	0.116
329.998	9.484	477.92	0.079	0.094
335.003	11.973	486.12	0.074	0.057
340.007	14.470	494.12	0.070	0.020
345.013	16.965	501.84	0.066	-0.016
319.999	2.064	426.84	0.114	0.062
325.006	4.432	436.97	0.103	0.103
329.997	6.793	446.45	0.094	0.115
335.002	9.139	455.13	0.087	0.096
340.007	11.502	463.64	0.081	0.070
345.013	13.861	471.75	0.076	0.037
325.004	1.764	396.62	0.136	-0.038
329.997	3.937	406.94	0.122	0.060
335.002	6.104	416.39	0.111	0.106
340.007	8.292	425.54	0.101	0.112

Table A.1-23. Measured speed of sound data for the system R-134a/1234ze(E) at a molar composition of (0.67102/0.32898) (continued)

T/K	p/MPa	$w/\text{m}\cdot\text{s}^{-1}$	$U_c/\%$	$\Delta w/\%$
345.013	10.485	434.26	0.093	0.096
329.996	2.021	374.75	0.155	-0.123
335.001	4.057	385.21	0.138	0.031
340.007	6.114	395.14	0.124	0.097
345.013	8.179	404.50	0.113	0.117
335.001	2.355	354.21	0.177	-0.179
340.007	4.283	365.13	0.155	0.004
345.013	6.220	375.25	0.139	0.094
340.007	2.528	330.08	0.211	-0.286
345.012	4.316	341.30	0.182	-0.048
345.013	2.760	306.71	0.253	-0.390

Table A.1-24. Measured speed of sound data for the system R-1234yf/1234ze(E) at a molar composition of (0.33584/0.66416)

T/K	p/MPa	$w/m \cdot s^{-1}$	$U_c/\%$	$\Delta w/\%$
229.999	0.263	806.07	0.039	0.280
230.014	0.267	806.10	0.039	0.290
235.008	0.521	784.77	0.040	0.266
240.003	0.542	761.96	0.041	0.211
245.003	0.534	739.27	0.043	0.187
250.004	0.543	716.62	0.044	0.145
254.995	0.542	694.03	0.046	0.109
259.987	0.551	671.60	0.048	0.080
264.995	0.547	649.01	0.051	0.052
269.992	2.854	645.90	0.050	0.075
269.991	2.931	646.50	0.050	0.072
274.995	6.403	652.94	0.049	0.075
279.999	9.895	659.50	0.047	0.065
269.991	1.097	631.33	0.053	0.052
274.994	4.515	638.06	0.051	0.056
279.999	7.939	644.80	0.049	0.048
285.000	11.337	651.32	0.047	0.034
274.993	1.131	609.30	0.056	0.017
279.998	4.419	616.37	0.054	0.016
285.000	7.667	623.04	0.052	0.003
290.002	10.969	630.08	0.050	-0.017
279.997	1.194	587.52	0.059	-0.022
285.000	4.323	594.65	0.057	-0.029
290.002	7.458	601.75	0.054	-0.045
294.998	10.584	608.69	0.052	-0.063
284.999	1.104	564.22	0.064	-0.073
290.001	4.108	571.77	0.061	-0.082
294.997	7.105	579.14	0.058	-0.096
299.999	10.097	586.32	0.055	-0.113
290.000	1.075	541.34	0.069	-0.134
294.997	3.934	549.11	0.065	-0.140
299.999	6.792	556.67	0.062	-0.150
304.997	9.651	564.09	0.059	-0.161
294.995	1.063	518.44	0.075	-0.215
299.998	3.801	526.62	0.071	-0.205
304.996	6.527	534.46	0.067	-0.203
309.999	9.236	541.90	0.063	-0.204
299.996	1.352	498.92	0.081	-0.291

Table A.1-24. Measured speed of sound data for the system R-1234yf/1234ze(E) at a molar composition of (0.33584/0.66416) (continued)

T/K	p/MPa	$w/\text{m}\cdot\text{s}^{-1}$	$U_c/\%$	$\Delta w/\%$
304.996	3.965	507.27	0.076	-0.265
309.999	6.596	515.51	0.071	-0.249
314.994	9.206	523.32	0.067	-0.238
304.994	1.235	474.32	0.090	-0.399
309.998	3.713	483.04	0.084	-0.338
314.994	6.188	491.40	0.078	-0.297
320.003	8.666	499.42	0.074	-0.272
309.997	1.379	452.78	0.100	-0.490
314.993	3.723	461.69	0.092	-0.391
320.004	6.073	470.18	0.086	-0.325
325.009	8.419	478.31	0.080	-0.285
314.992	1.642	432.89	0.110	-0.558
320.002	3.877	442.08	0.101	-0.420
325.008	6.112	450.77	0.093	-0.333
329.999	8.337	459.02	0.087	-0.282
320.001	1.562	407.47	0.127	-0.657
325.007	3.651	416.91	0.115	-0.457
329.999	5.740	425.83	0.106	-0.338
335.003	7.817	434.09	0.098	-0.272
325.006	1.684	384.70	0.145	-0.719
329.998	3.647	394.49	0.131	-0.464
335.003	5.598	403.39	0.120	-0.313
340.007	7.566	412.01	0.110	-0.241
329.998	1.945	364.29	0.165	-0.703
335.002	3.785	374.11	0.148	-0.417
340.007	5.635	383.35	0.134	-0.265
345.013	7.491	392.12	0.123	-0.191
335.001	2.049	340.38	0.197	-0.696
340.006	3.780	350.84	0.174	-0.360
345.012	5.516	360.52	0.155	-0.193
340.006	2.260	318.25	0.235	-0.612
345.012	3.869	328.91	0.204	-0.258
345.012	2.476	295.80	0.286	-0.475

Table A.1-25. Measured speed of sound data for the system R-1234yf/1234ze(E) at a molar composition of (0.66660/0.33340)

T/K	p/MPa	$w/m \cdot s^{-1}$	$U_c/\%$	$\Delta w/\%$
229.998	0.450	777.99	0.041	0.161
235.008	0.591	756.13	0.042	0.164
240.004	0.607	733.50	0.043	0.145
245.003	0.616	710.97	0.045	0.133
250.005	0.624	688.51	0.047	0.124
254.994	0.792	667.55	0.049	0.135
259.987	4.524	674.41	0.047	0.138
269.993	11.961	687.78	0.045	0.121
259.986	1.160	648.25	0.051	0.129
265.003	4.628	654.24	0.049	0.126
269.990	8.269	661.67	0.047	0.116
274.995	11.836	668.41	0.046	0.102
264.994	1.127	625.75	0.054	0.121
269.991	4.572	633.05	0.052	0.110
274.995	8.070	640.62	0.049	0.093
280.000	11.531	647.83	0.048	0.078
269.991	1.128	603.60	0.057	0.111
274.994	4.428	611.11	0.054	0.094
280.000	7.740	618.59	0.052	0.076
285.001	11.049	625.95	0.050	0.056
274.993	1.123	581.33	0.061	0.096
279.999	4.282	589.10	0.058	0.077
285.000	7.446	596.77	0.055	0.055
290.002	10.608	604.28	0.053	0.034
279.997	1.130	559.12	0.065	0.076
285.000	4.140	567.06	0.061	0.054
290.003	7.161	574.92	0.058	0.032
294.997	10.166	582.50	0.056	0.012
284.999	1.148	536.92	0.070	0.045
290.001	4.005	545.01	0.066	0.032
294.998	6.873	552.95	0.062	0.010
299.999	9.747	560.75	0.059	-0.009
290.000	1.030	513.07	0.077	0.012
294.997	3.758	521.57	0.072	-0.001
299.998	6.487	529.78	0.068	-0.015
304.998	9.212	537.70	0.064	-0.030
294.995	1.070	490.76	0.084	-0.037
299.998	3.690	499.76	0.078	-0.044

Table A.1-25. Measured speed of sound data for the system R-1234yf/1234ze(E) at a molar composition of (0.66660/0.33340) (continued)

T/K	p/MPa	$w/m \cdot s^{-1}$	$U_c/\%$	$\Delta w/\%$
304.997	6.300	508.33	0.073	-0.047
309.998	8.904	516.52	0.069	-0.054
299.996	1.030	467.14	0.093	-0.099
304.996	3.494	476.27	0.086	-0.079
310.000	5.961	485.01	0.080	-0.071
314.993	8.401	493.16	0.075	-0.063
304.995	1.196	446.00	0.103	-0.157
309.998	3.530	455.33	0.095	-0.110
314.994	5.869	464.26	0.088	-0.086
320.004	8.211	472.78	0.082	-0.074
309.997	0.984	418.91	0.119	-0.235
314.993	3.165	428.60	0.108	-0.148
320.005	5.351	437.71	0.100	-0.097
325.008	7.532	446.32	0.092	-0.077
314.991	1.535	403.52	0.129	-0.254
320.002	3.623	413.31	0.116	-0.151
325.008	5.715	422.57	0.107	-0.093
329.999	7.793	431.19	0.098	-0.069
320.002	1.614	380.30	0.148	-0.301
325.008	3.572	390.39	0.133	-0.159
329.999	5.527	399.80	0.121	-0.085
335.004	7.472	408.44	0.111	-0.057

A.1.4. Liquid-phase Viscosity Measurements

Instrument description. Dynamic viscosity measurements utilized a commercial oscillating piston viscometer (OPV). The instrument employs a variant of the falling body technique where the viscosity is determined from the time it takes a sensing element to travel a particular distance in a measurement chamber filled with sample liquid. A schematic of the main body of the instrument is shown in Figure A.1-7.

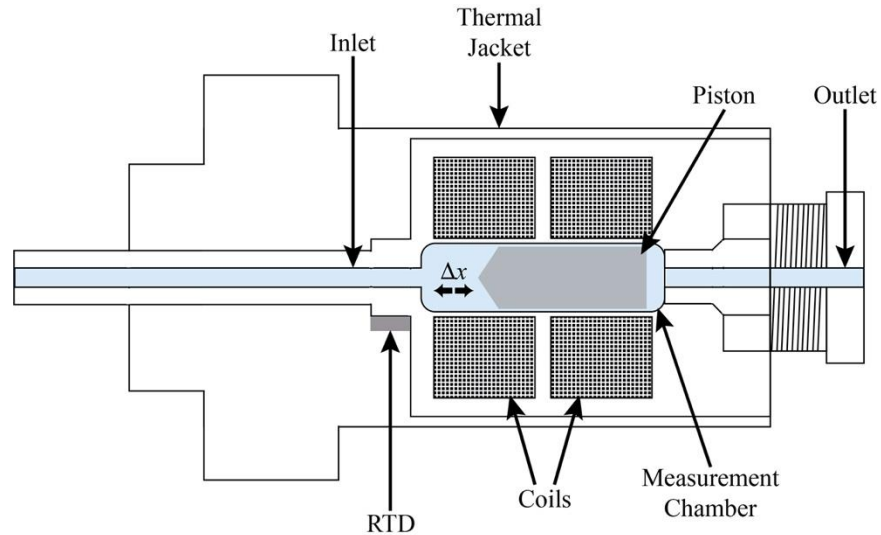


Figure A.1-7. Schematic of the main body of the OPV instrument

The measurement chamber has an inner diameter of 7.963 mm. The outer diameter of the 0.02–0.2 mPa·s sensing piston is 7.925 mm. The time it takes the piston to travel a fixed distance ($\Delta x = 5$ mm) during a complete up-down (or right-to-left) cycle is related to the dynamic viscosity of the fluid in the chamber.

The cylindrical measurement chamber is made of Inconel-718[®]. It has an inner diameter of 7.963 mm and an internal volume of approximately 8 mL and is rated to 137 MPa. Typically, the measurement chamber is inclined 45° against the direction of gravity, but for measurements employing the particular sensing piston used in this work, the chamber was oriented horizontally. The measurement chamber is surrounded by two magnetic coils that are used to magnetically drive the low-mass piston back and forth in the sample fluid. Specifically, one coil pulls the sensing piston towards it, while inducing a voltage in the second coil. The mutual inductance between the two coils makes it possible to accurately determine the position of the sensing piston. A full cycle of the piston is achieved by reversing the actuation of the coils. The time required for the piston to travel a fixed distance (Δx) of approximately 5 mm during a complete cycle is related to the dynamic viscosity of the fluid in the chamber (η) according to Eq. A.1-7.[103]

$$\eta = \frac{F \cdot \ln\left(\frac{r_c}{r_p}\right) \cdot (t_\uparrow + t_\downarrow)}{4 \cdot \pi \cdot L_p^2} \quad (\text{A.1-7})$$

In Eq. A.1-7, F is the magnetic force, r_c and r_p are the radii of the measurement chamber and the sensing piston, respectively, t_{\uparrow} and t_{\downarrow} are the times it takes the cylinder to travel from one end of the chamber to the other and back again, and L_p is the length of the piston.

The sensing piston is constructed of stainless steel and has a length of 24 mm, a diameter of 7.925 mm and is rated for viscosities from 0.02 mPa·s to 2 mPa·s. It should be noted that the highest viscosities measured in this work exceed the upper limit of the sensing piston. Ideally, the lower temperature (higher viscosity) measurements would have been performed using a second sensing piston rated for viscosities from 0.2 mPa·s to 2 mPa·s. However, doing so would have required a second sample loading, which, given the limited available sample volume and concerns regarding potentially significant changes in the bulk sample composition, was deemed undesirable. Therefore, all measurements were made using a single piston since the decision was made that it would be less problematic to extend measurements above the upper range of the sensing piston than below the lower range.



Figure A.1-8. Experimental setup for viscosity measurements. It includes: (1) a vacuum system, (2) a circulator, (3) a syringe pump, (4) the OPV, (5) a sample cylinder mount, (6) various instrument readouts and controls, and (7) a computer.

The full experimental setup is shown in Figure A.1-8. It includes a vacuum system for instrument and sample manifold evacuation, a circulator for temperature control, a syringe pump for sample loading/pressurization, the OPV, a sample cylinder mount, various instrument readouts and controls, and a computer for automation and data collection. Significant modifications have been made to improve thermal insulation, calibration, sample loading, cell pressurization, and instrument automation. A more detailed description of these changes can be found in Laesecke et al.[104]

The cell temperature was controlled between 270 K and 450 K via use of a small laboratory circulator that pumps polydimethylsiloxane heat transfer liquid through the surrounding thermal jacket. Cell temperature was measured with a 100 Ω platinum resistance temperature detector (RTD) that was calibrated and mounted on the outside of the pressure vessel by the manufacturer (see Figure A.1-8). Unfortunately, the RTD was located in a sealed space preventing its removal and independent verification of its calibration. The manufacturer-quoted uncertainty of the temperature measurement is 0.1 K.

The cell pressure is controlled with a high-pressure syringe pump rated to 137 MPa, with a maximum sample volume of 65 mL. Pressure was measured with a vibrating-quartz-crystal type pressure transducer with a full-scale pressure range of 69 MPa and a full-scale uncertainty of 0.01 %, or 0.007 MPa.

Viscosity calibration and measurement protocols. The OPV instrument underwent an initial calibration by the manufacturer during which the strength of the electromagnetic coupling was adjusted for each sensing piston and the cycling periods were correlated to dynamic viscosity using certified viscosity standards at room temperature and atmospheric pressure. However, it is also necessary to calibrate each sensor for the effects of temperature and pressure. The critical physical parameter that determines the viscosity is the annular spacing between the piston and the measurement chamber walls (see Figure A.1-7). When the temperature and/or pressures changes, the annular spacing also changes, and must therefore be accounted for. The manufacturer recommends applying the following temperature and pressure correction:

$$p_{corr} = 1 + \left(K_1 \cdot \left(\frac{p^{145.038}}{20000} \right) \right), \quad (\text{A.1-8})$$

$$t_{corr} = 1 + \left(K_2 \cdot \left(\frac{T-298.15}{100} \right) \right), \text{ and} \quad (\text{A.1-9})$$

$$\eta_{corr} = \eta_{meas} \cdot p_{corr} \cdot t_{corr}, \quad (\text{A.1-10})$$

where p_{corr} and t_{corr} are the corrections for pressure and temperature, respectively, p is the measured pressure in MPa, T is the measured temperature in K, K_1 and K_2 are calibration coefficients, η_{meas} is the uncorrected, measured viscosity, and η_{corr} is the corrected viscosity. Therefore, it was essential to calibrate the 0.02–0.2 mPa·s sensor over the full temperature, pressure, and viscosity ranges covered in this work.

For this work, R-134a was chosen as a reference liquid because there is an accurate viscosity correlation available within REFPROP; estimated uncertainties for the correlation range from 0.5 % to 3 %.[105] A total of 200 state points were measured for R-134a spanning viscosities from 0.013 mPa·s to 0.410 mPa·s, temperatures from 272.5 K to 393.6 K, and pressures from 1.146 MPa to 40.084 MPa. These measurements were dispersed throughout the measurement campaign and the data were fit using Eq. A.1-10 to obtain the calibration coefficients K_1 and K_2 . Two separate sensing pistons with a 0.02–0.2 mPa·s range were used in this work; each was individually calibrated. After calibrating, the maximum deviations from the reference correlation ranged from 1.1 % to 5.6 % for the two pistons.

Degassed saturated liquid refrigerant blends were prepared in 300 mL stainless steel cylinders as described in section A.1.6. The sample cylinder was inverted and mounted to the inlet of the viscometer manifold; inverting the cylinder facilitates sample loading from the liquid phase. The instrument and manifold were then evacuated overnight or longer. The syringe pump piston was repeatedly cycled during evacuation to ensure the removal of any residues from previous samples from the walls of the syringe pump cylinder.

Once sufficiently evacuated, the cell temperature was set to the desired loading temperature, typically 273 K, and the sample cylinder was warmed with a heat lamp to increase the internal cylinder pressure. To load sample, the syringe pump piston was set to the desired volume, the vacuum system and measurement chamber were isolated from the manifold, and the syringe pump cylinder was filled with liquid sample by opening the sample cylinder valve. Ideally, the sample would be loaded simultaneously into the syringe pump and the measurement chamber to avoid any potential shifts in sample composition. However, large, rapid pressure changes could damage the sensing piston; in an effort to avoid this, sample was slowly introduced into the measurement cell via a series of small pressure increases until the pressure no longer increased with additional valve cycles, indicating the cell was filled with liquid. This was then verified by closing the sample cylinder valve and running the syringe pump at a low rate of volume change; a rapid increase in pressure indicates a liquid-filled cell.

Once sample loading was complete, the cell was pressurized to the desired starting pressure and the sensing piston was set into motion to ensure sample mixing and to help with temperature equilibration. A custom LabView program was used to automate instrument control and data collection. For each measurement series, a sequence of target pressures and corresponding measurement periods were entered in the interface panel, and an initial waiting period of at least six hours was set to allow for sufficient temperature equilibration prior to starting measurements. For the binary refrigerant blends, measurements were made at eight pressures for each of five isotherms (273 K, 303 K, 333 K, 363 K, and 393 K). Pressures varied by sample and isotherm and were chosen such that each step represented an approximately constant change in density. At each isotherm, a series of eight pressures were measured for at least 15 minutes at each pressure, after which the instrument was slowly depressurized and then allowed to sit for four hours before repeating the previous pressure series. For each sample, two pressure series are completed for each of the five isotherms, followed by measurements of at least two additional pressure series at several temperatures (typically 273 K and 333 K, and sometimes 393 K). In this work, averaged temperature, pressure, and viscosity values are reported; averages are determined for the last five minutes of data at each pressure step.

Upon completion of measurements for a given refrigerant blend, the sample was removed by cryopumping into a waste cylinder. The instrument, syringe pump, and sample manifold were then evacuated for a minimum of overnight to remove any remaining sample prior to loading the next sample fluid.

Viscosity measurement uncertainties. The relative combined, expanded ($k = 2$) uncertainty on the viscosity measurement, $U_c(\eta)$, is estimated using equation A.1-11.

$$U_c(\eta) = 2 \cdot 100 \cdot \left(\frac{1}{\eta}\right) \cdot \sqrt{\begin{aligned} &\left(\frac{\partial \eta_{corr}}{\partial \eta_{meas}}\right)^2 \delta \eta_{meas}^2 + \left(\frac{\partial \eta_{corr}}{\partial p}\right)^2 \delta p^2 + \left(\frac{\partial \eta_{corr}}{\partial T}\right)^2 \delta T^2 \\ &+ \left(\frac{\partial \eta_{corr}}{\partial K_1}\right)^2 \delta K_1^2 + \left(\frac{\partial \eta_{corr}}{\partial K_2}\right)^2 \delta K_2^2 + \delta \eta_{REF}^2 + \left(\frac{\partial \eta_{corr}}{\partial x_i}\right)^2 \delta x_i^2 \end{aligned}} \quad (\text{A.1-11})$$

Contributions to $U_c(\eta)$ include uncertainties associated with the travel time of the piston, measured pressure, measured temperature, the pressure and temperature correction coefficients, the reference fluid used for calibration, and the mixture composition. The largest contributions to $U_c(\eta)$ arose from the measurement of travel time, specifically repeatability of the viscosity measurement ($\eta_{meas,rep}$), and the uncertainty associated with the reference data used for the calibration (η_{REF}). The next most significant contributions to $U_c(\eta)$ arose from the uncertainty associated with the pressure and temperature correction coefficients. Overall, the combined expanded uncertainty in the viscosity ranged from 0.014 mPa·s to 0.023 mPa·s.

Viscosity results. The measured dynamic viscosity data, as well as the relative combined, expanded ($k = 2$) uncertainties, are reported in Tables A.1-26 through A.1-31. As previously discussed, the reported temperature (T), pressure (p), and calibrated viscosity (η) values are averages calculated from the last five minutes of data at each pressure in a measurement series. The data are presented in order of increasing temperature and complete measurement series are separated by blank lines.

Table A.1-26. Measured viscosity data for the system R-1234yf/134a at a molar composition of (0.3194/0.6806)

Listed in Tables A.1-26 through A.1-31 are temperature T , pressure p , dynamic viscosity η . Results for each measurement series are separated by blank lines.

T/K	p/MPa	$\eta/mPa\cdot s$	T/K	p/MPa	$\eta/mPa\cdot s$
273.06	1.85	0.237	273.02	5.38	0.265
273.06	2.47	0.239	273.02	6.93	0.270
273.06	3.91	0.246	273.03	8.56	0.277
273.05	5.38	0.252	273.02	10.24	0.284
273.06	6.93	0.258	273.02	12.00	0.289
273.06	8.56	0.264	273.03	1.85	0.246
273.06	10.24	0.270	273.03	2.48	0.247
273.05	12.00	0.275	273.04	3.90	0.251
273.02	1.84	0.240	273.04	4.41	0.251
273.02	2.46	0.243	273.05	6.92	0.259
273.02	3.91	0.248	273.06	8.56	0.265
273.02	5.38	0.253	273.05	10.24	0.270
273.03	6.93	0.258	273.06	11.99	0.274
273.03	8.56	0.263			
273.03	10.23	0.268	273.03	1.86	0.234
273.03	12.01	0.275	273.03	2.46	0.236
			273.03	3.90	0.241
273.06	1.84	0.241	273.03	5.38	0.246
273.05	2.46	0.243	273.04	6.92	0.251
273.05	3.89	0.248	273.03	8.56	0.257
273.05	5.38	0.253	273.04	10.25	0.262
273.05	6.93	0.258	273.03	12.00	0.266
273.05	8.55	0.263	273.04	1.86	0.242
273.05	10.24	0.269	273.03	2.48	0.244
273.05	12.00	0.275	273.04	3.91	0.254
273.09	1.86	0.241	273.04	4.42	0.254
273.11	2.47	0.242	273.03	6.93	0.263
273.12	3.90	0.247	273.02	8.56	0.265
273.12	5.37	0.253	273.01	10.24	0.269
273.12	6.93	0.258	273.02	12.01	0.275
273.12	8.56	0.263			
273.12	10.24	0.269	302.93	1.84	0.171
273.12	12.00	0.274	302.94	2.34	0.173
			302.95	3.68	0.178
273.01	1.86	0.249	302.95	5.11	0.183
273.01	2.48	0.253	302.93	6.67	0.188
273.02	3.90	0.259	302.93	8.31	0.193

Table A.1-26 (continued)

T/K	p/MPa	$\eta/mPa\cdot s$	T/K	p/MPa	$\eta/mPa\cdot s$
302.91	10.08	0.199	333.06	3.40	0.118
302.83	11.97	0.206	333.06	4.18	0.122
302.97	1.83	0.172	333.06	5.04	0.125
302.97	2.34	0.173	333.06	5.95	0.129
302.98	3.69	0.178	333.06	6.94	0.133
302.98	5.11	0.182	333.05	8.02	0.137
302.99	6.68	0.188			
302.99	8.32	0.193	362.99	3.61	0.070
302.99	10.10	0.198	362.92	4.06	0.074
303.00	11.99	0.204	362.89	4.59	0.080
			362.90	5.25	0.084
333.00	2.02	0.115	362.91	6.00	0.089
333.03	2.69	0.118	362.92	6.89	0.093
333.08	3.41	0.122	362.94	7.93	0.097
333.11	4.19	0.125	363.03	3.62	0.069
333.10	5.03	0.128	362.96	4.06	0.074
333.12	5.95	0.132	362.93	4.59	0.079
333.11	6.94	0.136	362.93	5.24	0.083
333.11	8.01	0.139	362.92	6.00	0.088
333.05	2.03	0.116	362.93	6.90	0.093
333.05	2.69	0.119	362.94	7.94	0.098
333.06	3.41	0.122			
333.08	4.20	0.126	392.26	5.57	0.038
333.06	5.02	0.128	392.50	5.75	0.040
333.01	5.94	0.132	392.70	5.96	0.043
332.93	6.92	0.136	392.85	6.23	0.046
332.82	7.99	0.141	392.99	6.56	0.050
			393.10	6.96	0.054
333.02	2.03	0.111	393.19	7.44	0.059
333.01	2.67	0.114	393.26	8.05	0.064
333.01	3.41	0.118	392.35	5.57	0.037
333.01	4.19	0.121	392.54	5.75	0.040
333.01	5.03	0.124	392.71	5.96	0.044
333.01	5.95	0.128	392.85	6.23	0.047
333.00	6.94	0.132	392.98	6.54	0.051
333.01	8.02	0.136	393.08	6.96	0.055
333.04	2.04	0.111	393.18	7.45	0.059
333.06	2.69	0.115	393.26	8.03	0.063

Table A.1-27. Measured viscosity data for the system R-1234yf/134a at a molar composition of (0.6469/0.3531)

<i>T</i> /K	<i>p</i> /MPa	η /mPa·s	<i>T</i> /K	<i>p</i> /MPa	η /mPa·s
273.04	1.85	0.253	302.99	8.57	0.200
273.04	3.16	0.258	303.00	10.23	0.205
273.03	4.48	0.262	303.00	11.99	0.210
273.03	5.86	0.267	302.98	1.89	0.176
273.03	7.29	0.271	302.98	3.04	0.180
273.03	8.80	0.276	302.98	4.29	0.184
273.03	10.35	0.280	302.99	5.61	0.190
273.02	11.99	0.285	302.98	7.03	0.194
273.00	1.84	0.251	302.99	8.57	0.199
273.01	3.16	0.256	302.99	10.22	0.204
273.01	4.47	0.259	302.98	12.00	0.209
273.01	5.85	0.263			
272.94	7.26	0.268	333.07	3.83	0.126
272.93	8.78	0.273	333.08	4.11	0.127
272.95	10.35	0.278	333.08	4.46	0.129
272.97	11.98	0.284	333.07	4.91	0.131
			333.07	5.48	0.134
273.11	1.86	0.252	333.08	6.16	0.136
273.10	3.17	0.256	333.01	7.00	0.140
273.09	4.48	0.260	332.90	8.00	0.144
273.09	5.86	0.265	333.04	3.82	0.127
273.09	7.27	0.269	333.05	4.09	0.128
273.09	8.78	0.274	333.05	4.44	0.130
273.10	10.34	0.279	333.04	4.90	0.132
273.11	11.99	0.284	333.06	5.48	0.134
273.13	1.85	0.251	333.07	6.15	0.136
273.13	3.16	0.256	333.07	7.00	0.140
273.13	4.48	0.260	333.08	8.01	0.144
273.12	5.84	0.265			
273.00	7.27	0.269	332.97	2.31	0.122
273.00	8.80	0.274	332.98	2.89	0.125
273.04	10.35	0.279	332.97	3.56	0.129
273.06	12.00	0.283	332.98	4.28	0.132
			333.04	5.10	0.136
303.01	1.89	0.176	333.09	5.99	0.140
303.00	3.03	0.180	333.10	6.94	0.143
303.00	4.28	0.185	333.10	8.02	0.148
303.00	5.61	0.190	333.01	2.31	0.121
303.00	7.04	0.195	333.03	2.90	0.124

Table A.1-27 (continued)

<i>T</i> /K	<i>p</i> /MPa	η /mPa·s	<i>T</i> /K	<i>p</i> /MPa	η /mPa·s
333.00	3.56	0.128	363.04	6.16	0.089
333.02	4.30	0.131	363.09	7.00	0.094
333.02	5.09	0.135	363.11	8.00	0.099
333.01	5.99	0.138			
332.97	6.95	0.143	392.72	6.05	0.046
332.96	8.03	0.147	392.80	6.21	0.048
			392.90	6.41	0.050
362.97	3.82	0.070	392.97	6.62	0.053
363.01	4.09	0.073	393.02	6.87	0.056
363.05	4.45	0.077	393.10	7.20	0.059
363.08	4.91	0.081	393.17	7.57	0.061
363.13	5.47	0.085	393.22	8.03	0.065
363.17	6.15	0.089	392.48	6.04	0.047
363.19	7.00	0.094	392.57	6.21	0.052
363.21	8.00	0.099	392.68	6.41	0.053
362.88	3.82	0.070	392.77	6.63	0.055
362.83	4.09	0.073	392.85	6.89	0.058
362.84	4.46	0.077	392.91	7.21	0.061
362.91	4.91	0.081	392.99	7.58	0.063
362.98	5.46	0.085	393.05	8.03	0.067

Table A.1-28. Measured viscosity data for the system R-134a/1234ze(E) at a molar composition of (0.3330/0.6670)

<i>T</i> /K	<i>p</i> /MPa	η /mPa·s	<i>T</i> /K	<i>p</i> /MPa	η /mPa·s
272.59	1.73	0.268	273.00	26.12	0.320
272.58	4.98	0.281	273.00	32.77	0.338
272.58	9.47	0.297	273.00	40.07	0.358
272.57	14.42	0.313	272.99	1.87	0.246
272.57	19.93	0.329	272.99	5.10	0.257
272.59	26.00	0.347	272.99	9.58	0.271
272.60	32.65	0.367	272.99	14.55	0.287
272.60	39.97	0.387	272.99	20.06	0.303
272.54	1.73	0.266	272.99	26.11	0.320
272.52	4.97	0.278	272.99	32.77	0.339
272.52	9.44	0.293	273.01	40.06	0.359
272.51	14.40	0.309			
272.52	19.91	0.326	302.98	1.86	0.190
272.52	25.97	0.344	302.97	4.51	0.198
272.53	32.63	0.363	302.97	8.53	0.211
272.52	39.93	0.383	302.97	13.20	0.225
			302.98	18.63	0.242
273.03	1.86	0.246	302.99	24.88	0.257
273.04	5.11	0.256	302.98	31.99	0.273
273.03	9.59	0.271	302.99	40.06	0.291
273.04	14.55	0.286	302.96	1.86	0.191
273.04	20.06	0.302	302.95	4.51	0.200
273.04	26.13	0.320	302.95	8.53	0.213
273.04	32.77	0.338	302.94	13.22	0.226
273.04	40.08	0.358	302.93	18.64	0.240
273.09	1.87	0.246	302.93	24.89	0.254
273.09	5.11	0.257	302.93	32.00	0.271
273.09	9.60	0.271	302.94	40.07	0.287
273.09	14.57	0.286			
273.08	20.07	0.302	332.64	1.97	0.131
273.08	26.11	0.320	332.64	4.52	0.141
273.07	32.78	0.338	332.64	7.79	0.152
273.07	40.09	0.358	332.64	11.93	0.164
			332.64	17.06	0.177
272.99	1.85	0.246	332.64	23.33	0.193
272.99	5.10	0.257	332.63	30.92	0.210
273.00	9.58	0.271	332.63	39.99	0.230
273.00	14.56	0.286	332.58	1.91	0.128
273.00	20.06	0.303			

Table A.1-28 (continued)

<i>T</i> /K	<i>p</i> /MPa	η /mPa·s	<i>T</i> /K	<i>p</i> /MPa	η /mPa·s
332.59	4.45	0.138	333.14	12.01	0.158
332.59	7.73	0.150	333.14	17.16	0.172
332.60	11.88	0.163	333.14	23.41	0.188
332.60	17.02	0.177			
332.60	23.29	0.192	362.75	3.23	0.082
332.60	30.87	0.210	362.85	4.56	0.091
332.61	39.94	0.229	362.92	6.70	0.103
			362.96	9.86	0.115
333.06	2.04	0.126	363.14	14.40	0.129
333.07	4.60	0.137	363.29	20.61	0.145
333.09	7.86	0.148	363.37	28.97	0.164
333.10	12.01	0.160	363.41	39.98	0.188
333.10	17.15	0.174	363.06	3.32	0.083
333.11	23.41	0.190	363.14	4.66	0.093
333.12	31.00	0.207	363.18	6.79	0.105
333.11	40.06	0.226	363.24	9.95	0.118
333.10	2.02	0.126	363.26	14.46	0.132
333.11	4.58	0.136	363.27	20.67	0.147
333.12	7.86	0.147	363.28	29.01	0.165
333.12	12.00	0.159	363.30	40.02	0.187
333.12	17.14	0.173			
333.12	23.41	0.189	392.82	5.28	0.045
333.13	31.00	0.206	393.06	5.71	0.052
333.13	40.10	0.225	393.24	6.53	0.060
			393.40	8.17	0.072
333.09	2.03	0.127	393.54	11.22	0.085
333.09	4.60	0.137	393.64	16.61	0.102
333.11	7.86	0.148	393.72	25.61	0.124
333.12	12.01	0.160	393.78	40.09	0.155
333.12	17.14	0.174	392.78	5.28	0.045
333.10	23.41	0.189	393.00	5.71	0.052
333.11	31.00	0.206	393.22	6.53	0.061
333.12	40.07	0.225	393.42	8.17	0.072
333.12	2.04	0.125	393.55	11.22	0.086
333.12	4.58	0.134	393.62	16.59	0.103
333.13	7.86	0.146	393.46	25.61	0.126
			393.50	40.07	0.155

Table A.1-29. Measured viscosity data for the system R-134a/1234ze(E) at a molar composition of (0.6622/0.3378)

<i>T</i> /K	<i>p</i> /MPa	η /mPa·s	<i>T</i> /K	<i>p</i> /MPa	η /mPa·s
273.07	1.13	0.258	302.81	24.79	0.258
273.08	5.11	0.273	302.80	31.92	0.279
273.07	9.57	0.291	302.80	40.05	0.301
273.06	14.53	0.310	302.83	1.13	0.169
273.06	20.02	0.331	302.84	4.49	0.181
273.06	26.09	0.353	302.84	8.48	0.196
273.06	32.75	0.376	302.87	13.16	0.212
273.06	40.06	0.401	302.92	18.56	0.226
273.06	1.15	0.260	302.94	24.81	0.244
273.08	5.13	0.275	302.95	31.95	0.264
273.09	9.59	0.292	302.96	40.06	0.286
273.09	14.55	0.311			
273.10	20.04	0.331	332.79	2.17	0.114
273.11	26.09	0.354	332.81	4.63	0.123
273.11	32.75	0.376	332.83	7.85	0.134
273.10	40.06	0.400	332.83	11.94	0.148
			332.84	17.05	0.162
273.18	1.15	0.240	332.84	23.30	0.179
273.18	5.13	0.254	332.84	30.90	0.197
273.18	9.59	0.272	332.84	40.05	0.219
273.15	14.54	0.288	332.83	2.18	0.113
273.02	20.01	0.307	332.84	4.64	0.122
273.04	26.07	0.327	332.85	7.86	0.133
273.06	32.73	0.350	332.84	11.93	0.146
273.08	40.05	0.372	332.79	17.04	0.161
273.11	1.13	0.240	332.78	23.28	0.179
273.10	5.10	0.255	332.85	30.91	0.197
273.11	9.56	0.270	332.93	40.06	0.219
273.10	14.52	0.288			
273.10	20.00	0.306	362.73	3.64	0.071
273.10	26.07	0.327	362.84	4.87	0.079
273.10	32.72	0.347	362.90	6.87	0.088
273.09	40.05	0.372	362.93	9.06	0.101
			362.98	14.31	0.115
302.83	1.13	0.177	363.01	20.47	0.133
302.83	4.49	0.190	363.02	28.86	0.153
302.83	8.47	0.204	363.03	40.08	0.177
302.81	13.13	0.219	362.80	3.63	0.072
302.81	18.55	0.240	362.91	4.87	0.079

Table A.1-29 (continued)

<i>T</i> /K	<i>p</i> /MPa	η /mPa·s	<i>T</i> /K	<i>p</i> /MPa	η /mPa·s
362.98	6.87	0.089	391.62	5.04	0.028
363.04	9.93	0.100	392.23	5.40	0.034
362.89	14.30	0.114	392.56	5.93	0.042
362.84	20.47	0.132	392.86	7.24	0.055
362.84	28.86	0.154	393.12	10.86	0.074
362.84	40.09	0.178	393.23	19.90	0.101
			393.31	40.08	0.147
362.61	3.61	0.072			
362.70	4.85	0.079	392.20	5.74	0.041
362.78	6.85	0.089	392.41	6.21	0.047
362.81	9.90	0.101	392.63	7.11	0.056
362.83	14.29	0.115	392.72	8.77	0.067
362.82	20.45	0.132	392.86	11.81	0.079
362.83	28.85	0.153	392.94	17.12	0.096
362.82	40.06	0.177	393.03	25.95	0.118
			393.06	40.07	0.148
389.80	4.50	0.022	392.00	5.70	0.039
391.50	5.04	0.028	392.21	6.17	0.047
392.11	5.40	0.034	392.45	7.08	0.055
392.44	5.93	0.042	392.64	8.73	0.065
392.76	7.25	0.055	392.86	11.81	0.078
393.02	10.86	0.074	393.05	17.13	0.094
393.17	19.92	0.102	393.17	25.95	0.115
393.22	40.09	0.147	393.23	40.06	0.147
389.90	4.49	0.022			

Table A.1-30. Measured viscosity data for the system R-1234yf/1234ze(E) at a molar composition of (0.3224/0.6776)

<i>T</i> /K	<i>p</i> /MPa	η /mPa·s	<i>T</i> /K	<i>p</i> /MPa	η /mPa·s
273.07	1.89	0.250	302.92	8.66	0.200
273.08	3.19	0.254	302.91	10.27	0.204
273.07	4.53	0.259	302.91	11.99	0.209
273.08	5.91	0.263	302.91	1.89	0.178
273.08	7.35	0.268	302.91	3.08	0.182
273.08	8.85	0.272	302.90	4.33	0.186
273.08	10.39	0.276	302.84	5.69	0.191
272.96	12.00	0.281	302.84	7.13	0.195
273.10	1.88	0.250	302.85	8.66	0.200
273.10	3.18	0.254	302.85	10.27	0.205
273.11	4.51	0.258	302.85	11.99	0.209
273.10	5.89	0.263			
273.10	7.34	0.267	332.98	2.06	0.145
273.11	8.83	0.271	332.98	2.71	0.146
273.10	10.38	0.276	332.98	2.06	0.148
273.10	12.00	0.280	332.98	2.70	0.148
272.96	1.92	0.248	332.99	2.07	0.145
272.96	3.20	0.253	333.01	2.71	0.145
272.96	4.54	0.257	333.05	2.06	0.148
272.96	5.91	0.261	333.05	2.72	0.148
272.96	7.37	0.266			
272.96	8.85	0.271	362.51	3.28	0.111
272.99	10.40	0.275	362.54	3.64	0.113
273.01	12.02	0.279	362.58	4.10	0.115
273.05	1.91	0.249	362.61	4.63	0.116
273.05	3.19	0.253	362.63	5.29	0.119
273.04	4.52	0.258	362.67	6.04	0.121
273.03	5.91	0.262	362.69	6.94	0.122
273.02	7.35	0.266	362.71	7.98	0.125
273.01	8.85	0.271			
273.01	10.39	0.275	363.01	3.35	0.113
273.02	12.03	0.280	363.04	3.72	0.116
			363.07	4.18	0.118
			363.08	4.71	0.121
302.92	1.88	0.178	363.10	5.36	0.123
302.92	3.08	0.182	363.13	6.12	0.125
302.92	4.34	0.186	363.14	7.02	0.125
302.93	5.70	0.190	363.16	8.05	0.126
302.93	7.13	0.195			

Table A.1-30 (continued)

<i>T</i> /K	<i>p</i> /MPa	η /mPa·s	<i>T</i> /K	<i>p</i> /MPa	η /mPa·s
392.82	5.58	0.072	392.73	5.58	0.068
392.90	5.76	0.075	392.79	5.75	0.071
392.96	5.97	0.078	392.87	5.97	0.075
393.03	6.25	0.082	392.92	6.24	0.079
393.10	6.58	0.086	392.99	6.57	0.082
393.17	6.98	0.090	393.04	6.97	0.086
393.21	7.46	0.094	393.10	7.46	0.090
393.27	8.05	0.098	393.16	8.05	0.094
392.67	5.55	0.071	392.81	5.57	0.066
392.79	5.74	0.074	392.81	5.75	0.069
392.92	5.97	0.078	392.70	5.97	0.073
393.01	6.23	0.082	392.71	6.23	0.076
393.08	6.57	0.085	392.83	6.56	0.080
393.15	6.97	0.089	392.92	6.97	0.085
393.18	7.45	0.092	392.99	7.45	0.090
393.22	8.04	0.096	393.06	8.04	0.094

Table A.1-31. Measured viscosity data for the system R-1234yf/1234ze(E) at a molar composition of (0.6418/0.3582)

<i>T</i> /K	<i>p</i> /MPa	η /mPa·s	<i>T</i> /K	<i>p</i> /MPa	η /mPa·s
273.03	1.84	0.268	272.98	8.80	0.287
273.03	3.11	0.272	273.00	10.37	0.291
273.03	4.45	0.276	273.02	12.02	0.296
273.04	5.82	0.280	272.98	1.85	0.263
273.03	7.28	0.284	272.98	3.13	0.267
273.03	8.79	0.289	272.98	4.46	0.272
273.03	10.36	0.294	272.97	5.84	0.276
273.03	12.01	0.298	272.97	7.30	0.281
273.02	1.84	0.268	272.96	8.80	0.286
273.01	3.11	0.272	272.96	10.36	0.291
273.02	4.44	0.274	272.97	12.00	0.295
273.02	5.83	0.272			
273.03	7.27	0.274	302.95	1.84	0.187
273.03	8.78	0.278	302.95	2.99	0.194
273.02	10.34	0.283	302.95	4.26	0.198
273.04	12.00	0.287	302.94	5.59	0.203
			302.94	7.05	0.208
273.04	1.85	0.254	302.94	8.58	0.214
273.04	3.12	0.259	302.94	10.23	0.218
273.04	4.45	0.263	302.93	12.00	0.223
273.04	5.84	0.267	302.98	1.84	0.187
273.03	7.29	0.272	302.97	3.00	0.192
273.03	8.79	0.277	302.97	4.27	0.198
273.03	10.35	0.281	302.98	5.61	0.203
273.02	12.00	0.286	302.98	7.05	0.208
273.04	1.84	0.254	302.97	8.57	0.212
273.04	3.10	0.258	302.96	10.24	0.217
273.04	4.43	0.262	302.97	12.00	0.222
273.03	5.82	0.267			
273.02	7.27	0.272	333.02	2.16	0.136
273.02	8.78	0.276	333.02	2.78	0.140
273.01	10.35	0.281	333.02	3.46	0.144
273.01	12.00	0.286	333.03	4.22	0.147
			333.02	5.03	0.148
272.97	1.86	0.263	333.02	2.16	0.139
272.97	3.13	0.268	333.02	2.78	0.144
272.99	4.46	0.272	333.03	3.48	0.149
272.98	5.84	0.277	333.05	4.22	0.154
272.98	7.30	0.281	333.04	5.04	0.155

Table A.1-31 (continued)

<i>T</i> /K	<i>p</i> /MPa	η /mPa·s	<i>T</i> /K	<i>p</i> /MPa	η /mPa·s
332.62	2.11	0.135	363.22	6.11	0.102
332.62	2.73	0.139	363.24	7.00	0.107
332.63	3.41	0.143	363.26	8.06	0.113
332.63	4.16	0.146	362.75	3.54	0.080
332.67	4.99	0.147	362.78	3.85	0.084
332.69	2.12	0.140	362.81	4.26	0.088
332.69	2.75	0.145	362.86	4.76	0.092
332.70	3.44	0.150	362.90	5.36	0.097
332.71	4.19	0.154	362.92	6.10	0.102
332.71	5.01	0.156	362.93	6.99	0.107
			363.00	8.05	0.113
333.09	2.19	0.130			
333.10	2.80	0.134	392.92	6.08	0.056
333.12	3.48	0.138	392.99	6.25	0.058
333.11	4.24	0.142	393.04	6.46	0.061
333.11	5.05	0.143	393.10	6.71	0.063
333.14	2.18	0.137	393.14	6.97	0.065
333.14	2.80	0.141	393.18	7.28	0.068
333.14	3.48	0.146	393.21	7.64	0.071
333.13	4.23	0.151	393.25	8.06	0.074
333.14	5.06	0.153	392.90	6.07	0.057
			392.93	6.24	0.059
363.07	3.57	0.080	392.99	6.44	0.061
363.11	3.88	0.084	393.03	6.69	0.064
363.15	4.27	0.087	393.07	6.95	0.065
363.18	4.77	0.092	393.11	7.26	0.068
363.21	5.38	0.096	393.15	7.63	0.071
			393.10	8.04	0.074

A.1.5. Liquid-phase Thermal Conductivity Measurements

The transient hot wire (THW) apparatus is an absolute technique used to measure the thermal conductivity. The apparatus described in this study[106] can operate at temperatures ranging from 60 to 340 K and pressures up to 70 MPa. The basis of the THW apparatus are two platinum wires of differing lengths, which function as both heating elements and thermometers. The principle of the THW technique is to observe the temperature rise of the wire during a step power pulse through the wire over a short duration. The following equation,

$$\Delta T_{id} = \Delta T - \sum \delta T_i = \frac{q}{4\pi\lambda} \ln\left(\frac{4K}{a^2 C} t\right) \quad (\text{A.1-12})$$

relates the measured temperature rise ΔT to the ideal temperature rise ΔT_{id} of an infinite line source where q is the applied power, λ is the thermal conductivity, K is the thermal diffusivity, a is the radius of the wire, C is the exponential of Euler's constant, and t is the time. The equation for the infinite line source is an ideal scenario assuming a wire of near-zero diameter and infinite length with zero heat capacity and the term $\sum \delta T_i$ is the sum of corrections that are applied to the measured temperature rise to account for departures from the ideal case. A more in-depth explanation of each correction required is described in the work of Healy et al.[107]

The apparatus consisted of a measuring cell containing the hot wires situated in one arm of a Wheatstone bridge to measure the difference between the long-wire and short-wire resistances increases during heating. A beryllium copper pressure vessel rated to 70 MPa and a cryostat to maintain the temperature complete the basic apparatus. Figure A.1-9 shows the arrangement of the long and short hot wires on the Wheatstone bridge. The two-wire arrangement used in this THW apparatus allowed for the elimination of end effects. During measurements, an in-situ calibration is performed to correlate the wire resistances to their temperature. The heating of the platinum wires was done using a 1000 Hz alternating current power source to avoid polarization errors that may occur with ionic impurities in the refrigerants studied with bare hot wires.

Measurements were performed over a 1 s time period to minimize convective heat transfer and at five temperature rises to rule out any power-level dependency. The data were measured along isotherms from 200 to 340 K in 20 K increments. Increasing the system temperature causes the resistance of the long and short wires to increase. Therefore, prior to starting any measurements the Wheatstone bridge was balanced using decade resistors so that the voltage measured across the bridge read zero. Saturated binary liquid refrigerant mixture samples of HFO-1234yf, HFC-134a and HFO-1234ze(E) prepared in 300 mL transfer vessels were used to load the hot-wire system. The mixtures were prepared in such a manner to minimize the vapor space in the transfer vessel. When loading the sample the transfer vessel was inverted to load from the liquid phase. Given the two-phase nature of the sample, flash calculations using REFPROP were performed to correct for modest changes in the bulk sample composition as the sample was withdrawn. The liquid phase composition changes were found to be between 0.0002 and 0.0005 mole fraction of the bulk sample composition. For each fluid, measurements at nine pressures were performed along an isotherm starting from roughly 0.5 MPa above the bubble point pressure to 50 MPa. For mixtures containing HFO-1234yf the pressure was limited to 12 MPa because this component has the potential to polymerize at high pressures. The combined expanded uncertainty of the thermal conductivity measurement for the liquid mixtures measured here was less than 1%.

Figure A.1-10 shows the relationship between the thermal conductivity and density for each binary mixture.

Measured data are presented in Tables A.1-32 through A.1-37. For the sake of brevity, the tables present a single measured point at each nominal pressure, rather than the five distinct temperature rises actually measured. All of the measured data will be presented in a forthcoming journal paper.[108]

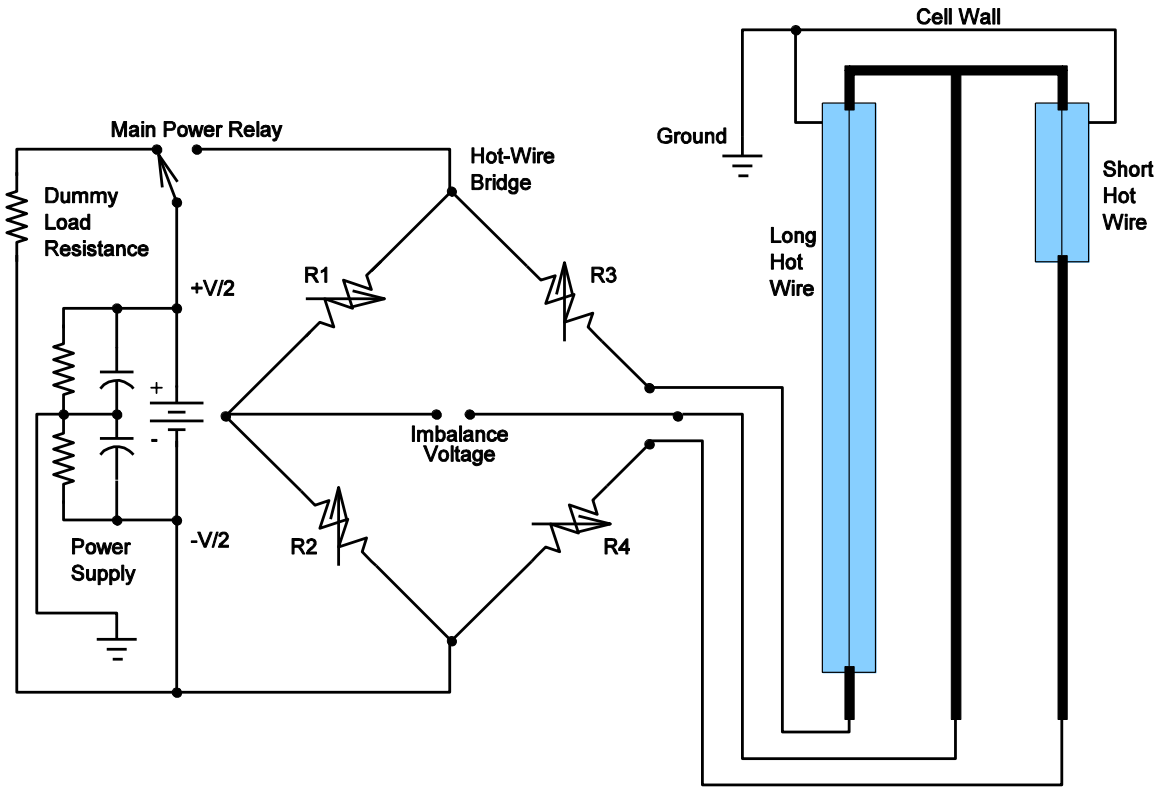


Figure A.1-9. Circuit diagram of the Wheatstone bridge and long and short hot wire arrangement

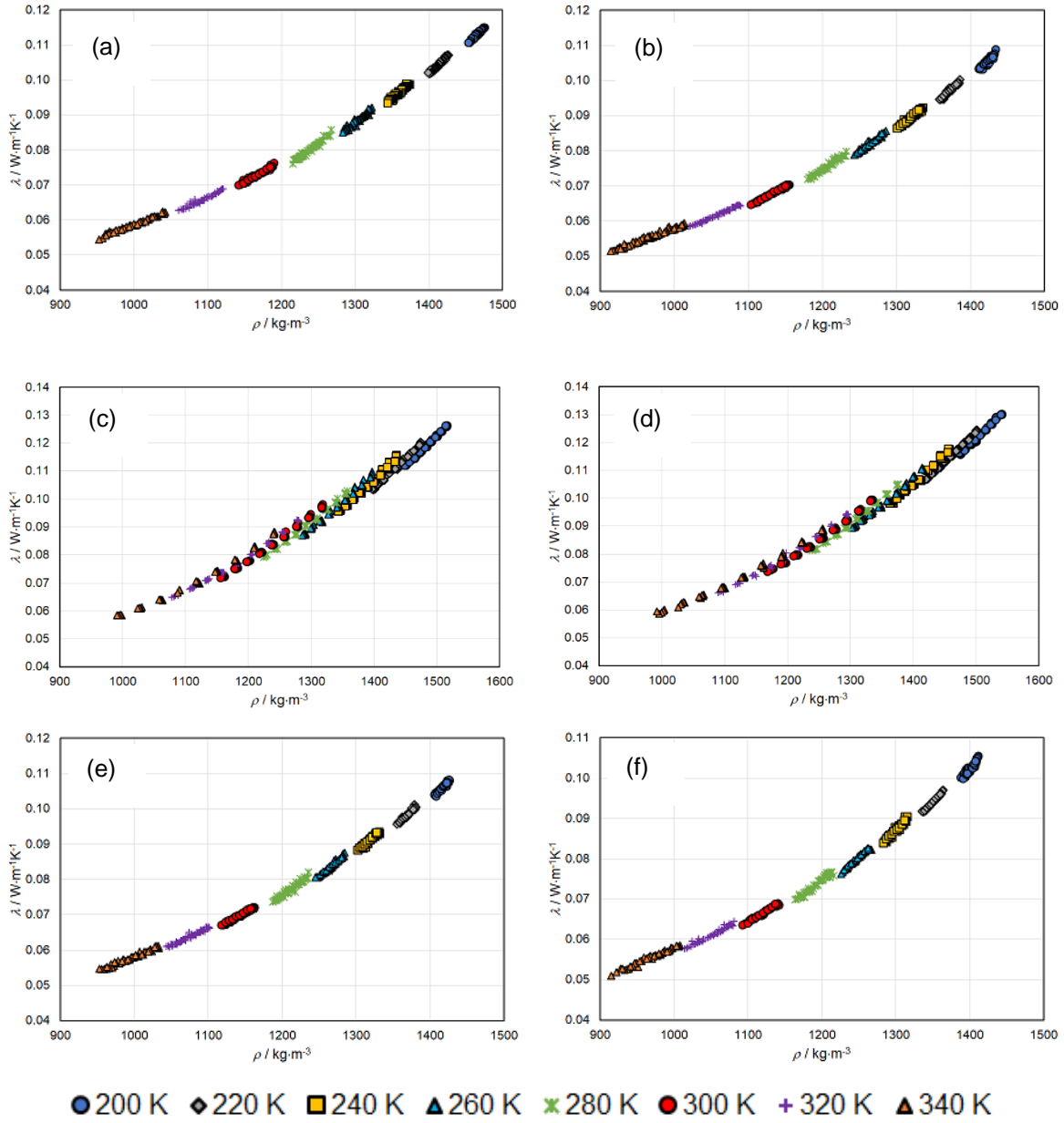


Figure A.1-10. Effect of density on the thermal conductivity for binary mixtures of R-1234yf, R-134a, and R-1234ze(E) at temperatures ranging from 200 K to 340 K

The mixtures are: (a) R-1234yf/134a (0.320/0.680 molar); (b) R-1234yf/134a (0.647/0.353 molar); (c) R-134a/1234ze(E) (0.334/0.666 molar); (d) R-134a/1234ze(E) (0.663/0.337 molar); (e) R-1234yf/1234ze(E) (0.323/0.677 molar); (f) R-1234yf/1234ze(E) (0.642/0.358 molar).

Table A.1-32. Representative thermal conductivity data measured for the system R-1234yf/134a at a molar composition of (0.320/0.680)

T / K	p / MPa	$\lambda / \text{W}\cdot\text{m}^{-1}\text{K}^{-1}$	T / K	p / MPa	$\lambda / \text{W}\cdot\text{m}^{-1}\text{K}^{-1}$
201.920	2.155	0.11140	282.240	2.300	0.07806
201.919	2.152	0.11161	282.224	1.078	0.07749
201.893	3.573	0.11198	282.175	2.126	0.07834
201.891	3.573	0.11179	282.356	1.050	0.07758
201.557	8.921	0.11391	282.361	2.070	0.07789
202.247	11.885	0.11494	282.260	3.289	0.07888
202.271	10.415	0.11427	282.264	4.704	0.07995
202.347	7.678	0.11310	282.182	6.006	0.08076
202.344	5.055	0.11286	282.197	7.420	0.08166
202.353	0.950	0.11111	282.118	8.924	0.08273
222.435	12.026	0.10695	282.039	11.634	0.08412
222.516	10.314	0.10628	302.260	1.157	0.07035
222.472	9.034	0.10560	302.271	2.011	0.07119
222.504	7.633	0.10502	302.270	2.888	0.07171
222.514	6.297	0.10455	302.273	3.599	0.07206
222.560	4.869	0.10364	302.264	4.346	0.07273
222.573	3.656	0.10321	302.241	5.327	0.07347
222.559	2.334	0.10277	302.230	6.113	0.07382
222.593	1.040	0.10199	302.218	7.070	0.07485
242.683	11.940	0.09869	302.198	7.905	0.07525
242.739	10.479	0.09787	322.071	1.909	0.06311
242.757	8.972	0.09692	321.974	2.440	0.06397
242.764	6.293	0.09659	322.022	3.119	0.06467
242.741	7.673	0.09629	322.015	3.843	0.06512
242.782	5.024	0.09540	321.927	4.558	0.06579
242.799	3.483	0.09499	321.915	5.342	0.06625
242.801	2.154	0.09437	321.921	6.093	0.06671
242.826	0.969	0.09325	321.921	7.042	0.06820
262.143	11.959	0.09162	321.900	7.920	0.06890
262.172	10.621	0.09055	342.135	2.579	0.05605
262.188	8.969	0.08970	342.208	2.979	0.05646
262.159	7.513	0.08927	342.181	3.464	0.05722
262.192	6.185	0.08881	342.175	4.056	0.05812
262.226	4.808	0.08875	342.031	4.670	0.05902
262.208	4.829	0.08812	342.399	5.405	0.05956
262.233	3.524	0.08651	342.420	6.237	0.06018
262.240	2.081	0.08620	342.382	6.964	0.06089
262.218	0.990	0.08561	342.340	7.878	0.06236

Table A.1-33. Representative thermal conductivity data measured for the system R-1234yf/134a at a molar composition of (0.647/0.353)

T / K	p / MPa	$\lambda / \text{W}\cdot\text{m}^{-1}\text{K}^{-1}$	T / K	p / MPa	$\lambda / \text{W}\cdot\text{m}^{-1}\text{K}^{-1}$
202.029	1.154	0.10308	281.872	3.306	0.07380
202.036	2.153	0.10403	281.818	4.506	0.07453
201.465	3.573	0.10469	281.905	6.008	0.07547
201.725	3.572	0.10469	281.875	7.681	0.07612
201.472	4.962	0.10517	281.809	7.700	0.07615
202.101	4.975	0.10469	281.128	8.935	0.07827
202.049	6.238	0.10480	282.007	10.353	0.07781
202.034	7.559	0.10495	282.028	11.999	0.07857
202.039	9.049	0.10585	302.464	1.299	0.06506
202.015	10.412	0.10713	302.105	1.997	0.06605
202.060	11.793	0.10701	302.248	2.737	0.06654
222.284	1.181	0.09488	302.133	3.483	0.06698
222.303	2.158	0.09514	301.907	4.298	0.06796
222.305	3.461	0.09616	301.874	5.131	0.06844
222.292	4.773	0.09669	302.199	6.288	0.06891
222.272	6.329	0.09752	302.105	7.096	0.06981
222.275	7.767	0.09758	302.176	8.035	0.07007
222.262	9.136	0.09832	322.289	1.638	0.05874
222.251	10.532	0.09885	322.225	2.316	0.05941
222.244	11.818	0.09926	322.172	2.976	0.06032
242.508	1.033	0.08689	322.219	3.707	0.06100
242.486	2.304	0.08751	322.121	4.434	0.06180
242.532	3.531	0.08780	322.001	5.249	0.06241
242.530	4.935	0.08832	322.139	6.155	0.06322
242.540	6.142	0.08895	322.083	7.072	0.06397
242.523	7.541	0.08974	322.045	8.031	0.06449
242.500	8.973	0.09024	342.621	2.401	0.05164
242.495	10.579	0.09077	342.534	2.847	0.05208
242.472	11.946	0.09184	342.736	3.460	0.05328
262.259	1.077	0.07923	342.613	3.980	0.05413
262.294	2.162	0.08018	342.476	3.966	0.05440
262.254	3.386	0.08084	342.501	4.729	0.05572
262.200	4.727	0.08119	342.640	4.770	0.05548
262.261	6.172	0.08160	342.474	5.410	0.05584
262.225	7.558	0.08285	342.357	6.220	0.05716
262.176	9.057	0.08327	342.474	7.052	0.05765
262.127	10.486	0.08422	341.938	7.035	0.05796
262.088	11.886	0.08514	342.045	7.968	0.05841
281.922	1.103	0.07236	341.993	7.955	0.05900
281.860	2.032	0.07294	342.226	2.698	0.05245

Table A.1-34. Representative thermal conductivity data measured for the system R-134a/1234ze(E)) at a molar composition of (0.334/0.666)

T / K	p / MPa	$\lambda / \text{W}\cdot\text{m}^{-1}\text{K}^{-1}$	T / K	p / MPa	$\lambda / \text{W}\cdot\text{m}^{-1}\text{K}^{-1}$
202.306	1.006	0.11192	282.586	1.027	0.07981
202.356	6.092	0.11376	282.497	5.018	0.08243
202.339	11.496	0.11505	282.413	9.586	0.08472
202.328	17.141	0.11665	282.314	14.660	0.08730
202.325	23.189	0.11893	282.249	20.585	0.09057
202.319	29.514	0.12054	282.287	27.011	0.09311
202.317	36.292	0.12279	282.114	34.280	0.09661
202.210	42.843	0.12437	282.010	41.528	0.09871
202.207	50.101	0.12622	282.115	50.057	0.10198
222.169	1.056	0.10367	302.384	0.961	0.07264
222.565	5.931	0.10541	302.252	4.796	0.07501
222.552	11.136	0.10792	302.093	8.766	0.07760
222.536	16.705	0.10965	302.017	13.756	0.08079
222.523	22.545	0.11217	302.041	19.225	0.08340
222.502	29.147	0.11436	301.872	25.374	0.08657
222.490	35.966	0.11594	301.831	32.621	0.09001
222.477	42.648	0.11734	301.760	40.836	0.09354
222.474	50.056	0.12027	301.735	50.102	0.09730
242.282	1.066	0.09586	322.937	1.401	0.06497
242.262	5.686	0.09794	322.899	4.685	0.06805
242.240	10.677	0.09960	322.696	8.283	0.07091
242.230	16.211	0.10246	322.692	12.567	0.07383
242.205	22.160	0.10487	322.674	17.834	0.07684
242.183	28.493	0.10626	322.579	23.979	0.08026
242.162	35.235	0.10873	322.458	31.757	0.08405
242.135	42.241	0.11054	321.971	40.469	0.08811
242.117	50.302	0.11354	321.578	49.979	0.09222
262.459	1.107	0.08759	342.146	2.213	0.05862
262.412	5.364	0.08999	341.996	4.487	0.06087
262.317	10.428	0.09243	341.895	7.685	0.06391
262.270	15.664	0.09503	342.268	7.683	0.06405
262.217	21.652	0.09751	341.838	11.489	0.06754
262.170	27.658	0.09965	341.916	16.350	0.07034
262.124	34.362	0.10199	341.899	22.524	0.07403
262.079	42.081	0.10489	342.360	22.522	0.07416
262.023	50.155	0.10792	341.766	30.150	0.07793
			341.625	39.113	0.08293
			341.507	50.178	0.08820

Table A.1-35. Representative thermal conductivity data measured for the system R-134a/1234ze(E)) at a molar composition of (0.663/0.337)

T / K	p / MPa	$\lambda / \text{W}\cdot\text{m}^{-1}\text{K}^{-1}$	T / K	p / MPa	$\lambda / \text{W}\cdot\text{m}^{-1}\text{K}^{-1}$
202.414	0.987	0.11549	282.675	0.976	0.08186
202.412	6.060	0.11748	282.606	5.044	0.08448
202.410	11.549	0.11964	282.552	9.791	0.08700
202.411	17.236	0.12010	282.475	14.660	0.08946
202.418	23.225	0.12327	282.413	20.690	0.09308
202.342	29.496	0.12454	282.382	26.559	0.09525
202.352	35.981	0.12704	282.328	33.614	0.09844
202.367	42.732	0.12895	282.272	41.127	0.10155
202.367	49.945	0.12998	282.249	49.838	0.10511
222.064	1.065	0.10711	302.774	1.302	0.07414
222.214	5.868	0.10911	302.671	4.832	0.07664
222.257	11.181	0.11148	302.597	8.887	0.07975
222.241	16.618	0.11292	302.619	13.716	0.08232
222.216	22.787	0.11515	302.479	19.229	0.08542
222.202	28.987	0.11771	302.335	25.600	0.08900
222.192	35.725	0.11943	302.237	32.919	0.09191
222.017	42.464	0.12160	302.301	40.862	0.09563
221.978	50.005	0.12412	302.176	49.796	0.09927
242.597	1.100	0.09880	322.776	1.570	0.06657
242.565	5.653	0.10123	322.781	4.653	0.06924
242.536	10.781	0.10295	322.086	8.416	0.07251
242.521	16.107	0.10506	321.956	13.014	0.07611
242.498	22.116	0.10631	321.887	17.630	0.07869
242.473	28.225	0.10981	322.338	24.025	0.08251
242.456	34.938	0.11133	321.852	39.832	0.09054
242.437	42.219	0.11428	322.164	50.069	0.09430
242.419	50.130	0.11722	342.332	2.379	0.05897
262.970	1.072	0.08986	342.189	4.494	0.06231
262.931	5.384	0.09218	342.127	7.289	0.06531
262.887	10.105	0.09439	342.046	11.277	0.06809
262.853	15.441	0.09723	341.971	16.146	0.07184
262.800	21.204	0.09959	341.882	22.092	0.07578
262.758	27.697	0.10202	341.772	29.594	0.07943
262.703	34.550	0.10423	341.695	38.837	0.08415
262.666	41.737	0.10805	341.629	50.136	0.08911
262.612	49.833	0.11047			

Table A.1-36. Representative thermal conductivity data measured for the system R-1234yf/1234ze(E) at a molar composition of (0.323/0.677)

T / K	p / MPa	$\lambda / \text{W}\cdot\text{m}^{-1}\text{K}^{-1}$	T / K	p / MPa	$\lambda / \text{W}\cdot\text{m}^{-1}\text{K}^{-1}$
202.374	1.088	0.10437	282.065	1.039	0.07407
202.342	2.401	0.10476	282.045	2.153	0.07456
202.348	3.644	0.10480	282.055	3.428	0.07570
202.400	4.960	0.10560	281.981	4.771	0.07657
202.395	6.309	0.10606	281.991	6.062	0.07716
202.587	8.086	0.10660	281.947	7.336	0.07787
202.579	9.299	0.10688	282.026	8.962	0.07881
202.570	10.592	0.10694	281.959	10.640	0.07939
202.566	11.912	0.10731	282.001	12.325	0.08024
222.322	1.028	0.09612	302.454	1.118	0.06715
222.311	2.300	0.09663	302.396	1.865	0.06788
222.299	3.552	0.09710	302.422	2.697	0.06870
222.277	4.896	0.09752	302.393	3.469	0.06919
222.271	6.165	0.09839	302.370	4.307	0.06956
222.256	7.719	0.09877	302.562	5.164	0.07011
222.234	9.091	0.09904	302.512	6.104	0.07065
222.226	10.750	0.10019	302.479	7.129	0.07158
222.057	12.065	0.09975	302.441	8.075	0.07193
242.560	1.127	0.08892	322.230	1.463	0.06079
242.557	2.313	0.08932	322.256	2.145	0.06158
242.543	3.553	0.08959	322.219	2.828	0.06223
242.512	4.916	0.09007	322.138	3.480	0.06300
242.490	6.300	0.09110	322.182	4.418	0.06493
242.465	7.672	0.09171	322.150	5.293	0.06421
242.436	8.979	0.09241	322.123	6.224	0.06504
242.498	10.373	0.09297	322.113	7.045	0.06538
242.482	11.940	0.09308	322.105	8.047	0.06607
262.821	1.020	0.08055	342.054	2.207	0.05453
262.331	2.316	0.08159	341.934	2.733	0.05601
262.401	3.564	0.08212	341.986	3.349	0.05687
262.302	4.849	0.08288	341.960	4.033	0.05685
262.301	6.199	0.08343	341.881	4.655	0.05804
262.222	7.587	0.08538	341.812	5.465	0.05821
262.133	8.944	0.08527	342.373	6.254	0.05875
262.098	10.612	0.08587	341.873	7.094	0.06015
262.180	11.997	0.08652	341.901	8.002	0.06093

Table A.1-37. Representative thermal conductivity data measured for the system R-1234yf/1234ze(E) at a molar composition of (0.642/0.358)

T / K	p / MPa	$\lambda / \text{W}\cdot\text{m}^{-1}\text{K}^{-1}$	T / K	p / MPa	$\lambda / \text{W}\cdot\text{m}^{-1}\text{K}^{-1}$
202.210	1.019	0.10063	282.395	0.916	0.07010
202.133	2.678	0.10049	282.367	2.179	0.07087
202.191	3.759	0.10202	282.313	3.392	0.07173
202.197	5.086	0.10246	282.261	4.656	0.07257
202.226	6.239	0.10248	282.139	6.225	0.07349
202.196	7.850	0.10265	282.141	7.739	0.07467
202.180	9.424	0.10287	282.038	9.183	0.07596
201.797	10.729	0.10362	282.083	10.489	0.07641
201.801	12.035	0.10472	282.106	11.877	0.07667
222.731	1.046	0.09173	302.587	1.090	0.06385
222.719	2.361	0.09268	302.518	1.939	0.06494
222.702	3.690	0.09303	302.442	2.694	0.06512
222.688	4.991	0.09363	302.357	3.521	0.06579
222.672	6.293	0.09420	302.380	4.214	0.06629
222.659	7.651	0.09471	302.283	5.050	0.06706
222.506	9.142	0.09493	302.314	6.072	0.06753
222.479	10.635	0.09549	302.290	7.078	0.06838
222.458	12.078	0.09613	302.250	7.996	0.06877
242.358	1.133	0.08430	322.788	1.475	0.05775
242.363	2.377	0.08508	322.756	2.215	0.05866
242.389	3.632	0.08568	322.753	2.789	0.05912
242.259	4.942	0.08661	322.657	3.256	0.05958
242.286	6.294	0.08717	322.645	4.395	0.06051
242.307	7.642	0.08788	322.641	5.290	0.06141
242.242	8.910	0.08816	322.514	6.137	0.06193
242.208	10.456	0.08835	322.532	7.099	0.06279
242.189	12.002	0.08916	322.436	7.960	0.06353
262.665	6.173	0.07972	343.282	2.172	0.05105
262.630	1.147	0.07707	343.167	2.801	0.05272
262.645	2.253	0.07758	343.087	3.351	0.05326
262.596	3.544	0.07877	342.997	4.040	0.05464
262.543	4.833	0.07958	343.920	4.956	0.05526
262.556	7.515	0.08049	343.259	5.456	0.05596
262.513	9.047	0.08141	342.640	6.125	0.05670
262.471	10.549	0.08238	342.593	7.006	0.05736
262.415	11.983	0.08226	342.450	7.928	0.05830

A.1.6. Mixture Preparation

All of the property measurements relied on preparation of the sample mixtures and accurate determination of their composition. The (p, ρ, T, x) and speed-of-sound measurements utilized gas-phase mixtures, while the VLE, thermal conductivity, and viscosity measurements utilized liquid-phase mixtures. The mixtures were prepared gravimetrically (by weighing) to achieve low uncertainties in the composition.

The pure-fluid refrigerants used to prepare the mixtures were used as received except that we degassed them (prior to preparing the mixtures) by freezing the pure components in liquid nitrogen, evacuating the vapor space, and thawing; this sequence was repeated until the residual pressure over the frozen sample was less than 0.01 Pa. We analyzed the pure-fluid refrigerants in-house using gas chromatography with mass spectrometry (GC-MS) and found no significant impurities.

The gas-phase blends were prepared in aluminum gas cylinders of approximately 6, 10 or 13 L internal volume depending on the pressure of the blend. The sample mass was determined by a double substitution weighing design as described by Harris and Torres [109] with a nearly identical “tare” or reference cylinder serving as the main substitution mass. Further details are provided by Richter and McLinden.[110] The uncertainty of the measured gas-phase mixture compositions, arising from the weighings, was 0.0001 mole fraction. The sample cylinders were loaded to pressures corresponding to the dew-point pressure at $T = 293.15$ K. There may have been a small amount of liquid in the sample cylinders after filling, but they were heated continuously to $T > 313$ K for the duration of the testing to ensure that only single-phase vapor was present. Due to sorption effects, the composition of the sample in the measuring cell could be different from that calculated from the sample masses loaded into the sample cylinder, and this contributed an additional uncertainty of 0.0002 mole fraction. The combined, expanded uncertainty was estimated to be 0.00022 mole fraction.

The liquid-phase mixtures were prepared in 300 mL stainless steel cylinders. The fluid with the higher boiling point was added first, then the second component. The vapor space above the mixture samples was degassed by freezing the sample with liquid nitrogen and opening the cylinder to vacuum. After evacuation, the sample was then heated to drive volatile impurities (such as air) into the vapor space. The entire cycle (freezing, evacuation, and heating) was repeated a minimum of three times for each sample. Mixtures were prepared with the goal of filling the sample cylinder with about 280 mL of liquid at ambient temperature. Thus, in each completed mixture cylinder there was a vapor space above the liquid phase.

A balance with a precision of 0.1 mg was used in the preparation of the liquid-phase mixtures. Utilizing the double-substitution weighing design of Harris and Torres,[109] measurement of the mass of each component consisted of weighing four masses: (1) a reference cylinder of approximately the same mass and volume as the empty sample cylinder, (2) the sample cylinder, (3) the sample cylinder plus a 20 g sensitivity weight, and (4) the reference cylinder plus the 20 g sensitivity weight. This weighing sequence was repeated four times for each mass determination. The density of ambient air was calculated based on measurements of temperature, pressure, and relative humidity, and the weighings were corrected for the effects of air buoyancy. The standard deviation of the repeat weighings was at most 1.5 mg. The uncertainty in the composition due to the weighings was less than 0.0001 mole fraction. Because of the two-phase nature of the liquid-

phase samples and because the weighings could determine only the overall (bulk) composition of the sample it was necessary to estimate the change in composition caused by the liquid/vapor fractionation inside the cylinder. This change was less than 0.0005 mole fraction, and its standard uncertainty was estimated to be less than 0.0001 mole fraction. Thus, the combined, expanded uncertainty in composition of the liquid-phase samples was estimated to be less than 0.00028 mole fraction.

A.1.7. Mixture Modeling

The multi-fluid modeling used in NIST REFPROP yields the most accurate mixture models available today. This approach combines the most accurate pure fluid equations of state with reducing and departure functions to correct for the changes to thermodynamics caused by mixture interactions. This approach forms the basis of the GERG-2008 model, used for custody transfer of natural gas mixtures, amongst many other uses. The refrigeration industry has been using the multi-fluid modeling approach for many years and will likely do so for many years to come.

Pure fluid equations of state. In this framework, the equation of state for a pure component is given in terms of the Helmholtz energy, in terms of the Massieu potential, given by $\alpha = a/(RT)$. Thermodynamic properties are obtained from combinations of the Helmholtz energy and its derivatives. For instance, the pressure is obtained from $p = -\partial\alpha/\partial v$. The total α is given as the sum of ideal-gas (non-interacting) and residual (interacting) contributions. The ideal-gas portion can in principle be obtained from theory for the given molecular species, and the residual contribution is entirely empirical, fit to experimental data as well and constrained to have the desired behavior at extremes in temperature and pressure. For most pure fluids, the residual Helmholtz energy can be expressed generically as

$$\alpha^r = \sum_i n_i \delta^{d_i} \tau^{t_i} \exp(-c_i \delta^{l_i} - \eta_i (\delta - \varepsilon_i)^2 - \beta_i (\tau - \gamma_i)^2) \quad (\text{A.1-13})$$

where $\tau = T_{\text{red}}/T$ and $\delta = \rho/\rho_{\text{red}}$ with T_{red} and ρ_{red} being the reducing temperature and reducing density, respectively. All remaining variables are empirical coefficients particular to the given fluid.

Mixture equation of state. The same thermodynamic identities hold for mixtures as for pure fluids. The Helmholtz energy for a mixture is commonly obtained as the sum of a corresponding states contribution and a departure term.

$$\alpha^r = \alpha_{CS}^r(\tau, \delta, \bar{x}) + \alpha_{dep}^r(\tau, \delta, \bar{x}) \quad (\text{A.1-14})$$

which becomes

$$\alpha^r = \sum_{i=1}^N x_i \alpha_{o,i}^r(\tau, \delta) + \sum_{i=1}^N \sum_{j=i+1}^N F_{ij} x_i x_j \alpha_{ij}^r(\tau, \delta), \quad (\text{A.1-15})$$

where the first summation arises from a composition-weighted sum of the pure fluid EOS terms and the double summation is the departure term, with the α_{ij}^r given by

$$\alpha_{ij}^r = \sum_k n_k \tau^{t_k} \delta^{d_k} \exp(-\text{sgn}(l_k) \delta^{l_k}) \quad (\text{A.1-16})$$

where the sgn function is the sign of the value: zero for an argument of zero, and 1 for positive arguments.

For mixtures $\tau = T_{red}(\bar{x})/T$ and $\delta = \rho/\rho_{red}(\bar{x})$. The reducing functions are given by

$$T_r(\bar{x}) = \sum_{i=1}^N \sum_{j=1}^N x_i x_j \beta_{T,ij} \gamma_{T,ij} \frac{x_i + x_j}{\beta_{T,ij}^2 x_i + x_j} (T_{c,i} \cdot T_{c,j})^{0.5} \quad (\text{A.1-17})$$

$$\frac{1}{\rho_r(\bar{x})} = \sum_{i=1}^N \sum_{j=1}^N x_i x_j \beta_{v,ij} \gamma_{v,ij} \frac{x_i + x_j}{\beta_{v,ij}^2 x_i + x_j} \frac{1}{8} \left(\frac{1}{\rho_{c,i}^{1/3}} + \frac{1}{\rho_{c,j}^{1/3}} \right)^3. \quad (\text{A.1-18})$$

Thus the reducing functions have four adjustable parameters per ij binary pair.

The phase equilibrium pressure is the result of an iterative calculation to equate pressure, temperature, chemical potentials of all species in all phases and amount of substances.

Parameter Optimization. We used the parameter optimization approach described in [111]. The parameters $\beta_{T,ij}$ and $\gamma_{T,ij}$ were obtained for each binary pair individually, leaving the other interaction parameters set to their default values. The experimental data were added to the database of experimental data used in the fitting tool. Then the python script was launched which carried out the optimization, doing a stochastic global optimization over the two interaction parameters with the DEAP software package. The approach used is a classical evolutionary optimization methodology with crossover/mutation, etc. This mixture behavior is ideal enough that simpler optimization approaches could have been used, but this implementation has proven to be reliable for fitting interaction parameters, particularly for fitting interaction parameters to outputs of iterative routines that can fail for a variety of different reasons. Failures of iterative routines are handled by adding a large contribution to the cost function. Derivatives are not used in the optimization approach, so the cost function to be minimized need not be differentiable.

The parameters thus obtained were given in the main text of the report in Tables 3.1-2 and 3.1-3.

Mixture viscosity model. In the extended corresponding states model used here, we represent the viscosity of a pure fluid as a sum of a dilute gas and a residual contribution, and apply a corresponding states principle to the residual contribution only[112],

$$\eta(T, \rho) = \eta^*(T) + \Delta\eta(T, \rho) = \eta^*(T) + \Delta\eta_0(T_0, \rho_0) F_\eta(T, \rho), \quad (\text{A.1-19})$$

where the superscript * denotes a dilute gas value, and the subscript 0 denotes a reference fluid value. The viscosity of the reference fluid is evaluated at a conformal temperature and density T_0 and ρ_0 given by

$$T_0 = T / f \quad (\text{A.1-20})$$

and

$$\rho_0 = \rho h. \quad (\text{A.1-21})$$

The quantities f and h are called equivalent substance reducing ratios, and relate the reference fluid to the fluid of interest using a ratio of critical parameters (denoted by the subscript c) and functions of temperature and density known as shape functions θ and Φ ,

$$f = \frac{T_c}{T_{c0}} \theta \quad (\text{A.1-22})$$

and

$$h = \frac{\rho_{c0}}{\rho_c} \phi. \quad (\text{A.1-23})$$

The shape factors can be considered functions of both temperature and density. Different can be used to determine shape factors, here we use a form of the “exact” shape factor method[113].

The dilute-gas viscosity in Eq. (1) is given by the Chapman-Enskog theory[114],

$$\eta^*(T) = \frac{5\sqrt{mk_B T}}{16\pi\sigma^2\Omega^{(2,2)}}, \quad (\text{A.1-24})$$

where the dilute-gas viscosity is η^* , m is the molecular mass, k_B is the Boltzmann constant, σ . Is the collision diameter, and T is the absolute temperature. We assume that a Lennard-Jones 12-6 potential applies, and use the correlation of Neufeld et al.[21] for the collision integral $\Omega^{(2,2)}$.

The factor F_η in Eq. (1) is found by using the expression

$$F_\eta = f^{1/2} h^{-2/3} \left[\frac{M}{M_0} \right]^{1/2} \quad (\text{A.1-25})$$

where M is the molar mass of the fluid and M_0 is the molar mass of the reference fluid. The functions f and h are found from thermodynamic data and are described in Klein et al.[22].

The extension of the model to mixtures is similar to that presented for pure fluids but involves an extra step. First, one represents the properties of the mixture in terms of a hypothetical pure fluid (denoted here by the subscript x) that is obtained through the use of mixing rules,

$$f_x = h_x^{-1} \sum_{j=1}^n \sum_{i=1}^n x_i x_j f_{ij} h_{ij} \quad (\text{A.1-26})$$

$$h_x = \sum_{j=1}^n \sum_{i=1}^n x_i x_j h_{ij} \quad , \quad (\text{A.1-27})$$

and combining rules,

$$f_{ij} = \sqrt{f_i f_j} (1 - k_{ij, f\eta}) \quad (\text{A.1-28})$$

$$h_{ij} = \frac{(h_i^{1/3} + h_j^{1/3})^3}{8} (1 - k_{ij, h\eta}), \quad (\text{A.1-29})$$

where $k_{ij, f\eta}$ and $k_{ij, h\eta}$ are binary interaction parameters we determined by fitting mixture experimental data.

We assume that the viscosity of the mixture obeys a corresponding states principle,

$$\eta(T, \rho, x) = \eta^*(T, x) + \Delta\eta(T, \rho, x) = \eta^*(T, x) + \Delta\eta_0(T_0, \rho_0) F_\eta(T, \rho), \quad (\text{A.1-30})$$

where the factor F_η for mixtures is found with

$$F_\eta = f_x^{1/2} h_x^{-2/3} g_x^{1/2}, \quad (\text{A.1-31})$$

$$g_x^{1/2} = \frac{\sum_{i=1}^n \sum_{j=1}^n x_i x_j f_{ij}^{1/2} h_{ij}^{4/3} M_{ij}^{1/2}}{f_x^{1/2} h_x^{4/3}} \quad (\text{A.1-32})$$

$$M_{ij} = \frac{2}{1/M_i + 1/M_j}. \quad (\text{A.1-33})$$

For the dilute gas viscosity, binary interaction parameters $k_{ij, \sigma}$ and $k_{ij, \varepsilon}$ are used,

$$\sigma_{ij} = (1 - k_{ij, \sigma}) \sqrt{\sigma_i \sigma_j} \quad (\text{A.1-34})$$

$$\varepsilon_{ij} / k_B = (1 - k_{ij, \varepsilon}) \sqrt{(\varepsilon_i / k_B)(\varepsilon_j / k_B)}. \quad (\text{A.1-35})$$

where σ_i and ε_i/k are the Lennard-Jones size and energy parameters for the pure fluid. When there are sufficient dilute-gas viscosity data available, the binary interaction parameters are obtained by fitting experimental data. Otherwise, they are set to zero. The parameters are given in Table A.1-35.

Mixture thermal conductivity model (ECS). According to the procedure of Ely and Hanley[28] and we represent the thermal conductivity of a fluid as the sum of translational (from collisions between molecules) and internal (due to internal motions of the molecule) modes of energy transfer,

$$\lambda(T, \rho) = \lambda^{\text{int}}(T) + \lambda^{\text{trans}}(T, \rho). \quad (\text{A.1-36})$$

The translational contribution may be further divided into a translational dilute-gas contribution (denoted here by a superscript *) that is a function only of temperature, a residual contribution, and a critical enhancement,

$$\lambda^{\text{trans}}(T, \rho) = \lambda^*(T) + \lambda^r(T, \rho) + \lambda^{\text{crit}}(T, \rho), \quad (\text{A.1-37})$$

leading to the following expression for the thermal conductivity

$$\lambda(T, \rho) = \lambda^{\text{int}}(T) + \lambda^*(T) + \lambda^r(T, \rho) + \lambda^{\text{crit}}(T, \rho). \quad (\text{A.1-38})$$

We use an Eucken correlation for the internal contribution

$$\lambda^{\text{int}}(T) = \frac{f_{\text{int}} \eta^*}{M} \left[C_p^* - \frac{5}{2} R \right], \quad (\text{A.1-39})$$

where C_p^* is the ideal-gas heat capacity in J/(mol·K), R is the molar gas constant (8.314 472 J/(mol·K)), η^* is the dilute-gas viscosity ($\mu\text{Pa}\cdot\text{s}$) as given in Eq. (6), f_{int} is set to $1.32 \cdot 10^{-3}$, and λ is in W/(m·K). If sufficient dilute-gas thermal conductivity data are available, f_{int} is fit to a polynomial in temperature,

$$f_{\text{int}} = a_0 + a_1 T. \quad (\text{A.1-40})$$

For the dilute-gas translational contribution (in W/(m·K)) we use

$$\lambda^*(T) = \frac{15 \times 10^{-3} R \eta^*}{4M}, \quad (\text{A.1-41})$$

where the dilute gas viscosity η^* is from the pure fluid correlation implemented in REFPROP. The residual contribution is found using extended corresponding states:

$$\lambda^r(T, \rho) = \lambda_0^r(T_0, \rho_0) F_\lambda, \quad (\text{A.1-42})$$

with

$$F_\lambda = f^{1/2} h^{-2/3} \left[\frac{M_0}{M} \right]^{1/2}. \quad (\text{A.1-43})$$

The critical contribution is computed using a simplified crossover model developed by Olchowy and Sengers [29, 30], that we will not discuss here.

The extension of the model to mixtures is similar to that presented for viscosity,

$$\lambda(T, \rho, x) = \lambda^*(T, x) + \lambda^{\text{int}}(T, x) + \Delta \lambda^r(T, \rho) + \lambda^{\text{crit}}(T, \rho, x) \quad (\text{A.1-44})$$

and only the residual contribution is treated with corresponding states.

$$\lambda(T, \rho, x) = \lambda^*(T, x) + \lambda^{\text{int}}(T, x) + \Delta\lambda_0(T_0, \rho_0)F_\lambda(T, \rho) + \lambda^{\text{crit}}(T, \rho, x) \quad (\text{A.1-45})$$

The internal and translational dilute-gas contributions for the mixture are found with the empirical mixing rule,

$$\lambda_{\text{mix}}^{\text{int}}(T, x) + \lambda_{\text{mix}}^*(T, x) = \frac{\sum_{j=1}^n x_j (\lambda_j^{\text{int}}(T) + \lambda_j^*(T))}{\sum_{i=1}^n x_i \phi_{ji}}, \quad (\text{A.1-46})$$

with

$$\phi_{ji} = \frac{(1 - k_{ij,\lambda}) \left(1 + \sqrt{\eta_j^* / \eta_i^*} (M_j / M_i)^{1/4}\right)^2}{\left(8(1 + M_j / M_i)\right)^{1/2}} \quad (\text{A.1-47})$$

All quantities are evaluated at the mixture temperature T , and the dilute-gas viscosity is found with the pure fluid equation implemented in REFPROP. The parameter $k_{ij,\lambda}$ is an empirical binary interaction parameter for the dilute gas region determined by fitting experimental data.

The residual contribution for the mixture requires calculation of a mixture F_λ with

$$F_\lambda = f_x^{1/2} h_x^{-2/3} g_x^{1/2}, \quad (\text{A.1-48})$$

$$g_x^{1/2} = \frac{M_0^{1/2}}{f_x^{1/2} h_x^{4/3}} \sum_{i=1}^n \sum_{j=1}^n x_i x_j (f_{ij})^{1/2} \left(\frac{2}{1/g_i + 1/g_j}\right)^{-1/2} (h_{ij})^{4/3}, \quad (\text{A.1-49})$$

with g_i found with

$$g_i = M_0 \left(\frac{\lambda_0^i(T_0, \rho_0)}{\lambda_j^i(T_j, \rho_j)}\right)^2 f_j h_j^{-4/3} \quad (\text{A.1-50})$$

Similar to the procedure for the calculation of the viscosity, we use the combining rules

$$f_{ij} = \sqrt{f_i f_j} (1 - k_{ij,f\lambda}) \quad (\text{A.1-51})$$

$$h_{ij} = \frac{(h_i^{1/3} + h_j^{1/3})^3}{8} (1 - k_{ij,h\lambda}), \quad (\text{A.1-52})$$

where binary interaction parameters $k_{ij,f\lambda}$ and $k_{ij,h\lambda}$ can be determined by fitting experimental data when available. Otherwise, they are set to zero.

As observed for pure fluids, there also is an enhancement of the thermal conductivity observed near the critical point; however, theory for mixtures is not as well developed as for pure fluids. We will not discuss that term here, further details can be found in Chichester and Huber[24]

We fit experimental data as discussed below to obtain binary interaction parameters used in the equations for the ECS models for viscosity and thermal conductivity in REFPROP v10.0. The parameters are summarized in Table A.1-38 below and are included in the HMX.BNC file also included with this report. Details on the data used and comparisons with data are in the following paragraphs.

Table A.1-38. Binary interaction parameters for the ECS models for viscosity and thermal conductivity for use with REFPROP v10.0

Mixture	$k_{ij,\sigma}$	$k_{ij,\varepsilon}$	$k_{ij,f\eta}$	$k_{ij,h\eta}$	$k_{ij,\lambda}$	$k_{ij,f\lambda}$	$k_{ij,h\lambda}$
R-134a/1234yf	0	0	-0.0614	0.0167	0	-0.094	0.092
R-134a/1234ze(E)	0	0	-0.0019	-0.0204	0.05552	-0.24518	0.14319
R-1234yf/1234ze(E)	0.0248	-0.4166	0.0373	-0.0127	0	0.007	0.039
R-1234ze(E)/227ea	0.0990	-0.7885	-0.0413	0.0005	0.01781	0.00834	0.01654
R-1234ze(E)/125	0.0990	-0.7885	-0.0413	0.0005	0.01781	0.00834	0.01654

Mixture viscosity and thermal conductivity—comparisons to data:

R-134a/1234yf.

Interaction parameters for the viscosity were fit to literature data of Bi et al.[115], Yang et al.[116] and Liang et al.[117] The Bi et al. [115] data are presented as kinematic viscosity and were converted to absolute viscosity using densities calculated from REFPROP v10. A total of 113 points were found, covering both liquid and vapor phases near saturation. The data cover six different compositions, 0.25, 0.32, 0.5, 0.6, 0.77, and 0.8 mole fraction R-134a. The average absolute deviation (AAD) was 0.91 %, with an estimated uncertainty at the 95 % level of 2.3%. Deviations as a function of temperature are shown in Figure A.1-11. The thermal conductivity model parameters were obtained by fitting the NIST data thermal conductivity data obtained in this work. The AAD for 781 liquid phase points from NIST at pressures up to 12 MPa is 0.82%, with an estimated uncertainty of 1.6% for the liquid phase. There was one additional very limited set of data found in the literature, by Kim et al.[118] The data cover compositions of 0.35, 0.50, and 0.68 mole fraction of R-134a. Deviations as a function of temperature are shown in Figure A.1-12.

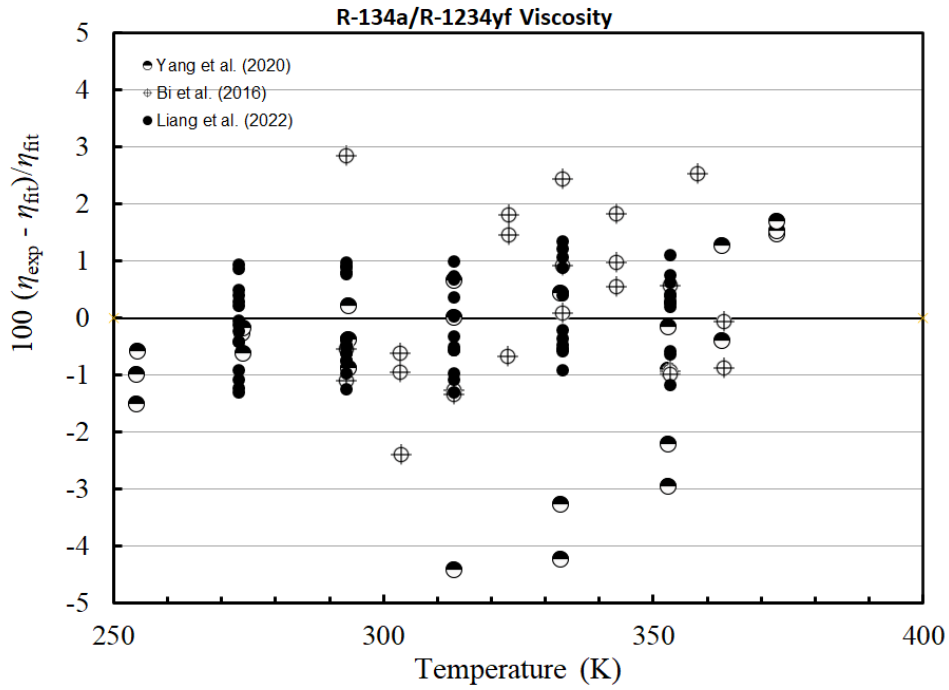


Figure A.1-11. Deviation plot for viscosity of R-134a/1234yf mixtures as a function of temperature

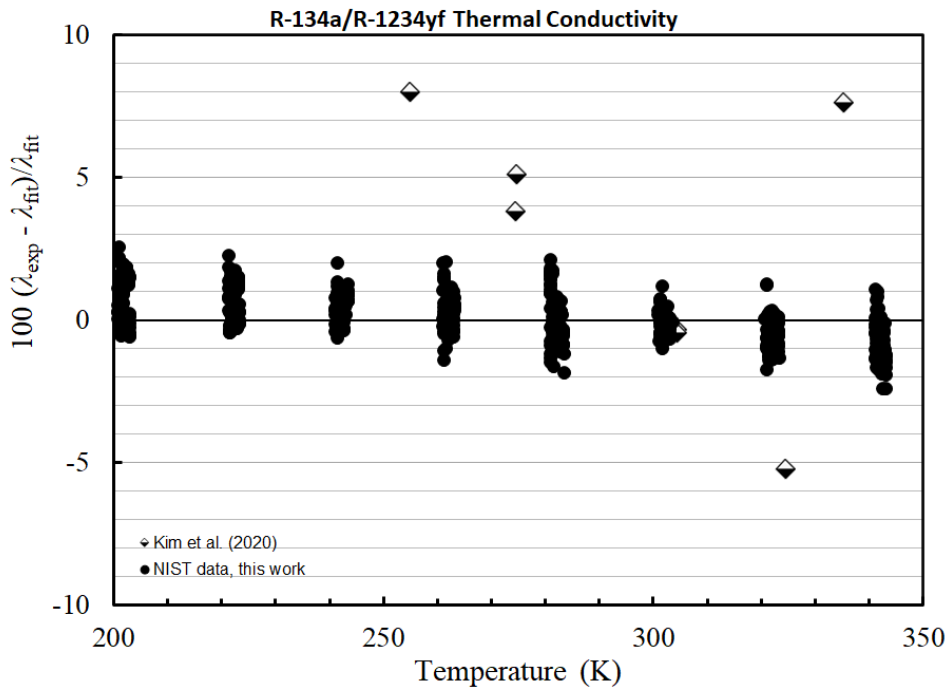


Figure A.1-12. Deviation plot for thermal conductivity of R-134a/1234yf mixtures as a function of temperature

R-134a/1234ze(E)

Interaction parameters for the viscosity were fit to literature data of Bi et al.[115] and Liang et al.[117] The Bi et al.[115] data are presented as kinematic viscosity and were converted to absolute viscosity using densities calculated from REFPROP v10. A total of 69 points were found, all liquid. The data are at a mole fraction of 0.2429, 0.44, 0.4982, and 0.7506 R-134a. The average absolute deviation (AAD) was 0.9 %, with an estimated uncertainty at the 95 % level of 2.4%. Deviations as a function of temperature are shown in Figure A.1-13. The thermal conductivity data from NIST obtained in this work, and the vapor points of Mylona et al.[119] were fit to obtain the parameters in Table 1. The AAD for 685 liquid phase points from NIST at pressures up to 50 MPa is 0.7%, with an estimated uncertainty of 1.8% for the liquid phase. There was one additional very limited set of data found in the literature, by Mylona et al.[119] that contained both vapor and liquid points near saturation. The data cover compositions of 0.32, 0.50, and 0.64 mole fraction of R-134a. Deviations as a function of temperature are shown in Figure A.1-14.

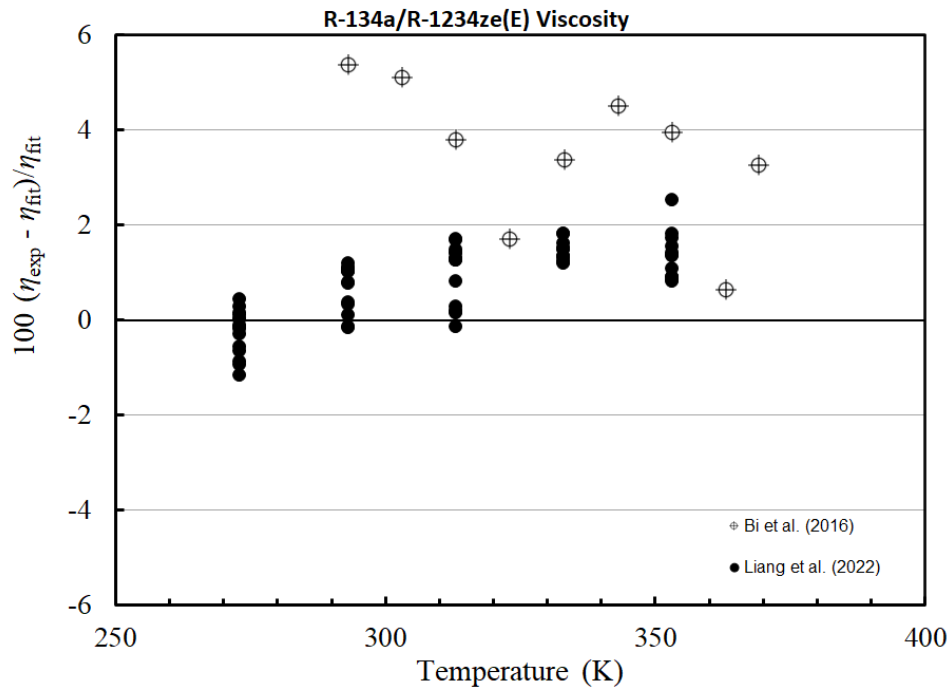


Figure A.1-13. Deviation plot for viscosity of R-134a/R-1234ze(E) mixtures as a function of temperature

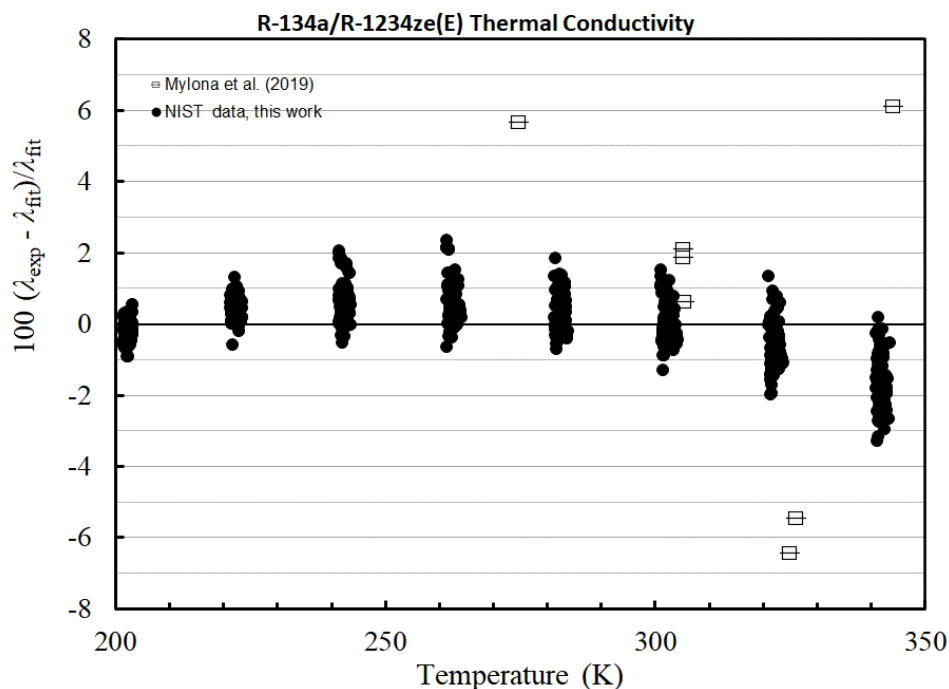


Figure A.1-14. Deviation plot for thermal conductivity of R-134a/1234ze(E) mixtures as a function of temperature

R-1234yf/1234ze(E)

Interaction parameters for the viscosity were obtained by fitting the literature data of Akhfish et al. [120] and Liang et al.[117]. A total of 69 points were fit covering liquid at pressures to 15 MPa and vapor states near saturation. The data are at a mole fraction of 0.2577, 0.5, and 0.7511 R-1234yf. The average absolute deviation (AAD) was 0.9 %, with an estimated uncertainty at the 95 % level of 2.0%. Deviations as a function of temperature are shown in Figure A.1-15. The thermal conductivity data parameters were obtained by fitting the NIST data in this work. The AAD for 693 liquid phase points from NIST at pressures up to 12 MPa is 0.84%, with an estimated uncertainty of 1.8% for the liquid phase. There was one additional very limited set of data found in the literature, by Mylona et al.[119] The data cover compositions of 0.334, 0.50, and 0.663 mole fraction of R-1234yf. Deviations as a function of temperature are shown in Figure A.1-16.

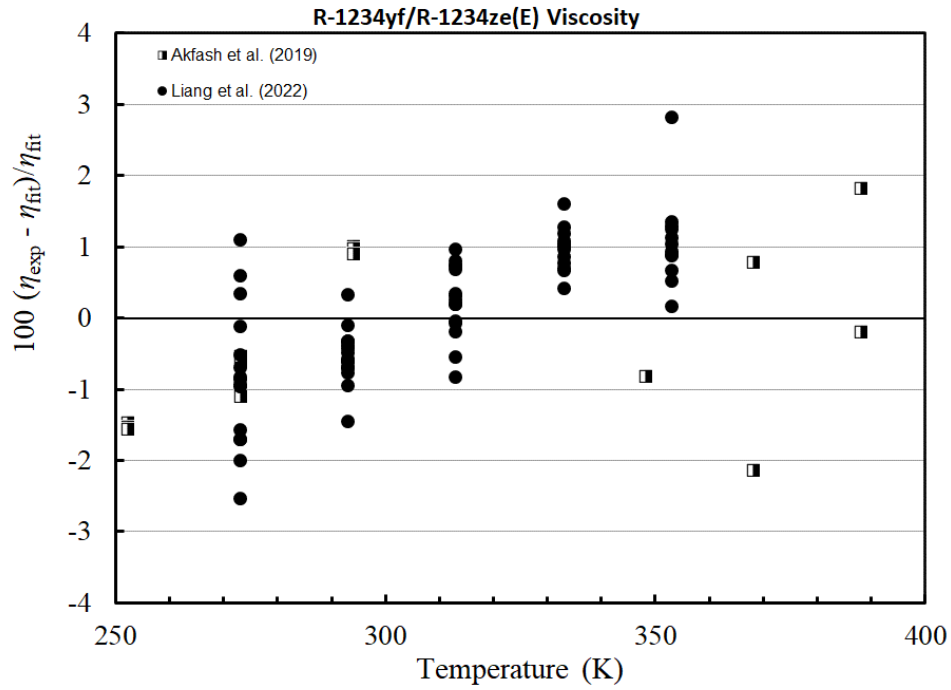


Figure A.1-15. Deviation plot for viscosity of R-1234yf/1234ze(E) mixtures as a function of temperature.

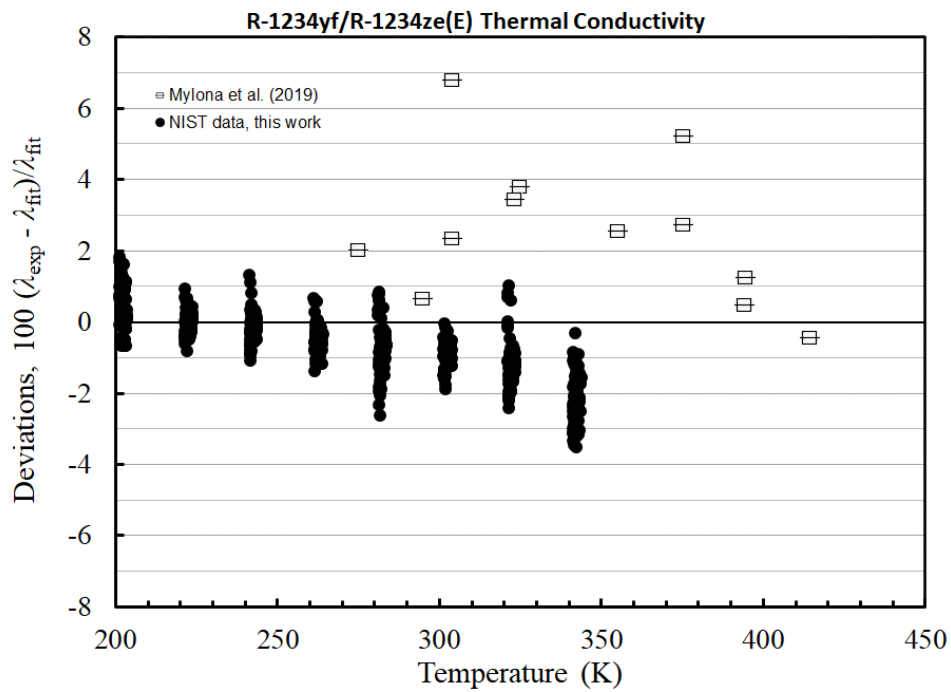


Figure A.1-16. Deviation plot for thermal conductivity of R-1234yf/R-1234ze(E) mixtures as a function of temperature

R1234ze(E)/R227ea

We were unable to locate experimental data for thermal conductivity or viscosity of R-227ea mixed with R-1234ze(E). In fact, we were unable to locate experimental viscosity or thermal conductivity data of R-227ea mixed with *any* compound! There are data for viscosity[120] and thermal conductivity[119] for mixtures of R-125 and R-1234ze(E), and these data were fit to obtain binary interaction parameters for R-125/R-1234ze(E). R-227ea (1,1,1,2,3,3,3-heptafluoropropane, C₃HF₇) and R-125 (pentafluoroethane, C₂HF₅) are both highly fluorinated n-alkanes that should have similar interaction behavior with R-1234ze(E). These parameters should provide a reasonable estimation for the R-1234ze(E)/R-227ea mixture. We estimate the uncertainty in the liquid phase for viscosity and for thermal conductivity should be on the order of 5-10%. Figures A.1-17 and A.1-18 show the viscosity and thermal conductivity deviations for the surrogate system R-1234ze(E)/125.

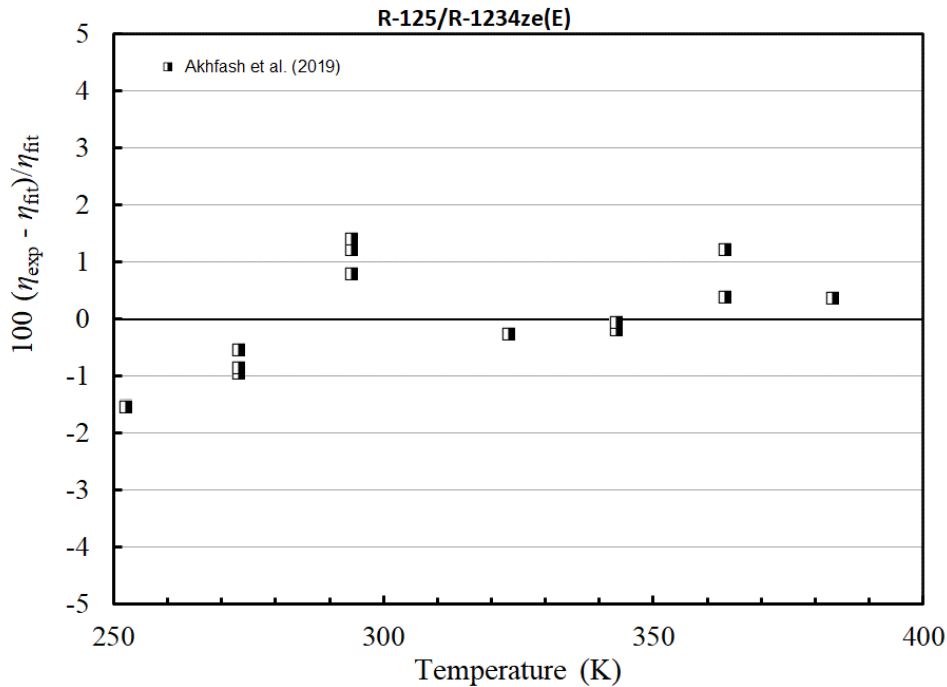


Figure A.1-17. Deviation plot for viscosity of R-125/R-1234ze(E) mixtures as a function of temperature

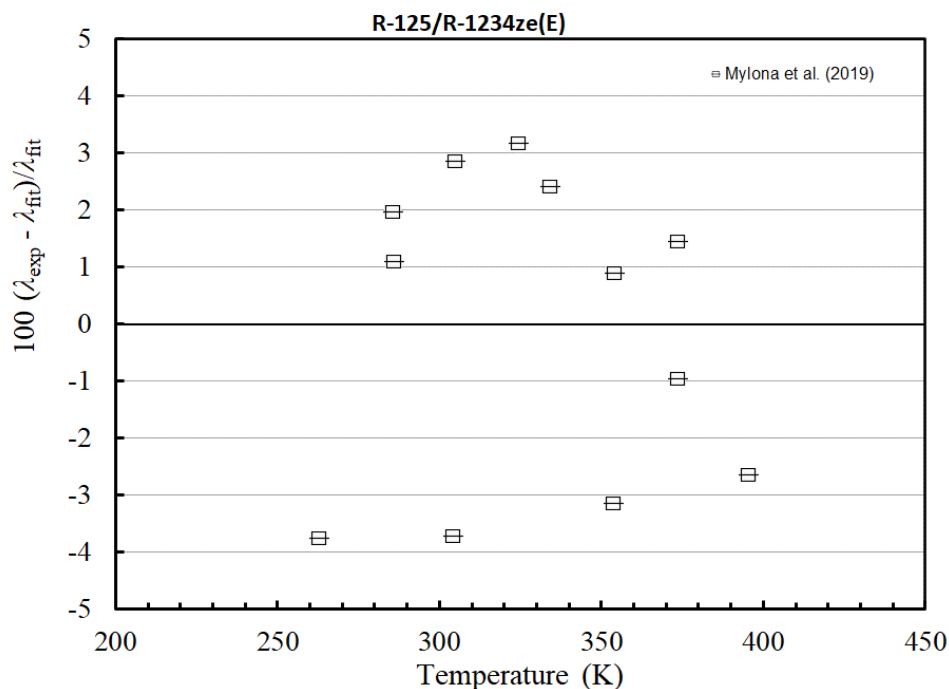


Figure A.1-18. Deviation plot for thermal conductivity of R-125/R-1234ze(E) mixtures as a function of temperature

Mixture thermal conductivity model (Entropy Scaling). In recent years it has become increasingly clear that the transport properties are strongly connected with the residual entropy (i.e., the entropy of a fluid minus the contribution of the ideal-gas, or zero-density limit). This result was first proposed by Rosenfeld in 1977 [121] based on the limited molecular dynamics simulations available at that time. The advent of modern computational resources has meant that Rosenfeld’s suggestion has been investigated much in greater detail in recent years. The Lennard-Jones 12-6 fluid, one of the most popular molecular model fluids because it includes physically reasonable attraction and repulsion contributions, has recently been shown to follow entropy scaling for viscosity, thermal conductivity, and self-diffusion. [122] Additional studies have demonstrated that the general framework of modified residual entropy scaling allows for an excellent collapse of the experimental transport data for other systems, including the viscosity of propane[123], normal alkanes[124], and refrigerants.[125]

Other researchers[126-129] have applied an older variant of entropy scaling to refrigerant mixtures, but their overall approach of reducing by the dilute-gas viscosity does not follow the correct theoretical constraints in the liquid phase, which is particularly problematic for small molecules like methane and argon.

The approach of modified residual entropy scaling meets the required theoretical limits in the liquid phase, does not diverge at zero density like the original Rosenfeld scaling approach, and also allows for a formulation consistent with highly accurate dilute-gas measurements and modeling.

In this work we follow the modified residual entropy scaling approach. To begin, the residual entropy is defined by

$$s^r \equiv s(T, \rho) - s^{\text{ig}}(T, \rho) \quad (\text{A.1-53})$$

where s is the entropy per particle and s^{ig} is the ideal-gas entropy per particle, so the value of the reduced scaled residual entropy is given by $s^+ \equiv -s^r/k_B$ if s^r is on a per-particle basis. The residual entropy s^r is a measure of the structure of the fluid phase. Intermolecular interactions have the impact of reducing the possible microstates, so s^r is generally negative, and therefore s^+ is positive.

The Rosenfeld-scaled (or macroscopically scaled) thermal conductivity is defined based on non-dimensionalizing the thermal conductivity by the appropriate length, time, and energy scales for the liquid phase. This yields the definition

$$\tilde{\lambda} = \frac{\lambda}{k_B \rho_N^{2/3} \sqrt{k_B T/m}} \quad (\text{A.1-54})$$

As the number density $\rho_N = \rho N_A$ goes to zero at constant temperature, the value of $\tilde{\lambda}$ diverges, but this divergence can be repaired by taking advantage of the result noted by Rosenfeld for inverse-power-law (IPL) fluids of very low but finite density that scaled transport properties are proportional to $(s^+)^{-2/3}$, which allows for the definition of a term that breaks the zero-density divergence:

$$\lambda^+ = \tilde{\lambda} \times (s^+)^{2/3} \quad (\text{A.1-55})$$

Thus, λ^+ is a function of the reduced scaled residual entropy s^+ , with a factor including the molar density ρ , Boltzmann constant k_B , Avogadro's constant N_A , temperature T , and mass of a molecule m . All dimensional quantities are expressed in base-SI units (kg, m, Pa, etc.).

In the case of mixtures, a mixing rule must be defined for the effective mass of one particle m . In other works, the mass of the heaviest particle has been used [130]. Mass-fraction weighting of the molecular masses of the components has proven to be the most successful scaling approach in this case, slightly better than mole-fraction weighting of the molecular masses. Otherwise, the quantities ρ_N and s^+ are obtained from an empirical equation of state. In this case, we have used the updated interaction parameters fitted in this work.

In these scaled coordinates, the experimental mixture thermal conductivity data fall very nearly along a single curve, as shown in Figure A.1-19(a). The curve is given by a simple polynomial fitted to the experimental data by unweighted linear least squares:

$$\lambda^+ = \sum_i c_i (s^+)^i \quad (\text{A.1-56})$$

where the coefficients c_i are given in Table A.1-39, and the deviations are shown in Figure A.1-19(b). The average absolute deviation is 1.32 % and the central 95.5 percentiles of the signed relative errors (approximately equivalent to a 95 % confidence interval) span the range -2.82 % to 2.98 %. This quality of fit is rather remarkable given that a total of six mixtures formed of

three different components are collapsed to a single curve with no empirical tuning parameters. While this interim correlation was fitted to only liquid phase data, with a dilute-gas model and a critical enhancement model, its range of validity can be extended to the entire phase diagram, from dilute gas to the melting line.

Table A.1-39. Coefficients for entropy scaling of thermal conductivity data (Eq. A.1-56).

i	c_i
0	15.19495
1	-6.29123
2	2.74329
3	-0.12635

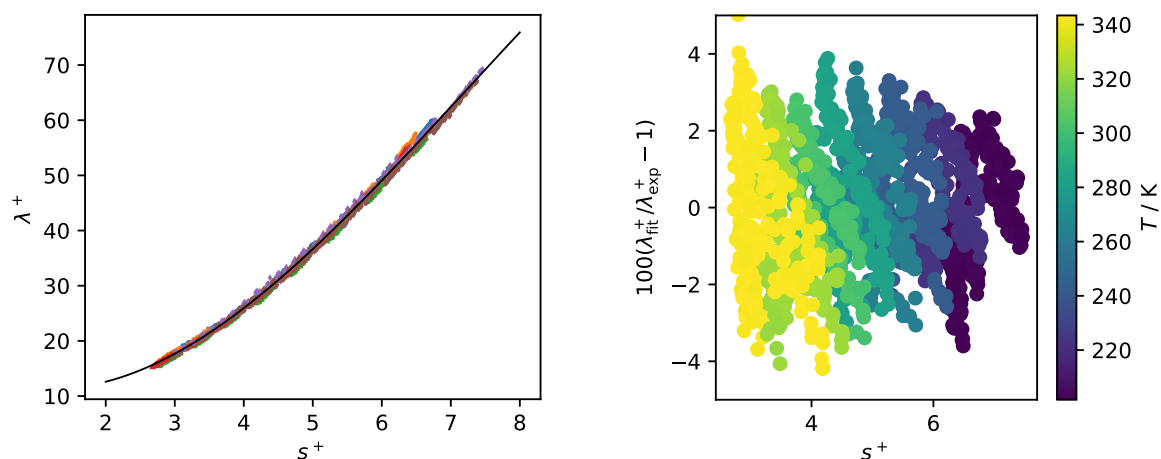


Figure A.1-19. Entropy scaling model for the thermal conductivity of the three blends studied here; (a) plus-scaled thermal conductivity λ_+ as a function of reduced scaled residual entropy s_+ , the different symbols denote the different measured blends; (b) relative deviations in λ_+

A.1.8. Mixture Parameter File for Use With REFPROP (HMX.bnc)

The following file contains the mixture parameters fitted in this work in the form needed for use with the NIST REFPROP database.

HMX !Mnemonic for mixture model, must match hfmix on call to SETUP.
4 !Version number

! Changelog:
! -----

! 03-30-22 IHB, Add interaction models for Army mixtures R134a/R1234yf, R134a/R1234ze(E),
! R1234yf/R1234ze(E), R1234ze(E)/R227ea, R125/R1234yf, R1234yf/R152a
! 03-30-22 MLH, Add transport binints for Army mixtures R134a/R1234yf, R134a/R1234ze(E),
! R1234yf/R1234ze(E), R1234ze(E)/R227ea, R125/R1234ze(E)
!
! Note: This file is only for documentation of the above binary pairs; users
! should request a "complete" HMC.bnc file from NIST for doing any computations
! with REFPROP.

#BNC !Binary mixing coefficients
BNC

? Binary mixing coefficients for the various mixing rules used with the HMX model:

?
? B0i: ---> Mixing rules developed for low-GWP refrigerant mixtures, see Bell, JPCRD,
? 2022. DOI:10.1063/5.0086060

? model BetaT GammaT BetaV GammaV Fij not used

? TRN: ---> Transport mixing rules

? model a1 a2 a3 a4 a5 a6

? Coefficients for binary critical lines (where the # sign is a number from 1 to 7):

?
? TC#: (type I mixtures)

? model a1 a2 a3 a4 a5 a6

? Where Tc of the mixture is calculated with the following equation:

? $T_c = x_1 T_{c1} + x_2 T_{c2} + x_2 (a_1 x_1 + a_2 x_1^{**2} + a_3 x_1^{**3} + a_4 x_1^{**4} + a_5 x_1^{**5} + a_6 x_1^{**6})$

? VC#: (type I mixtures)

? model a1 a2 a3 a4 a5 a6

? Where Vc of the mixture is calculated with the following equation:

? $V_c = x_1 V_{c1} + x_2 V_{c2} + x_2 (a_1 x_1 + a_2 x_1^{**2} + a_3 x_1^{**3} + a_4 x_1^{**4} + a_5 x_1^{**5} + a_6 x_1^{**6})$

? Format for a binary pair:

? Line 1: Comments beginning with '?' (these are read by Fortran and displayed by GUI)

? 2: Additional comments beginning with '?' (multiple lines with a ? can be used)

? 3: HASH_1 / HASH_2

? 4: model binary parameters

? 5: model Tc line parameters

? 6: model Vc line parameters

? 7: model Pr line parameters

? 8: separator line (!)

? Only lines 3 and 8 are required

?
?
?

? Selection of mixture model when more than one is present:

?
? If the GERG-08 model is off, The last line in the HMX.BNC for a given
? binary pair will always be the one used.

? If the GERG-08 option is on, the line containing GG is used if available.

? New mixture models always follow the lines with GG in the HMX.BNC.

? Order of sorting of binary pairs:

?
? 1. Each binary pair is internally sorted by normal boiling point temperatures of the fluids.

? For instance for the pair hydrogen + water, hydrogen has a lower NBP, therefore the order

? is hydrogen, water.
 ?
 ? Exception: Methane is always the first fluid listed in the binary pair.
 ?
 ? 2. The binary pairs (once internally sorted) are first sorted by the NBP of the first
 ? component, then, by the NBP of the second component.
 ?
 ? Note: If you need to swap the order of a binary pair, the kij (for PR), Fij, gammaT,
 ? and gammaV values do not need to be adjusted, but $\beta_{ij} = 1/\beta_{ji}$,
 ? thus the betaT and betaV values need to be modified, which will introduce a
 ? small discrepancy from tabulated values. Also, the coefficients for the critical
 ? line (TCx, VCx) need to be refitted. Other models are mostly symmetric so no
 ? swapping of parameters is needed.
 ?
 ? Here is a sample entry (the block must start in column 1, not column 3 as shown below):
 ?
 ?!
 ? ?Rxxx/Rxxx
 ? ?Example setup for a new mixture
 ? HASH_1/HASH_2
 ? KW0 1. 1. 1. 1. 0. 0.
 ? TC1 0. 0. 0. 0. 0. 0.
 ? VC1 0. 0. 0. 0. 0. 0.
 ?!
 ?
 ? Some entries in the binary pairs refer to the following notes:
 ? a) The GG model comes from the Kunz and Wagner (2007) equation of state and has been
 ? replaced with a newer model, details are given above.
 ? The line is only active when the "use full GERG natural gas mixture model" preference
 ? is selected in the GUI.
 ? b) The values of betaT and betaV are reciprocals of the published values, but deviations
 ? are expected to be less than 1 ppb.
 ?
 !
 ?R125/R1234yf [R125/R1234YF]
 ?Bell, JPCRD, 2022. DOI:10.1063/5.0086060
 25c5a3a0/40377b40
 XR0 1. 0.999 1. 1. 0. 0. 0.0.0.0.0.
 XR0 0.9996370 0.9993560 1.0000000 1.0000000 0.0000000 0. 0.0.0.0.0.
 TC1 5.8338929 -1.2922015 -0.60358991 4.6840411 -6.3807961 2.8779543 0.0.0.0.0.
 VC1 0.03465322 -0.18596521 0.54735835 -0.86652592 0.68531297 -0.20631724 0.0.0.0.0.0.
 !
 ?R125/R1234ze(E) [R125/R1234ZEE]
 ?E.W. Lemmon, NIST (2015); fit of data from Honeywell
 ?MLH NIST (2022); viscosity data of Akhfash et al. (2019) AAD 0.8% for 14 points, gas and liquid.
 ?MLH NIST (2022); k data of Mylona et al. (2019) AAD:2.3% 6 vapor and 6 liquid pts
 25c5a3a0/9905ef70
 XR0 1.003 1.0071 1. 1. 0. 0. 0.0.0.0.0.
 TC1 16.462433 -1.8778443 4.1582447 -3.6877402 -0.76361202 0.59145319 0.0.0.0.0.0.
 VC1 0.12776123 -1.1258322 4.2941427 -8.1990093 7.5649086 -2.6898164 0.0.0.0.0.0.
 TRN 0.0990 -0.7885 -0.0413 0.0005 0.01781 0.00834 0.01654 0.0.0.0.0.
 !
 ?R1234yf/R134a [R1234YF/R134A]
 ?Bell, JPCRD, 2022. DOI:10.1063/5.0086060
 ? MLH NIST (2022) NIST thermal conductivity data fit AAD 0.8% for 781 points
 ? MLH NIST (2022) literature data sets (Bi 2016, Yang 2020, Liang 2022) fit AAD 1% for 113 points
 40377b40/ff1c0560
 XR0 1.000 0.985 1. 1. 0. 0. 0.0.0.0.0.
 B01 1.0000260 0.9870570 1.0002720 1.0037470 1.000000 0. 0.0.0.0.0.0.
 TC1 -9.9853692 -9.5430775 34.128183 -62.871803 59.248474 -21.306207 0.0.0.0.0.0.
 VC1 -0.008312969 0.02313789 -0.046892213 0.12833899 -0.14875803 0.06357655 0.0.0.0.0.0.
 TRN 0.0 -0.0 -0.0614 0.0167 0.0 -0.094 0.092 0.0.0.0.0.
 !

?R1234yf/R152a [R1234YF/R152A]
 ?Bell, JPCRD, 2022. DOI:10.1063/5.0086060
 40377b40/63f364b0
 XR0 0.99630004 0.98112 1. 1. 0. 0. 0. 0. 0. 0. 0.
 XR0 1.00291800 0.98392800 1.00000000 1.00000000 0.00000000 0. 0. 0. 0. 0. 0.
 TC1 -15.787637 0.34244368 5.6604042 -1.9003625 0.5890511 -0.49678279 0. 0. 0. 0. 0. 0.
 VC1 -0.01928418 0.03417393 -0.03988139 0.0835224 -0.09022803 0.03654228 0. 0. 0. 0. 0. 0.

!
 ?R1234yf/R1234ze(E) [R1234YF/R1234ZEE]
 ?I.H. Bell, JPCRD, 2022. DOI:10.1063/5.0086060
 ?MLH NIST (2022); Army project fit viscosity of Akfash et al. (2019) and Liang et al. (2022) , AAD 0.8% for 69 points.
 ?MLH NIST (2022); Army project fit NIST thermal conductivity data, AAD 0.84% 693 points
 40377b40/9905ef70
 XR0 1. 0.987 1. 1. 0. 0. 0. 0. 0. 0. 0.
 B00 0.9988860 0.99330900 0.99930200 0.99859000 1.00000000 0. 0. 0. 0. 0. 0.
 TC1 -7.1434447 -4.9702253 2.8323449 -1.4755042 1.3431936 -0.43993195 0. 0. 0. 0. 0. 0.
 VC1 0.03373132 -0.32571815 1.2166965 -2.2685455 2.0656689 -0.7261691 0. 0. 0. 0. 0. 0.
 TRN 0.0248 -0.4166 0.0373 -0.0127 0.0 0.007 0.039 0. 0. 0. 0. 0. 0.

!
 ?R134a/R1234ze(E) [R134A/R1234ZEE]
 ?I.H. Bell, JPCRD, 2022. DOI:10.1063/5.0086060
 ?MLH NIST (2022); viscosity data of Bi et al. (2016), Liang et al. (2022), AAD 0.9% for 69 liq points
 ?MLH NIST (2022); NIST thermal conductivity data fit, AAD 0.65% for 685 points
 ff1c0560/9905ef70
 XR0 1. 0.992 1. 1. 0. 0. 0. 0. 0. 0. 0.
 B02 0.998593 0.992009 0.998995 0.998621 1.0 0. 0. 0. 0. 0. 0.
 TC1 -3.6537383 -0.6615805 -14.544807 42.74642 -52.267112 23.681845 0. 0. 0. 0. 0. 0.
 VC1 0.10856663 -0.8791067 3.2991192 -6.1823073 5.6013068 -1.9553393 0. 0. 0. 0. 0. 0.
 TRN 0.0 0.0 -0.0019 -0.0204 0.05552 -0.24518 0.14319 0. 0. 0. 0. 0. 0.

!
 #MXM !Mixture model specification
 XR0 Reducing functions only
 ?
 ?.....
 ?Mixture model for binaries that are based on mixing rules for the reducing
 ? parameters only. Excess functions cannot be included in this model.
 ?
 ?The mixing rules are based on those of Kunz and Wagner (2008), but all binaries
 ? that use the XR0 rules were developed by others.
 ?
 ?.....
 !
 BetaT GammaT BetaV GammaV not used not used !Binary-specific parameters
 1.0 1.0 1.0 1.0 0.0 0.0 !Default values (i.e. ideal-solution)
 0.0 0 0.0 0.0 0.0 0.0 !# terms, # coefs/term for norm, K-W, Gaussian terms.

#MXM !Mixture model specification
 B00 R1234yf/R1234ze(E) mixture
 ?
 ?.....
 ? I.H. Bell
 ? Mixture Models for Refrigerants R-1234yf/134a, R-1234yf/1234ze(E), and R-134a/1234ze(E)
 ? and Interim Models for R-125/1234yf, R-1234ze(E)/227ea, and R-1234yf/152a
 ? J. Phys. Chem. Ref. Data 51, 013103 (2022)
 ? DOI:https://doi.org/10.1063/5.0086060
 ?.....
 !
 BetaT GammaT BetaV GammaV not used not used !Binary-specific parameters
 1.0 1.0 1.0 1.0 0.0 0.0 !Default values (i.e. ideal-solution)
 2.4 0 0.0 0.0 0.0 0.0 !# terms, # coefs/term for norm, K-W, Gaussian terms.
 0.07264 0.012643 1.0 1.0 ! n(i),t(i),d(i),l(i) in term n_i*tau^t_i*delta^d_i*exp(-delta^l_i)
 -0.024746 3.992829 2.0 2.0

A.2. Task 2 - Flammability Experiments and Test Data

First, the experimental data for the ASHRAE Standard 34 E681 test are presented. Following that, the modified Japanese High-Pressure Gas Law test is described and the experimental results in that device are presented. The next section presents the experimental approach for the laminar burning velocity measurements in the 2-L chamber, and the experimental results for that test are provided.

A.2.1. ASHRAE Standard 34 E681 Test Data

Table A.2-1. E681 test results for R-513A, NIST-ternary blend, R-450A, R-515B, and blends of R-1234yf/134a at a molar composition of (0.26/0.74), (0.28/0.72), and (0.30/0.70).

Volume Fraction (%)	Pressure (mmHg)	Air R.H. (%)	Flame Angles (degrees)	Result (Go/NoGo)	Comment
R-1234yf/134a/1234ze(E) (32.0/52.0/16.0 by vol%) flammability at 60 °C					
6	760	49.3	No angle	No Go	Just spark, no flame
7	760	50.2	No angle	No Go	Little flame bubble around the spark, disappears within 1"
8	760	49.4	No angle	No Go	Little flame bubble around the spark, disappears within 1"
9	760	49.7	No angle	No Go	Little flame bubble around the spark, disappears within 1"
10	760	51.8	No angle	No Go	Little flame bubble around the spark, disappears within 1"
11	760	51.8	No angle	No Go	Little flame bubble around the spark, disappears within 1"
12	760	52.0	No angle	No Go	Little flame bubble around the spark, disappears within 1"
13	760	51.5	No angle	No Go	Little flame bubble around the spark, disappears within 1"
R-1234yf/134a (74.0/26.0 by vol%) flammability at 60 °C					
6	760	51.1	No angle	No Go	Candle flame
7	760	51.1	No angle	No Go	Flame didn't reach the top
7	760	51.3	No angle	No Go	Flame didn't reach the top
8	760	52	86	No Go	
8	760	50.3	95	Go	
8	760	49.9	100	Go	
9	760	51.6	92	Go	
9	760	51.2	85	No Go	

9	760	51.2	90	No Go
10	760	51.7	88	No Go
10	760	51.5	91	Go
10	760	51.2	98	Go
11	760	51.8	100	Go
11	760	51.5	81	No Go
11	760	50.6	82	No Go
12	760	51.7	88	No Go
12	760	50.7	88	No Go
13	760	50.6	No angle	No Go

R-1234yf/134a (72.0/28.0 by vol%) flammability at 60 °C

6	760	50.4	No angle	No Go	
7	760	50.3	No angle	No Go	Flame didn't reach the top
8	760	51.9	90	No Go	
8	760	48.9	95	Go	
8	760	49.8	88	Go	
9	760	52.0	91	Go	
9	760	50.5	91	Go	
9	760	49.9	95	Go	
10	760	51.9	100	Go	
10	760	48.9	90	No Go	
10	760	50.2	92	Go	
11	760	48.9	95	Go	
11	760	51.9	97	Go	
11	760	51.3	95	Go	
12	760	51.4	No angle	No Go	Flame fell apart
13	760	51.8	No angle	No Go	Flame fell apart at the top of the flask

R-1234yf/134a (70.0/30.0 by vol%) flammability at 60 °C

6.1	760	49.7	No angle	No Go	Spark only
7.0	760	50.4	No angle	No Go	Flame didn't reach the top
8.0	760	52.0	55	No Go	Practically no angle, flame didn't reach the top, it was around 55 deg wide before it disappeared
8.0	760	50.6	80	No Go	
8.0	760	49.7	80	No Go	

8.9	760	50.8	91	Go	
8.9	760	50.1	76	No Go	
8.9	760	50.4	85	No Go	
10.0	760	50.0	90	No Go	
10.0	760	50.2	73	No Go	
10.0	760	49.2	80	No Go	
11.1	760	51.0	90	No Go	
11.1	760	49.5	80	No Go	
11.1	760	49.4	90	No Go	
12.0	760	51.5	45	No Go	Practically no angle, flame didn't reach the top, it was around 45 deg wide before it disappeared
12.0	760	49.5	No angle	No Go	Fell apart before reaching the top of the flask
13.0	760	50.1	No angle	No Go	Didn't reach the top

R-1234yf/134a/227ea (56.0/40.0/4.0 by vol%) flammability at 60 °C

6.1	760	51.8	No angle	No Go	Spark only
7.0	760	51.4	No angle	No Go	Small candle like flame, doesn't reach the top
8.0	760	50.9	No angle	No Go	Small candle like flame, doesn't reach the top
8.9	760	50.6	No angle	No Go	Small candle like flame, doesn't reach the top
8.9	760	51.7	No angle	No Go	Small candle like flame, doesn't reach the top
10.0	760	52.8	No angle	No Go	Small candle like flame, doesn't reach the top
11.1	760	50.7	No angle	No Go	Small candle like flame, doesn't reach the top
12.0	760	52.0	No angle	No Go	Small candle like flame, doesn't reach the top
13.0	760	52.4	No angle	No Go	Small candle like flame, doesn't reach the top

A.2.2. Japanese High-Pressure Gas Law Test

JHPGL Experiment Description. The constant-volume combustion device [49] is based on the Japanese High Pressure Gas Law (JHPGL), and is similar to the design of Takizawa [131], Shebeko [132], and others. The experimental 2-L apparatus is shown in Figure A.2-1 while the plumbing schematic is shown in Figure A.2-2. The chamber consists of a stainless steel (316) sphere with an inner diameter of 15.24 cm, a volume of 1.85 L, and wall thickness of 2.54 cm; the vessel has nine tapped openings for gas inlet and outlet ports, and various transducers. Gases are introduced via the partial pressure mixing technique, and ignition is provided by a fused platinum wire (Alfa Aesar 43014-BY). Rather than basing flammability on a thermocouple temperature rise as specified in the JHPGL, a dynamic pressure transducer was added, allowing a pressure-based criterion.



Figure A.2-1. Spherical 2-L chamber for JHPGL tests and constant volume method laminar burning velocity measurements

Component partial pressures are determined with an absolute pressure transducer (Omega PX811-030AV, 0 to 206.8 kPa range) with a claimed accuracy of $\pm 0.1\%$, coupled to a digital strain gage readout (Omega* DP80). These are periodically calibrated against a Baratron 627D (claimed accuracy of 0.12%) and a Wallace & Tiernan 1500 (claimed accuracy of 0.066%) pressure gage. Uncertainty in the pressure reading is estimated to be 2 % of the reading. The refrigerants were HFC-134a , HFO-1234yf , R-513A , HFO-1234ze(E) , and R-515B.

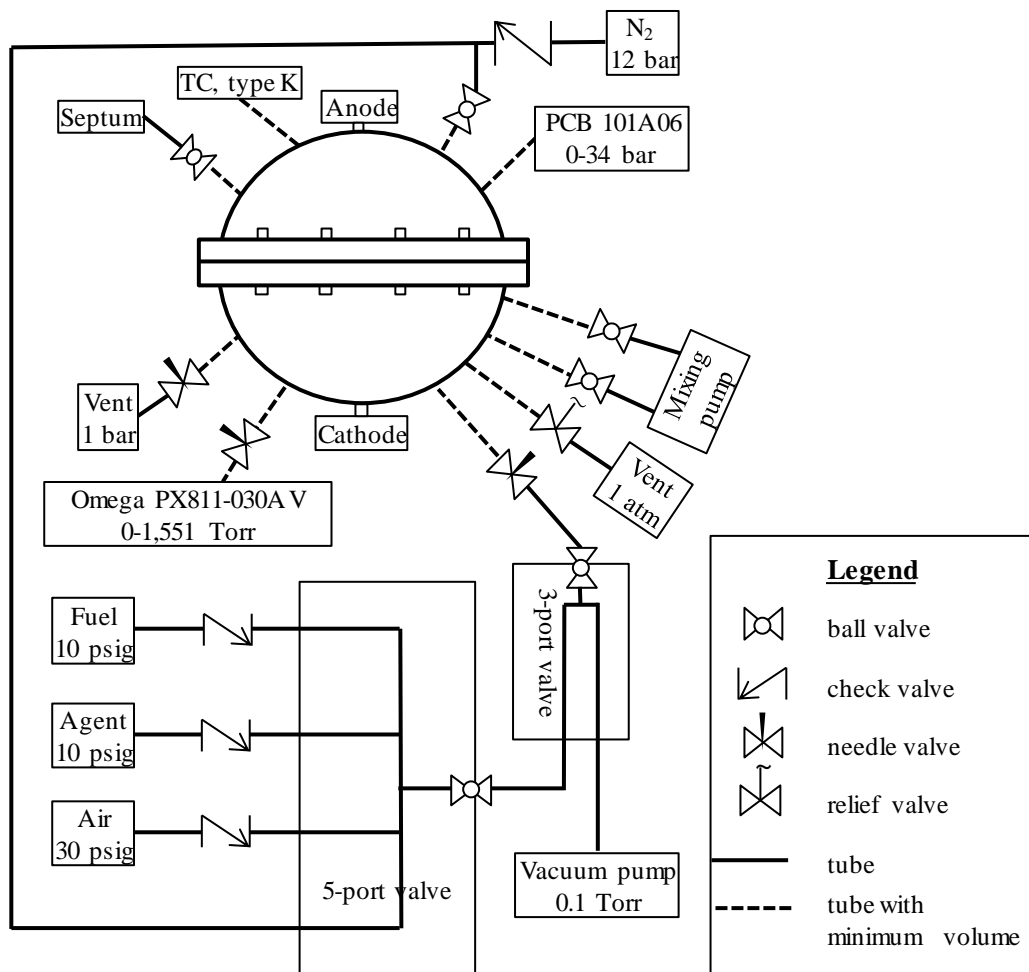


Figure A.2-2. Plumbing schematic diagram for 2-L chamber

The air was house compressed air (filtered and dried) which is additionally cleaned by passing it through an 0.01 μm filter, a carbon filter, and a desiccant bed to remove small aerosols, organic vapors, and water vapor. The relative humidity of the dry shop air was measured in previous work to be less than 2 % at 22°C. When desired, water was added as a reactant using a 50 μL syringe (Millipore Sigma, Model # 22269-U) through a septum (subsequently closed-off via a ball valve) and allowed to vaporize. After all gases were added they were mixed by a stainless-steel bellows pump in an external loop (evacuated between tests) and allowed to settle for 5 minutes before ignition. The initial temperature of the vessel, measured by a fine type-K thermocouple on the chamber exterior wall, was typically (26.2 ± 0.6) °C.

The igniter configuration was modified slightly from that recommended in the JHPGL. Rather than the igniter leads entering the chamber from two locations at right angles to each other, two parallel copper leads (57 mm long, 1 mm diameter) were used separated by 4 mm and with Teflon insulation around the copper wires in select locations. Crimp-on connections (Digi-Key A2161-ND and A34501-ND) were used between the copper and platinum wires instead of welds. Hence, the igniter could be inserted through a single 6.35 mm inner diameter orifice, with easily replaceable fusible wire. A variable transformer AC power supply (Powerstat, model

30N116C) provided 100 VAC to the igniter, and its manual switch- controlled ignition. An isolation transformer (Hammond Manufacturing, model 171G, 1000 VA) was used to separate the ignition system from the house electrical supply. This provided a more consistent energy to the igniter and prevented blowing the 10 A fuse in the variable transformer. The platinum wire (20 mm long, 0.3 mm diameter) melted and ruptured violently during each ignition and was replaced.

A data acquisition system (DAS, National Instruments models NI USB-6259 and NI SCC-68, with LabVIEW VI) connected to a personal computer (Dell OptiPlex 7060) recorded the dynamic pressure during each experiment. A dynamic pressure sensor (PCB Piezotronics, model 101A06) with a rise time of 1.5 μ sec, a range of 3450 kPa, and reported accuracy of 0.07 kPa, measured the pressure rise in the chamber. The DAS collected data for 60 s at 100 Hz.

Product gases were removed from the chamber at the end of each test to prevent contamination for the subsequent test. Gaseous nitrogen was introduced to the chamber soon after the ignition: 1.) to quickly purge the corrosive acid gases present for some experiments, and 2.) to reduce the temperature of the product gases (to protect components). After ignition, followed by a 10 s delay, gaseous nitrogen at $11 \cdot 10^{-2}$ kPa pressurized the chamber for 5 s after which the exhaust valve was opened, and N₂ flowed continuously for 10 sec. Following the nitrogen purge, clean and dried shop air flushed the chamber for ten minutes, the chamber was evacuated and maintained for 2 minutes, followed by dry air purge for 2 minutes (with these last two steps repeated).

Japanese High-Pressure Gas Law Test Data

Table A.2-2. Japanese High-Pressure Gas Law test results obtained at NIST for: R-513A, NIST-ternary blend, R-450A, R-515B, and blends of R-1234yf/134a, all with dry or 50 % r.h. air as listed.

Volume Fraction %	Nominal Humidity	Run No.	Run Date	Partial Pressure, torr					P _{tot}	P	Pressure Rise, x 10 ⁻² kPa
				p ₁	p ₂	p ₃	p _{air}	p _w			
R-513A (R134a/1234yf) (0.469/0.531, mole fraction)											
7.0	Dry	16	2020-10-22	26.2	29.7	N/A	742.4	N/A	798.2	759.8	0.003
8.0		17	2020-10-22	29.9	33.9		734.5		798.3	759.9	0.097
9.3		1	2020-10-20	34.6	39.3		724.4		798.2	760.0	0.080
10.0		2	2020-10-20	37.4	42.4		718.6		798.3	759.9	0.202
10.5		3	2020-10-20	39.3	44.5		714.5		798.2	759.7	0.178
11.0		4	2020-10-20	41.2	46.7		710.5		798.3	760.0	0.191
11.0		18	2020-10-22	41.1	46.7		710.5		798.2	759.8	0.214
11.3		10	2020-10-21	42.1	47.7		708.7		798.4	760.3	0.253
11.5		11	2020-10-21	43.0	48.8		706.6		798.4	760.0	0.242
12.0		12	2020-10-21	44.9	50.9		702.8		798.4	760.0	0.255
12.5		7	2020-10-21	46.7	53.0		698.7		798.4	760.1	0.178
13.0		8	2020-10-21	48.6	55.1		694.6		798.3	760.1	0.209
14.0		9	2020-10-21	52.4	59.4		686.7		798.3	760.1	0.239
15.0		13	2020-10-22	56.1	63.6		678.7		798.4	759.7	0.165
16.0		15	2020-10-22	59.9	67.9		670.5		798.2	760.0	0.164
17.0		14	2020-10-22	63.6	72.1		662.8		798.4	760.3	0.004
11.5		5	2020-10-20	43.0	48.8		706.6		798.4	760.0	0.094
12.0		6	2020-10-21	44.9	50.9		702.7		798.5	760.1	0.004
5.0		42	2020-11-12	18.7	21.2	N/A	747.7	11.0	798.3	759.8	0.027
6.0		52	2020-11-12	22.4	25.4		739.7	10.9	798.3	759.2	0.061
7.0		46	2020-11-12	26.2	29.7		732.1	10.4	798.2	759.4	0.077
8.0		55	2020-11-12	29.9	33.9		724.4	10.3	798.3	759.5	0.096
10.0		50	2020-11-10	37.4	42.4		707.8	10.9	798.3	759.5	0.306
11.0		58	2020-11-10	41.1	46.7		700.1	10.8	798.4	759.8	0.446
12.0		58	2020-11-10	44.9	50.9		692.0	10.7	798.3	759.3	0.474
13.0		55	2020-11-12	48.6	55.1		683.5	11.2	798.1	759.2	0.330
14.0		45	2020-11-10	52.3	59.4		676.3	10.4	798.2	759.4	0.173
16.0		53	2020-11-10	59.8	67.9		660.1	11.0	798.5	759.7	0.095
18.0		53	2020-11-12	67.3	76.3		644.4	10.5	798.3	759.4	0.035
19.0		58	2020-11-12	71.1	80.6		636.3	10.6	798.4	759.7	0.002
R-450A (R134a/1234ze(E)) (0.447/0.553, mole fraction)											
4.0	Dry	13	2020-11-25	14.3	17.7	N/A	766.7	N/A	798.2	759.9	0.044
6.0		10	2020-11-25	21.4	26.4		750.8		798.2	760.1	0.027
8.0		6	2020-11-24	28.6	35.3		734.7		798.2	759.6	0.046
10.0		1	2020-11-24	35.7	44.2		718.8		798.4	760.2	0.141
10.9		11	2020-11-25	39.2	48.5		715.6		803.0	760.3	0.061
12.0		3	2020-11-24	42.8	53.0		702.9		798.2	760.2	0.258
13.0		4	2020-11-24	46.4	57.4		695.0		798.3	760.0	0.147
15.0		7	2020-11-24	53.5	66.2		679.0		798.2	759.9	0.164
16.0		12	2020-11-25	57.1	70.6		671.0		798.2	759.9	0.137
18.0		8	2020-11-25	64.2	79.4		655.0		798.2	759.6	0.030
20.0		9	2020-11-25	71.4	88.3		639.0		798.2	760.0	0.028

22.0		14	2020-11-25	78.5	97.1		623.3		798.4	759.9	0.014
11.0		2	2020-11-24	39.3	48.6		710.8		798.2	760.1	0.004
11.0		5	2020-11-24	39.2	48.5		710.7		798.1	759.4	0.003
5.0	53	14	2020-11-23	17.8	22.1	N/A	747.7	11.1	798.3	759.5	0.012
6.0	53	5	2020-11-20	21.3	26.4		739.6	11.1	798.2	760.2	0.066
7.0	56	6	2020-11-20	25.0	30.9		731.2	11.6	798.4	760.1	0.095
8.0	42	1	2020-11-19	28.5	35.4		726.2	8.5	798.3	759.7	0.128
9.0	56	7	2020-11-20	32.1	39.8		715.6	11.2	798.3	760.0	0.186
10.0	53	2	2020-11-19	35.6	44.2		708.4	10.5	798.4	759.6	0.262
11.0	55	8	2020-11-20	39.2	48.6		700.3	10.8	798.4	759.8	0.124
12.5	58	13	2020-11-23	44.6	55.1		687.7	11.2	798.3	759.3	0.185
13.0	57	9	2020-11-20	46.4	57.3		683.9	10.9	798.2	759.7	0.161
14.0	56	3	2020-11-19	50.0	61.8		676.1	10.7	798.3	759.5	0.205
15.0	58	10	2020-11-20	53.5	66.2		668.0	10.8	798.2	759.8	0.156
16.0	57	4	2020-11-19	57.1	70.6		660.4	10.7	798.3	759.5	0.019
17.0	59	15	2020-11-23	60.9	74.9		652.1	10.9	798.4	759.4	0.083
19.0	60	16	2020-11-23	67.8	83.9		636.2	10.8	798.3	759.6	0.060
11.0	50	11	2020-11-20	39.2	48.6		700.9	9.9	798.3	759.9	0.083
13.0	55	12	2020-11-23	46.3	57.6		684.2	10.5	798.3	759.7	0.141

NIST Ternary Blend (R134a/1234yf/1234ze(E) (0.52/0.32/0.16, mole fraction)

10.5	Dry	7	2020-11-04	311.9	192.1	96.0	714.5	N/A	798.4	760.2	0.003
11.0		5	2020-11-04	312.0	192.0	96.2	710.6		798.5	760.0	0.003
11.3		8	2020-11-04	312.0	192.1	95.9	708.5		798.3	760.2	0.210
11.4		1	2020-11-03	311.8	192.1	95.9	711.4		803.2	764.8	0.211
12.0		6	2020-11-04	312.0	192.1	95.9	702.6		798.4	759.9	0.203
12.5		2	2020-11-03	312.0	191.9	96.0	698.4		798.3	760.0	0.123
13.5		3	2020-11-03	312.0	192.0	95.9	690.5		798.4	760.0	0.000
14.0		4	2020-11-04	312.0	191.9	96.0	686.6		798.4	760.1	0.001
8.0	54	5	2020-11-06	33.2	20.5	10.2	723.6	11.0	798.3	759.3	0.002
9.0	53	4	2020-11-06	37.3	23.0	11.5	716.0	10.7	798.3	759.7	0.138
10.0	55	7	2020-11-09	41.5	25.5	12.7	707.9	11.0	798.4	758.7	0.192
11.0	52	1	2020-11-06	45.3	28.2	14.0	700.9	10.3	798.4	759.8	0.406
12.0	50	9	2020-11-09	49.8	30.6	15.3	691.9	10.9	798.3	759.6	0.451
13.0	50	2	2020-11-06	53.9	33.2	16.6	685.2	9.6	798.3	759.8	0.234
15.0	57	3	2020-11-06	62.2	38.3	19.1	668.2	10.7	798.3	759.4	0.131
16.0	63	6	2020-11-06	66.4	40.9	20.5	659.2	11.6	798.3	759.6	0.120
17.0	57	10	2020-11-09	70.5	43.5	21.7	652.5	10.5	798.3	759.8	0.083
18.0	60	11	2020-11-09	74.7	46.0	22.9	644.0	10.9	798.4	759.8	0.048
12.0	57	8	2020-11-09	49.8	30.6	15.4	691.8	11.0	798.4	760.2	0.023

R-515B (R1234ze(E)/R227ea) (0.939/0.061, mole fraction)

4.0	Dry	15	2020-11-16	2.0	30.0	N/A	766.6	N/A	798.1	759.7	0.005
5.0		14	2020-11-16	2.5	37.5		758.8		798.4	759.9	0.072
6.0		13	2020-11-16	2.9	45.0		750.7		798.3	759.8	0.101
7.0		7	2020-11-13	3.4	52.5		742.7		798.3	759.0	0.053
8.0		6	2020-11-13	3.9	60.0		734.7		798.3	759.6	0.415
9.0		9	2020-11-13	4.4	67.5		726.7		798.3	759.6	0.507
9.6		1	2020-11-13	4.7	72.0		721.6		798.1	759.7	1.031
9.6		17	2020-11-18	4.7	71.9		722.2		798.4	760.3	1.564
10.0		8	2020-11-13	4.9	74.9		718.7		798.2	759.8	1.221
10.0		16	2020-11-18	4.9	74.9		718.9		798.3	760.4	0.852
11.0		2	2020-11-13	5.4	82.4		710.8		798.4	760.0	0.400

12.0		3	2020-11-13	5.9	89.9		702.8		798.3	759.7	0.329
13.0		4	2020-11-13	6.4	97.4		694.7		798.2	759.7	0.241
14.0		10	2020-11-16	6.9	104.9		686.9		798.3	759.6	0.227
16.0		11	2020-11-16	7.9	119.9		671.0		798.4	760.0	0.058
17.0		12	2020-11-16	8.3	127.3		663.0		798.3	759.8	0.004
9.0		5	2020-11-13	4.4	67.5		726.6		798.2	759.7	0.169
9.3		18	2020-11-18	4.6	69.7		724.4		798.2	759.6	0.213
4.0	50	13	2020-11-18	2.0	29.9	N/A	756.2	10.7	798.4	760.1	0.018
5.0	53	11	2020-11-18	2.5	37.4		747.6	11.2	798.3	759.6	0.053
6.0	53	10	2020-11-18	2.9	44.9		740.1	10.9	798.5	760.2	0.002
8.0	45	9	2020-11-18	3.9	59.9		725.4	9.1	798.2	759.8	0.150
9.0	55	8	2020-11-17	4.4	67.4		715.9	11.0	798.5	759.8	1.269
10.0	52	2	2020-11-16	4.9	74.9		708.2	10.4	798.1	759.2	1.658
11.0	55	4	2020-11-17	5.4	82.3		700.2	10.8	798.3	759.6	0.974
12.0	53	12	2020-11-18	5.9	89.9		691.6	11.3	798.3	760.1	0.210
13.0	50	5	2020-11-17	6.4	97.3		685.1	9.6	798.2	758.6	0.186
15.0	58	6	2020-11-17	7.4	112.3		668.1	10.8	798.3	758.6	0.086
17.0	58	7	2020-11-17	8.3	127.3		652.2	10.7	798.2	759.8	0.013
9.0	42	1	2020-11-16	4.4	67.4		718.2	8.5	798.2	759.1	0.134
11.0	46	3	2020-11-17	5.4	82.4		701.6	9.0	798.1	758.8	0.036

R134a/1234yf (0/1.0, mole fraction)

7.0	Dry	1	2020-12-14	56.0		N/A	N/A	743.9	N/A	799.1	760.5	0.060
8.0		2	2020-12-14	64.0				735.2		798.4	759.4	1.462
8.5		8	2020-12-15	67.8				731.2		798.3	760.1	2.666
9.0		3	2020-12-14	72.0				727.2		798.4	760.0	3.667
10.0		4	2020-12-14	79.8				719.3		798.3	759.7	1.981
11.0		5	2020-12-14	87.8				713.0		800.0	760.4	0.815
12.0		6	2020-12-14	95.8				703.5		798.4	759.6	0.006
13.0		7	2020-12-14	103.8				695.3		798.3	759.7	0.183
8.0	44	4	2021-01-12	63.8		N/A	N/A	727.0	9.0	798.5	759.6	2.81
9.0	45	3	2021-01-12	71.8				718.5	9.1	798.2	759.5	4.61
10.0	45	5	2021-01-12	79.7				711.4	9.1	798.8	759.9	1.87
9.0	47	1	2021-01-12	71.8				718.2	9.5	798.2	759.9	2.55
8.9	46	2	2021-01-12	71.8				723.0	9.4	802.9	760.2	2.57

R134a/1234yf (0.2/0.8, mole fraction)

7.0	Dry	8	2020-12-22	11.2	44.7	N/A	743.2	N/A	798.2	759.9	0.089
8.0		1	2020-12-15	12.9	50.9		735.3		798.3	759.9	0.494
9.0		9	2020-12-22	14.4	57.6		727.3		798.4	760.0	1.540
10.0		11	2020-12-22	16.1	63.8		719.4		798.2	759.7	0.466
11.0		5	2020-12-18	17.5	70.4		711.2		798.4	759.9	0.678
12.0		6	2020-12-18	19.2	76.6		703.3		798.3	759.8	0.006
9.0		7	2020-12-18	14.4	57.4		727.3		798.3	760.2	0.239
9.0		2	2020-12-15	14.4	57.5		727.2		798.3	759.6	0.013
10.0		3	2020-12-15	16.0	63.8		719.4		798.4	760.1	0.990
11.0		4	2020-12-15	17.6	70.2		711.5		798.4	760.1	0.223
10.0		10	2020-12-22	16.0	63.8		719.5		798.3	760.0	0.071
8.0	47	3	2021-01-06	12.7	51.2	N/A	726.1	9.5	798.3	759.4	1.271
9.0	47	1	2021-01-05	14.3	57.4		718.3	9.4	798.2	759.2	1.987
10.0	46	2	2021-01-06	15.9	63.9		710.4	9.2	798.3	759.7	0.795

R134a/1234yf (0.3/0.7, mole fraction)

8.0	Dry	5	2021-01-08	19.2	44.7	N/A	735.8	N/A	798.4	759.9	0.087
9.0		3	2021-01-08	21.6	50.3		730.9		801.4	760.1	0.787
10.0		4	2021-01-08	24.0	55.8		719.8		798.3	760.0	0.780
11.0		2	2021-01-08	26.4	61.5		711.9		798.4	759.9	0.203
10.0		1	2021-01-08	24.0	55.8		719.9		798.4	760.2	0.524
9.0	46	5	2021-01-06	21.5	50.3	N/A	718.4	9.3	798.3	759.5	0.003
10.0	51	4	2021-01-05	23.9	55.9		709.7	10.1	798.3	759.5	1.271
11.0	53	3	2021-01-05	26.2	61.7		701.0	10.5	798.2	759.2	1.047
12.0	43	1	2021-01-05	28.6	67.1		695.3	8.4	798.2	759.3	0.592
11.0	47	2	2021-01-05	26.2	61.5		702.5	9.3	798.2	759.5	0.310

R134a/1234yf (0.4/0.6, mole fraction)

9.0	Dry	5	2021-01-11	28.8	43.2	N/A	727.6	N/A	798.3	760.1	0.090
10.0		2	2021-01-11	31.9	48.0		719.8		798.4	760.2	0.239
11.0		4	2021-01-11	35.2	52.6		711.8		798.4	760.2	0.119
11.0		3	2021-01-11	35.2	52.7		711.9		798.4	760.2	0.067
11.0		1	2021-01-11	35.2	52.7		711.9		798.5	760.4	0.024
10.0	51	2	2021-01-06	31.9	47.9	N/A	709.5	10.2	798.2	758.5	0.865
11.0	53	1	2021-01-06	35.1	52.7		701.4	10.4	798.4	759.5	0.936
12.0	51	3	2021-01-06	38.4	57.4		693.7	10.0	798.2	759.5	0.783

R134a/1234yf (0.5/0.5, mole fraction)

7.0	Dry	13	2020-12-23	28.0	27.9	N/A	743.4	N/A	798.4	760.1	0.067
8.0		10	2020-12-07	32.0	31.9		735.1		798.3	759.4	0.114
10.0		6	2020-12-04	40.0	40.0		719.2		798.7	760.1	0.152
11.0		1	2020-11-30	44.0	43.9		710.9		798.2	759.2	0.205
11.5		3	2020-12-01	45.9	45.9		707.2		798.5	759.7	0.261
12.0		4	2020-12-03	47.9	47.8		703.0		798.3	759.7	0.315
13.0		7	2020-12-07	51.9	52.2		694.8		798.3	759.6	0.227
15.0		8	2020-12-07	59.9	59.9		679.1		798.3	759.3	0.146
17.0		9	2020-12-07	67.9	67.9		663.3		798.3	759.3	0.117
18.0		11	2020-12-23	71.9	71.8		655.6		798.4	760.4	0.104
20.0		12	2020-12-23	79.9	79.7		639.8		798.4	760.3	0.032
10.0		5	2020-12-04	40.0	39.8		719.1		798.3	759.6	0.026
11.5		2	2020-11-30	45.9	45.9		707.1		798.4	759.5	0.059

R134a/1234yf (0.55/0.45, mole fraction)

9.0	46	6	2021-01-22	39.6	32.5	N/A	718.6	9.2	798.3	758.9	0.065
10.0	53	5	2021-01-22	44.0	35.9		709.3	10.5	798.3	759.7	0.121
11.0	50	4	2021-01-22	48.3	39.5		702.2	9.8	798.4	759.7	0.227
12.0	58	3	2021-01-22	52.7	43.1		692.9	11.3	798.4	759.7	0.271
13.0	58	11	2021-01-25	57.1	46.6		685.2	11.1	798.4	759.8	0.147
14.0	59	12	2021-01-25	61.5	50.3		677.1	11.2	798.4	759.6	0.041
15.0	59	7	2021-01-22	65.9	53.8		669.1	11.2	798.4	759.7	0.172
16.0	66	8	2021-01-25	70.3	57.4		659.9	12.2	798.3	759.5	0.131
17.0	63	10	2021-01-25	74.7	61.0		652.8	11.5	798.4	759.6	0.102
18.0	59	9	2021-01-25	79.0	64.6		645.8	10.6	798.4	760.0	0.008
13.0	58	1	2021-01-21	57.1	46.7		684.6	11.3	798.2	758.5	0.078
13.4	59	2	2021-01-22	58.7	48.1		681.5	11.3	798.3	759.3	0.007

R134a/1234yf (0.7/0.3, mole fraction)

7.0	Dry	9	2020-12-09	39.2	16.7	N/A	743.1	N/A	798.3	759.2	0.006
8.0		5	2020-12-08	44.8	19.1		735.1		798.3	759.7	0.071
10.0		4	2020-12-08	55.9	23.9		719.2		798.3	759.7	0.072
11.0		6	2020-12-08	61.5	26.4		711.2		798.4	759.0	0.171
12.0		1	2020-12-08	67.1	28.7		703.1		798.3	759.9	0.176
13.0		7	2020-12-08	72.7	31.1		695.4		798.4	759.0	0.154
14.0		2	2020-12-08	78.3	33.5		687.1		798.3	759.9	0.160
15.0		8	2020-12-09	83.8	35.9		679.2		798.3	759.8	0.149
16.0		3	2020-12-08	89.4	38.2		671.2		798.2	759.5	0.005
17.0		10	2020-12-11	95.0	40.7		663.4		798.2	759.6	0.049
18.0		11	2020-12-23	100.6	43.1		655.7		798.3	760.2	0.015

R134a/1234yf (0.8/0.2, mole fraction)

11.0	Dry	4	2020-12-09	70.3	17.5	N/A	711.2	N/A	798.3	759.5	0.004
12.0		5	2020-12-09	76.7	19.1		703.2		798.3	759.6	0.006
13.0		1	2020-12-09	83.0	20.7		695.3		798.4	759.8	0.082
14.0		2	2020-12-09	89.4	22.4		687.3		798.3	759.8	0.124
15.1		3	2020-12-09	95.8	25.2		678.0		798.2	759.9	0.107
16.0		6	2020-12-09	102.2	25.6		671.4		798.5	760.0	0.034
17.0		7	2020-12-10	108.5	27.2		663.0		798.3	759.9	0.070
18.0		8	2020-12-11	115.0	28.7		655.4		798.4	759.9	0.101
19.0		9	2020-12-11	121.3	30.3		647.3		798.2	760.1	0.110
20.0		10	2020-12-11	127.8	31.9		639.5		798.3	759.8	0.033

R134a/1234yf (0.9/0.1, mole fraction)

13.0	Dry	4	2020-12-10	93.4	10.4	N/A	695.1	N/A	798.3	759.8	0.023
14.0		1	2020-12-10	100.6	11.1		687.2		798.3	759.8	0.155
15.0		2	2020-12-10	107.8	12.1		679.1		798.3	760.1	0.070
16.0		3	2020-12-10	115.0	12.8		671.2		798.2	759.9	0.034
17.0		5	2020-12-10	122.1	13.5		663.4		798.2	760.0	0.113
18.0		6	2020-12-11	129.3	14.4		655.4		798.4	760.1	0.132
19.0		7	2020-12-11	136.6	15.0		647.4		798.4	759.8	0.016

R134a/1234yf (1.0/0, mole fraction)

13.0	57	11	2021-01-21	103.8	N/A	N/A	685.2	10.9	798.3	759.2	0.023
14.0	55	2	2021-01-15	111.7			677.6	10.4	798.2	759.1	0.087
15.0	44	1	2021-01-15	119.6			671.8	8.3	798.3	759.5	0.102
16.0	58	3	2021-01-15	127.7			661.2	10.8	798.4	759.3	0.103
17.0	60	4	2021-01-19	135.7			652.8	11.0	798.2	759.7	0.030
17.9	62	5	2021-01-19	143.6			647.2	11.3	800.6	759.8	0.033
19.0	60	6	2021-01-19	151.7			637.3	10.8	798.2	759.7	0.096
20.0	61	7	2021-01-19	159.7			629.3	10.8	798.4	759.7	0.095
20.9	68	8	2021-01-19	167.5			620.2	11.9	798.3	759.6	0.068
22.0	65	9	2021-01-21	175.6			612.9	11.2	798.3	759.2	0.053
22.9	65	10	2021-01-21	183.5			605.2	11.1	798.3	759.3	0.053

A.2.3. Constant Volume (2 L) Laminar Burning Velocity Measurements

Experiment Description. The experimental approach for measuring the laminar burning velocity LBV in the 2-L chamber from the pressure rise has been described in previous work [46, 47, 60, 133], and this description is an updated version of that in Pagliaro et al. [47]. The experiment uses the same 2-L chamber and gas preparation system as described above for the modified JHPGL test. Instead of the hot-wire ignition, the LBV measurement uses an electrical spark from a capacitive discharge ignition system (based on the work of Shepherd et al. [134]). A 1 kV to 15 kV power supply and custom-made capacitor banks (1 nF to 50 nF) provide variable ignition energies, with an estimated operating range of 0.05 mJ to 500 mJ. Two tungsten electrodes form a gap in the center of the chamber. Thin electrodes (0.4 mm diameter) minimize heat loss from the flame, and the spark gap is adjustable (2 mm, typical).

Gases and mixture preparation are the same as in the JHPGL test, with the additional refrigerant HFC-152a (Honeywell). Ignition is attempted several times, while gradually increasing the capacitor charging voltage, until ignition occurs. This ensures the ignition energy is within an order of magnitude of the minimum value. The explosion pressure is recorded at 4000 Hz with the dynamic pressure sensor, and the product gases are immediately purged, as described above. Laminar burning velocity is determined from the pressure trace using a thermodynamic model, developed by Metghalchi and Keck [135, 136] and further refined by others [137, 138]. A brief overview of the method follows; however, the current work uses an updated software package that allows for inclusion of radiation heat losses, burned gas dissociation, and accounts for extrapolation errors due to the range of selected pressure-rise data [69]. Nonetheless, the present data were reduced assuming adiabatic conditions and using a 2-zone model as described below.

Burning Velocity from the Pressure Trace. The content of the chamber is divided into burned and unburned zones separated by a reaction sheet, assumed to be infinitely thin, spherical, and smooth (no instabilities). Initially, the unburned gas is considered perfectly mixed and at rest. As the unburned gases react, a spatially uniform increase in pressure occurs. The burned gas is in chemical equilibrium and both the burned and unburned gases are considered as ideal, semi-perfect gases. Both zones are adiabatic, and the unburned gas is isentropically compressed as the mixture reacts in the flame sheet.

With these assumptions, the instantaneous flame radius and burning velocity can be expressed in terms of the chamber pressure by applying conservation of mass. The results are given in Eq. A.2-1 and Eq. A.2-2 (detailed formulation of the equations can be found in refs. [135, 137]),

$$r_f = R \left[1 - (1 - x_b) (P_0/P)^{1/\gamma_u} \right]^{1/3} \quad (\text{A.2-1})$$

$$S_L = R/3 (R/r_f)^2 (P_0/P)^{1/\gamma_u} (dx_b/dt) \quad (\text{A.2-2})$$

in which r_f is the flame radius, S_u is the laminar burning velocity, R is the chamber radius, x_b is the mass fraction of burned gas, P is the instantaneous pressure, P_0 is the initial pressure, and γ_u is the unburned gas specific heat ratio. To determine burning velocity, the mass fraction of burned gas x_b must be related to the chamber pressure (for simplification, early studies applied a linear relationship [139]). Alternatively, a thermodynamic closed system analysis on the contents within the chamber can be performed. A two-zone approach is used in the present

work. The burned gas zone also can be modeled using incremental shell volumes [140, 141], allowing burned gas density and temperature gradients; nonetheless, since previous studies have shown that (for adiabatic flames) inclusion of the gradients has negligible effect on the burning velocity [136, 137], we retain the two-zone model. The fraction of mass burned x_b is found from simultaneous solution of the conservation of mass and energy equations given in Eq. A.2-3 and Eq. A.2-4, applied for the two zones,

$$\frac{V}{M} = \int_0^{x_b} v_b dx + \int_{x_b}^1 v_u dx \quad (\text{A.2-3})$$

$$\frac{E}{M} = \int_0^{x_b} e_b dx + \int_{x_b}^1 e_u dx \quad (\text{A.2-4})$$

where V is the volume of the chamber, E is the total internal energy of the gases in the chamber, M is the mass of the gas in the chamber, e and v are the internal energy and specific volume of the gas, and the subscripts b and u refer to the burned and unburned gas.

Thermodynamic data for the unburned and burned gases are required for model implementation. Data for all of the species are taken from the recent detailed kinetic model of Babushok et al. [66].

The unburned gas properties are related to the chamber pressure through isentropic compression:

$$T_u = T_{u0} \left(\frac{P}{P_0} \right)^{(\gamma_u - 1)/\gamma_u} \quad (\text{A.2-5})$$

in which T_{u0} is the initial unburned temperature. Since γ_u is a function of the unburned gas temperature T_u and the initial mixture composition, T_u and γ_u are solved iteratively at each pressure increment. The properties of the unburned gas mixture, v_u and e_u , are determined from the mixture composition and temperature.

The remaining unknowns in the conservation equations (v_b , e_b , and x_b) are found through iteration of T_b (v_b and e_b are functions of temperature) and x_b at each pressure increment, until the proper values of T_b and x_b are obtained. Burned gas species concentrations, required for the determination of v_b and e_b , are estimated for each value of T and P using a constant volume equilibrium calculation performed via the open-source Cantera software package [51]. Once $x_b(P)$ is known, the burning velocity $S_u(P, T_u)$ is calculated over the experimental range of pressure and temperature using Eq. A.2-2.

Data Reduction. Figure A.2-3 shows a typical pressure trace (solid line) from an experiment (CH_4 -air, $\phi=1.0$), along with T_b , T_u , and r_f , which are outputs of the two-zone model calculation. Only a portion of the pressure data is used for obtaining burning velocity, as denoted by the thick line on the pressure trace. For small r_f , the flame behavior is affected by flame stretch and the ignition process, and for large r_f , by heat losses to the walls and cellular instabilities; hence, typically only the central 75 % of the pressure data are used. The present data reduction was performed using a new NIST-developed tool, CVDART (Constant Volume Data Reduction

Tool) [69] which allows for detailed examination of the effects of different data ranges. The data range selected for each test was manually selected to minimize the effects of ignition and flame instabilities due to cellular flame formation at the larger radii.

Spherically propagating flames are subject to stretch rates inversely proportional to the flame radius [142],

$$\kappa = \frac{2}{r_f} \frac{dr_f}{dt} \quad (\text{A.2-6})$$

where κ is the stretch rate and dr_f/dt is the flame front velocity. Figure A.2-3 also shows the stretch rate for this experiment.

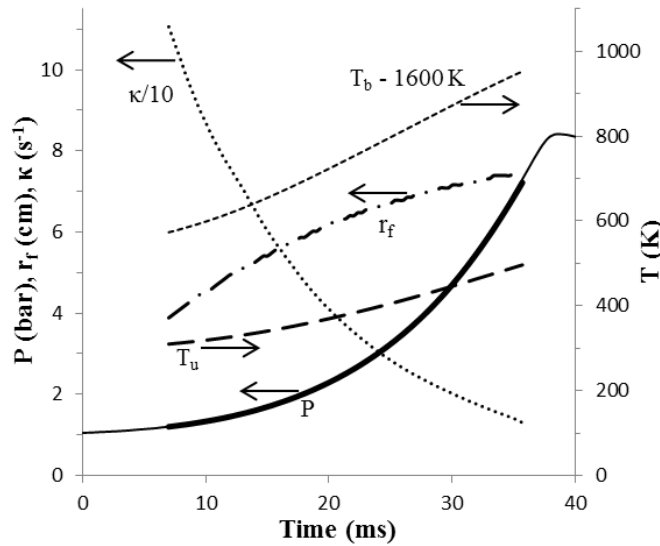


Figure A.2-3. Experimental pressure trace P , flame radius r_f , flame stretch rate κ , and gas temperature (unburned T_u and burned T_b) as a function of time

A single experiment provides burning velocity data for a range of pressure and temperature of the unburned gas, and these data are fit to the equation [33]:

$$S_L = S_{L,0} \left(\frac{T}{T_0} \right)^\alpha \left(\frac{P}{P_0} \right)^\beta \quad (\text{A.2-7})$$

in which S_L is the laminar burning velocity, P_0 is the initial pressure, T_0 is the initial temperature, $S_{L,0}$ is the laminar burning velocity at the initial conditions; α , β , and $S_{L,0}$ are the fitting parameters. In the experiments performed, T_0 is 299 ± 2 K, and P_0 is $0.868 \cdot 10^{-2}$ kPa, $1 \cdot 10^{-2}$ kPa, and $1.13 \cdot 10^{-2}$ kPa, (to provide more data for the curve fit). As described in Takizawa et al. [143], S_u^0 , α , and β depend upon ϕ and can be fit to the following equations (2–4):

$$S_{L0} = S_{L0,max} + s_1(f - f_{max})^2 + s_2(f - f_{max})^3 \quad (\text{A.2-8})$$

$$a = a_1 + a_2(f - 1) \quad (\text{A.2-9})$$

$$b = b_1 + b_2(f - 1) \quad (\text{A.2-10})$$

Thus, a_1 , a_2 , b_1 , b_2 , s_1 , s_2 , $S_{L0,max}$, and f_{max} are fitting parameters to the data, with $S_{L0,max}$ the maximum laminar burning velocity over all ϕ , and ϕ_{max} , the value of ϕ at which it occurs.

Figure A.2-4 shows the burning velocity of stoichiometric methane-air as a function of unburned gas temperature and chamber pressure. The light grey surface is the fit following Eq. A.2-7, and the darker grey data points (and lines through them) are the S_L values at each combination of unburned gas pressure and temperature for a specific run, to which Eq. A.2-7 is fit.

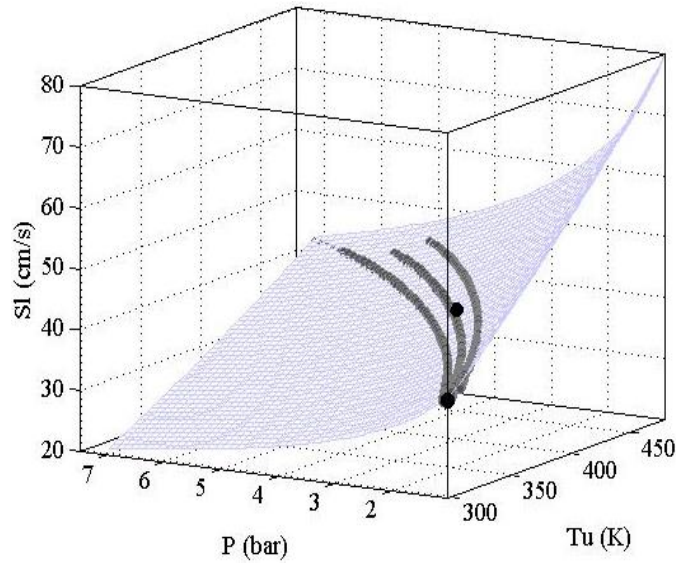


Figure A.2-4. Three-dimensional plot of burning velocity as a function of pressure P and unburned gas temperature T_u

The dark grey dots represent the data from three experiments, one at each initial pressure. The light grey surface represents the fitted results using Eq. A.2-7 and the black dots are the reported S_L at ambient ($T_0=298$ K, $P_0=101$ kPa) and compressed ($T_0=400$ K, $P_0=303$ kPa) conditions.

In the present method, spherical flame propagation is a critical condition for accurate determination of S_L from the pressure trace. Buoyancy can distort the shape of the flame, especially for slow burning mixtures (which are of particular interest in the present work). Takizawa et al. [138] estimated the minimum burning velocity measurable without error associated with buoyancy. Results showed that burning velocities as low as 6 cm/s could be measured with the constant-volume method. In the present work, cellular instabilities, which also invalidate the spherical flame assumption, are monitored through inspection of the S_L data of individual test runs. The onset of cellular instabilities is typically detected via a distinct

increase in S_L [140, 144], and these data (if occurring) are omitted during the experimental data fitting.

Uncertainties. Uncertainties in the measured parameters presented as expanded uncertainties ku_c from a combined standard uncertainty (estimated standard deviation) u_c , and a coverage factor $k=2$ (level of confidence approximately 95%). Relative uncertainties ku_c/X are reported, with X being the measured value of the parameter under consideration. Uncertainties in initial temperature and pressure, dynamic pressure rise, agent volume fraction, equivalence ratio, and burning velocity calculation and fitting to Eq. A.2-7 are considered. The expanded relative uncertainties related to reactant mixture preparation are 1.0% for the equivalence ratio, 0.3% for the volume fraction of air, and 0.8% for the volume fraction of fuel. Uncertainty in the volume fraction of refrigerant ranged from 4% at low concentrations (volume fraction of 0.01) to <1% at higher concentrations (volume fraction of 0.05). Relative uncertainties for the dynamic pressure rise, initial pressure, and initial temperature are 1.3%, 0.7%, and 0.4%. Thus, the maximum expanded relative uncertainty (ku_c/X) for the reported experimental burning velocities is 12%. This does not consider the uncertainty due to the selected data range for the extrapolation, which are discussed in detail for the present data in Kim et al.[145].

Experimental Burning Velocity Test Data. Table A.2.3 lists the fitting parameters (Eq. A.2-8, to A.2.10) for the burning velocity as a function of with ϕ , T_u and P for pure HFC-152a and its mixtures with HFC-134a and HFO-1234yf. The corresponding raw experimental data are given in Table A.2.4.

Table A.2-3. Fitting parameters for the variation of S_L with ϕ , T_u and P for experimental burning velocity data obtained in 2-L experiment from pressure rise data for R-152a/134a and R-152a/1234yf mixtures. Data presented for 298 K, 101 kPa initial conditions, and dry air (<2% r.h.) of wet air (50 % r.h.) as noted.

Composition (mole frac)	Humidity	S_{u0} (cm/s)				α		β	
		$S_{u0,max}$	s1	ϕ_{max}	s2	a1	a2	b1	b2
R-152a									
(1.0)	Dry	22.92	-85.94	1.10	-13.80	1.25	-0.56	-0.06	0.20
R-152a/134a									
(0.8/0.2)		18.05	-75.78	1.09	-6.23	2.26	-2.01	-0.71	-0.33
R-152a/134a									
(0.5/0.5)		9.99	-35.48	1.04	20.44	1.96	0.21	-0.19	-0.17
R-152a/1234yf									
(0.5/0.5)		13.40	-39.50	1.04	3.51	1.86	-1.49	-0.15	0.35
(0.4/0.6)		9.38	-50.71	0.99	61.30	2.48	-3.06	-0.21	0.75
(0.4/0.6)	Wet	11.61	-13.87	0.88	-11.07	2.36	-2.54	-0.27	0.69
(0.3/0.7)	Dry	5.74	-44.45	1.00	77.11	1.12	2.99	0.19	-0.51

Table A.2-4. Experimental burning velocity data obtained in 2-L experiment from pressure rise data for R-152a/134a and R-152a/1234yf mixtures. Data presented for 298K, 101 kPa initial conditions, dry air (<2% r.h.) and wet air (50 % r.h.) as noted. Blend compositions given in mole fraction.

Equivalence Ratio (ϕ)	Nominal Humidity	Run #	Run Date	Partial Pressure, torr				P_{tot}	P_{final}	Capacitance [nF]	Voltage [kV]	Nominal Spark Energy [mJ]
				p_1	p_2	p_{air}	p_w					
R-152a												
0.8	Dry	2	2019-12-05	43.6	N/A	647.9	N/A	692.2	659.7	10	10	2.5
		1	2019-12-05	50.3		747.4		798.3	760.1	10	10	2.5
		3	2019-12-09	57.0		846.6		904.3	860.2	10	10	2.5
0.9		4	2019-12-11	48.7		642.9		692.2	660.0	10	10	2.5
		5	2019-12-11	56.1		741.5		798.3	760.2	10	10	2.5
		6	2019-12-11	63.6		840.0		904.3	860.0	10	10	2.5
1		19	2019-12-16	53.7		637.8		692.2	659.9	10	10	2.5
		20	2019-12-16	62.0		735.7		798.3	760.2	10	10	2.5
		21	2019-12-16	70.1		833.5		904.3	860.2	10	10	2.5
1.1		7	2019-12-11	58.6		632.9		692.2	659.9	10	10	2.5
		8	2019-12-11	67.6		730.1		798.3	759.9	10	10	2.5
		9	2019-12-11	76.6		827.0		904.2	860.0	10	10	2.5
1.2		10	2019-12-11	63.5		628.1		692.1	659.7	10	10	2.5
		11	2019-12-11	73.2		724.5		798.3	760.1	10	10	2.5
		12	2019-12-11	82.9		820.7		904.3	859.8	10	10	2.5
1.3		13	2019-12-12	68.2		623.3		692.2	660.8	10	10	2.5
		14	2019-12-12	78.7		719.0		798.4	760.4	10	10	2.5
		15	2019-12-12	89.1		814.6		904.3	860.3	10	10	2.5
1.4		16	2019-12-12	72.9		618.7		692.2	660.0	10	10	2.5
		17	2019-12-12	84.1		713.6		798.3	760.5	10	10	2.5
		18	2019-12-12	95.3		808.5		904.3	859.9	10	10	2.5
R-152a/134a (0.8/0.2)												
0.8	Dry	21	2019-01-02	37.8	9.4	644.4	N/A	692.2	659.7	50	10	12.5
		2	2019-12-20	43.5	10.9	743.3		798.3	760.5	50	10	12.5
		9	2019-12-23	49.3	12.3	842.0		904.3	860.4	50	10	12.5
0.9		20	2019-01-02	42.1	10.5	638.9		692.2	659.7	50	10	12.5
		3	2019-12-20	48.6	12.1	737.0		798.3	760.4	50	10	12.5
		10	2019-12-23	55.0	13.7	834.9		904.3	860.1	50	10	12.5

1	16	2019-01-02	45.7	12.3	633.6		692.2	659.8	50	10	12.5
	4	2019-12-20	53.5	13.4	730.8		798.3	760.3	50	10	12.5
	11	2019-12-23	60.6	15.1	827.9		904.3	860.3	50	10	12.5
1.1	1	2019-01-02	50.6	12.6	628.3		692.2	660.1	50	10	12.5
	5	2019-12-20	58.4	14.6	724.7		798.3	760.3	50	10	12.5
	12	2019-12-23	66.1	16.5	821.1		904.3	860.0	50	10	12.5
1.2	17	2019-01-02	54.7	13.7	623.1		692.2	659.9	50	10	12.5
	6	2019-12-20	63.1	15.8	718.8		798.3	760.1	50	10	12.5
	13	2019-12-23	69.5	19.9	814.2		904.3	859.9	50	10	12.5
1.3	18	2019-01-02	58.8	14.7	618.0		692.2	659.8	50	10	12.5
	7	2019-12-20	67.8	17.0	712.9		798.3	760.0	50	10	12.5
	14	2019-12-23	76.8	19.2	807.6		904.3	859.8	50	10	12.5
1.4	19	2019-01-02	62.9	15.7	613.0		692.2	660.4	50	10	12.5
	8	2019-12-20	72.5	18.1	707.0		798.3	760.3	50	10	12.5
	15	2019-12-23	82.1	20.5	801.1		904.3	859.9	50	10	12.5

R-152a/134a (0.5/0.5)

0.8	Dry	12	2019-11-08	26.9	26.8	637.8	N/A	692.2	659.7	100	15	56.3
		3	2019-11-01	31.0	31.0	736.3		799.0	760.5	100	15	56.3
		4	2019-11-01	31.0	30.9	736.3		798.9	760.8	100	15	56.3
		18	2019-11-12	35.1	35.0	833.3		904.1	859.7	100	15	56.3
0.85		25	2019-11-13	28.4	28.4	634.7		692.1	659.7	100	15	56.3
		5	2019-11-01	32.8	32.7	732.8		799.0	760.9	100	15	56.3
		24	2019-11-13	37.1	37.1	829.2		904.1	859.5	100	15	56.3
0.9		11	2019-11-08	30.0	29.9	631.7		692.2	659.9	100	15	56.3
		2	2019-11-01	34.6	34.5	729.2		799.0	760.9	100	15	56.3
		19	2019-11-12	39.1	39.0	825.4		904.1	859.7	100	15	56.3
1		10	2019-11-08	33.0	32.9	625.7		692.2	659.9	100	15	56.3
		1	2019-11-01	38.0	38.0	722.3		799.0	760.5	100	15	56.3
		17	2019-11-12	43.0	42.9	816.8		903.4	859.3	100	15	56.3
1.1		13	2019-11-08	35.9	35.8	619.9		692.1	659.7	100	15	56.3
		6	2019-11-01	41.4	41.4	715.4		798.9	760.4	100	15	56.3
		20	2019-11-12	46.9	46.8	809.8		904.0	859.6	100	15	56.3
1.2		14	2019-11-08	38.8	38.7	614.0		692.2	659.8	100	15	56.3
		7	2019-11-01	44.8	44.7	708.8		799.0	760.8	100	15	56.3
		23	2019-11-13	50.7	50.6	802.2		904.1	859.8	100	15	56.3
1.3		15	2019-11-12	41.6	41.6	608.4		692.2	659.7	100	15	56.3
		8	2019-11-01	48.1	48.0	702.2		799.0	760.6	100	15	56.3
		21	2019-11-13	54.3	54.3	794.9		904.1	859.7	100	15	56.3
1.4		16	2019-11-12	44.4	44.3	602.8		692.2	660.3	100	15	56.3
		9	2019-11-04	51.2	51.2	695.8		799.0	760.8	100	15	56.3
		22	2019-11-13	58.0	57.9	787.5		904.1	859.8	100	15	56.3

R-152a/1234yf (0.5/0.5)

0.7	Dry	8	2020-02-12	22.3	22.2	753.2	N/A	798.3	759.9	100	15	56.3
0.8	Dry	9	2020-02-12	21.9	21.7	647.8		692.1	659.5	100	15	56.3
		2	2020-02-11	25.2	25.1	747.2		798.3	759.7	100	15	56.3
		16	2020-02-13	28.6	28.5	846.5		904.2	859.6	100	15	56.3
0.9		10	2020-02-12	24.4	24.3	642.7		692.1	659.5	100	15	56.3
		3	2020-02-12	28.1	28.1	741.4		798.3	760.1	100	15	56.3
		17	2020-02-13	31.8	31.8	839.9		904.2	859.5	100	15	56.3
1		11	2020-02-13	26.9	26.8	637.8		692.2	659.5	100	15	56.3
		1	2020-02-11	31.0	30.9	735.7		798.3	759.8	100	15	56.3
		18	2020-02-14	35.1	35.0	833.4		904.2	859.7	100	15	56.3
1.1		12	2020-02-13	29.3	29.3	632.8		692.2	659.5	100	15	56.3
		4	2020-02-12	33.8	33.8	730.0		798.3	760.2	100	15	56.3
		19	2020-02-14	38.3	38.2	827.1		904.3	860.0	100	15	56.3
1.2		13	2020-02-13	31.7	31.7	628.0		692.1	660.0	100	15	56.3
		5	2020-02-12	36.6	36.6	724.5		798.3	760.1	100	15	56.3
		20	2020-02-14	41.5	41.3	820.7		904.2	860.0	100	15	56.3
1.3		14	2020-02-13	34.1	34.1	623.2		692.1	660.0	100	15	56.3
		6	2020-02-12	39.5	39.3	718.8		798.3	759.9	100	15	56.3
		21	2020-02-14	44.5	44.5	814.5		904.3	859.8	100	15	56.3
1.4		15	2020-02-13	36.5	36.4	618.7		692.4	659.7	100	15	56.3
		7	2020-02-12	42.1	42.0	713.6		798.3	759.8	100	15	56.3
		22	2020-02-14	47.6	47.6	808.3		904.3	859.7	100	15	56.3

R-152a/1234yf (0.4/0.6)

0.8	Dry	1	2020-02-20	17.5	26.1	647.8	N/A	692.2	660.0	100	15	56.3
0.9	Dry	2	2020-02-20	19.5	29.2	647.8		692.2	659.9	100	15	56.3
		8	2020-02-21	22.5	33.7	642.8		798.3	760.4	100	15	56.3
		14	2020-02-21	25.5	38.2	741.4		904.3	860.1	100	15	56.3
1		3	2020-02-20	21.5	32.2	839.9		692.2	659.9	100	15	56.3
		9	2020-02-21	24.8	37.1	637.8		798.3	760.0	100	15	56.3
		15	2020-02-24	28.1	42.0	735.6		904.3	860.0	100	15	56.3
1.1		4	2020-02-20	23.5	35.1	833.4		692.2	659.8	100	15	56.3
		10	2020-02-21	27.1	40.5	633.0		798.3	759.9	100	15	56.3
		16	2020-02-24	30.7	45.9	730.0		904.3	859.8	100	15	56.3
1.2		5	2020-02-20	25.4	38.0	826.9		692.2	659.7	100	15	56.3
		11	2020-02-21	29.3	43.8	628.1		798.3	760.2	100	15	56.3
		17	2020-02-24	33.2	49.7	724.4		904.3	859.8	100	15	56.3
1.3		6	2020-02-20	27.3	40.9	820.6		692.2	659.7	100	15	56.3
		12	2020-02-21	31.5	47.1	623.2		798.2	760.1	100	15	56.3
		18	2020-02-24	35.7	53.4	718.8		904.3	859.8	100	15	56.3
1.4		7	2020-02-20	29.2	43.7	814.4		692.1	659.6	100	15	56.3
		13	2020-02-21	33.7	50.4	618.6		798.2	760.0	100	15	56.3

		19	2020-02-24	38.1	57.1	713.4		904.3	859.7	100	15	56.3
0.9	46.1	16	Feb-9-2020	19.2	28.8	636.2	8.2	692.2	659.8	100	15	56.3
	41.7	18	Feb-9-2020	22.1	33.3	734.7	8.6	798.4	759.8	100	15	56.3
	39.0	17	Feb-9-2020	25.0	37.7	832.7	9.1	904.3	859.8	100	15	56.3
1	47.6	3	Feb-1-2020	21.2	31.9	630.6	8.4	692.1	659.7	100	15	56.3
	45.0	1	Feb-1-2020	24.3	36.7	728.0	9.2	798.3	759.5	100	15	56.3
	40.2	2	Feb-1-2020	27.7	41.4	825.6	9.3	904.2	859.5	100	15	56.3
1.1	51.8	6	Feb-2-2020	23.2	34.7	625.1	9.1	692.1	659.1	100	15	56.3
	44.6	4	Feb-2-2021	26.7	40.1	722.3	9.1	798.4	759.1	100	15	56.3
	39.6	5	Feb-2-2022	30.3	45.3	819.4	9.1	904.2	859.7	100	15	56.3
1.2	49.8	7	Feb-2-2020	24.9	37.5	620.9	8.7	692.2	659.9	100	15	56.3
	42.2	9	Feb-3-2020	28.8	43.3	716.9	9.0	798.3	759.9	100	15	56.3
	38.3	8	Feb-3-2020	32.7	49.0	812.8	9.6	904.3	859.7	100	15	56.3
1.3	49.2	11	Feb-4-2020	26.9	40.4	616.2	8.5	692.1	659.4	100	15	56.3
	44.6	10	Feb-4-2020	31.2	46.4	711.6	8.9	798.3	758.9	100	15	56.3
	41.8	12	Feb-4-2020	35.2	52.7	806.8	9.5	904.3	859.4	100	15	56.3
1.4	50.2	14	Feb-4-2020	28.8	43.2	611.5	8.6	692.1	659.3	100	15	56.3
	45.2	13	Feb-4-2020	33.2	49.8	706.1	9.0	798.3	759.3	100	15	56.3
	41.3	15	Feb-5-2020	37.5	56.5	800.9	9.3	904.3	859.7	100	15	56.3

R-152a/R234yf (0.3/0.7)

0.9	Dry	1	2020-02-17	16.9	39.2	742.7	N/A	798.4	760.8	100	15	56.3
1		7	2020-02-17	16.2	37.5	639.1		692.1	659.8	100	15	56.3
		2	2020-02-17	18.6	43.3	737.0		798.4	760.6	100	15	56.3
		12	2020-02-19	21.2	48.9	834.8		904.2	859.9	100	15	56.3
1.1		8	2020-02-17	17.7	40.9	634.2		692.2	659.9	100	15	56.3
		3	2020-02-17	20.4	47.2	731.4		798.4	760.5	100	15	56.3
		13	2020-02-19	23.0	53.6	828.2		904.2	859.9	100	15	56.3
1.2		9	2020-02-19	19.0	44.4	629.2		692.2	660.0	100	15	56.3
		4	2020-02-17	22.1	51.0	725.7		798.2	760.2	100	15	56.3
		14	2020-02-19	25.0	57.8	822.0		904.2	859.9	100	15	56.3
1.3		10	2020-02-19	20.5	47.8	624.6		692.3	660.0	100	15	56.3
		5	2020-02-17	23.7	55.0	720.3		798.3	760.2	100	15	56.3
		15	2020-02-19	26.8	62.3	815.8		904.2	859.7	100	15	56.3
1.4		11	2020-02-19	22.0	51.0	619.9		692.3	660.6	100	15	56.3
		6	2020-02-17	25.3	58.9	714.8		798.4	759.9	100	15	56.3
		16	2020-02-19	29.5	65.7	809.7		904.2	859.6	100	15	56.3

A.3 Task 4 - Tabulated Flow-Boiling Heat-Transfer Measurements

Table A.3-1. Measured flow-boiling heat-transfer data for R-515B, R-450A, R-513A, and HFC-134a

Listed are Nusselt number Nu , thermodynamic quality x_q , reduced pressure p , Boiling number Bo , Bond number B_{nd} , Reynolds number Re , and the relative combined, expanded ($k = 2$) uncertainty in the Nusselt number U_c . Data are presented in the sequence measured. The last column provides the test refrigerant.

Nu	x_q	P_r	Bo	B_{nd}	Re	$U_c/\%$	fluid
207.5	0.15	0.11	0.000128	0.0224	5853.3	27.0	R-513A
532.5	0.29	0.11	0.000424	0.0225	5836.2	21.0	R-513A
527.8	0.40	0.11	0.000463	0.0225	5831.9	20.0	R-513A
514.0	0.61	0.10	0.000529	0.0225	5820.7	20.0	R-513A
497.5	0.83	0.10	0.000590	0.0223	5805.9	21.0	R-513A
478.7	0.99	0.10	0.000653	0.0223	5787.9	22.0	R-513A
456.7	0.99	0.10	0.000723	0.0223	5766.5	24.0	R-513A
172.8	0.12	0.11	0.000108	0.0225	5818.1	27.0	R-513A
434.5	0.24	0.10	0.000352	0.0225	5803.0	21.0	R-513A
428.6	0.33	0.10	0.000384	0.0225	5798.8	20.0	R-513A
415.6	0.51	0.10	0.000438	0.0222	5788.0	20.0	R-513A
401.2	0.69	0.10	0.000489	0.0223	5773.4	20.0	R-513A
385.3	0.91	0.10	0.000541	0.0223	5753.8	21.0	R-513A
367.6	0.99	0.10	0.000598	0.0221	5729.9	23.0	R-513A
161.5	0.10	0.10	0.000084	0.0223	6801.2	27.0	R-513A
369.9	0.19	0.10	0.000254	0.0223	6782.9	21.0	R-513A
364.3	0.26	0.10	0.000277	0.0223	6779.1	20.0	R-513A
350.2	0.38	0.10	0.000317	0.0223	6766.7	19.0	R-513A
334.6	0.52	0.10	0.000354	0.0221	6748.3	19.0	R-513A
317.4	0.67	0.10	0.000391	0.0221	6722.1	20.0	R-513A
298.3	0.86	0.10	0.000432	0.0219	6684.8	22.0	R-513A
139.6	0.08	0.10	0.000062	0.0225	7943.2	27.0	R-513A
323.5	0.15	0.10	0.000191	0.0222	7918.7	20.0	R-513A
318.3	0.20	0.10	0.000208	0.0223	7914.5	19.0	R-513A
305.9	0.29	0.10	0.000237	0.0223	7900.0	19.0	R-513A
291.4	0.39	0.10	0.000265	0.0223	7878.1	19.0	R-513A
275.2	0.51	0.10	0.000293	0.0221	7846.7	19.0	R-513A
257.5	0.65	0.10	0.000324	0.0221	7801.7	21.0	R-513A
140.0	0.13	0.11	0.000113	0.0225	3867.1	28.0	R-513A
281.2	0.23	0.11	0.000281	0.0225	3860.8	23.0	R-513A
283.5	0.30	0.11	0.000306	0.0225	3859.0	23.0	R-513A
285.1	0.44	0.10	0.000350	0.0225	3854.4	23.0	R-513A

Table A.3-1. (continued)

Nu	x_q	Pr	Bo	B_{nd}	Re	$U_c/\%$	fluid
285.4	0.59	0.10	0.000390	0.0225	3848.5	24.0	R-513A
284.1	0.76	0.10	0.000432	0.0223	3840.6	26.0	R-513A
281.8	0.97	0.10	0.000478	0.0223	3829.8	29.0	R-513A
340.0	0.24	0.10	0.000293	0.0223	3969.0	25.0	R-513A
337.8	0.32	0.10	0.000320	0.0223	3967.4	24.0	R-513A
330.9	0.46	0.10	0.000366	0.0223	3963.0	23.0	R-513A
323.1	0.62	0.10	0.000408	0.0223	3957.0	23.0	R-513A
313.6	0.79	0.10	0.000452	0.0223	3948.7	24.0	R-513A
302.3	0.99	0.10	0.000499	0.0221	3937.4	26.0	R-513A
309.4	0.21	0.10	0.000252	0.0223	4170.2	25.0	R-513A
306.9	0.27	0.10	0.000275	0.0223	4168.7	24.0	R-513A
300.2	0.40	0.10	0.000314	0.0223	4164.2	23.0	R-513A
292.1	0.53	0.10	0.000351	0.0223	4158.1	23.0	R-513A
282.7	0.68	0.10	0.000388	0.0223	4149.9	24.0	R-513A
272.2	0.87	0.10	0.000429	0.0221	4138.4	26.0	R-513A
201.8	0.05	0.11	0.000190	0.0225	5732.2	22.0	R-513A
201.3	0.13	0.11	0.000161	0.0225	5728.1	21.0	R-513A
198.2	0.19	0.10	0.000135	0.0225	5723.5	20.0	R-513A
191.8	0.24	0.10	0.000111	0.0225	5718.7	21.0	R-513A
177.4	0.28	0.10	0.000083	0.0225	5712.3	29.0	R-513A
208.2	0.20	0.10	0.000200	0.0223	2673.0	29.0	R-513A
207.4	0.25	0.10	0.000218	0.0223	2672.3	27.0	R-513A
204.8	0.35	0.10	0.000249	0.0223	2670.5	25.0	R-513A
201.6	0.45	0.10	0.000278	0.0223	2668.2	25.0	R-513A
197.6	0.58	0.10	0.000308	0.0223	2665.2	25.0	R-513A
192.8	0.72	0.10	0.000341	0.0221	2661.0	27.0	R-513A
168.4	0.04	0.10	0.000211	0.0225	6109.5	18.0	R-513A
172.4	0.13	0.10	0.000180	0.0222	6104.1	17.0	R-513A
174.9	0.20	0.10	0.000151	0.0222	6097.9	16.0	R-513A
174.7	0.25	0.10	0.000124	0.0223	6091.1	17.0	R-513A
169.4	0.30	0.10	0.000093	0.0223	6082.3	24.0	R-513A
183.7	0.28	0.10	0.000194	0.0222	2675.8	30.0	R-513A
184.0	0.28	0.10	0.000194	0.0222	2675.1	30.0	R-513A
182.4	0.28	0.10	0.000196	0.0223	2647.4	30.0	R-513A
219.1	0.33	0.10	0.000231	0.0223	2653.5	30.0	R-513A
205.2	0.31	0.10	0.000217	0.0223	2656.5	30.0	R-513A
148.3	0.08	0.11	0.000077	0.0225	6063.3	30.0	R-513A
145.1	0.10	0.11	0.000086	0.0225	6062.2	26.0	R-513A
315.8	0.18	0.10	0.000248	0.0225	6046.8	20.0	R-513A

Table A.3-1. (continued)

Nu	x_q	Pr	Bo	B_{nd}	Re	$U_c/\%$	fluid
298.3	0.37	0.10	0.000309	0.0222	6033.5	18.0	R-513A
285.9	0.50	0.10	0.000345	0.0223	6019.1	18.0	R-513A
272.7	0.66	0.10	0.000382	0.0223	5998.8	19.0	R-513A
258.1	0.84	0.10	0.000422	0.0221	5970.2	20.0	R-513A
162.7	0.04	0.11	0.000160	0.0224	7327.9	19.0	R-513A
164.6	0.10	0.11	0.000135	0.0225	7320.8	18.0	R-513A
164.2	0.16	0.11	0.000113	0.0225	7312.8	17.0	R-513A
161.1	0.20	0.10	0.000092	0.0225	7304.0	18.0	R-513A
151.2	0.23	0.10	0.000068	0.0225	7292.5	25.0	R-513A
204.6	0.07	0.11	0.000248	0.0224	4385.6	23.0	R-513A
202.8	0.17	0.11	0.000210	0.0224	4382.8	22.0	R-513A
198.5	0.25	0.11	0.000175	0.0225	4379.7	21.0	R-513A
190.6	0.31	0.11	0.000143	0.0225	4376.5	22.0	R-513A
174.7	0.37	0.11	0.000105	0.0225	4372.4	30.0	R-513A
235.9	0.08	0.11	0.000285	0.0225	4308.2	23.0	R-513A
234.9	0.20	0.11	0.000243	0.0225	4305.5	22.0	R-513A
231.5	0.29	0.11	0.000203	0.0225	4302.4	21.0	R-513A
224.7	0.36	0.10	0.000167	0.0225	4299.3	22.0	R-513A
209.4	0.43	0.10	0.000125	0.0225	4295.3	30.0	R-513A
250.7	0.12	0.11	0.000456	0.0225	4247.8	18.0	R-513A
251.4	0.31	0.11	0.000389	0.0225	4242.7	17.0	R-513A
249.3	0.46	0.10	0.000326	0.0225	4237.1	16.0	R-513A
244.3	0.58	0.10	0.000268	0.0225	4231.2	17.0	R-513A
231.5	0.68	0.10	0.000201	0.0223	4223.6	23.0	R-513A
194.6	0.05	0.10	0.000232	0.0225	7621.9	16.0	R-513A
199.1	0.15	0.10	0.000197	0.0225	7611.6	15.0	R-513A
201.1	0.23	0.10	0.000165	0.0222	7599.5	14.0	R-513A
199.9	0.29	0.10	0.000135	0.0222	7586.0	15.0	R-513A
192.2	0.34	0.10	0.000100	0.0223	7567.9	21.0	R-513A
230.7	0.13	0.11	0.000496	0.0224	2301.6	26.0	R-513A
230.6	0.34	0.11	0.000426	0.0225	2300.0	24.0	R-513A
228.8	0.51	0.11	0.000362	0.0225	2298.5	23.0	R-513A
225.3	0.63	0.11	0.000303	0.0225	2297.1	25.0	R-513A
219.5	0.08	0.11	0.000327	0.0225	7652.6	16.0	R-513A
225.9	0.22	0.10	0.000279	0.0225	7637.3	14.0	R-513A
230.7	0.33	0.10	0.000235	0.0222	7619.0	13.0	R-513A
232.3	0.41	0.10	0.000194	0.0223	7598.4	14.0	R-513A
227.9	0.49	0.10	0.000147	0.0223	7570.3	19.0	R-513A
220.8	0.52	0.10	0.000121	0.0221	7552.8	28.0	R-513A

Table A.3-1. (continued)

Nu	x_q	P_r	Bo	B_{nd}	Re	$U_c/\%$	fluid
190.1	0.58	0.10	0.000108	0.0218	7386.0	28.0	R-513A
219.8	0.61	0.09	0.000108	0.0216	7363.3	30.0	R-513A
136.0	0.08	0.08	0.000084	0.0197	4810.7	28.0	R-450A
135.8	0.11	0.08	0.000094	0.0197	4810.5	24.0	R-450A
261.5	0.19	0.08	0.000235	0.0195	4798.4	19.0	R-450A
259.7	0.25	0.08	0.000257	0.0195	4797.9	18.0	R-450A
253.4	0.37	0.08	0.000294	0.0195	4793.3	18.0	R-450A
245.1	0.49	0.08	0.000328	0.0195	4785.0	18.0	R-450A
235.2	0.64	0.08	0.000363	0.0193	4772.1	19.0	R-450A
223.8	0.81	0.08	0.000402	0.0194	4752.6	21.0	R-450A
129.3	0.06	0.08	0.000051	0.0195	7087.3	28.0	R-450A
127.2	0.07	0.08	0.000057	0.0195	7085.8	24.0	R-450A
264.0	0.13	0.08	0.000162	0.0196	7056.5	18.0	R-450A
259.4	0.17	0.08	0.000177	0.0196	7054.0	17.0	R-450A
247.2	0.25	0.08	0.000202	0.0194	7040.9	16.0	R-450A
233.0	0.34	0.08	0.000225	0.0194	7018.5	16.0	R-450A
217.5	0.44	0.08	0.000250	0.0192	6984.5	17.0	R-450A
200.9	0.56	0.07	0.000276	0.0191	6934.2	17.0	R-450A
139.3	0.11	0.08	0.000098	0.0195	3818.6	28.0	R-450A
253.9	0.19	0.08	0.000227	0.0195	3811.8	23.0	R-450A
255.1	0.25	0.08	0.000247	0.0195	3812.0	23.0	R-450A
253.0	0.37	0.08	0.000283	0.0195	3810.3	23.0	R-450A
248.4	0.49	0.08	0.000316	0.0195	3806.2	24.0	R-450A
241.5	0.62	0.08	0.000350	0.0194	3799.4	26.0	R-450A
232.6	0.79	0.08	0.000388	0.0194	3788.9	28.0	R-450A
191.7	0.21	0.08	0.000209	0.0195	2137.3	29.0	R-450A
196.4	0.27	0.08	0.000228	0.0195	2137.6	28.0	R-450A
202.4	0.37	0.08	0.000261	0.0195	2138.1	29.0	R-450A
209.1	0.78	0.08	0.000382	0.0192	4845.5	19.0	R-450A
123.1	0.06	0.08	0.000049	0.0195	7014.5	29.0	R-450A
120.9	0.07	0.08	0.000055	0.0195	7012.9	25.0	R-450A
245.5	0.12	0.08	0.000153	0.0196	6982.2	19.0	R-450A
241.0	0.16	0.08	0.000167	0.0196	6979.1	18.0	R-450A
229.6	0.24	0.08	0.000191	0.0194	6965.6	17.0	R-450A
216.7	0.32	0.08	0.000213	0.0194	6943.3	17.0	R-450A
202.8	0.42	0.08	0.000235	0.0192	6910.3	17.0	R-450A
187.8	0.53	0.07	0.000260	0.0191	6861.9	18.0	R-450A
132.8	0.11	0.08	0.000097	0.0195	3856.4	27.0	R-450A
239.5	0.19	0.08	0.000226	0.0195	3849.3	21.0	R-450A

Table A.3-1. (continued)

Nu	x_q	P_r	Bo	B_{nd}	Re	$U_c/\%$	fluid
238.6	0.25	0.08	0.000247	0.0195	3849.4	20.0	R-450A
234.8	0.36	0.08	0.000282	0.0195	3847.6	20.0	R-450A
229.2	0.48	0.08	0.000315	0.0195	3843.7	20.0	R-450A
222.4	0.62	0.08	0.000350	0.0194	3837.2	21.0	R-450A
214.3	0.79	0.08	0.000387	0.0194	3827.4	23.0	R-450A
134.3	0.09	0.08	0.000089	0.0195	3861.3	30.0	R-450A
133.9	0.11	0.08	0.000100	0.0195	3861.6	27.0	R-450A
246.5	0.20	0.08	0.000236	0.0195	3855.9	21.0	R-450A
245.5	0.26	0.08	0.000257	0.0195	3856.2	20.0	R-450A
241.6	0.38	0.08	0.000294	0.0195	3854.9	19.0	R-450A
235.6	0.50	0.08	0.000329	0.0195	3851.1	20.0	R-450A
228.5	0.65	0.08	0.000364	0.0195	3844.8	21.0	R-450A
219.8	0.82	0.08	0.000404	0.0193	3834.8	23.0	R-450A
130.7	0.09	0.08	0.000089	0.0195	3969.6	29.0	R-450A
130.6	0.11	0.08	0.000100	0.0195	3969.9	26.0	R-450A
242.4	0.20	0.08	0.000240	0.0195	3961.2	20.0	R-450A
241.4	0.26	0.08	0.000262	0.0195	3961.1	19.0	R-450A
237.0	0.38	0.08	0.000299	0.0195	3959.0	19.0	R-450A
231.4	0.51	0.08	0.000335	0.0195	3954.6	19.0	R-450A
224.3	0.66	0.08	0.000371	0.0194	3947.7	21.0	R-450A
216.0	0.83	0.08	0.000410	0.0194	3937.0	22.0	R-450A
171.4	0.18	0.08	0.000177	0.0195	2141.7	30.0	R-450A
177.0	0.22	0.08	0.000193	0.0195	2142.0	29.0	R-450A
184.0	0.31	0.08	0.000221	0.0195	2142.3	30.0	R-450A
175.2	0.09	0.08	0.000315	0.0195	4915.4	16.0	R-450A
182.2	0.22	0.08	0.000273	0.0195	4912.2	15.0	R-450A
188.2	0.33	0.08	0.000234	0.0195	4905.5	14.0	R-450A
192.6	0.41	0.08	0.000198	0.0195	4895.9	15.0	R-450A
195.2	0.49	0.08	0.000157	0.0194	4880.9	19.0	R-450A
194.0	0.53	0.08	0.000134	0.0194	4870.6	26.0	R-450A
168.4	0.60	0.07	0.000124	0.0190	4760.3	26.0	R-450A
192.9	0.63	0.07	0.000124	0.0190	4746.4	29.0	R-450A
155.4	0.07	0.08	0.000250	0.0195	5792.4	15.0	R-450A
163.7	0.17	0.08	0.000217	0.0195	5786.7	14.0	R-450A
171.5	0.26	0.08	0.000186	0.0195	5776.6	14.0	R-450A
178.1	0.33	0.08	0.000158	0.0195	5763.0	15.0	R-450A
183.4	0.39	0.08	0.000126	0.0194	5742.3	20.0	R-450A
184.1	0.42	0.08	0.000108	0.0194	5728.4	26.0	R-450A
174.1	0.49	0.07	0.000115	0.0190	5577.4	25.0	R-450A

Table A.3-1. (continued)

Nu	x_q	P_r	Bo	B_{nd}	Re	$U_c/\%$	fluid
196.0	0.52	0.07	0.000115	0.0190	5557.3	27.0	R-450A
192.3	0.11	0.08	0.000402	0.0195	3779.3	17.0	R-450A
196.6	0.28	0.08	0.000348	0.0195	3779.5	16.0	R-450A
200.4	0.41	0.08	0.000298	0.0195	3777.4	15.0	R-450A
203.0	0.52	0.08	0.000252	0.0195	3773.6	15.0	R-450A
204.4	0.62	0.08	0.000198	0.0194	3766.7	20.0	R-450A
203.9	0.66	0.08	0.000168	0.0194	3761.8	28.0	R-450A
181.1	0.10	0.08	0.000371	0.0195	2443.5	23.0	R-450A
183.0	0.26	0.08	0.000320	0.0195	2445.5	21.0	R-450A
183.7	0.38	0.08	0.000273	0.0195	2446.6	21.0	R-450A
182.6	0.48	0.08	0.000230	0.0195	2446.9	22.0	R-450A
178.5	0.57	0.08	0.000179	0.0195	2446.4	28.0	R-450A
157.0	0.06	0.08	0.000226	0.0197	6589.4	15.0	R-450A
167.0	0.16	0.08	0.000196	0.0197	6582.2	15.0	R-450A
176.2	0.23	0.08	0.000168	0.0197	6570.1	14.0	R-450A
184.7	0.30	0.08	0.000143	0.0197	6554.3	16.0	R-450A
192.6	0.35	0.08	0.000114	0.0195	6530.5	20.0	R-450A
195.0	0.38	0.08	0.000097	0.0195	6514.6	26.0	R-450A
187.4	0.44	0.07	0.000111	0.0191	6331.6	25.0	R-450A
209.3	0.47	0.07	0.000110	0.0190	6307.1	27.0	R-450A
185.5	0.09	0.08	0.000336	0.0195	4754.0	17.0	R-450A
192.5	0.24	0.08	0.000291	0.0195	4751.2	15.0	R-450A
198.2	0.35	0.08	0.000250	0.0195	4744.9	14.0	R-450A
202.6	0.44	0.08	0.000211	0.0195	4735.9	15.0	R-450A
204.9	0.52	0.08	0.000166	0.0194	4721.6	20.0	R-450A
203.7	0.56	0.08	0.000141	0.0194	4712.0	28.0	R-450A
169.1	0.64	0.07	0.000125	0.0190	4607.5	27.0	R-450A
195.2	0.67	0.07	0.000125	0.0190	4594.3	29.0	R-450A
124.1	0.08	0.08	0.000057	0.0196	6739.5	26.0	R-450A
252.4	0.14	0.08	0.000163	0.0194	6713.0	19.0	R-450A
246.2	0.18	0.08	0.000178	0.0194	6711.1	18.0	R-450A
232.9	0.26	0.08	0.000204	0.0194	6699.6	17.0	R-450A
219.2	0.35	0.08	0.000227	0.0194	6679.4	17.0	R-450A
205.2	0.45	0.08	0.000252	0.0192	6648.7	17.0	R-450A
190.1	0.57	0.07	0.000278	0.0191	6602.9	18.0	R-450A
129.5	0.09	0.08	0.000075	0.0196	4900.2	30.0	R-450A
126.7	0.11	0.08	0.000084	0.0196	4900.0	26.0	R-450A
250.1	0.19	0.08	0.000222	0.0194	4885.5	19.0	R-450A
246.2	0.24	0.08	0.000242	0.0194	4884.4	18.0	R-450A

Table A.3-1. (continued)

Nu	x_q	P_r	Bo	B_{nd}	Re	$U_c/\%$	fluid
237.7	0.36	0.08	0.000276	0.0194	4878.8	18.0	R-450A
228.9	0.47	0.08	0.000309	0.0194	4869.5	18.0	R-450A
219.3	0.61	0.08	0.000342	0.0192	4855.6	19.0	R-450A
208.8	0.78	0.08	0.000378	0.0192	4835.1	21.0	R-450A
133.9	0.11	0.08	0.000091	0.0196	3827.2	29.0	R-450A
231.4	0.18	0.08	0.000205	0.0194	3821.3	22.0	R-450A
229.3	0.23	0.08	0.000224	0.0194	3821.5	21.0	R-450A
224.1	0.34	0.08	0.000256	0.0194	3819.7	20.0	R-450A
217.5	0.44	0.08	0.000285	0.0194	3815.2	21.0	R-450A
209.9	0.57	0.08	0.000316	0.0194	3807.8	22.0	R-450A
201.3	0.72	0.08	0.000350	0.0192	3796.3	23.0	R-450A
178.5	0.09	0.08	0.000275	0.0197	5855.7	17.0	R-450A
187.8	0.21	0.08	0.000238	0.0197	5850.3	15.0	R-450A
196.4	0.30	0.08	0.000204	0.0195	5840.1	15.0	R-450A
203.6	0.37	0.08	0.000173	0.0195	5826.2	16.0	R-450A
209.1	0.44	0.08	0.000136	0.0194	5804.6	21.0	R-450A
209.5	0.48	0.08	0.000116	0.0194	5790.2	28.0	R-450A
191.2	0.54	0.07	0.000123	0.0190	5632.9	25.0	R-450A
216.0	0.58	0.07	0.000122	0.0190	5612.2	28.0	R-450A
132.7	0.04	0.08	0.000110	0.0194	6649.7	23.0	R-450A
139.7	0.09	0.08	0.000097	0.0194	6645.6	21.0	R-450A
146.1	0.13	0.08	0.000085	0.0194	6638.9	19.0	R-450A
151.7	0.16	0.08	0.000074	0.0194	6630.2	20.0	R-450A
156.7	0.19	0.08	0.000061	0.0194	6617.2	27.0	R-450A
158.5	0.11	0.08	0.000086	0.0197	5053.7	28.0	R-450A
311.8	0.19	0.08	0.000229	0.0197	5041.0	21.0	R-450A
306.4	0.25	0.08	0.000250	0.0197	5040.5	20.0	R-450A
294.8	0.37	0.08	0.000286	0.0195	5035.7	19.0	R-450A
282.2	0.49	0.08	0.000319	0.0195	5026.7	19.0	R-450A
268.5	0.63	0.08	0.000354	0.0195	5012.6	20.0	R-450A
253.3	0.80	0.08	0.000392	0.0194	4991.4	21.0	R-450A
154.4	0.11	0.09	0.000082	0.0199	5310.3	28.0	R-450A
321.6	0.19	0.09	0.000229	0.0200	5296.8	21.0	R-450A
317.6	0.25	0.09	0.000250	0.0199	5296.9	20.0	R-450A
306.8	0.36	0.09	0.000286	0.0199	5292.8	19.0	R-450A
294.6	0.49	0.08	0.000320	0.0198	5284.3	19.0	R-450A
281.0	0.63	0.08	0.000354	0.0198	5270.4	19.0	R-450A
265.9	0.80	0.08	0.000392	0.0196	5249.0	20.0	R-450A
163.6	0.12	0.09	0.000084	0.0204	5148.1	29.0	R-450A

Table A.3-1. (continued)

Nu	x_q	P_r	Bo	B_{nd}	Re	$U_c/\%$	fluid
346.1	0.20	0.09	0.000239	0.0202	5139.1	22.0	R-450A
341.6	0.26	0.09	0.000260	0.0202	5139.8	21.0	R-450A
330.5	0.38	0.09	0.000298	0.0202	5137.7	20.0	R-450A
318.7	0.51	0.09	0.000333	0.0202	5132.0	20.0	R-450A
305.3	0.66	0.09	0.000369	0.0202	5122.1	20.0	R-450A
290.5	0.83	0.09	0.000409	0.0200	5106.7	22.0	R-450A
186.3	0.13	0.08	0.000109	0.0196	4838.3	30.0	R-450A
253.1	0.21	0.08	0.000194	0.0194	4817.5	19.0	R-450A
252.8	0.26	0.08	0.000212	0.0194	4814.8	18.0	R-450A
248.1	0.35	0.08	0.000242	0.0194	4806.3	17.0	R-450A
240.6	0.46	0.08	0.000271	0.0192	4794.4	17.0	R-450A
231.1	0.58	0.08	0.000300	0.0192	4777.6	18.0	R-450A
219.4	0.72	0.07	0.000332	0.0191	4753.8	18.0	R-450A
242.7	0.17	0.10	0.000075	0.0221	8878.1	28.0	R-513A
237.9	0.19	0.10	0.000081	0.0221	8873.5	26.0	R-513A
225.8	0.23	0.10	0.000093	0.0221	8859.2	24.0	R-513A
212.7	0.27	0.10	0.000104	0.0221	8838.4	23.0	R-513A
198.7	0.32	0.10	0.000115	0.0219	8809.2	22.0	R-513A
184.0	0.37	0.10	0.000127	0.0219	8768.0	23.0	R-513A
216.1	0.12	0.10	0.000051	0.0219	10756.5	29.0	R-513A
213.2	0.13	0.10	0.000056	0.0219	10751.5	28.0	R-513A
204.0	0.16	0.10	0.000064	0.0219	10735.6	26.0	R-513A
193.3	0.19	0.10	0.000071	0.0217	10712.3	25.0	R-513A
181.2	0.22	0.10	0.000079	0.0217	10679.7	24.0	R-513A
167.7	0.26	0.09	0.000087	0.0218	10633.5	24.0	R-513A
187.1	0.08	0.10	0.000037	0.0219	12967.9	30.0	R-513A
184.9	0.10	0.10	0.000042	0.0219	12952.6	28.0	R-513A
178.8	0.12	0.10	0.000047	0.0217	12929.5	27.0	R-513A
170.2	0.14	0.10	0.000052	0.0217	12896.7	27.0	R-513A
159.8	0.17	0.10	0.000057	0.0218	12850.2	28.0	R-513A
174.1	0.12	0.10	0.000038	0.0219	12997.6	30.0	R-513A
163.7	0.14	0.10	0.000042	0.0219	12966.5	29.0	R-513A
152.2	0.16	0.10	0.000046	0.0217	12923.1	28.0	R-513A
185.8	0.11	0.10	0.000034	0.0221	13308.7	30.0	R-513A
177.7	0.13	0.10	0.000038	0.0221	13284.5	28.0	R-513A
167.9	0.15	0.10	0.000042	0.0221	13251.9	26.0	R-513A
156.7	0.17	0.10	0.000046	0.0219	13207.1	25.0	R-513A
243.9	0.15	0.10	0.000085	0.0221	10042.7	24.0	R-513A
238.1	0.17	0.10	0.000092	0.0221	10037.1	23.0	R-513A

Table A.3-1. (continued)

Nu	x_q	P_r	Bo	B_{nd}	Re	$U_c/\%$	fluid
225.2	0.21	0.10	0.000106	0.0221	10018.1	21.0	R-513A
211.1	0.26	0.10	0.000118	0.0221	9989.5	21.0	R-513A
196.3	0.31	0.10	0.000130	0.0219	9948.6	21.0	R-513A
180.5	0.38	0.10	0.000144	0.0217	9890.1	21.0	R-513A
265.2	0.17	0.10	0.000093	0.0221	9862.3	23.0	R-513A
262.0	0.19	0.10	0.000102	0.0221	9856.1	22.0	R-513A
250.8	0.24	0.10	0.000116	0.0221	9836.0	21.0	R-513A
236.9	0.29	0.10	0.000130	0.0221	9806.5	20.0	R-513A
221.4	0.35	0.10	0.000144	0.0219	9765.2	20.0	R-513A
204.2	0.42	0.10	0.000159	0.0219	9706.4	21.0	R-513A
273.5	0.18	0.10	0.000092	0.0223	9967.4	23.0	R-513A
273.2	0.21	0.10	0.000101	0.0223	9960.0	22.0	R-513A
265.1	0.26	0.10	0.000115	0.0221	9938.0	20.0	R-513A
252.3	0.31	0.10	0.000128	0.0221	9906.9	20.0	R-513A
236.5	0.36	0.10	0.000142	0.0219	9863.6	19.0	R-513A
218.5	0.44	0.10	0.000157	0.0219	9802.8	20.0	R-513A
279.1	0.20	0.10	0.000101	0.0223	9599.6	23.0	R-513A
277.9	0.22	0.10	0.000110	0.0223	9592.1	22.0	R-513A
269.2	0.28	0.10	0.000126	0.0223	9569.9	20.0	R-513A
255.4	0.33	0.10	0.000140	0.0221	9538.7	20.0	R-513A
239.4	0.39	0.10	0.000155	0.0221	9495.5	19.0	R-513A
220.9	0.47	0.10	0.000171	0.0219	9434.8	20.0	R-513A
258.8	0.19	0.10	0.000096	0.0223	9731.8	23.0	R-513A
255.0	0.21	0.10	0.000105	0.0223	9724.7	21.0	R-513A
243.2	0.26	0.10	0.000120	0.0221	9702.9	20.0	R-513A
229.2	0.31	0.10	0.000134	0.0221	9671.7	20.0	R-513A
213.6	0.37	0.10	0.000148	0.0219	9628.2	20.0	R-513A
196.8	0.45	0.10	0.000164	0.0219	9566.8	20.0	R-513A
187.4	0.18	0.10	0.000070	0.0225	7689.0	29.0	R-513A
268.3	0.24	0.10	0.000136	0.0223	7655.8	22.0	R-513A
265.4	0.27	0.10	0.000149	0.0223	7651.0	21.0	R-513A
255.6	0.34	0.10	0.000170	0.0223	7635.9	20.0	R-513A
243.6	0.42	0.10	0.000190	0.0223	7614.1	20.0	R-513A
230.0	0.50	0.10	0.000210	0.0221	7583.5	20.0	R-513A
214.6	0.60	0.10	0.000232	0.0219	7540.2	21.0	R-513A
251.5	0.14	0.11	0.000352	0.0230	8096.8	22.0	R-513A
241.7	0.29	0.11	0.000287	0.0228	8076.1	19.0	R-513A
226.2	0.40	0.11	0.000227	0.0228	8053.5	17.0	R-513A
203.6	0.47	0.11	0.000172	0.0228	8029.8	19.0	R-513A

Table A.3-1. (continued)

Nu	x_q	Pr	Bo	B_{nd}	Re	$U_c/\%$	fluid
95.4	0.60	0.10	0.000057	0.0223	7811.5	26.0	R-513A
110.7	0.61	0.10	0.000056	0.0221	7791.2	30.0	R-513A
218.7	0.14	0.11	0.000064	0.0227	10291.5	28.0	R-513A
272.3	0.18	0.11	0.000109	0.0225	10235.3	21.0	R-513A
270.4	0.21	0.11	0.000119	0.0225	10227.2	20.0	R-513A
260.4	0.27	0.10	0.000135	0.0225	10202.2	19.0	R-513A
247.0	0.33	0.10	0.000151	0.0223	10166.6	19.0	R-513A
231.1	0.40	0.10	0.000167	0.0223	10116.7	19.0	R-513A
213.5	0.48	0.10	0.000185	0.0221	10046.3	19.0	R-513A
185.9	0.12	0.11	0.000054	0.0224	10276.3	28.0	R-513A
266.3	0.17	0.10	0.000107	0.0225	10226.4	21.0	R-513A
262.7	0.19	0.10	0.000117	0.0225	10219.3	20.0	R-513A
250.9	0.25	0.10	0.000133	0.0222	10196.3	19.0	R-513A
236.9	0.31	0.10	0.000149	0.0223	10162.5	19.0	R-513A
221.0	0.37	0.10	0.000165	0.0223	10114.4	19.0	R-513A
203.8	0.46	0.10	0.000182	0.0221	10046.0	19.0	R-513A
145.7	0.11	0.11	0.000041	0.0225	10406.6	29.0	R-513A
260.0	0.15	0.10	0.000104	0.0222	10362.5	21.0	R-513A
254.1	0.18	0.10	0.000113	0.0222	10356.8	20.0	R-513A
239.9	0.23	0.10	0.000129	0.0223	10335.4	19.0	R-513A
224.8	0.29	0.10	0.000144	0.0223	10302.5	19.0	R-513A
208.8	0.35	0.10	0.000160	0.0221	10255.0	19.0	R-513A
192.0	0.43	0.10	0.000176	0.0219	10186.5	19.0	R-513A
146.7	0.13	0.10	0.000045	0.0223	9688.8	29.0	R-513A
269.9	0.18	0.10	0.000120	0.0223	9640.0	21.0	R-513A
263.0	0.21	0.10	0.000130	0.0223	9633.2	20.0	R-513A
247.5	0.27	0.10	0.000149	0.0221	9610.6	19.0	R-513A
231.4	0.33	0.10	0.000166	0.0221	9577.1	18.0	R-513A
214.6	0.41	0.10	0.000184	0.0219	9529.2	19.0	R-513A
196.8	0.50	0.10	0.000203	0.0217	9460.9	19.0	R-513A
224.6	0.16	0.11	0.000068	0.0225	9810.0	29.0	R-513A
290.0	0.21	0.10	0.000122	0.0223	9752.1	21.0	R-513A
287.0	0.24	0.10	0.000133	0.0223	9743.4	20.0	R-513A
274.9	0.30	0.10	0.000152	0.0223	9717.4	19.0	R-513A
259.6	0.37	0.10	0.000170	0.0221	9680.6	19.0	R-513A
241.8	0.45	0.10	0.000188	0.0221	9629.3	19.0	R-513A
222.4	0.54	0.10	0.000208	0.0219	9557.1	19.0	R-513A
149.9	0.22	0.10	0.000060	0.0223	7112.6	30.0	R-513A
291.8	0.28	0.10	0.000165	0.0223	7080.6	22.0	R-513A

Table A.3-1. (continued)

Nu	x_q	Pr	Bo	B_{nd}	Re	$U_c/\%$	fluid
285.5	0.32	0.10	0.000180	0.0221	7075.5	21.0	R-513A
271.5	0.40	0.10	0.000205	0.0221	7060.2	20.0	R-513A
256.6	0.49	0.10	0.000229	0.0221	7038.2	20.0	R-513A
240.8	0.59	0.10	0.000253	0.0219	7007.5	21.0	R-513A
223.7	0.72	0.10	0.000280	0.0219	6964.1	21.0	R-513A
187.2	0.21	0.10	0.000078	0.0223	7244.2	28.0	R-513A
286.3	0.28	0.10	0.000163	0.0223	7208.1	21.0	R-513A
283.6	0.32	0.10	0.000178	0.0223	7202.3	21.0	R-513A
274.4	0.40	0.10	0.000203	0.0221	7186.1	20.0	R-513A
262.6	0.49	0.10	0.000226	0.0221	7163.8	20.0	R-513A
248.9	0.59	0.10	0.000250	0.0219	7133.0	21.0	R-513A
233.0	0.71	0.10	0.000277	0.0219	7090.2	22.0	R-513A
263.2	0.21	0.10	0.000401	0.0221	6198.9	21.0	R-513A
250.3	0.38	0.10	0.000331	0.0219	6181.2	19.0	R-513A
233.5	0.50	0.10	0.000265	0.0219	6163.7	17.0	R-513A
211.8	0.59	0.10	0.000205	0.0219	6146.5	19.0	R-513A
189.1	0.33	0.07	0.000223	0.0190	4108.2	23.0	R-515B
193.7	0.42	0.07	0.000189	0.0188	4095.4	22.0	R-515B
196.9	0.49	0.07	0.000158	0.0188	4082.7	23.0	R-515B
198.7	0.55	0.07	0.000129	0.0188	4070.4	27.0	R-515B
174.6	0.10	0.08	0.000338	0.0196	5553.1	22.0	R-515B
177.3	0.24	0.08	0.000281	0.0196	5537.5	20.0	R-515B
177.5	0.35	0.08	0.000228	0.0194	5519.8	18.0	R-515B
173.2	0.43	0.08	0.000179	0.0194	5500.6	20.0	R-515B
222.6	0.15	0.07	0.000386	0.0192	4749.5	25.0	R-515B
215.9	0.31	0.07	0.000319	0.0190	4735.7	22.0	R-515B
205.2	0.43	0.07	0.000256	0.0191	4721.4	21.0	R-515B
189.7	0.52	0.07	0.000198	0.0191	4707.1	22.0	R-515B
87.5	0.66	0.07	0.000066	0.0187	4569.7	28.0	R-515B
153.7	0.17	0.07	0.000134	0.0188	5036.2	27.0	R-515B
159.2	0.22	0.07	0.000113	0.0188	5024.3	27.0	R-515B
163.7	0.27	0.07	0.000094	0.0188	5012.1	28.0	R-515B
218.5	0.21	0.07	0.000093	0.0187	6243.5	29.0	R-515B
196.2	0.25	0.07	0.000103	0.0186	6223.3	26.0	R-515B
175.3	0.30	0.06	0.000114	0.0186	6194.5	25.0	R-515B
155.1	0.36	0.06	0.000126	0.0184	6153.3	24.0	R-515B
304.9	0.23	0.07	0.000175	0.0189	5518.9	27.0	R-515B
290.8	0.27	0.07	0.000190	0.0189	5514.6	25.0	R-515B
263.8	0.36	0.07	0.000217	0.0188	5498.7	24.0	R-515B

Table A.3-1. (continued)

Nu	x_q	P_r	Bo	B_{nd}	Re	$U_c/\%$	fluid
238.3	0.46	0.07	0.000243	0.0188	5473.6	23.0	R-515B
214.3	0.56	0.07	0.000268	0.0187	5437.2	23.0	R-515B
190.7	0.70	0.07	0.000296	0.0186	5384.4	23.0	R-515B
340.8	0.28	0.07	0.000197	0.0188	5037.0	26.0	R-515B
327.5	0.33	0.07	0.000214	0.0188	5031.7	25.0	R-515B
299.5	0.43	0.07	0.000245	0.0187	5015.0	23.0	R-515B
272.4	0.54	0.07	0.000273	0.0187	4990.7	22.0	R-515B
246.1	0.66	0.07	0.000302	0.0186	4956.5	22.0	R-515B
219.5	0.81	0.06	0.000334	0.0185	4908.1	21.0	R-515B
292.5	0.17	0.07	0.000153	0.0192	6319.2	25.0	R-515B
279.0	0.21	0.07	0.000167	0.0192	6315.8	23.0	R-515B
252.5	0.28	0.07	0.000191	0.0190	6299.0	21.0	R-515B
227.6	0.37	0.07	0.000213	0.0191	6270.8	21.0	R-515B
203.7	0.46	0.07	0.000235	0.0189	6228.6	20.0	R-515B
180.4	0.58	0.07	0.000260	0.0188	6166.4	20.0	R-515B
276.8	0.12	0.08	0.000121	0.0193	7884.4	24.0	R-515B
268.3	0.15	0.08	0.000132	0.0193	7881.5	22.0	R-515B
245.9	0.21	0.08	0.000151	0.0193	7861.6	21.0	R-515B
221.7	0.28	0.07	0.000169	0.0192	7826.1	20.0	R-515B
197.8	0.35	0.07	0.000187	0.0192	7771.6	20.0	R-515B
173.8	0.45	0.07	0.000206	0.0191	7690.4	19.0	R-515B
280.0	0.10	0.07	0.000087	0.0192	9565.4	26.0	R-515B
269.5	0.13	0.07	0.000095	0.0192	9560.3	24.0	R-515B
244.3	0.17	0.07	0.000108	0.0192	9533.8	22.0	R-515B
218.3	0.22	0.07	0.000121	0.0190	9488.8	21.0	R-515B
193.0	0.28	0.07	0.000134	0.0189	9421.0	20.0	R-515B
168.7	0.34	0.07	0.000147	0.0188	9320.9	19.0	R-515B
320.0	0.34	0.07	0.000237	0.0188	3539.5	30.0	R-515B
308.0	0.45	0.07	0.000270	0.0188	3534.2	29.0	R-515B
293.9	0.56	0.07	0.000302	0.0188	3525.8	29.0	R-515B
277.6	0.69	0.07	0.000334	0.0188	3513.5	29.0	R-515B
259.4	0.86	0.07	0.000370	0.0187	3495.6	30.0	R-515B
123.1	0.06	0.08	0.000089	0.0194	9535.8	25.0	R-515B
129.5	0.09	0.08	0.000075	0.0195	9515.4	23.0	R-515B
134.6	0.12	0.08	0.000062	0.0193	9493.1	23.0	R-515B
137.1	0.15	0.08	0.000051	0.0193	9470.0	26.0	R-515B
120.3	0.09	0.08	0.000041	0.0196	7256.6	30.0	R-450A
221.6	0.13	0.08	0.000103	0.0194	7231.8	23.0	R-450A
217.9	0.16	0.08	0.000113	0.0194	7230.2	21.0	R-450A

Table A.3-1. (continued)

Nu	x_q	P_r	Bo	B_{nd}	Re	$U_c/\%$	fluid
206.9	0.21	0.08	0.000129	0.0194	7219.1	20.0	R-450A
194.7	0.27	0.08	0.000144	0.0194	7199.2	20.0	R-450A
181.2	0.33	0.08	0.000159	0.0193	7168.7	20.0	R-450A
166.7	0.41	0.07	0.000176	0.0191	7123.2	21.0	R-450A
126.0	0.13	0.08	0.000053	0.0196	6630.2	29.0	R-450A
239.0	0.18	0.08	0.000142	0.0194	6603.5	21.0	R-450A
233.7	0.21	0.08	0.000154	0.0194	6602.0	20.0	R-450A
220.9	0.29	0.08	0.000176	0.0194	6590.6	20.0	R-450A
207.0	0.36	0.08	0.000197	0.0192	6569.6	19.0	R-450A
192.1	0.45	0.08	0.000218	0.0192	6537.0	20.0	R-450A
176.1	0.56	0.07	0.000241	0.0191	6488.0	20.0	R-450A
209.2	0.09	0.08	0.000059	0.0193	8808.1	27.0	R-450A
209.7	0.10	0.08	0.000065	0.0193	8806.5	26.0	R-450A
203.9	0.13	0.08	0.000074	0.0191	8794.8	25.0	R-450A
193.6	0.17	0.07	0.000082	0.0191	8773.9	24.0	R-450A
181.0	0.21	0.07	0.000091	0.0192	8742.0	24.0	R-450A
166.1	0.25	0.07	0.000101	0.0190	8694.5	24.0	R-450A
186.6	0.15	0.07	0.000054	0.0189	8255.8	30.0	R-450A
171.9	0.17	0.07	0.000060	0.0189	8234.8	27.0	R-450A
156.9	0.20	0.07	0.000066	0.0188	8204.8	26.0	R-450A
141.6	0.23	0.07	0.000073	0.0188	8162.2	25.0	R-450A
203.5	0.28	0.09	0.000103	0.0210	4653.4	30.0	R-134a
254.4	0.35	0.09	0.000170	0.0208	4639.4	23.0	R-134a
252.0	0.40	0.09	0.000185	0.0208	4637.2	21.0	R-134a
245.2	0.48	0.09	0.000211	0.0208	4631.3	20.0	R-134a
237.0	0.57	0.08	0.000236	0.0208	4623.4	20.0	R-134a
227.5	0.67	0.08	0.000261	0.0208	4612.7	21.0	R-134a
216.8	0.80	0.08	0.000289	0.0207	4598.0	22.0	R-134a
181.0	0.13	0.09	0.000075	0.0210	6514.1	28.0	R-134a
260.4	0.18	0.08	0.000144	0.0208	6482.6	20.0	R-134a
258.5	0.22	0.08	0.000157	0.0208	6477.9	19.0	R-134a
249.8	0.29	0.08	0.000179	0.0208	6464.3	18.0	R-134a
238.2	0.37	0.08	0.000200	0.0207	6445.3	18.0	R-134a
224.5	0.46	0.08	0.000221	0.0207	6419.3	18.0	R-134a
209.1	0.57	0.08	0.000245	0.0205	6382.7	19.0	R-134a
254.9	0.20	0.08	0.000178	0.0208	4418.1	24.0	R-134a
251.9	0.25	0.08	0.000194	0.0208	4415.7	22.0	R-134a
244.4	0.34	0.08	0.000222	0.0208	4409.6	21.0	R-134a
236.2	0.43	0.08	0.000247	0.0208	4401.6	21.0	R-134a

Table A.3-1. (continued)

Nu	x_q	P_r	Bo	B_{nd}	Re	$U_c/\%$	fluid
227.4	0.54	0.08	0.000274	0.0207	4391.2	22.0	R-134a
217.4	0.67	0.08	0.000303	0.0207	4376.9	24.0	R-134a
189.8	0.10	0.09	0.000080	0.0210	6100.5	30.0	R-134a
272.5	0.16	0.09	0.000156	0.0208	6072.8	21.0	R-134a
269.1	0.20	0.09	0.000170	0.0208	6068.4	20.0	R-134a
259.6	0.28	0.08	0.000194	0.0208	6056.9	19.0	R-134a
248.4	0.36	0.08	0.000217	0.0208	6041.2	19.0	R-134a
235.8	0.46	0.08	0.000240	0.0207	6019.9	19.0	R-134a
221.6	0.57	0.08	0.000265	0.0207	5990.3	20.0	R-134a
230.6	0.21	0.09	0.000179	0.0208	3728.4	25.0	R-134a
227.8	0.25	0.09	0.000195	0.0208	3726.8	24.0	R-134a
221.7	0.34	0.08	0.000223	0.0208	3723.1	22.0	R-134a
215.4	0.44	0.08	0.000249	0.0208	3718.5	23.0	R-134a
208.3	0.55	0.08	0.000275	0.0208	3712.4	23.0	R-134a
200.6	0.68	0.08	0.000305	0.0208	3704.4	25.0	R-134a
201.5	0.31	0.08	0.000189	0.0208	2590.4	29.0	R-134a
197.6	0.39	0.08	0.000211	0.0208	2589.1	28.0	R-134a
193.6	0.48	0.08	0.000233	0.0208	2587.4	29.0	R-134a
189.5	0.59	0.08	0.000258	0.0207	2585.3	30.0	R-134a
162.1	0.06	0.09	0.000239	0.0210	4487.0	17.0	R-134a
171.9	0.17	0.09	0.000217	0.0210	4482.3	17.0	R-134a
182.3	0.25	0.09	0.000196	0.0210	4476.3	16.0	R-134a
193.0	0.33	0.09	0.000177	0.0210	4469.6	17.0	R-134a
207.4	0.40	0.09	0.000155	0.0210	4460.2	21.0	R-134a
216.3	0.44	0.09	0.000143	0.0208	4454.3	25.0	R-134a
193.4	0.08	0.09	0.000276	0.0210	3457.3	20.0	R-134a
201.3	0.20	0.09	0.000249	0.0210	3454.3	19.0	R-134a
209.6	0.30	0.09	0.000225	0.0210	3450.8	20.0	R-134a
218.8	0.38	0.09	0.000202	0.0210	3447.0	21.0	R-134a
231.6	0.46	0.09	0.000176	0.0208	3441.9	25.0	R-134a
240.4	0.50	0.09	0.000162	0.0208	3438.7	29.0	R-134a
158.8	0.05	0.09	0.000167	0.0208	6618.6	19.0	R-134a
170.4	0.12	0.08	0.000151	0.0208	6607.9	18.0	R-134a
181.8	0.18	0.08	0.000136	0.0208	6594.4	18.0	R-134a
192.8	0.24	0.08	0.000122	0.0208	6579.0	19.0	R-134a
205.4	0.29	0.08	0.000106	0.0207	6557.3	22.0	R-134a
211.8	0.31	0.08	0.000097	0.0207	6543.6	26.0	R-134a
227.5	0.38	0.08	0.000124	0.0204	6400.3	27.0	R-134a
244.5	0.41	0.08	0.000124	0.0203	6380.2	28.0	R-134a

Table A.3-1. (continued)

Nu	x_q	P_r	Bo	B_{nd}	Re	$U_c/\%$	fluid
150.4	0.07	0.09	0.000233	0.0210	2561.5	25.0	R-134a
158.4	0.17	0.09	0.000215	0.0210	2560.0	23.0	R-134a
167.5	0.25	0.09	0.000199	0.0210	2558.6	23.0	R-134a
177.7	0.33	0.09	0.000183	0.0210	2557.1	25.0	R-134a
193.3	0.40	0.09	0.000166	0.0208	2555.2	29.0	R-134a
167.3	0.06	0.09	0.000231	0.0210	4564.3	18.0	R-134a
176.3	0.16	0.09	0.000209	0.0210	4559.1	17.0	R-134a
185.7	0.25	0.09	0.000188	0.0208	4552.6	17.0	R-134a
195.0	0.32	0.09	0.000168	0.0208	4545.4	18.0	R-134a
207.0	0.39	0.08	0.000146	0.0208	4535.4	22.0	R-134a
213.9	0.42	0.08	0.000134	0.0208	4529.1	26.0	R-134a
216.4	0.49	0.08	0.000141	0.0205	4464.3	30.0	R-134a
165.4	0.06	0.09	0.000227	0.0210	4588.4	18.0	R-134a
174.4	0.16	0.09	0.000204	0.0210	4583.2	17.0	R-134a
184.0	0.24	0.09	0.000184	0.0208	4576.9	17.0	R-134a
193.4	0.31	0.09	0.000165	0.0208	4569.7	18.0	R-134a
205.6	0.38	0.08	0.000143	0.0208	4559.8	22.0	R-134a
212.8	0.41	0.08	0.000131	0.0208	4553.6	26.0	R-134a
160.8	0.06	0.09	0.000170	0.0210	6691.8	19.0	R-134a
171.5	0.13	0.09	0.000152	0.0210	6680.9	18.0	R-134a
181.9	0.19	0.09	0.000136	0.0208	6667.2	18.0	R-134a
191.7	0.24	0.09	0.000122	0.0208	6651.6	18.0	R-134a
202.4	0.30	0.08	0.000104	0.0208	6629.9	22.0	R-134a
207.5	0.32	0.08	0.000095	0.0208	6616.2	26.0	R-134a
223.9	0.39	0.08	0.000123	0.0204	6470.7	26.0	R-134a
240.2	0.42	0.08	0.000122	0.0204	6450.0	28.0	R-134a
160.3	0.06	0.09	0.000167	0.0210	6722.4	18.0	R-134a
171.2	0.13	0.09	0.000150	0.0210	6711.0	18.0	R-134a
181.6	0.19	0.09	0.000134	0.0208	6696.7	17.0	R-134a
191.2	0.24	0.08	0.000120	0.0208	6680.5	18.0	R-134a
201.4	0.29	0.08	0.000103	0.0208	6657.8	22.0	R-134a
205.9	0.32	0.08	0.000094	0.0207	6643.5	25.0	R-134a
220.8	0.38	0.08	0.000122	0.0204	6494.4	26.0	R-134a
236.4	0.41	0.08	0.000121	0.0204	6473.6	28.0	R-134a
261.0	0.47	0.08	0.000121	0.0203	6434.4	30.0	R-134a
182.1	0.08	0.09	0.000277	0.0210	3425.8	20.0	R-134a
189.9	0.20	0.09	0.000249	0.0210	3422.9	19.0	R-134a
198.3	0.29	0.09	0.000224	0.0210	3419.5	19.0	R-134a
207.2	0.38	0.09	0.000201	0.0210	3415.8	20.0	R-134a

Table A.3-1. (continued)

Nu	x_q	P_r	Bo	B_{nd}	Re	$U_c/\%$	fluid
219.2	0.46	0.09	0.000174	0.0210	3410.8	24.0	R-134a
227.2	0.50	0.09	0.000159	0.0210	3407.6	29.0	R-134a
149.0	0.07	0.08	0.000236	0.0208	2613.7	25.0	R-134a
157.0	0.17	0.08	0.000218	0.0208	2612.1	23.0	R-134a
166.0	0.26	0.08	0.000201	0.0208	2610.4	23.0	R-134a
176.1	0.33	0.08	0.000186	0.0208	2608.7	24.0	R-134a
191.2	0.41	0.08	0.000168	0.0208	2606.5	28.0	R-134a
252.8	0.18	0.08	0.000169	0.0208	4663.7	23.0	R-134a
249.5	0.23	0.08	0.000184	0.0208	4661.2	22.0	R-134a
241.5	0.31	0.08	0.000211	0.0208	4654.7	20.0	R-134a
233.1	0.40	0.08	0.000235	0.0208	4646.2	20.0	R-134a
223.5	0.51	0.08	0.000261	0.0207	4634.8	21.0	R-134a
213.0	0.63	0.08	0.000288	0.0207	4619.2	22.0	R-134a
181.2	0.10	0.09	0.000076	0.0208	6297.1	28.0	R-134a
252.3	0.16	0.08	0.000147	0.0208	6266.6	20.0	R-134a
248.4	0.20	0.08	0.000161	0.0208	6262.4	19.0	R-134a
238.1	0.27	0.08	0.000183	0.0207	6249.8	18.0	R-134a
226.5	0.35	0.08	0.000205	0.0207	6232.1	18.0	R-134a
213.9	0.44	0.08	0.000227	0.0207	6207.6	18.0	R-134a
199.9	0.55	0.08	0.000251	0.0205	6173.4	19.0	R-134a
186.6	0.11	0.08	0.000078	0.0208	6309.8	29.0	R-134a
251.8	0.16	0.08	0.000147	0.0207	6276.8	20.0	R-134a
246.7	0.20	0.08	0.000161	0.0207	6272.1	19.0	R-134a
235.6	0.28	0.08	0.000184	0.0207	6258.7	18.0	R-134a
223.4	0.35	0.08	0.000205	0.0207	6239.8	18.0	R-134a
210.1	0.45	0.08	0.000227	0.0205	6213.9	18.0	R-134a
195.9	0.56	0.08	0.000251	0.0206	6177.4	19.0	R-134a
241.9	0.20	0.08	0.000169	0.0207	3901.0	26.0	R-134a
238.2	0.24	0.08	0.000184	0.0207	3899.3	24.0	R-134a
230.7	0.33	0.08	0.000210	0.0207	3895.1	23.0	R-134a
222.9	0.42	0.08	0.000235	0.0207	3889.9	22.0	R-134a
214.6	0.52	0.08	0.000260	0.0207	3882.9	23.0	R-134a
205.8	0.65	0.08	0.000288	0.0207	3873.5	24.0	R-134a
204.1	0.79	0.08	0.000191	0.0208	2659.5	29.0	R-134a
200.1	0.87	0.08	0.000213	0.0208	2658.1	28.0	R-134a
195.7	0.96	0.08	0.000236	0.0208	2656.3	29.0	R-134a
191.2	0.99	0.08	0.000262	0.0208	2654.0	30.0	R-134a

A.4 Task 7 - Evaluation of Blend Performance in a Military ECU

Table A.4-1. Comparison of test and simulation results for ECU using HFC-134a

Parameter		Outdoor temperature			
		27.8 °C	35.0 °C	46.1 °C	51.7 °C
Total Capacity# W	Test	12386	11756	10225	9221
	Simulation	11681	11378	10015	9306
	Discrepancy*	-0.057	-0.032	-0.021	0.009
Refrigerant mass flow rate kg/h	Test	349.3	361.8	346.0	334.7
	Simulation	339.4	358	361.9	362.1
	Discrepancy*	-0.028	-0.011	0.046	0.082
Compressor Power W	Test	5139	6038	7687	8572
	Simulation	5040	5996	7380	8166
	Discrepancy*	-0.019	-0.007	-0.040	-0.047
Total Power W	Test	7459	8312	10000	10860
	Simulation	7324	8280	9664	10450
	Discrepancy*	-0.018	-0.004	-0.034	-0.038
COP	Test	1.661	1.414	1.023	0.849
	Simulation	1.595	1.374	1.036	0.891
	Discrepancy*	-0.040	-0.028	0.014	0.049

Refrigerant side; *(Simulation value/Test value) – 1

Table A.4-2. Comparison of test and simulation results for ECU using R-515B

Parameter		Outdoor temperature			
		27.8 °C	35.0 °C	46.1 °C	51.7 °C
Total Capacity# W	Test	10206	9516	7865	7385
	Simulation	10144	9436	8166	7413
	Discrepancy*	-0.006	-0.008	0.038	0.004
Refrigerant mass flow rate kg/h	Test	312.0	316.9	342.8	353.3
	Simulation	325.1	328.6	331.4	331.0
	Discrepancy*	0.042	0.037	-0.033	-0.063
Compressor Power W	Test	3762	4354	5459	6130
	Simulation	3698	4268	5244	5799
	Discrepancy*	-0.017	-0.020	-0.039	-0.054
Total Power W	Test	6082	6680	7709	8371
	Simulation	5982	6552	7528	8083
	Discrepancy*	-0.016	-0.019	-0.023	-0.034
COP	Test	1.678	1.425	1.020	0.882
	Simulation	1.696	1.440	1.085	0.917
	Discrepancy*	0.010	0.011	0.063	0.040

Refrigerant side; *(Simulation value/Test value) – 1

Table A.4-3. Comparison of test and simulation results for ECU using Tern-1

Parameter		Outdoor temperature			
		27.8 °C	35.0 °C	46.1 °C	51.7 °C
Total Capacity [#] W	Test	12178	11518	10112	9296
	Simulation	12249	11308	9846	9112
	Discrepancy[*]	0.006	-0.018	-0.026	-0.020
Refrigerant mass flow rate kg/h	Test	369.5	385.4	379.5	379.7
	Simulation	398.5	405.8	414.9	413.8
	Discrepancy[*]	0.078	0.053	0.093	0.090
Compressor Power W	Test	5037	5952	7575	8534
	Simulation	5243	6050	7458	8178
	Discrepancy[*]	0.041	0.016	-0.015	-0.042
Total Power W	Test	7356	8265	9877	10827
	Simulation	7553	8360	9768	10488
	Discrepancy[*]	0.027	0.011	-0.011	-0.031
COP	Test	1.656	1.394	1.024	0.859
	Simulation	1.622	1.353	1.008	0.869
	Discrepancy[*]	-0.020	-0.029	-0.015	0.012

[#] Refrigerant side; ^{*}(Simulation value/Test value) – 1

Table A.4-4. Comparison of test and simulation results for ECU using R-513A

Parameter		Outdoor temperature			
		27.8 °C	35.0 °C	46.1 °C	51.7 °C
Total Capacity [#] W	Test	12518	11875	10515	9670
	Simulation	12235	11293	9858	8986
	Discrepancy[*]	-0.057	-0.032	-0.021	0.009
Refrigerant mass flow rate kg/h	Test	396.4	404.7	440.4	430.4
	Simulation	420.2	426.5	434.2	433.3
	Discrepancy[*]	0.060	0.054	-0.014	0.007
Compressor Power W	Test	5508	6511	7971	8907
	Simulation	5410	6220	7641	8374
	Discrepancy[*]	-0.018	-0.045	-0.041	-0.060
Total Power W	Test	7841	8768	10271	11192
	Simulation	7802	8805	10265	11201
	Discrepancy[*]	-0.005	0.004	-0.001	0.001
COP	Test	1.596	1.354	1.024	0.864
	Simulation	1.568	1.283	0.960	0.802
	Discrepancy[*]	-0.018	-0.053	-0.062	-0.071

[#] Refrigerant side; ^{*}(Simulation value/Test value) – 1

Table A.4-5. Relative refrigerant-side capacity and COP of R-515B, Tern-1, R-513A versus HFC-134a from ECU laboratory tests

Fluid	$Q/Q_{\text{HFC-134a}} - 1$				$\text{COP}/\text{COP}_{\text{HFC-134a}} - 1$			
	Outdoor temperature				Outdoor temperature			
	27.8 °C	35.0 °C	46.1 °C	51.7 °C	27.8 °C	35.0 °C	46.1 °C	51.7 °C
R-515B	-0.176	-0.191	-0.231	-0.199	0.010	0.004	-0.003	0.039
Tern-1	-1.000	-1.000	-1.000	-1.000	-0.003	-0.017	0.001	0.012
R-513A	0.011	0.010	0.028	0.049	-0.039	-0.045	0.001	0.018

Table A.4-6. Relative refrigerant-side capacity and COP of R-515B, Tern-1, R-513A versus HFC-134a from modified ECU simulations with matching capacity at 35.0 °C test

Fluid	$Q/Q_{\text{HFC-134a}} - 1$				$\text{COP}/\text{COP}_{\text{HFC-134a}} - 1$			
	Outdoor temperature				Outdoor temperature			
	27.8 °C	35.0 °C	46.1 °C	51.7 °C	27.8 °C	35.0 °C	46.1 °C	51.7 °C
R-515B	0.021	0.000	-0.041	0.015	-0.108	-0.122	-0.136	-0.096
Tern-1	0.001	0.000	0.015	0.026	-0.014	-0.021	-0.011	-0.006
R-513A	0.004	-0.001	0.019	0.039	-0.018	-0.008	0.028	0.064

Table A.4-7. Relative refrigerant-side capacity and COP of CO₂ versus HFC-134a from modified ECU simulations with matching capacity at 35.0 °C test

ECU	$Q_{\text{CO}_2}/Q_{\text{HFC-134a}} - 1$				$\text{COP}_{\text{CO}_2}/\text{COP}_{\text{HFC-134a}} - 1$			
	Outdoor temperature				Outdoor temperature			
	27.8 °C	35.0 °C	46.1 °C	51.7 °C	27.8 °C	35.0 °C	46.1 °C	51.7 °C
Basic	0.021	0.000	-0.041	0.015	-0.108	-0.122	-0.136	-0.096
LLSL-HX	0.001	0.000	0.015	0.026	-0.014	-0.021	-0.011	-0.006

Appendix B: List of Scientific/Technical Publications

- Babushok, V. I., Burgess, D. R. Jr, Kim, D. K., Hegetschweiler, M. J., Linteris, G. T., Modeling of Combustion of Fluorine-Containing Refrigerants, (NIST Technical Note TN 2170), 2021, National Institute of Standards and Technology, Gaithersburg, MD, DOI: <https://doi.org/10.6028/NIST.TN.2170>.
- Bell, I. H., Mixture Models for Refrigerants R-1234yf/134a, R-1234yf/1234ze(E), and R-134a/1234ze(E) and Interim Models for R-125/1234yf, R-1234ze(E)/227ea, and R-1234yf/152a. *J. Phys. Chem. Ref. Data* 2022, 51, 013103.
- Bell, I. H., Domanski, P. A., McLinden, M. O., Linteris, G. T., The hunt for nonflammable refrigerant blends to replace R-134a, *Int. J. of Refrigeration* 104 2019 484-495.
- Fortin, T. J.; McLinden, M. O., Vapor and liquid (p- ρ -T-x) measurements of binary refrigerant blends containing R-134a, R-1234yf, and R-1234ze(E). *J. Chem. Engr. Data* 2023 (to be submitted).
- Hegetschweiler, M. J., Pagliaro, J. L., Berger, L., Hesse, R., Beeckmann, J., Bariki, C., Pitsch, H., Linteris, G. T., Data reduction considerations for spherical R-32 (CH₂F₂)-air flame experiments 2022, *Combust. Flame* 237 (2022) 111806.
- Hesse, R., Bariki, C., Hegetschweiler, M. J., Linteris, G., Pitsch, H., Beeckmann, J., Elucidating the challenges in extracting ultra-slow flame speeds in a closed vessel - A CH₂F₂ microgravity case study using optical and pressure-rise data, *Proc. Combust. Inst.* 2022 39, in press.
- Linteris, G. T., Bell, I. H., McLinden, M. O., An Empirical Model for Refrigerant Flammability Based on Molecular Structure and Thermodynamics, *Int. J. of Refrigeration* 104 2019 144-150. Outcalt, S. L.; Rowane, A. J., Bubble point measurements of mixtures of HFO and HFC refrigerants. *J. Chem. Eng. Data* 2021, 66, 4670-4683.
- Rowane, A. J.; Bell, I. H.; Huber, M. L.; Perkins, R. A., Thermal conductivity of binary mixtures of 1,1,1,2-tetrafluoroethane, 2,3,3,3-tetrafluoropropene, and trans-1,3,3,3-tetrafluoropropene refrigerants. *Ind. Eng. Chem. Res.* 2022, 66, 1365-1377.
- Rowane, A. J.; Perkins, R. A., Speed of sound measurements of binary mixture of 1,1,1,2-tetrafluoroethane (R-134a), 2,3,3,3-tetrafluoropropene (R-1234yf), and 1,3,3,3-tetrafluoropropene (R-1234ze(E)) refrigerants. *J. Chem. Engr. Data* 2022, 67, 1365-1377.
- Skye, H., Domanski, P., Brignoli, R., Lee, S., Bae, H.; Validation of and Optimization with a Vapor Compression Cycle Model Accounting for Refrigerant Thermodynamic and Transport Properties: With Focus on Low Global-Warming-Potential Refrigerants (NIST Technical Note 2233), 2022, <https://doi.org/10.6028/NIST.TN.2233>